

Non-equilibrium dynamics of a driven-dissipative dimerized spin-1/2 chain

Mohsen Yarmohammadi

A thesis presented for the degree of
Dr. rer. nat.

Theoretische Physik I
Fakultät Physik
Technische Universität Dortmund
Germany

2022

First reviewer: Prof. Dr. Götz. S. Uhrig
Second reviewer: Prof. Dr. Stephan W. Haas

Submission date: December 21, 2021
Defense date: March 3, 2022

Contents

Abstract	7
Acknowledgements	9
1 Introduction	11
1.1 Motivation	11
1.2 Non-equilibrium phenomena	12
1.3 Challenge and goal	15
1.4 Target materials	16
1.5 Outline	17
2 Method	19
2.1 The basic concept: operators in quantum mechanics	19
2.2 Mean-field approximation	20
2.3 Bond-operator representation	21
2.3.1 Sachdev's representation	22
2.3.2 Triplon operator representation	23
2.4 The Heisenberg equation of motion and Fermi's golden rule	23
2.5 The Magnus expansion	24
2.5.1 Magnus expansion for two driven coupled harmonic oscillators	25

2.6	Phonons in solids	26
2.7	Open quantum systems	28
2.7.1	The Lindblad master equation	28
2.7.2	Damped harmonic oscillator	32
2.8	The Lindemann criterion	33
2.9	The damped driven harmonic oscillator	34
2.10	Chapter summary	35
3	A dimerized spin-1/2 chain	37
3.1	Experimental observations	37
3.2	The J-model Hamiltonian	40
3.3	Approximations	42
3.4	Observables	47
3.5	Equations of motion	47
3.6	Chapter summary	50
4	Weak coupling regime: J-model	53
4.1	NESS in the phonon-driven spin system	53
4.1.1	Switch-on and switch-off processes	58
4.1.2	The influence of driving and SPC	59
4.1.3	Quantitative analysis of the convergence timescale in the spin NESS	62
4.1.4	A systematic study of the existence of NESS	65
4.2	Harmonic decompositions of the spin NESS	66
4.2.1	The influence of spin damping	69
4.3	Energy flow	70
4.4	Discussion on the heating issue	74
4.5	Experimental perspectives	76
4.6	Chapter summary	77
5	Strong coupling regime: J-model	79
5.1	Characterization of strong coupling regime	80
5.1.1	Late-time behavior of signals in the NESS	82
5.1.2	NESS occupations in the strong SPCs	84
5.2	Giant resonant self-blocking effect	85
5.2.1	Energy flows in the presence of a strong SPC	90
5.3	Strong SPC-induced magnetic-phononic hybrid states	91
5.3.1	Triplon mode dependence of SPC	97
5.3.2	SPC-induced harmonic decompositions	98

5.4	Off-resonant SPC-induced input energy flow	99
5.5	Chapter summary	100
6	Coupling based on J'-model	103
6.1	J' -model	103
6.1.1	Equations of motion	104
6.1.2	Energy flow	106
6.2	Numerical comparisons between the J - and J' -model	107
6.2.1	Resonant $\omega = \omega_0$	107
6.2.2	Off-resonant $\omega \neq \omega_0$	111
6.3	Chapter summary	114
7	Spin-band renormalization	115
7.1	Static spin-band renormalization	116
7.1.1	J -model	116
7.1.2	J' -model	118
7.2	Dynamic spin-band renormalization	121
7.2.1	J -model	122
7.2.2	J' -model	123
7.3	Driving effects on the spin-band	126
7.3.1	Pump driving effect	126
7.3.2	Probe driving effect	128
7.4	Chapter summary	131
8	Summary and outlook	133
A	Spin Hamiltonian	137
B	Triplon dispersion relation	141
C	Equations of motion	145
D	Resonant triplon criterion	151
E	Detuned triplon criterion	155
F	Renormalized triplon dispersion	159
G	Energy flow $P^{\text{SP},\text{B}}(t)$	161

List of figures	163
Bibliography	171
Articles	171
Books and Dissertations	188

Abstract

Due to the rise in experimental progress in several photonic facilities, theoretical addressing the non-equilibrium behavior in driven-dissipative quantum systems has triggered considerable interest in recent times. This thesis is devoted to the analysis of dynamics of a dimerized spin chain model which is driven out-of-equilibrium by the presence of a classical steady laser field. A particular study is given on the spin-phonon coupling effect treated as weak-to-strong perturbations, that the infrared-active phonon is driven by the laser. All systems in nature are interacting with their surroundings and the effects of the environment have to be approximated. To begin with, we employ the quantum Markovian master equation, which follows the construction of the dissipation path to a phononic bath for both phonon and spin sectors in the driven coupled spin-lattice system.

We approach this thesis by exploring how the non-equilibrium steady states (NESS) are created, controlled, and preserved by the internal and external interactions. This includes a detailed study of non-equilibrium dynamics of driven-dissipative quantum magnetic materials. First, we prepare the tools, protocols, and approximations needed to model a dimerized spin-1/2 chain as a chain of non-interacting triplons. The spin-phonon coupling is treated by the theoretical framework of the mean-field formalism. Second, we approximate the phononic bath with constant damping for each sector to easily derive the master equations of motion for the physical observables in the entire system. Third, we discuss the validity of such approximative master equations by considering many physical degrees of freedom. These settings produce a large variety of interesting phenomena and physical insights.

We firstly endeavor to thoroughly show that laser-driven infrared-active phonon

and triplons reach a coherent steady-state. We present the numerical results by implementing resonant and off-resonant levels for the driven phonon in the triplon-band limit as well as in the weak-to-strong coupling regime. Adopting useful arguments, we derive the analytic expressions for the average of observable dynamics to compare them with the numerical data in the NESS; we find some quantitative agreement. We look at different regimes of the driving frequency and consider what properties they possess; while higher driving frequencies satisfy the description of some aspects, very low ones can create unphysical states. The advantage of the different regimes is that one can better understand the model. To control and preserve the NESS, the region of applicability of all parameters with various regimes is considered. Moreover, a preliminary detailed analysis suggests that the energy flows in different parts of the system can secure a better understanding of the driving, coupling, and damping effect.

We employ the same model and equations of motion to study the dynamics in the strong coupling regime by investigating the spin system responses in and around the triplon band to the driven phonon. We find that the stationary state in the strong coupling regime leads to a giant resonant self-blocking effect between the phonon and triplons. We introduce hybrid states representing the frequency renormalization of both lattice and spin sectors over the strong couplings. Understanding how the spin-phonon coupling to both leading and the next-nearest-neighbor magnetic interactions with the same degrees of freedom responds to the laser field is an intriguing problem. This problem will be approached in detail for the sake of completeness.

To characterize the dimerization of the spin system in all spin-phonon coupling scenarios, we measure the modulation of superexchange integral in the spin sector by the vibration. Furthermore, we analyze the predictions of spin-band renormalization and verify them by comparison with the pump-probe protocols. These protocols also cover another phenomenon – the self-hybrid effect (static effect) – in the presence of very weak probe driving fields. In the final part, the applicability of results in possible materials in the experiment as well as the possible extensions of the implementation are presented.

Acknowledgements

In this thesis, a few people contributed, in a direct or indirect way, to making the results possible. My gratitude goes foremostly to my supervisor Prof. Dr. Götz S. Uhrig, under whose fatherly mentorship this work was completed. His inexhaustible amount of ideas, endless patience, modesty, and wide interest in physical problems gave me the boost and self-confidence. His motivation and encouragement allowed me to grow so much and to face this PhD. I really appreciate his effort in teaching me to open my mind to physics, to the research process, and to broaden my knowledge. Next, I am very grateful to Dr. Bruce Normand, who was directly involved in my research and in particular in most of the work presented in this thesis, for his useful discussions and feedback.

Very special thanks go to all of my colleagues in the Chair of Theoretical Physics I, the Technical University of Dortmund, whose company I've enjoyed during those years – Timo Gräßer who was always joyful, Philipp Schering, Philip Bleicker, Maik Malki, Leanna Müller, Gary Ferkinghoff, Constantin Meyer, and Frederik Keim, in any order, for numerous interesting, for their contribution to the development of a friendly environment, and for the lunch times and coffee break discussions. Philipp Schering, I want to especially thank you for reading some chapters of this thesis and for many delightful conversations about many different philosophical topics.

Since 2019, the world ironically enough has been in an out-of-equilibrium state! But, a big heartfelt thank you to my family that have so fervently supported me during these hard times, even when the workload seemed insurmountable; none of it would have been possible without them. To all of them, I dedicate this work.

1. Introduction

In this chapter, we introduce the 10 years old research field of driven-dissipative quantum many-body systems, at the boundaries of quantum optics and condensed matter physics. Section 1.1 simply motivates the reader with a few examples on the changes in the states and phases of matter from equilibrium to non-equilibrium. In Sec. 1.2, we will discuss the importance of non-equilibrium dynamics in recent investments in different areas of science and engineering. A discussion on magnetic quantum materials as the beloved materials in this thesis is included as well. These, in turn, present the motivations to do this thesis going through the most recent rapid theoretical and experimental developments. In Sec. 1.3, the challenge and goal of the thesis will be presented. In Sec. 1.4, we will propose a few materials that are emerging as proper magnetic quantum materials for the present thesis. Finally, in Sec. 1.5, the outline of the thesis will be presented and several open questions will be left for the next chapters.

1.1 Motivation

In many living organisms, the interaction between essentially independent agents can lead to astonishingly stable and regular behavior on a larger scale, that is, macroscopic regularity emerges from microscopic complexity. For instance, the global economy emerges from individual customers and enterprises and it is somehow hopeless to see how every single constituent behaves, but the behavior of the whole set can be followed using effective laws arose from the complicated interactions of the basic elements. Everything around us is composed of atoms and molecules and the same procedure can be applied. Looking at the behavior of

elements and the interaction between them individually is extremely complicated, but we can easily study the formed macroscopic objects by them. Looking at how the pieces that make up the material interact can teach us why the material does what it does, and teach us about fundamental physics with materials as a playground. So, we in this thesis intend to contribute to this puzzle in many-body quantum systems via the fully-fledged theory called *quantum mechanics* [1, 2]. This theory contains fundamental principles which help to macroscopically understand the outcome of microscopic processes in a system comprised of atoms and molecules.

Many processes in our everyday life experience practically undergo state and/or phase changes, i.e. internal or external interactions change their state and initial phase. Of these processes, we can think of two blended liquids, shattered glass on the floor, or a melted ice-cream in a warm room. Consider the ice-cream example; when the ice is interacting with its surrounding, the initial temperature difference between the ice and the environment approaches zero over time. If we wait even longer, the cream can be evaporated. In this example, we notice that the long-time behavior of the system to determine the final state/phase of the system is more important than the intermediate time steps. In other words, the rest/relaxation mood of things in a given setting is the main aim of microscopic processes because things will never calm down microscopically. In more technical terms, finding a macroscopically stationary state (a fully melted ice-cream, not an ice-cream soup) for a non-equilibrium state at some point in time is the main aim of recent developments in real applications.

One could simply think of the common part of the world – the Sun-Earth system – in which the state of the Earth is always changing due to the position and temperature of the Sun and finally, it is driven to a new state (whatever it could be). Thus, the world is somehow a driven-system. We nowadays know that the total entropy of the universe is continually increasing because of different types of internal and external driving effects. This implies that there are many phenomena in our life that undergo some changes in their equilibrium state and then achieve a new state out-of-equilibrium. By these, it is natural to explore various phenomena in many fields of science due to the changes in the states/phases. Thereby, in addition to the relaxation process discussed before, external forces in practice may affect the behavior of systems (dynamics) in a given setup.

1.2 Non-equilibrium phenomena

From the basic principles, particles interacting with each other produce collective phenomena that arise by realizing spectacular macroscopic quantum states. Although the thermodynamic equilibrium assumption leads to the quantum statistics describing the equilibrium states of particles, it does not allow to study of the dynamics towards equilibration. For this reason, a microscopic modeling

such as “driving” is proposed for dynamical balances. This could be realized with the invention of the laser. The rapid technological progress of laser sources in different areas of the industry, science, and engineering has opened up new research directions on the dynamical properties of systems far from equilibrium [3, 4]. Non-equilibrium physics explores various questions and aims, such as the analysis of unconventional dynamical behaviors in different contexts at any time of our history, technological advances, and the discovery of new states of matter.

In this far-reaching subject, the underlying motivation and interpretation behind the experimental observations in the nonlinear optics and laser spectroscopy play crucial roles in successful theoretical research [5]. On the one hand, to compensate for losses of particles and energy in a system when coupling to the environment, driving through external forces establishes a dynamical balance between driving forces and losses. This, in turn, realizes a non-equilibrium stationary state at the end. On the other hand, recent progress in quantum information science has attracted both experimental and theoretical researchers to create/control/preserve the quantum states of many-body systems for various applications [6–10]. Recent developments in time-resolved laser techniques [11, 12] has provided rich progress in controlling cold atoms [10, 13, 14] and many condensed matter systems [15, 16], which our understanding of non-equilibrium phenomena in quantum materials can be increased with. These advances, in turn, opened new doors to explore novel ultrafast control of material phases in quantum mechanics and statistical physics [15, 17, 18]. Of such phases one may mention the hidden orders [19], time crystals [20, 21], metastable state [22], photoinduced superconductivity [23, 24], and non-equilibrium topological phases [25, 26].

The natural systems to study the non-equilibrium phases of matter are the driven-dissipative many-body systems [27], so-called open driven quantum systems. Of the most famous open quantum systems are atomic, optical, and solid-state systems with coherent external driving, dissipative dynamics, nonlinearity, and different interactions [28–30]. Trapped ions [31], mesoscopic quantum circuits [32, 33], cold atoms [34, 35], arrays of coupled circuit quantum electrodynamic units [36], and spin ensembles embedded into the microwave cavities [37, 38] are examples of these open systems providing novel dynamical properties [39–42]. In general, light-matter systems are the proper candidates for this realm due to unavoidably coupling to a bath and subjecting to external drives [43–47]. It is well-known that driving and dissipation may generate topological quantum states considering a tailored bath [48] or time-periodic (Floquet) driving [49–51].

There are many ways to design a driven-system for different purposes [10], e.g. lattice shaking [52–55] and Raman-laser-assisted tunneling [56, 57] are common ways to realize systems with artificial gauge driving fields. Laser driving usually affects a material by changing the Hamiltonian, commonly referred to as “Floquet engineering” [58–66] and by creating excitation [67]. The latter may excite too many phonon modes, leading to nonlinear phononics [68–70], and then to heating

issues. In this situation, a regime inevitably comes up in which the time variation of the system quantities cannot be relaxed and out-of-equilibrium behaviors emerge. Additionally, the time-periodic external field is a central role in the study of driving systems because periodically driven systems naturally arise in many experimental setups, such as irradiated materials with electromagnetic waves or when one looks at the mechanical responses to periodic deformations in a system. However, one of the key concerns of non-equilibrium physics is the late-time steady-state, coherent state, where the system observables no longer evolve in time [71–73]. It is also worth noting that a weak laser driving and/or coupling to one or several reservoirs [74–79] are well justified to have long coherence times.

It should be mentioned that there is no guarantee that a driven-dissipative system will ever reach a time-independent state, so-called *non-equilibrium steady state (NESS)*, because the quantum features can be lost by dissipation. Thus, the dissipative processes should also be engineered in such a way that they generate quantum coherent states rather than suppressing them. Coupling many external degrees of freedom to a quantum system leads to energy transfer, while the interaction with the principle system leads to a process called decoherence, that is, decay of the superposition states to a large environment, thus restricting it to certain basis states. The loss of quantum features in the decoherence process and ordinary damping in the form of relaxation are direct consequences of a large environment which are ubiquitous in physical applications [80–82]. These phenomena are the subject of dissipative quantum mechanics to mimic and explain the underlying dynamics of open quantum systems and related applications. Understanding the precise nature of both the relaxation and decoherence effects is important for a variety of applications.

In the past decade, various open quantum systems have become popular to investigate non-equilibrium physical insights. The spin chain model as a beloved toy model of magnetism is the protagonist of the present thesis due to potential spin-based technologies in the future [83]. The first observation of the non-equilibrium dynamics of magnetic systems can be dedicated to the discovery of magnetic order reduction in laser-induced subpicosecond demagnetization of ferromagnetic Ni [84]. This observation led to more discoveries: discovery of ultrafast coherent control of spin waves [85], all-optical magnetic switching [86–88], and ultrafast generation of ferromagnetic order [89]. Remarkably, nontrivial exact analytic steady-state solutions of various many-body spin chain models have been studied [90–97]. It is well-known that quantum spin chains propose various interesting phenomena such as spin-Peierls transition [98], the appearance of the Haldane gap [99–102], and high-temperature superconductivity [103, 104]. In the past decade, the discovery of very large magnetic heat-conduction [105–107] and long nuclear magnetic relaxation times [108] have also attracted researchers to study the magnetic transport in quantum magnetic chains. Although numerous insights on the equilibrium physics of quantum magnets have been provided

using integrable spin chains [109–111], it was also possible to provide numerous novel non-equilibrium physics of these systems [112–114]. A perfect setting to understand the role of interactions and symmetries in the non-equilibrium situation is the XXZ spin-1/2 chain [115, 116]. It should be noted that the light-induced picosecond spin dynamics has been mostly hitherto interpreted using the classical methods [87, 117–121], however, it has been found that driving spins far from the equilibrium underpins novel quantum dynamics [122]. Despite the highly intriguing works on spin chains, theoretically studying the non-equilibrium physics of such systems is still a frontier research topic.

Given this background, one can think of other aspects of the spin chains. It has been found that the interplay between phonons and spins in spin chains leads to drastic phenomena such as femtosecond magnetization control [123–126] and spin Seebeck effect [127, 128]. Spin-phonon coupling (SPC) is usually weak due to the canceled contributions of the symmetric vibrations of relevant atoms from negative and positive displacements. However, in the systems with low symmetry or anisotropic dispersion curves, SPC can be modulated [129]. Interestingly, recent optical techniques have provided novel insights into the coherent SPC [130–132]. The driving of coherent lattice displacements to produce resonant excitation of the quantum spin dynamics is already getting more interesting in both quantum optics and condensed matter physics [133]. This is covered by the “magnetophononics” in which the highly frequency-specific nature of the resonant SPC is mainly exploited [133, 134].

Even though the available theoretical tools for open quantum systems are relatively limited, the Lindblad quantum master equation (more in the next chapter) for driven-dissipative many-body systems is often employed to treat an open quantum system coupled to a Markovian bath [27, 135]. This equation has widely been applied to the spin lattices [136, 137], coupled quantum-electrodynamics cavities and circuits [138–140], lattice Rydberg atoms [141–144], and nonlinear photonic modes [145, 146]. In the Lindblad equation, the coherent evolution and the dissipator are present to describe the dynamics of local observables by nonlinear equations. The dissipator described by a set of jump operators is responsible for dephasing and relaxation processes.

1.3 Challenge and goal

Generically, open driven quantum systems in the presence of dissipation effects attain a unique NESS [147–149]. However, one major challenge in non-equilibrium physics is the study of and/or control of the long-time steady states with a sufficient degree of universality. To this end, many situations have been discussed over the past decade [5, 97, 150–155]. With such an introduction, it is natural to explore novel physical insights when the spin and phonon sectors in a quantum system are externally driven by the laser and strongly coupled to each other.

The laser continuously pumps energy into the system and then drives it out of equilibrium. The interplay between SPC, driving parameters, and dissipative dynamics in tuning the stability of non-equilibrium order and in exploring the new phenomena are the overarching theme of the present thesis.

In the first step, we establish the equations of motion for the coupled lattice and spin sectors governing the basic physics of quantum NESS in an alternating spin chain. Concentrating on the regime of “weak SPC”, we show numerically that NESS can indeed be established in the response of the separate lattice and spin sectors and can be tuned by the primary system parameters. A complete investigation of the dynamical properties of the NESS in such a system will be performed.

In the second step, we concentrate on the regime of “strong SPC”. In particular, the SPC can be treated as a perturbation for the spin system. The strong SPC makes the dynamics more intricate since unexpected blocking of transferring energies in different frequency regimes comes into play role in significantly showing a negative spin feedback effects; so-called a *giant resonant self-blocking effect*. Thus, following the strong self-blocking effects, phonon frequency and spin-band frequency shifts will come up associated with extensive physics far from equilibrium.

In both the first and second steps, we consider two models for the SPC, but in both cases, we work with a steady driving field, which operates in a steady state regime, i.e. we hope that the steady input of power gives a steady output. It is necessary to note that it is practically impossible to 100% validate the theoretical predictions in a controlled way for macroscopic systems consisting of roughly 10^{23} individual atoms. However, in all these investigations, we explore the dynamics of systems with many degrees of freedom which their results stay worth by standing up to thorough testing to some extent.

1.4 Target materials

Since the discovery of Haldane system many spin gap systems have been found in the low-dimensional quantum spin systems [99, 156–158]. The valence bond solid is responsible for the explanation of the existence of the spin gap since all spins are distributed to certain localized static bonds in these systems. Inorganic spin chain compounds comprising dimerization of the lattice of a Heisenberg model are of the best-known systems in low-dimensional physics. In half-filled chain CuGeO_3 compound [157, 159], each Cu site holds one hole with spin-1/2 and the spin-spin interaction occurs via oxygen orbitals. On the other hand, phonons due to the interionic distances modulate the spin-spin interactions, leading to a non-zero SPC [160, 161]. Inorganic vanadyl pyrophosphate $(\text{VO})_2\text{P}_2\text{O}_7$ is also another confirmed alternating spin chain system with the spin gap 3.1 meV [162–165]. Although these two systems propose strong SPCs, $\text{Cu}(\text{NO}_3)_2$ [166] as a quasi-one-

dimensional alternating spin-1/2 chain with spin gap 0.38 meV shows a weak SPC. Furthermore, recently discovered alternating spin chains NaVOAsO₄ [167] and AgVOAsO₄ [168] are also available. Thereby, we have great amount of appropriate candidates for the listed purposes of the present thesis.

1.5 Outline

Once more, this thesis is devoted to the study of non-equilibrium physics of quantum magnetic materials, particularly a driven-dissipative dimerized spin-1/2 chain. These systems represent natural platforms in present-day experiments of modern solid-state physics to explore fundamental concepts and questions about matter far from the equilibrium, having at the same time a potential impact on emerging various applications in spintronics. The goal is to figure out the dynamical phenomena determined by the interplay of internal and external interactions, dissipation, and non-equilibrium conditions.

The outline of the thesis is organized as follows. In chapter 2 we will overview the theoretical background and basic concepts to approach the primary prerequisites of the project. Moreover, we will present some concepts of open quantum systems and the conditions in solids at which the sample starts to melt, looking in particular at a harmonic oscillator in the presence of additional damping and forcing terms. In chapter 3, we will introduce the system under study and essential approximations, as well as the system's physical observables, we need to pave the way in the rest of the thesis. In chapter 4, we will study the dynamical properties of a driven dissipative dimerized spin-1/2 chain in detail, characterized by NESS in the “weakly” coupled spin-lattice system rather than transient and relaxation processes and energy flows, which is mostly based on Ref. [169]. In chapter 5, we will turn to the spin feedback effect, giant resonant self-blocking effect, and to the phonon and spin-band frequency shifts caused by the “strong” SPC regime, which is potentially relevant for undergoing experiments. In chapter 6, some developments towards using the J' -model (phonon coupled to the next-nearest-neighbor magnetic interaction) will extend the SPC effect on the dynamical properties beyond the J -model. As the last results, in chapter 7 some developments towards using pump-probe protocols will extend the topic beyond the single pump driving, which is potentially useful in experiments. Most of chapter 5 and parts of chapters 6 and 7 are based on Ref. [170]. Finally, in chapter 8, we will provide a summary of the project and will discuss promising possible future perspectives.

2. Method

For the project, the required methods to be applied for the final equations of motions are presented in this chapter. Before going further, we would state that reduced Planck constant $\hbar = 1$ is taken throughout the thesis, except for a few parts where we want to make contact with an experimental progress.

First, we give a short review to the key operators in quantum mechanics in Sec. 2.1. Next, in Sec. 2.2, we briefly introduce the mean-field approximation. In Sec. 2.3, we discuss the useful representations on which the system is modeled based on. Section 2.4 presents the general formulation of the Heisenberg equation of motion and Fermi's golden rule. The Magnus expansion will be introduced in Sec. 2.5 and in Sec. 2.6 the phonons in solids are introduced. In Sec. 2.7, the Lindblad formalism is discussed to introduce the quantum dissipation effects. The important Lindemann criterion is given in Sec. 2.8 and in Sec. 2.9 an example of an open system in an environment, a damped driven harmonic oscillator, is discussed. Finally, a conclusion of the chapter is provided in Sec. 2.10.

2.1 The basic concept: operators in quantum mechanics

Historically, one of the independent formulations of quantum mechanics is called matrix mechanics, which was developed by Heisenberg in 1925 to describe atomic structure starting from the observed spectral lines. He has a theory on the notion that the only allowed values of energy exchange between microphysical systems are those that are discrete: quanta. Expressing dynamical quantities such as energy, position, momentum, and angular momentum in terms of matrices, he obtained an eigenvalue problem that describes the dynamics of microscopic systems; the

diagonalization of the Hamiltonian matrix yields the energy spectrum and the state vectors of the system. To describe the dynamics of matter at the microscopic scale, which is the main aim of quantum mechanics, operators come into play role.

In general, an operator as a mathematical rule that when applied to a state, transforms it into another state follows two algebra relations: commutator and anticommutator. The commutator of two operators A and B denoted by $[A, B]$ is defined by

$$[A, B] = AB - BA, \quad (2.1)$$

and the anticommutator $\{A, B\}$ is defined by

$$\{A, B\} = AB + BA. \quad (2.2)$$

Two operators are said to commute if their commutator is equal to zero and hence $AB = BA$.

For the fermions, the fermionic operators satisfy the relations

$$\{f_i, f_j\} = 0, \quad \{f_i^\dagger, f_j^\dagger\} = 0, \quad \{f_i, f_j^\dagger\} = \delta_{i,j}, \quad (2.3)$$

where the indices i and j can be any finite set of numbers. However, for the bosons, bosonic operators should satisfy

$$[b_i, b_j] = 0, \quad [b_i^\dagger, b_j^\dagger] = 0, \quad [b_i, b_j^\dagger] = \delta_{i,j}. \quad (2.4)$$

For the present thesis, spins are important. The existence of spin was confirmed experimentally by Stern and Gerlach in 1922 using silver atoms. The spin, an intrinsic degree of freedom, is a purely quantum mechanical concept with no classical analog. Unlike the orbital angular momentum, the spin cannot be described by a differential operator. A spin operator is neither of bosonic nor of fermionic type, however, there are many ways to transform them into operators that are at least close to being bosonic or fermionic. The simplest example of a spin Hamiltonian is the nearest-neighbor Heisenberg model, $\mathcal{H} = -J \sum_{\langle ij \rangle} \vec{S}_i \cdot \vec{S}_j$, where $J > 0$ is the ferromagnetic case, i.e. the diagonal terms in the Hamiltonian favorable spins aligning, and $J < 0$ is the antiferromagnetic case, i.e. the diagonal terms favor antialignment.

2.2 Mean-field approximation

In general, the physics of interacting particles in a many-body system is typically complicated. However, it is possible to include the interactions on the average, treating the effect of all the other particles as a mean density leaving a soluble single-particle problem.

For the models which can only be exactly solved in special cases, mean-field approximation as the first recourse always tries to construct a simple model. This

approximation assumes that the system's thermal fluctuations are relatively small and can therefore be neglected to a certain extent, which is helpful to treat a system of interacting particles as a system of non-interacting particles. Thus, it is assumed that each particle interacts with a *mean-field* that captures the average behavior of the particles around it. Therefore, to decouple an interacting many-body Hamiltonian into a simpler Hamiltonian describing a non-interacting system, one has to resort to the mean-field approximation.

Consider an interaction between two kinds of particles being the product of two operators A and B , i.e. $\mathcal{H}_{\text{int}} = AB$, with the averages (expectation values) respectively $\langle A \rangle$ and $\langle B \rangle$. The small deviations of these operators from their average can also be respectively defined as $d_A = A - \langle A \rangle$ and $d_B = B - \langle B \rangle$. Assuming that only interactions between different kinds of particles are relevant, we can write

$$\begin{aligned} \mathcal{H}_{\text{int}} &= AB = (d_A + \langle A \rangle)(d_B + \langle B \rangle) \\ &= d_A \langle B \rangle + d_B \langle A \rangle + \langle A \rangle \langle B \rangle + \cancel{d_A d_B}^0 \\ &= (A - \langle A \rangle) \langle B \rangle + (B - \langle B \rangle) \langle A \rangle + \langle A \rangle \langle B \rangle \\ &= A \langle B \rangle + B \langle A \rangle - \langle A \rangle \langle B \rangle, \end{aligned} \tag{2.5}$$

where the last term in the second line is neglected in the mean-field and finally only single-particle operators are left in the interaction. This, in turn, amounts to assume that the A and B particles are uncorrelated. Depending on the system model, there are various ways to calculate the averages. This approximation will be used in the spin-phonon coupling Hamiltonian of the present thesis to decouple the operators acting on the spin and phonon sectors.

2.3 Bond-operator representation

It is well-known that the bond-operator representation is very useful in doing calculations for the systems where a pairs of spins (dimers) act as basic units. For quantum $S = \frac{1}{2}$ spins this was pioneered by Sachdev and Bhatt as a useful design to specifically understand the properties of dimerized phases [171–175]. For the case of general spin- S , however, Kumar derived another bond-operator representation [176]. In this representation, the spin eigenstates of a dimer are constructed and a distinct bosonic creation operator called bond operator is formed. Depending on the definition of the vacuum state, the representation can be constructed in two different ways: Sachdev's representation and triplon



Figure 2.1: The singlet and triplet states of two spin-1/2 particles in a dimer.

operator representation. In both ways, the Hamiltonian for the structurally dimerized antiferromagnetic spin chain is transformed by expressing the two spin operators on each dimer. Each way is useful where the calculations are needed to be simplified. Let us describe each one separately in the following.

2.3.1 Sachdev's representation

Consider a dimer with index i consisting of two $S = \frac{1}{2}$ spins, $\vec{S}_{1,i}$ and $\vec{S}_{2,i}$. There are four states in the Hilbert space on each dimer ($|\uparrow\uparrow\rangle$, $|\uparrow\downarrow\rangle$, $|\downarrow\uparrow\rangle$, and $|\downarrow\downarrow\rangle$). One can associate these with a canonical singlet state $|s\rangle$ and the three triplet states $|t_x\rangle$, $|t_y\rangle$ and $|t_z\rangle$, see Fig. 2.1. In the Sachdev's representation, the four states of this two-spin system in the dimer i is created by applying the creation operators s_i^\dagger , $t_{x,i}^\dagger$, $t_{y,i}^\dagger$ and $t_{z,i}^\dagger$ on the some reference vacuum state $|0\rangle$ as [171]

$$|s\rangle_i = s_i^\dagger |0\rangle = \frac{1}{\sqrt{2}} (|\uparrow\downarrow\rangle_i - |\downarrow\uparrow\rangle_i), \quad (2.6a)$$

$$|t_x\rangle_i = t_{x,i}^\dagger |0\rangle = -\frac{1}{\sqrt{2}} (|\uparrow\uparrow\rangle_i - |\downarrow\downarrow\rangle_i), \quad (2.6b)$$

$$|t_y\rangle_i = t_{y,i}^\dagger |0\rangle = \frac{i}{\sqrt{2}} (|\uparrow\uparrow\rangle_i + |\downarrow\downarrow\rangle_i), \quad (2.6c)$$

$$|t_z\rangle_i = t_{z,i}^\dagger |0\rangle = \frac{1}{\sqrt{2}} (|\uparrow\downarrow\rangle_i + |\downarrow\uparrow\rangle_i). \quad (2.6d)$$

By these, the elements of the spin operators \vec{S}_1 and \vec{S}_2 lead to the representation

$$S_{1,i}^\alpha = \frac{1}{2} \left(s_i^\dagger t_{\alpha,i} + t_{\alpha,i}^\dagger s_i - i \sum_{\beta\zeta} \epsilon_{\alpha\beta\zeta} t_{\beta,i}^\dagger t_{\zeta,i} \right), \quad (2.7a)$$

$$S_{2,i}^\alpha = -\frac{1}{2} \left(s_i^\dagger t_{\alpha,i} + t_{\alpha,i}^\dagger s_i + i \sum_{\beta\zeta} \epsilon_{\alpha\beta\zeta} t_{\beta,i}^\dagger t_{\zeta,i} \right), \quad (2.7b)$$

where ϵ is the totally antisymmetric tensor, the Levi-Civita symbol, considering different flavors x , y , and z . Note that the vacuum state $|0\rangle$ does not correspond to the physical state of the spin system. The physical states always have a single bond boson for any dimer i and so satisfy the constraint

$$s_i^\dagger s_i + \sum_{\alpha} t_{\alpha,i}^\dagger t_{\alpha,i} = 1, \quad (2.8)$$

so-called hard-core constraint. These new bosonic operators obey the following commutator relations

$$[s_i, s_j^\dagger] = \delta_{i,j}, \quad (2.9a)$$

$$[t_{\alpha,i}, t_{\beta,j}^\dagger] = \delta_{\alpha,\beta} \delta_{i,j}, \quad (2.9b)$$

$$[s_i, s_j] = [t_{\alpha,i}, t_{\beta,j}] = [s_i, t_{\alpha,j}] = [s_i^\dagger, t_{\alpha,j}] = 0, \quad (2.9c)$$

$$[s_i^\dagger, s_j^\dagger] = [t_{\alpha,i}^\dagger, t_{\beta,j}^\dagger] = [s_i, t_{\alpha,j}^\dagger] = [s_i^\dagger, t_{\alpha,j}^\dagger] = 0. \quad (2.9d)$$

2.3.2 Triplon operator representation

In the second way, the singlet state is considered as the vacuum state

$$|s\rangle_i = |0\rangle = \frac{1}{\sqrt{2}} (|\uparrow\downarrow\rangle_i - |\downarrow\uparrow\rangle_i), \quad (2.10)$$

and if one sets $s_i = 1$ in Eq. (2.6a), it leads to the same expression as above. Furthermore, the spin operators yield the following new forms

$$S_{1,i}^\alpha = \frac{1}{2} \left(t_{\alpha,i} + t_{\alpha,i}^\dagger - \mathbf{i} \sum_{\beta\zeta} \epsilon_{\alpha\beta\zeta} t_{\beta,i}^\dagger t_{\zeta,i} \right), \quad (2.11a)$$

$$S_{2,i}^\alpha = -\frac{1}{2} \left(t_{\alpha,i} + t_{\alpha,i}^\dagger + \mathbf{i} \sum_{\beta\zeta} \epsilon_{\alpha\beta\zeta} t_{\beta,i}^\dagger t_{\zeta,i} \right), \quad (2.11b)$$

as well as the new hard-core constraint

$$|s\rangle_i \langle s|_i + \sum_{\alpha} t_{\alpha,i}^\dagger t_{\alpha,i} = 1. \quad (2.12)$$

Additionally, one simply finds the following commutator relations

$$t_{\alpha,i} t_{\beta,i} = t_{\alpha,i}^\dagger t_{\beta,i}^\dagger = 0, \quad (2.13a)$$

$$[t_{\alpha,i}, t_{\beta,j}^\dagger] = \delta_{i,j} \left(\delta_{\alpha,\beta} \left(1 - \sum_{\gamma} t_{\gamma,i}^\dagger t_{\gamma,i} \right) - t_{\beta,i}^\dagger t_{\alpha,i} \right). \quad (2.13b)$$

The latter is called the hard-core bosonic commutation relation. These representations will be applied to our model to transform the Hamiltonians and to simplify the equations of motion. In such a way, all excitations in the dimer are described by the *triplon* (singlet-triplet) excitation.

2.4 The Heisenberg equation of motion and Fermi's golden rule

One of the pictures encountered most frequently in quantum mechanics is the Heisenberg picture, which is useful when describing phenomena with the time-dependent Hamiltonians. In this picture, the time dependence of the state vectors is completely frozen, and it is obtained from the Schrödinger picture by applying the time-evolution operator U to finally obtain the equation of motion that regulates the time evolution of operators within the Heisenberg picture:

$$\frac{dO_{\text{H}}(t)}{dt} = \partial_t U^\dagger(t) O U(t) + U^\dagger(t) O \partial_t U(t) + \partial_t O(t) = \mathbf{i}[\mathcal{H}, O_{\text{H}}(t)] + \partial_t O(t), \quad (2.14)$$

where we have assumed that the operator O does depend explicitly on time ($\partial_t O(t) \neq 0$).

Another interesting and important special case in the time-dependent perturbation theory is a form of Fermi's golden rule [1]. Let us consider here only

those phenomena that are described by Hamiltonians which can be split into two parts, a time-independent part \mathcal{H}_0 and a time-dependent part $V(t)$ that is small compared to \mathcal{H}_0 :

$$\mathcal{H}(t) = \mathcal{H}_0 + V(t), \quad (2.15)$$

where \mathcal{H}_0 is assumed to have exact solutions that are known. The well-known time-evolution operator in the interaction picture $U_I(t, t_0) = e^{i\mathcal{H}_0 t} U(t, t_0) e^{-i\mathcal{H}_0 t}$ for such a system produces

$$i \frac{dU_I(t, t_0)}{dt} = V_I(t) U_I(t, t_0), \quad (2.16)$$

with $U_I(t, t_0) = I - i \int_{t_0}^t V_I(t') U_I(t', t_0) dt'$. We assume that $V_I(t)$ is small and then proceed iteratively to find approximate solutions to this integral equation, leading to the Dyson series. With the aid of this, one could find the transition probability corresponding to a transition from an initial unperturbed state ψ_i to another unperturbed state ψ_f . For instance, in the presence of a constant perturbation V , we obtain

$$P_{if}(t) = \frac{4 |\langle \psi_f | V | \psi_i \rangle|^2}{\omega_{fi}^2} \sin^2(\omega_{fi} t / 2), \quad (2.17)$$

where $\omega_{fi} = E_f - E_i$ is the difference between the initial and final energies of states. If we calculate the transition into a *continuum* of final states with the number of final states within the energy interval E_f and $E_f + dE_f$, which is equal to $\rho(E_f) dE_f$ – $\rho(E_f)$ is the density of final states – the total transition rate can be obtained from

$$W_{if} = \int \frac{P_{if}(t)}{t} \rho(E_f) dE_f = 2\pi |\langle \psi_f | V | \psi_i \rangle|^2 \rho(E_i). \quad (2.18)$$

This relation is called the *Fermi's golden rule*. It implies that, in the case of a constant perturbation, if we wait long enough, the total transition rate becomes constant (time-independent).

2.5 The Magnus expansion

As well-known, independent variables, functions, and derivatives of functions are related to each other in a differential equation and it is worth briefly mentioning the solution of an n th-order ordinary differential equation, which is nicely approximated by Wilhelm Magnus [177]. For such equations, we generally have $Y'(t) = A(t) Y(t)$ in which $A(t)$ is an $n \times n$ matrix called the coefficient matrix and $Y(t)$ is an $n \times 1$ vector of unknown functions. In the Magnus expansion, a way to approximate the fundamental matrix of this system is provided such that the solution is expressed as the exponential of the $n \times n$ matrix function $S(t)$,

$$Y(t) = e^{S(t)}, \quad (2.19)$$

which is subsequently constructed as a series expansion, also called the Magnus expansion,

$$S(t) = \sum_{i=0}^{\infty} S_i(t). \quad (2.20)$$

In this thesis, we skip the lemma's which are used to prove this valuable theorem because we only need this expansion in a short part of the thesis. Finally, the first three symmetric terms of this series read

$$S_1(t) = \int_0^t A(t_1) dt_1, \quad (2.21a)$$

$$S_2(t) = \frac{1}{2} \int_0^t \int_0^{t_1} [A(t_1), A(t_2)] dt_2 dt_1, \quad (2.21b)$$

$$S_3(t) = \frac{1}{6} \int_0^t \int_0^{t_1} \int_0^{t_2} \left([A(t_1), [A(t_2), A(t_3)]] \right. \\ \left. + [[A(t_1), A(t_2)], A(t_3)] \right) dt_3 dt_2 dt_1, \quad (2.21c)$$

wherein the integrals can easily be computed. It is necessary to mention that for the dynamical systems, $A(t)$ denotes the state matrix and can directly be replaced with the time-dependent Hamiltonian of the system in the interaction picture.

2.5.1 Magnus expansion for two driven coupled harmonic oscillators

In this example, we consider a continuous driving perturbation such as $\mathcal{V}_p(t) = v_p \cos(\omega t)$ which depends harmonically on time. Such a perturbation in this example is encountered when two harmonic oscillators interact with an electromagnetic field such as light. If we label the first and second harmonic oscillator with the same oscillation frequency ω_0 , respectively, with $\{a, a^\dagger\}$ and $\{b, b^\dagger\}$ operators, the total Hamiltonian of the system in the presence of external time-dependent perturbation field $\mathcal{V}_p(t)$ is given by $\mathcal{H}(t) = \mathcal{H}_0 + \omega_0 + \mathcal{H}_p(t)$, where the first and second terms represent the free Hamiltonian of the two oscillators:

$$\mathcal{H}_0 = \omega_0 (a^\dagger a + b^\dagger b), \quad (2.22a)$$

$$\mathcal{H}_p(t) = \mathcal{V}_p(t) (a^\dagger b^\dagger + ab). \quad (2.22b)$$

Note that, neglecting coupling of $a^\dagger b$ and $b^\dagger a$, the remaining coupling between the two oscillators is generated by the external force $\mathcal{V}_p(t)$ with strength v_p . Now, we employ the Magnus expansion to find the second-order approximation of energy of this driven system. To proceed, we first calculate $A(t) = \mathcal{H}_1(t)$ through

$$\mathcal{H}_1(t) = e^{i\mathcal{H}_0 t} \mathcal{H}_p(t) e^{-i\mathcal{H}_0 t} = \mathcal{V}_p(t) e^{i\mathcal{H}_0 t} (a^\dagger b^\dagger + ab) e^{-i\mathcal{H}_0 t}, \\ = \mathcal{V}_p(t) (e^{2i\omega_0 t} a^\dagger b^\dagger + e^{-2i\omega_0 t} ab). \quad (2.23)$$

It should be mentioned that the first-order approximation of Magnus expansion is not our interest here which is a function of off-diagonal operators – usefulness

for the shift of energy purposes compared to the diagonal operators. For the second-order approximation, we need to calculate

$$[\mathcal{H}_1(t_1), \mathcal{H}_1(t_2)] = \frac{v_p^2}{2} \cos(\omega t_1) \left[e^{2i\omega_0 t_1} \left(e^{i(\omega-2\omega_0)t_2} + e^{-i(\omega+2\omega_0)t_2} \right) - e^{-2i\omega_0 t_1} \left(e^{i(\omega+2\omega_0)t_2} + e^{-i(\omega-2\omega_0)t_2} \right) \right] [a^\dagger b^\dagger, a b], \quad (2.24)$$

where $[a^\dagger b^\dagger, a b] = -(1 + a^\dagger a + b^\dagger b)$. To have $S_2(t)$ in Eq. (2.21b), we still need the solution of the following integrals

$$\int_0^{t_1} [\mathcal{H}_1(t_1), \mathcal{H}_1(t_2)] dt_2 = 4i \frac{\omega_0}{4\omega_0^2 - \omega^2} v_p^2 (1 + a^\dagger a + b^\dagger b) \cos(\omega t_1) [\cos(2\omega_0 t_1) - \cos(\omega t_1)], \quad (2.25a)$$

$$\begin{aligned} \int_0^t \int_0^{t_1} [\mathcal{H}_1(t_1), \mathcal{H}_1(t_2)] dt_2 dt_1 &= 4i \frac{\omega_0}{4\omega_0^2 - \omega^2} v_p^2 (1 + a^\dagger a + b^\dagger b) \times \\ &\times \left[\frac{1}{2} \left[\frac{1}{\omega + 2\omega_0} \sin[(\omega + 2\omega_0)t] + \frac{1}{\omega - 2\omega_0} \sin[(\omega - 2\omega_0)t] \right] \right. \\ &\quad \left. - \frac{t}{2} - \frac{1}{4\omega} \sin(2\omega t) \right]. \end{aligned} \quad (2.25b)$$

In the last relation, however, we need to average over one period of oscillations, $\{T = 2\pi/\omega, T = 2\pi/(\omega - 2\omega_0), T = 2\pi/(\omega + 2\omega_0)\}$, stemming from the sine functions to get rid of fast oscillations, which the remaining $-1/2$ value of the integral leads to

$$\bar{S}_2 = \frac{v_p^2 \omega_0}{\omega^2 - 4\omega_0^2} (1 + a^\dagger a + b^\dagger b), \quad (2.26)$$

by which the second-order correction to the shift of frequency ω_0 can be stated as

$$\Delta^{(2)}\omega_0 = \frac{v_p^2 \omega_0}{\omega^2 - 4\omega_0^2}, \quad (2.27)$$

which is an order of v_p^2 as expected from the perturbation theory.

2.6 Phonons in solids

Vibrations of the crystal lattice associated with the low energy excitations up to 240 meV (60 THz) [178, 179] introduce phonons as elementary quanta of these excitations. If a phonon consisting of the collective motion of positive and negative ions along a specific eigenvector carries an electric dipole, it is called an infrared-active (otherwise Raman active [180]) phonon that directly couples to the electric field of light. In linear response of an infrared-active optical phonon to a monochromatic light field, the phonon can be considered as a charged harmonic

oscillator driven by the oscillating electric field of light (Lorentz model). However, in the nonlinear response, the intense electric fields drive the phonons to large amplitudes. In this thesis, we stick to weak electric fields of light and accordingly, linear response.

For small displacements (q) of ions in a solid, so-called harmonic approximation, the following energy potential

$$U = \frac{1}{2}\omega_0^2 q^2, \quad (2.28)$$

is felt by the ions, where ω_0 is the phonon frequency. Therefore, a restoring force $F = -\partial U/\partial q = -\omega_0^2 q$ can be experienced by the phonon when the ions are displaced from their equilibrium position. This finally results in the oscillation of atoms at the resonance frequency ω_0 described by the equation of motion

$$\frac{d^2 q}{dt^2} + \omega_0^2 q = 0. \quad (2.29)$$

For the infrared-active phonons, considering the Born effective charge Q^* associated with the phonon dipole as well as the effective mass \mathcal{M} of the phonon, the driving field \mathcal{E} can be incorporated into this equation, i.e.

$$\frac{\partial^2 q}{\partial t^2} + \omega_0^2 q = \frac{Q^*}{\mathcal{M}} \mathcal{E}. \quad (2.30)$$

This is still an unphysical scenario because, in real solids, the energy can be transferred among different modes and anharmonicities of the lattice potential result in a finite lifetime of the phonon oscillations: damping effect. Thus, we need the following new equation of motion

$$\frac{\partial^2 q}{\partial t^2} + \gamma \frac{\partial q}{\partial t} + \omega_0^2 q = \frac{Q^*}{\mathcal{M}} \mathcal{E}, \quad (2.31)$$

where the damping γ is inversely proportional to the lifetime of the phonon mode.

For a time-dependent monochromatic electromagnetic field with strength \mathcal{E}_0 , we have $\mathcal{E}(t) = \mathcal{E}_0 e^{-i\omega t}$ and then the solution $q(t) = q_0 e^{-i\omega t}$ is obtained, where $q_0 = Q^* \mathcal{E}_0 / \mathcal{M} (\omega_0^2 - \omega^2 - i\gamma\omega)$ is the amplitude of the phonon oscillations. From this amplitude, it is clear that the highest modulation amplitudes appear for the resonance condition $\omega = \omega_0$. Having the number of unit cells per unit volume (N) of a sample, the polarization of the sample due to a single charged oscillator can be calculated via $\mathcal{P}(t) = NQ^* q(t)$, which is useful for optical properties of the sample. In the nonlinear response regime, the electric field is strong and can be treated as $\mathcal{E}(t) = \mathcal{E}_0(t) e^{-i\omega t}$, where the amplitude is a Gaussian pulse. In this case, the phonon dynamics becomes highly nonlinear, and higher terms of the energy potential U corresponding to the anharmonic contributions must be taken into account (out of the scope of the present thesis).

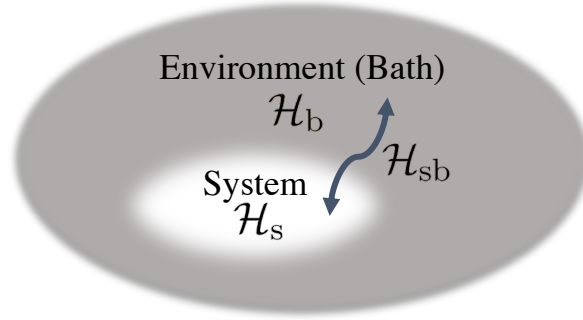


Figure 2.2: Schematic illustration of an open quantum system and its environment that together constitute a closed quantum system.

2.7 Open quantum systems

This thesis is focused on the phenomena which occur in open quantum systems, that is, systems which are coupled to an external environment. No physical system is really closed. The Schrödinger equation is not appropriate to describe an open quantum system coupled to an uncontrolled environment because the state is a mixed state in Hilbert space, rather than a pure one. Even though we cannot track the dynamics of the environment, we still want to understand the effect it has on the system of interest. An environment is defined as an infinite set of degrees of freedom with a continuous spectrum to describe a true irreversible and dissipative dynamics. However, one of the useful approaches to treat such systems is called the Markovian (Lindblad) quantum master equation. In this approach the memory of the environment is neglected, which is a reasonable simplification in many physical scenarios.

2.7.1 The Lindblad master equation

Our goal in this part is to find a more general procedure that allows us to obtain an equation of motion for the density matrix of the system. We consider a situation where the system is *weakly* coupled to the bath. The total Hamiltonian is assumed to have the form

$$\mathcal{H} = \mathcal{H}_s + \mathcal{H}_b + \mathcal{H}_{sb}, \quad (2.32)$$

where the first term is the system Hamiltonian, the second one is the bath Hamiltonian and the last one is the interaction Hamiltonian between the system and bath, see Fig. 2.2. In the next step, we transform into the interaction picture, using the unitary transformation $U_I(t) = \exp[-i(\mathcal{H}_s + \mathcal{H}_b)t]$. The density matrix ρ of the total system, i.e. system plus bath, then evaluates in time according to the non-Markovian equation

$$\frac{\partial}{\partial t} \rho(t) = -i[\mathcal{H}_I(t), \rho(t)], \quad (2.33)$$

with $\mathcal{H}_I(t) = U_I^\dagger(t)\mathcal{H}_{\text{sb}}U_I(t)$. Formally integrating the equation above yields

$$\rho(t) = \rho(0) - \mathbf{i} \int_0^t dt' [\mathcal{H}_I(t'), \rho(t')], \quad (2.34)$$

and after inserting this result into the differential equation, we obtain

$$\frac{\partial}{\partial t}\rho(t) = -\mathbf{i}[\mathcal{H}_I(t), \rho(0)] - \int_0^t dt' [\mathcal{H}_I(t), [\mathcal{H}_I(t'), \rho(t')]]. \quad (2.35)$$

In the next step, we take the trace over the bath degrees of freedom and assume that $\text{Tr}_b[\mathcal{H}_I(t), \rho(0)] = 0$; this is true when the state of the bath and system factorise at $t = 0$, which we assume – see below. Thus the density matrix of the system evaluates according to

$$\frac{\partial}{\partial t}\rho_s(t) = \frac{\partial}{\partial t}\text{Tr}_b[\rho(t)] = - \int_0^t dt' \text{Tr}_b[\mathcal{H}_I(t), [\mathcal{H}_I(t'), \rho(t')]]. \quad (2.36)$$

Born approximation

In this approximation, it is assumed that the coupling between the system and the bath is weak. Thus, the density matrix of the bath is only negligibly affected by the interaction. The total density matrix at time t may then be approximated by a tensor product; $\rho(t) = \rho_s(t) \otimes \rho_b$. This yields a closed inhomogeneous differential equation:

$$\frac{\partial}{\partial t}\rho_s(t) = - \int_0^t dt' \text{Tr}_b[\mathcal{H}_I(t), [\mathcal{H}_I(t'), \rho_s(t') \otimes \rho_b]]. \quad (2.37)$$

Markov approximation

In this approximation, $\rho_s(t')$ is replaced by $\rho_s(t)$, which will be justified by the fact that bath correlations/excitations decay on a much shorter timescale than that of any relevant dynamics of the system. This yields the real field equation:

$$\frac{\partial}{\partial t}\rho_s(t) = - \int_0^t dt' \text{Tr}_b[\mathcal{H}_I(t), [\mathcal{H}_I(t'), \rho_s(t) \otimes \rho_b]]. \quad (2.38)$$

The final step is to perform the change of variable $t' \rightarrow t - t'$ and to shift the upper integration boundary to infinity. This is justified when the integrand vanishes sufficiently fast. This yields the Markovian quantum master equation:

$$\frac{\partial}{\partial t}\rho_s(t) = - \int_0^\infty dt' \text{Tr}_b[\mathcal{H}_I(t), [\mathcal{H}_I(t - t'), \rho_s(t) \otimes \rho_b]]. \quad (2.39)$$

Secular (rotating wave) approximation

Ultimately, this approximation entails an averaging over rapidly oscillating terms. It will allow us to bring the master equation into a conventional shape, which is called the Lindblad form. The starting point is the following general decomposition of the system-bath interaction:

$$\mathcal{H}_{\text{sb}} = \sum_{\alpha} A_{\alpha} \otimes B_{\alpha}, \quad (2.40)$$

where A_α (B_α) is the system (bath) operator with the features $A_\alpha^\dagger = A_\alpha$ and $B_\alpha^\dagger = B_\alpha$. As a first step towards the envisaged averaging procedure we introduce the operators $A_\alpha(\omega) = \sum_{E', E=\omega} \Pi(E) A_\alpha \Pi(E')$, where the $\Pi(E)$ are projectors onto the energy eigenspaces with energy E of \mathcal{H}_s . They obey $\Pi(E) = 1$ such that

$$\mathcal{H}_s = \sum_{E', E} \Pi(E) A_\alpha \Pi(E') = \sum_E E \Pi(E), \quad (2.41)$$

and hence we have $A_\alpha = \sum_{E', E} \Pi(E) A_\alpha \Pi(E') = \sum_\omega \sum_{E'-E=\omega} \Pi(E) A_\alpha \Pi(E') = \sum_\omega A_\alpha(\omega)$. We thus find that

$$[\mathcal{H}_s, A_\alpha(\omega)] = -\omega A_\alpha(\omega), \quad (2.42a)$$

$$[\mathcal{H}_s, A_\alpha^\dagger(\omega)] = +\omega A_\alpha^\dagger(\omega), \quad (2.42b)$$

where $A_\alpha(\omega)$ and $A_\alpha^\dagger(\omega)$ are the eigenoperators of \mathcal{H}_s and as a consequence their time-evaluation in the interaction picture is

$$e^{i\mathcal{H}_s t} A_\alpha(\omega) e^{-i\mathcal{H}_s t} = e^{-i\omega t} A_\alpha(\omega), \quad (2.43a)$$

$$e^{i\mathcal{H}_s t} A_\alpha^\dagger(\omega) e^{-i\mathcal{H}_s t} = e^{+i\omega t} A_\alpha^\dagger(\omega). \quad (2.43b)$$

The interaction picture representation of the system-bath interaction thus becomes

$$\mathcal{H}_I(t) = \sum_\alpha e^{-i\omega t} A_\alpha(\omega) \otimes B_\alpha(\omega), \quad (2.44)$$

where $B_\alpha(\omega) = e^{i\mathcal{H}_b t} B_\alpha e^{-i\mathcal{H}_b t}$. It should be noted that with this decomposition the condition $\text{Tr}_b[\mathcal{H}_I(t), \rho(0)] = 0$ can be transformed as

$$\langle B_\alpha(t) \rangle = \text{Tr}[B_\alpha(t) \rho_b] = 0, \quad (2.45)$$

i.e. the average of $B_\alpha(t)$ is zero. This can be always achieved by a redefinition of the system-bath coupling (a possible constant peak will simply be absorbed in the system Hamiltonian). The master equation becomes, thus,

$$\begin{aligned} \frac{\partial}{\partial t} \rho_s(t) &= \int_0^\infty dt' \text{Tr}_b \left[\mathcal{H}_I(t-t') \rho_s(t) \rho_b \mathcal{H}_I(t) - \mathcal{H}_I(t) \mathcal{H}_I(t-t') \rho_s(t) \rho_b \right] \\ &\quad + \text{h.c.} \\ &= \sum_{\omega, \omega'} \sum_{\alpha, \beta} e^{i(\omega' - \omega)t} \Gamma_{\alpha\beta}(\omega) \left(A_\beta(\omega) \rho_s(t) A_\alpha^\dagger(\omega') - A_\alpha^\dagger(\omega') A_\beta(\omega) \rho_s(t) \right) \\ &\quad + \text{h.c.}, \end{aligned} \quad (2.46)$$

where $\Gamma_{\alpha\beta}(\omega) = \int_0^\infty dt' e^{i\omega t'} \text{Tr}_b [B_\alpha^\dagger(t) B_\alpha(t-t') \rho_b] = \int_0^\infty dt' e^{i\omega t'} \langle B_\alpha^\dagger(t) B_\alpha(t-t') \rangle$ is the Fourier transform of the bath two-time correlation function. When the bath is in a stationary state (which we assume), this correlation function does not depend on the absolute time t , but only on the time differences, i.e. $\langle B_\alpha^\dagger(t) B_\alpha(t-t') \rangle = \langle B_\alpha^\dagger(t') B_\alpha(0) \rangle$.

The assumption underlying the Markov approximation was that this correlation function decays sufficiently fast. When the relaxation timescale of the open system is much larger than the intrinsic timescale, typical values of $(\omega - \omega')^{-1}$, we perform the secular approximation, i.e. $\exp[i(\omega - \omega')t] \rightarrow \delta_{\omega\omega'}$. In quantum optics, we have $|\omega - \omega'| \simeq 10^{15}$ Hz, which leads to a decay rate of $\simeq 10^9$ Hz. Thereby,

$$\frac{\partial}{\partial t} \rho_s(t) = \sum_{\omega, \alpha, \beta} \Gamma_{\alpha\beta}(\omega) \left(A_\beta(\omega) \rho_s(t) A_\alpha^\dagger(\omega) - A_\alpha^\dagger(\omega) A_\beta(\omega) \rho_s(t) \right) + \text{h.c.} . \quad (2.47)$$

In a final step, we decompose

$$\Gamma_{\alpha\beta}(\omega) = \frac{1}{2} \gamma_{\alpha\beta}(\omega) + \text{i} S_{\alpha\beta}(\omega), \quad (2.48)$$

where $\gamma_{\alpha\beta}(\omega) = \Gamma_{\alpha\beta}(\omega) + \Gamma_{\alpha\beta}^*(\omega) = \int_{-\infty}^{\infty} dt' e^{i\omega t'} \langle B_\alpha^\dagger(t') B_\alpha(0) \rangle$, so-called the Kossakowski matrix, refers to the decay rates. The final result is the Lindblad-Kossakowski master equation:

$$\frac{d}{dt} \rho_s(t) = -\text{i} [\mathcal{H}_{\text{LS}}, \rho_s(t)] + \mathcal{D} \rho_s(t), \quad (2.49)$$

with the Lamb-shift Hamiltonian $\mathcal{H}_{\text{LS}} = \sum_{\omega, \alpha, \beta} S_{\alpha\beta}(\omega) A_\alpha^\dagger(\omega) A_\beta(\omega)$ and the dissipator

$$\mathcal{D} \rho_s(t) = \sum_{\omega, \alpha, \beta} \gamma_{\alpha\beta}(\omega) \left(A_\beta(\omega) \rho_s(t) A_\alpha^\dagger(\omega) - \frac{1}{2} \left\{ A_\alpha^\dagger(\omega) A_\beta(\omega), \rho_s(t) \right\} \right). \quad (2.50)$$

Let us make one further simplification of the dissipator. We introduce the eigenvalues and eigenvectors of the Kossakowski matrix

$$\gamma(\omega) = \sum_{\alpha} \gamma_{\alpha}(\omega) v_{\alpha}(\omega) v_{\alpha}^\dagger(\omega). \quad (2.51)$$

This allows us to write

$$\mathcal{D} \rho_s(t) = \sum_{\omega, \alpha} \gamma_{\alpha}(\omega) \left(L_{\alpha}(\omega) \rho_s(t) L_{\alpha}^\dagger(\omega) - \frac{1}{2} \left\{ L_{\alpha}^\dagger(\omega) L_{\alpha}(\omega), \rho_s(t) \right\} \right), \quad (2.52)$$

where $L_{\alpha}(\omega) = \sum_i v_{\alpha_i}(\omega) A_i(\omega)$ are the jump operators. This makes the master equation to the Lindblad form [135, 181, 182]

$$\frac{d}{dt} \rho_s(t) = \mathcal{L} \rho_s(t) = -\text{i} [\mathcal{H}, \rho_s(t)] + \sum_i \gamma_i \left(L_i \rho_s(t) L_i^\dagger - \frac{1}{2} \left\{ L_i^\dagger L_i, \rho_s(t) \right\} \right), \quad (2.53)$$

where \mathcal{H} describes the total system's Hamiltonian and \mathcal{L} is referred to as the Liouvillian/Lindblad super-operator. The operators L_i are referred to as ‘‘Lindblad operators’’ and can be microscopically determined by specifying the coupling Hamiltonian between the reduced system and bath (if it is in thermal equilibrium), while γ_i takes the role of damping parameters for $i \in [1, N_s^2 - 1]$ in which N_s

denotes the dimension of the Hilbert space of the open system. This is called the Lindblad equation, or adjoint quantum master equation, which is the most general time evolution equation for the density matrix of an open dissipative system.

It is well-known that an arbitrary operator $O_{\text{H}}(t)$ in the Heisenberg picture can be transformed into the Schrödinger picture through the relation

$$O_{\text{H}}(t) = e^{\mathcal{L}^\dagger(t-t_0)} O(t_0), \quad (2.54)$$

where \mathcal{L} is the Liouville generator above-introduced, leading to

$$\frac{d}{dt} O_{\text{H}}(t) = \mathcal{L}^\dagger O_{\text{H}}(t). \quad (2.55)$$

Thus, with the aid of the defined generator \mathcal{L} in Eq. (2.53), we obtain

$$\frac{d}{dt} O_{\text{H}}(t) = \mathfrak{i}[\mathcal{H}, O_{\text{H}}(t)] + \sum_i \gamma_i \left(L_i^\dagger O_{\text{H}}(t) L_i - \frac{1}{2} \left\{ O_{\text{H}}(t), L_i^\dagger L_i \right\} \right). \quad (2.56)$$

2.7.2 Damped harmonic oscillator

Let us focus on an important special example of an open system in an environment, a damped driven harmonic oscillator, to find the corresponding Lindblad quantum master equation in the presence of the dissipation effect. In such a system, the ordinary harmonic oscillator is the introduced reduced system. For the harmonic oscillator system, L_i operators up to the bilinear choice would take $L_1 = a$, $L_2 = a^\dagger$, $L_3 = a^\dagger a$, and $L_4 = aa^\dagger$ operators. Thereby, let us label the corresponding damping parameters with $\gamma_1, \gamma_2, \gamma_3$, and γ_4 , respectively. Since the environment is supposed to be the same for all these operators, one allows to rewrite the above damping parameters as $\gamma r_1, \gamma r_2, \gamma r_3$, and γr_4 , respectively, in which r_i refers to the arrival rates of states after interacting with the surrounding with the same strength γ . For the two first operators, since the weak interaction with many atoms is supposed to simulate the coupling to a thermal bath with temperature T , the rates r_1 and r_2 must be related to each other by a Maxwell-Boltzmann factor [183, 184], i.e.

$$\frac{r_2}{r_1} = e^{-\omega_0/k_{\text{B}}T} = \frac{n(\omega_0)}{n(\omega_0) + 1}, \quad (2.57)$$

where $n(\omega_0) = 1/(e^{\omega_0/k_{\text{B}}T} - 1)$ is the mean number of energy quanta in the mode corresponding to the frequency ω_0 and k_{B} is the Boltzmann constant. Hence, for $L_1 = a$ and $L_2 = a^\dagger$, the quantum master equation reads

$$\begin{aligned} \frac{d}{dt} O_{\text{H}}(t) = & \mathfrak{i}[\mathcal{H}, O_{\text{H}}(t)] + \gamma(n(\omega_0) + 1) \left(a^\dagger O_{\text{H}}(t) a - \frac{1}{2} a^\dagger a O_{\text{H}}(t) - \frac{1}{2} O_{\text{H}}(t) a^\dagger a \right) \\ & + \gamma n(\omega_0) \left(a O_{\text{H}}(t) a^\dagger - \frac{1}{2} a a^\dagger O_{\text{H}}(t) - \frac{1}{2} O_{\text{H}}(t) a a^\dagger \right). \end{aligned} \quad (2.58)$$

However, for the two latter choices, the states corresponding to $a^\dagger a$ and aa^\dagger operators have the same arrival rates because they are not acting as the single ladder operators and do not change the states when interacting. So, $r_3 = r_4 = n(\omega_0)$ result in

$$\begin{aligned} \frac{d}{dt}O_H(t) = & \text{i} [\mathcal{H}, O_H(t)] + \gamma n(\omega_0) \left(a^\dagger O_H(t) a - \frac{1}{2} a^\dagger a O_H(t) - \frac{1}{2} O_H(t) a^\dagger a \right) \\ & + \gamma n(\omega_0) \left(a O_H(t) a^\dagger - \frac{1}{2} a a^\dagger O_H(t) - \frac{1}{2} O_H(t) a a^\dagger \right). \end{aligned} \quad (2.59)$$

2.8 The Lindemann criterion

The mechanism of melting in the bulk of a system was first proposed by Lindemann [185] to explain the melting transition via the vibration of atoms in the simple crystals (crystals containing more complex structures exhibit a vibrational complexity). In his theory, the melting process initiates when the atoms start to invade the space of their nearest neighbors and disturb them, implying that the fraction of root-mean-square amplitude and the interatomic distance become so large at some point as the temperature is increased. In practice, the increase of temperature leads to the increase of the average amplitude of thermal vibrations and the certain threshold value in his theory is determined when the amplitude reaches at least 10% of the nearest neighbor distance. However, this critical value of the Lindemann parameter may vary ranging from 5% to 15% depending on the magnitude of quantum effects, crystal structure, and nature of interparticle interactions [186–188]. Immediately, thus, considering the lattice constant l , one is able to argue that the maximum displacement of atoms in a solid must satisfy

$$x_{\max} \lesssim 0.05 \dots 0.15 \cdot l. \quad (2.60)$$

Additionally, the threshold value for the upper limit to the (quasi) particle density or phonon number can be obtained as an important factor in solids. The starting point to derive the critical value of this density based on the Lindemann criterion x_{\max} is the investigation of the harmonic oscillator to a first-order approximation with the following Hamiltonian

$$\mathcal{H} = \omega_0 \left(a^\dagger a + \frac{1}{2} \right), \quad (2.61a)$$

$$a^\dagger = \sqrt{\frac{m_a \omega_0}{2}} \left(x - \text{i} \frac{p}{m_a \omega_0} \right), \quad (2.61b)$$

$$a = \sqrt{\frac{m_a \omega_0}{2}} \left(x + \text{i} \frac{p}{m_a \omega_0} \right), \quad (2.61c)$$

where ω_0 is the oscillation frequency, a^\dagger and a are the bosonic creation and annihilation operators, respectively. The parameter m_a is the atomic mass, x is the position operator, and p is the momentum operator. The amplitude of thermal vibration discussed above in the Lindemann criterion can be related to

the maximum displacement $x = x_{\max}$ at which the momentum vanishes, i.e. $p = 0$. Thus, the phonon number $\langle a^\dagger a \rangle$ can be found as

$$\langle a^\dagger a \rangle = \frac{m_a \omega_0}{2} x_{\max}^2. \quad (2.62)$$

If one simply applies the approximation $\omega_0 = \omega_D$, where $\omega_D \simeq 2 \cdot (10^{12} - 10^{13})$ rad/s is the Debye frequency, as well as considering $m_a \simeq (1 \text{ u} - 100 \text{ u})$ and $l \simeq (0.1 - 0.01) \text{ nm}$, $\langle a^\dagger a \rangle$ is obtained as

$$\langle a^\dagger a \rangle \lesssim 10, \quad (2.63)$$

meaning that the total number per atom of phonons should not exceed 10 to keep the integrity of the periodic lattice and to avoid lattice melting.

2.9 The damped driven harmonic oscillator

In this section, we focus on a damped driven harmonic oscillator to find the critical value of the driving field, which is tightly connected to the lattice melting issue. To do so, we introduce both a driving force and damping in a harmonic oscillator system, leading to the equation

$$\ddot{x}(t) + \gamma \dot{x}(t) + \omega_0^2 x(t) = \frac{1}{m_a x_0} \mathcal{E}(t). \quad (2.64)$$

The term \ddot{x} is the acceleration of the system, ω_0 is the oscillation frequency, γ is the damping parameter, and the term $\omega_0^2 x$ is a classical restoring force that follows Hooke's law. Meanwhile, $\mathcal{E}(t) = a \cos(\omega t)$ is an external electric field as a periodic driving, with a and ω being the amplitude and the frequency of the driving, respectively. Also, m_a and $x_0 = \sqrt{1/2m_a \omega_0}$ is the atomic mass and the maximum displacement of the undamped harmonic oscillator, respectively.

Introducing $z(t) = x(t) + iy(t)$, one simply solves the equation

$$\ddot{z}(t) + \gamma \dot{z}(t) + \omega_0^2 z(t) = \frac{1}{m_a x_0} a e^{i\omega t}, \quad (2.65)$$

for which only the real part of $z(t)$ is important here. Using the simple ansatz $z(t) = z_{\max} e^{i\omega t}$, we obtain

$$z_{\max} = -\frac{a}{m_a x_0} \frac{1}{(\omega^2 - \omega_0^2) - i\gamma\omega}. \quad (2.66)$$

This equation can be rewritten as $z_{\max} = |z_{\max}| e^{i\varphi}$, resulting in the expression $z(t) = |z_{\max}| e^{i(\varphi + \omega t)}$. From equation $z(t) = x(t) + iy(t)$, we then find the particular solution of Eq. (2.64)

$$x(t) = x_{\max} \cos(\omega t + \varphi), \quad x_{\max} = |z_{\max}| = \frac{a}{m_a x_0} \frac{1}{\sqrt{(\omega^2 - \omega_0^2)^2 + \gamma^2 \omega^2}}. \quad (2.67)$$

In the case of resonance condition $\omega = \omega_0$, one finds $x_{\max} = a/m_a x_0 \gamma \omega_0$. Looking simply at Eq. (2.62), one deduces

$$\langle a^\dagger a \rangle = \left(\frac{a}{\gamma} \right)^2. \quad (2.68)$$

So, according to the Lindemann criterion, the following relation

$$a \lesssim 3.3 \gamma. \quad (2.69)$$

has to hold for the threshold driving field strength a to avoid lattice melting in the presence of damping effects.

2.10 Chapter summary

In this chapter, we overviewed the basic concepts on the fermionic and bosonic operators in quantum mechanics required to formulate our future model. Next, we benchmarked the bond-operator representation to a two-spin-1/2 system. This representation separates the singlet and triplet states and even rewrites the reduced system's Hamiltonian in terms of singlet or triplet operators. We reviewed the Heisenberg equation of motion and Fermi's golden rule in the absence and presence of damping, later called the Lindblad quantum master equation in open quantum systems. We also introduced the term including the damping effect when a harmonic oscillator as the reduced system is damped in an environment.

With the aid of the Lindemann criterion, we also calculated the upper limit to the particle density in a damped driven harmonic oscillator, which is linked to the maximum displacement of atoms in a solid. From this data, we found the threshold driving field to be applied to avoid lattice melting in a reduced system.

3. A dimerized spin-1/2 chain

As mentioned before, magnetic quantum systems are the protagonist of the present thesis due to their potential spin-based electronics in the future [83]. In this chapter, a simple driven well-dimerized spin-1/2 chain coupled to a phonon system (mediator) and bath is chosen to serve as the principal model to benchmark and test the nonequilibrium physics of such systems. The stress is on the “well-dimerized” spin chains, meaning that the system does not, either at equilibrium or in its driven state, approach a phase transition to a magnetically ordered, to a gapless quantum disordered, or to any other different magnetic states. First, we will give an overview of the model experimentally point of view in Sec. 3.1. The model Hamiltonian is given in Sec. 3.2 to show how the system is comprised of different parts. In Sec. 3.3 we will discuss the approximations applied to the model to not be too complicated to simulate. We define the observables and expectation values for both lattice and spin systems in Sec. 3.4. In Sec. 3.5 we derive the equations of motion governing the time-dependent dissipative observables with the aid of the Lindblad formalism and finally the chapter ends with a summary in Sec. 3.6.

3.1 Experimental observations

Historically, as mentioned in the introduction, the magnetic order reduction in a magnetic system was first devoted to the laser-induced subpicosecond demagnetization of ferromagnetic Ni [84], leading to the ultrafast phenomena [85–89]. Quantum spin chains are valuable in this thesis [98–104]. In general, inorganic spin chain compounds comprising dimerization of the lattice of a Heisenberg model

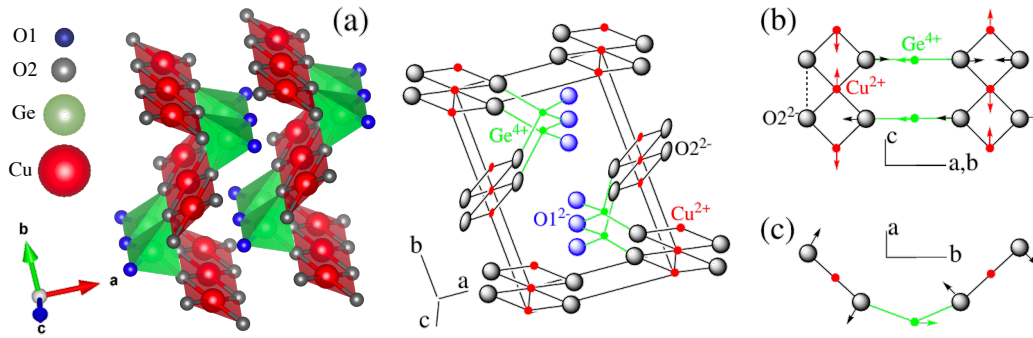


Figure 3.1: (a) The octahedral crystal structure of CuGeO_3 constructed of CuO_2 ribbons connected to each other via GeO_4 tetrahedra. (b) and (c) CuO_2 ribbons projected in the a,b,c , and $a-b$ plane, respectively. The nearest and next-nearest neighbor exchange constant corresponds respectively to the path $\text{Cu-O}_2\text{-Cu}$ and dashed line in (b) [202, 203].

are the best candidates in low-dimensional physics. Although there have been found several solids as alternating spin chain systems with different properties, we provide some examples here as appropriate candidates in this regard.

Let us focus on CuGeO_3 . The space group of this structure shown in Fig. 3.1 (a) is $Pbmm$ with the lattice parameters of the orthorhombic unit cell $a = 4.8 \text{ \AA}$, $b = 8.4 \text{ \AA}$ and $c = 2.9 \text{ \AA}$. In general, there are two different types of oxygen O^{2-} ions shown in gray (O_2) and blue (O_1). In this structure, Cu^{2+} ions in $3d^9$ configuration form antiferromagnetic spin-1/2 chains. Thus, in a half-filled chain [157, 159], a comparably simple ansatz, each Cu site holds one hole with spin-1/2 and the spin-spin interaction occurs via oxygen orbitals. In Fig. 3.1(b), the $\text{Cu-O}_2\text{-Cu}$ exchange path gives rise to the leading antiferromagnetic exchange constant, while the dashed line belongs to the next-nearest-neighbor exchange path. Also, the distortion of the lattice in the ordered phase is shown via the arrows in Figs. 3.1(b) and 3.1(c).

In 1993 Hase and co-workers [157] found an exponential drop in the magnetic susceptibility of this compound below $\sim 14 \text{ K}$ indicating the opening of a spin gap (see below) in its magnetic spectrum. Immediately, the gap was confirmed via the neutron scattering experiments [189] and quasi one-dimensionality of the structure was shown via the strongly anisotropic dispersion of the magnetic excitations [190]. Moreover, it was shown both theoretically and experimentally that CuGeO_3 can be well described by a Heisenberg chain with next-nearest-neighbor interaction [190–201]. While the correct value of the next-nearest-neighbor (interdimer) interaction is still controversial, the leading magnetic exchange constant in a dimer of this structure is approximately $J = 10 \text{ meV}$ [159]. The temperature at which the susceptibility has a broad maximum is near 57 K , which is proportional to almost half of $J/k_B \simeq 116 \text{ K}$, leading to a spin gap and bandwidth of about 7 meV and 10.4 meV , respectively.

The phonon modes (due to the swinging of positive and negative ions against

each other) involve motion of the CuO_2 ribbons, and not of the magnetic (Cu^{+2}) ions themselves, implying that the correlations between displacements may safely be neglected, and the approximation of Einstein phonons can easily be justified.

Meanwhile, interionic distances (phonons) modulate the spin-spin interactions, resulting in the spin-phonon coupling (SPC) [160, 161]. This coupling is based on the magnetoelastic effects between the magnetic ions and the magnetic energy produced by the lattice deformations. To understand the main origin of SPC, we use the relativistic effect through the spin-orbital interaction. The phonon modes and/or lattice displacements effectively change the hybridization between Cu-3d and O-2p in the CuGeO_3 structure via the hopping integrals. This, in turn, changes the orbital motion of atomic electrons. On the other hand, it is well-known that there is a coupling between the electron's spin and orbital degrees of freedom (e.g. described by the Kugel–Khomskii coupling [204, 205]). The SPC effect can then be understood as the tendency towards the suppressed superexchange interaction under the structural distortion along the phonon mode. In order to study the SPC effect, one could compute the superexchange coupling as functions of various phonon amplitudes. Then, the quadratic dependence of the hopping integral on the phonon amplitudes enables us to use a quadratic coefficient to measure the SPC strengths for the individual hopping process. So, the number of effectively coupled electronic hopping processes is the key to the SPC strength.

Another confirmed alternating spin chain system with the spin gap of about 3.5 meV is the inorganic vanadyl pyrophosphate $(\text{VO})_2\text{P}_2\text{O}_7$ [162–165]. In addition to these two systems with strong SPCs, $\text{Cu}(\text{NO}_3)_2$ [166] is also a quasi-one-dimensional alternating spin-1/2 chain with spin gap 0.38 meV and a weak SPC. Furthermore, recently NaVOAsO_4 [167] and AgVOAsO_4 [168] have been discovered as new alternating spin chains with the spin gap in the range of 5 meV. Another class of candidate systems is the set of metal-organic TTF compounds [98, 206], and even purely organic TCNQ compounds [207], in which the spin-Peierls transition has been observed and the distorted (low-temperature) state is an alternating spin chain. In addition to these compounds, alternating antiferromagnetic-ferromagnetic spin-1/2 chains such as $\text{Na}_3\text{Cu}_2\text{SbO}_6$ [208] and $(\text{CH}_3)_2\text{NH}_2\text{CuCl}_3$ [209] with negative next-nearest-neighbor couplings are further category of interest in quantum magnetism.

Although many lattices can be listed here as spin chains, in this thesis, we mostly focus on the spin chain inspired by CuGeO_3 . The need to consider the full quantum model comes from the fact that in most materials the phonon frequency is of the same order of magnitude of J . Thus, away from the static limit, the properties of the system may be largely affected by phonon dynamics. For example, a finite SPC is needed to drive the system into a gapped (dimerized) state. Indeed, since the phonon displacement is coupled to the dimerization operator, a small spin-phonon perturbation gives rise to a next-nearest-neighbor

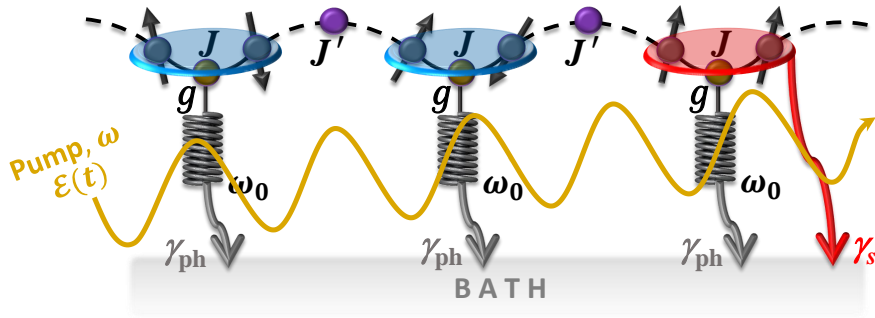


Figure 3.2: Schematic of the system under study consisting of the spin system, driven Einstein phonon, laser field, and the bath. The intradimer spin-spin coupling, interdimer spin-spin coupling, the SPC, phonon damping, and spin damping are described respectively by $J = 10$ meV, J' , g , γ_{ph} , and γ_s . The laser continuously pumps energy into the system and then drives it out of equilibrium. Blue ellipses display dimer singlets and the red one a triplon excitation.

spin-spin interaction J' , and it is well known that a finite J'/J is needed to open a spin gap in one dimension [210, 211]. These arguments have been confirmed by accurate density matrix renormalization group calculations [212] and Monte Carlo simulations [213]. In addition, including vibrations and displacements of the lattice is important for several magnetic materials, either in magnetically ordered phases (where phonons may affect the magnon dispersion) or in the absence of magnetic long-range order (where phonons stand up in the competition between valence-bond solids and spin liquids).

3.2 The J -model Hamiltonian

With this introduction, it is then natural to explore new physical insights when the spin and phonon sectors in an open quantum system are externally driven and weakly/strongly coupled to each other. Thus, we intend to look at the dynamics of the alternating spin chain shown in Fig. 3.2. We model the system as follows. The laser driving excites an Einstein phonon that couples to the leading magnetic exchange constant in the spin chain and the dissipation is modeled via the bath operators in the Lindblad formalism that directly damp both the lattice and spin sectors.

Building on the described system above, the total Hamiltonian constitutes of four terms: (i) the dimerized spin chain Hamiltonian \mathcal{H}_s , (ii) the phonon Hamiltonian \mathcal{H}_p , (iii) the SPC term \mathcal{H}_{sp} , and (iv) the coupling of laser field and phonon \mathcal{H}_l . It should be noted that the coupling of both phonon and spin systems to the bath is not explicitly in these terms but will be introduced via the Lindblad formalism [27, 135]. Thus, we have

$$\mathcal{H} = \mathcal{H}_s + \mathcal{H}_p + \mathcal{H}_{\text{sp}} + \mathcal{H}_l. \quad (3.1)$$

By inspiration of the periodic boundary condition for spin operators \vec{S} , the first term reads

$$\mathcal{H}_s = \sum_{i=1}^N J \vec{S}_{1,i} \cdot \vec{S}_{2,i} + J' \vec{S}_{2,i} \cdot \vec{S}_{1,i+1}, \quad (3.2)$$

where J and J' , respectively, refer to the intradimer and interdimer spin-spin coupling strength [see Fig. 3.2]. To describe an antiferromagnetic system, in general, $J > J' > 0$ has to hold. Moreover, N is the number of dimers or system size. It is necessary to mention that in real 3d transition-metal compounds, anisotropy terms are generally weak and negligible for simplicity.

The second term, phonon Hamiltonian, can simply be described by an ordinary harmonic oscillator through the bosonic creation b^\dagger and annihilation b operators. Thereby, one writes

$$\mathcal{H}_p = \sum_{i=1}^N \omega_0 b_i^\dagger b_i, \quad (3.3)$$

with ω_0 being the phonon frequency. Note that the Brillouin zone (BZ) is defined from $-\pi$ to π , i.e. the phonon mode contributes to i -th site of N dimer by $q_i = -\pi + \frac{2\pi i}{N}$.

The third term refers to the coupling of the phonon (including real-space bosonic operators) and leading magnetic exchange coupling J in the spin system with strength g . We include magnetoelastic effects, by assuming that the J is affected linearly by lattice distortions along the chain, as [161, 214]

$$\mathcal{H}_{sp} = \sum_{i=1}^N g (b_i + b_i^\dagger) \left(\vec{S}_{1,i} \cdot \vec{S}_{2,i} - \langle \vec{S}_{1,i} \cdot \vec{S}_{2,i} \rangle_{\text{eq}} \right), \quad (3.4)$$

in which $\langle \vec{S}_{1,i} \cdot \vec{S}_{2,i} \rangle_{\text{eq}}$ is the equilibrium value, while $(b_i + b_i^\dagger)$ refers to the phonon displacement. The subtraction of equilibrium value in the equation above is needed to set the vacuum as the ground state of both phonon and spin systems. We call the present coupling of the phonon to the leading magnetic interaction the J -model. The linear SPC Hamiltonian can be justified with the fact that the lattice distortions (stemming from the small degree of buckling) are rather small in our target material, CuGeO_3 [215], and we do not expect higher-order contributions, $(b_i + b_i^\dagger)^{\geq 2}$, to play a crucial role. Also, we assume that a phonon driven to large amplitudes by the laser field can not significantly transfer energy to other vibrational modes, meaning that the nonlinear phonon–phonon coupling is neglected. The phonon can also be coupled to the next-nearest-neighbor interaction J' , called J' -model, which will be addressed in chapter 6 in detail.

The fourth term in Eq. (3.1) is the coupling of a classical oscillating electric field to the phonon displacement: laser-phonon coupling. Physically point of view, this coupling stems from the time-varying electric dipole moment of phonons,

which first induces local electric fields during the lattice motion and then couples to the electric field. The coupling can be written as

$$\mathcal{H}_1 = \sum_{i=1}^N \mathcal{E}(t) (b_i + b_i^\dagger), \quad (3.5)$$

where $\mathcal{E}(t) = a \cos(\omega t)$ is the pump driving field and a (ω) describes the laser amplitude (frequency). In this notation, the laser electric field with strength E_0 is $E(t) = E_0 \cos(\omega t)$ and moves an ion (Oxygen ion in our target material) with a certain mass and the displacement x . On the other hand, the electric dipole moment of Oxygen ions is $-ex$, leading to a time-dependent potential energy of $\mathcal{E}(t) = exE_0 \cos(\omega t) = a \cos(\omega t)$, where $a = exE_0$. So, there is a charge and spatial dependence hidden in the a . This driving is a bulk effect, meaning that the Einstein phonon of every bond is stimulated. This driving is continuous and may inevitably lead to heating and eventually to destroy the coherence of the system, and later the system itself. Thus, we must remediate the system via a heat sink to maintain a constant (low) system temperature despite the steady drive. The reality of the situation in our model will be more detailed in Sec. 4.4.

3.3 Approximations

Now, it is time to simplify the terms described above by applying valid approximations to later pave the way to solve the equations of motion corresponding to the systems' observables.

As well-known, a dimer comprising of two spins-1/2 is described by a four-dimensional Hilbert space including a singlet state and three triplet states. These states can be expressed by the creation operators obeying the bosonic statistics. The elementary magnetic excitations in the magnetic insulators containing localized spin-1/2 are triply degenerate $S = 1$ quasiparticles called triplons. In this case, the bond-operator representation uses these operators/quasiparticles to define the spin operators [171, 175]

$$S_{1(2),i}^\alpha = \pm \frac{1}{2} \left(t_{\alpha,i} + t_{\alpha,i}^\dagger \mp \mathbf{i} \sum_{\beta\zeta} \epsilon_{\alpha\beta\zeta} t_{\beta,i}^\dagger t_{\zeta,i} \right), \quad (3.6)$$

where ϵ is the totally antisymmetric tensor considering different flavors x , y , and z . Because the triplon operators are hard-core bosons, one should follow the corresponding statics given in Sec. 2.3. However, hard-core bosons are difficult to treat analytically, because the hard-core constraint corresponds to a strong interaction so it is typically impossible to use the perturbation theory. On the other hand, as it will be mentioned in the following, we work with the zero temperature in this thesis and it is well-known that for small temperatures $T \ll J$, the bosons are so dilute and the hard-core interaction contribution is not significant and can be neglected [216]. It implies that for relatively low densities and weak

interdimer coupling $J'/J \leq 0.5$, we are allowed to approximate the triplons as non-interacting bosons [173]. Of course, for further studies, larger interdimer coupling and a unitary transformation controlled to high orders in J'/J can be considered instead of the standard Bogoliubov transformation [174, 217, 218]. Therefore, hereinafter we treat triplon operators as ordinary bosonic operators, i.e. we use the commutation relations $[t_{\alpha,i}^\dagger, t_{\beta,j}] = \delta_{\alpha\beta}\delta_{ij}$ and $[t_{\alpha,i}^\dagger, t_{\beta,j}^\dagger] = [t_{\alpha,i}, t_{\beta,j}] = 0$ throughout the thesis.

In the next step, we apply the Fourier transformation to transform the operators into the momentum space using

$$t_{\alpha,i} = \frac{1}{\sqrt{N}} \sum_k t_{k,\alpha} e^{-ikr_i}, \quad t_{\alpha,i}^\dagger = \frac{1}{\sqrt{N}} \sum_k t_{k,\alpha}^\dagger e^{ikr_i}. \quad (3.7)$$

Inserting reciprocal space version of Eq. (3.6) into the Eq. (3.2) results in [see Appendix A for the corresponding calculations and details]

$$\sum_{i=1}^N \vec{S}_{1,i} \cdot \vec{S}_{2,i} = -\frac{3}{4}N + \sum_{k,\alpha} t_{k,\alpha}^\dagger t_{k,\alpha}, \quad (3.8a)$$

$$\sum_{i=1}^N \vec{S}_{2,i} \cdot \vec{S}_{1,i+1} = -\frac{1}{4} \sum_{k,\alpha} \cos(k) \left(2t_{k,\alpha}^\dagger t_{k,\alpha} + t_{k,\alpha} t_{-k,\alpha} + t_{k,\alpha}^\dagger t_{-k,\alpha}^\dagger + 3 \right), \quad (3.8b)$$

wherein we take only bilinear terms into account, i.e. the triplet-triplet interactions are neglected for simplicity. Thus, the spin Hamiltonian can be rewritten as

$$\begin{aligned} \mathcal{H}_s = & \underbrace{-\frac{3}{4}JN - \frac{3}{4}J' \sum_k \cos(k)}_{\mathcal{H}_0} + J \sum_{k,\alpha} t_{k,\alpha}^\dagger t_{k,\alpha} \\ & - \frac{1}{4}J' \sum_{k,\alpha} \cos(k) \left(2t_{k,\alpha}^\dagger t_{k,\alpha} + t_{k,\alpha} t_{-k,\alpha} + t_{k,\alpha}^\dagger t_{-k,\alpha}^\dagger \right), \end{aligned} \quad (3.9)$$

where the term \mathcal{H}_0 is a constant value and does not contribute to the system dynamics (we ignore it where it is not needed), but it contributes to the ground state energy of the system. To achieve the ground state of the triplon system in equilibrium, the above Hamiltonian needs to be diagonalized. We employ a Bogoliubov transform through [see Appendix B]

$$t_{k,\alpha} = \tilde{t}_{k,\alpha} \cosh(\theta_k) + \tilde{t}_{-k,\alpha}^\dagger \sinh(\theta_k), \quad (3.10a)$$

$$t_{k,\alpha}^\dagger = \tilde{t}_{k,\alpha}^\dagger \cosh(\theta_k) + \tilde{t}_{-k,\alpha} \sinh(\theta_k), \quad (3.10b)$$

to obtain

$$t_{k,\alpha}^\dagger t_{k,\alpha} = y_k \left(\tilde{t}_{k,\alpha}^\dagger \tilde{t}_{k,\alpha} + \frac{1}{2} \right) - \frac{1}{2} + \frac{1}{2} y_k' \left(\tilde{t}_{k,\alpha}^\dagger \tilde{t}_{-k,\alpha}^\dagger + \tilde{t}_{k,\alpha} \tilde{t}_{-k,\alpha} \right), \quad (3.11)$$

where $\exp(-2\theta_k) = \sqrt{1 - \lambda \cos(k)}$ [$\lambda = J'/J$ being the ratio of the magnetic interactions] has to hold true for a diagonalized Hamiltonian. We have exchanged

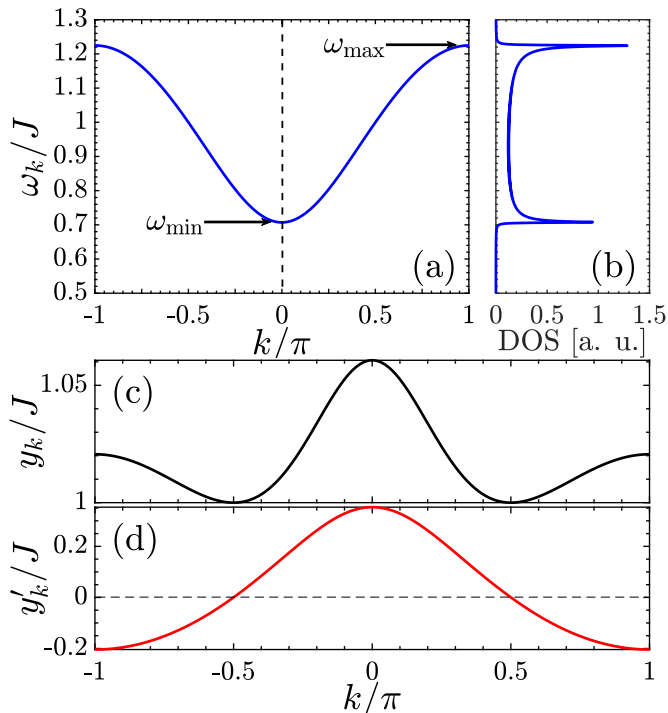


Figure 3.3: (a) One-triplon band spectrum and (b) corresponding density of states (in arbitrary units) of a dimerized spin-1/2 chain, respectively. The triplon mode-dependent prefactors y_k and y'_k are presented respectively in (c) and (d).

k by $-k$ where necessary since the expression is invariant due to $\cos(k) = \cos(-k)$. Also, we have defined [see Appendix B]

$$y_k = \frac{1 - \frac{\lambda}{2} \cos(k)}{\sqrt{1 - \lambda \cos(k)}}, \quad (3.12a)$$

$$y'_k = \frac{\frac{\lambda}{2} \cos(k)}{\sqrt{1 - \lambda \cos(k)}}. \quad (3.12b)$$

After tedious calculations one deduces [\mathcal{H}_0 plus a constant term given in Appendix B are neglected]

$$\mathcal{H}_s = \sum_{k,\alpha} \omega_k \tilde{t}_{k,\alpha}^\dagger \tilde{t}_{k,\alpha}. \quad (3.13)$$

In the above equation, the triplon dispersion energy is given by

$$\omega_k = J \sqrt{1 - \lambda \cos(k)}, \quad (3.14)$$

where we here numerically set the coupling strength of a dimer to be unity, $J = 1$, wishing to measure other quantities in units of J . Also, we choose $\lambda = 1/2$ to ensure that the dimerization still works for the spin chain, consistent with low temperature estimation for the interaction ratio $\lambda \lesssim 1/2$ in a spin ladder [173].

For $\lambda = 1/2$, it gives rise to a spin gap of about 7 meV, as mentioned at the beginning of the present chapter. The plot of this dispersion is shown in Fig. 3.3(a) in which one triply degenerate band is dispersing from $\omega_{\min} = \sqrt{1/2}J$ at $k = 0$ to $\omega_{\max} = \sqrt{3/2}J$ at $k = \pm\pi$, so-called one-triplon band. Inspired by the relation $\text{DOS} = (-1/\pi)\text{Im} \sum_{k \in \text{BZ}} (\omega + i\eta - \omega_k)^{-1}$ with the phenomenological broadening parameter $\eta = 1$ meV, Fig. 3.3(b) shows the density of states of a dimerized spin-1/2 chain. It is evident that the dominant feature is the singularity at $k = \pm\pi$ corresponding to the upper limit of the one-triplon band, ω_{\max} . This dominant contribution will manifest itself in dynamic response of the systems' observables.

Following the seminal triplon dispersion, we look at the triplon mode dependency of prefactors in Eq. (3.12) in Figs. 3.3(c) and 3.3(d), respectively, which are important in the presence of SPC, g [see Eq. (3.18)]. Two points are in order here. First is nonzero $y_k = 1$ at $k = \pm\pi/2$ and second is negative values of y'_k for $k > \pi/2$ and $k < -\pi/2$. In both cases, $k = 0$ gives rise to the maximum energy, while $k = \pm\pi/2$ ($\pm\pi$) shows the minimum one for y_k (y'_k). To provide more information about these prefactors, we would mention that $y_k - y'_k = \omega_k/J$ holds valid. The above points will become important to justify the behaviors of triplon observables and later the discrepancy between the J and J' models.

For the phonon Hamiltonian, we only take the Einstein phonon with mode $q = 0$ into account since the laser-phonon interaction is generally a long-range order and this mode is enforced by the nature of the driving photons. By these, we mean that our Einstein optical phonon is IR-active to be driven by the laser field through a time-varying electric dipole moment [133]. Therefore, using the Fourier transform Eq. (3.3) becomes

$$\mathcal{H}_p = \omega_0 b_0^\dagger b_0. \quad (3.15)$$

As for the SPC contribution, we again use the bond-operator representation and bosonic statistics to transform the spin operators into the triplon ones. However, we further use the mean-field theory [see Sec. 2.2] to obtain a bilinear Hamiltonian and to calculate the microscopic coupling constants between the lattice and the spin chain – mean-field enables us to describe the SPC in terms of operators acting on the spin and phonon systems separately. It should be pointed out that the mean-field decoupling of the driven phonon and the spin system is acceptable because the relative size of the quantum fluctuations in a phononic system, which is macroscopically occupied, is negligible. Following the Fourier transform and zero phonon mode, we define the phonon displacement

$$d = \frac{1}{\sqrt{N}} (b_0 + b_0^\dagger), \quad (3.16)$$

and finally have the following expression for the SPC Hamiltonian [see Appendix A]

$$\mathcal{H}_{\text{sp}} = g \langle d \rangle \underbrace{\left[\sum_{k,\alpha} t_{k,\alpha}^\dagger t_{k,\alpha} - \sum_{k,\alpha} \langle t_{k,\alpha}^\dagger t_{k,\alpha} \rangle_{\text{eq}} \right]}_{\mathcal{H}_{\text{sp,s}}} + g \underbrace{\left\langle \sum_{k,\alpha} t_{k,\alpha}^\dagger t_{k,\alpha} - \sum_{k,\alpha} \langle t_{k,\alpha}^\dagger t_{k,\alpha} \rangle_{\text{eq}} \right\rangle}_{\mathcal{H}_{\text{sp,p}}} d, \quad (3.17)$$

where $\mathcal{H}_{\text{sp,s}}$ ($\mathcal{H}_{\text{sp,p}}$) refers to the operator acting on the spin (phonon) system. Here the product of the two expectation values (common in the mean-field theory) is neglected since it does not influence the dynamics of the system at all. Plugging Eq. (3.11) in the above equation yields

$$\mathcal{H}_{\text{sp,s}} = g \langle d \rangle \sum_{k,\alpha} \left[y_k \left(\tilde{t}_{k,\alpha}^\dagger \tilde{t}_{k,\alpha} - n(\omega_k) \right) + \frac{1}{2} y'_k \left(\tilde{t}_{k,\alpha}^\dagger \tilde{t}_{-k,\alpha}^\dagger + \tilde{t}_{k,\alpha} \tilde{t}_{-k,\alpha} \right) \right], \quad (3.18)$$

where $n(\omega_k) = [\exp(\hbar\omega_k/k_B T) - 1]^{-1}$ represents the Bose-Einstein statistics, classifying the equilibrium mean number of energy quanta in the triplon mode k corresponding to the triplon frequency ω_k .

And for the laser-phonon coupling, we immediately use the Fourier transform and Eq. (3.16) to obtain

$$\mathcal{H}_l = N \mathcal{E}(t) d. \quad (3.19)$$

As mentioned before, the laser field which is mainly responsible for driving the optical phonon is treated as a classical oscillating field, meaning that the quantum fluctuations of the laser field are negligible relative to its expectation value.

In addition to the applied approximations above-listed, we restrict ourselves to the zero temperature for simplicity, leading to $n(\omega_k) = 0$. In our system which the spins are localized on the sites of a lattice, the spin and lattice temperatures are the same. However, it is not impossible to obtain electronic or spin temperatures different from the lattice temperature in some systems. In such irradiated systems, there are two ways to control the system temperature; system geometry and the laser driving procedure. If we apply temperature gradient across a system with a given length, the interplay between the laser field and the temperature gradient may tune the temperature of degrees of freedom. Or, if we apply a laser pulse as the driving field instead of a continuous field, the system temperature can also be controlled.

In a nutshell, the full Hamiltonian \mathcal{H} in the J -model can be denoted as $\mathcal{H} = \mathcal{H}_s + \mathcal{H}_p + \mathcal{H}_{\text{sp}} + \mathcal{H}_l$ with

$$\mathcal{H}_s = \sum_{k,\alpha} \omega_k \tilde{t}_{k,\alpha}^\dagger \tilde{t}_{k,\alpha}, \quad (3.20a)$$

$$\mathcal{H}_p = \omega_0 b_0^\dagger b_0, \quad (3.20b)$$

$$\mathcal{H}_{\text{sp,s}} = g \langle d \rangle \sum_{k,\alpha} \left[y_k \left(\tilde{t}_{k,\alpha}^\dagger \tilde{t}_{k,\alpha} - n(\omega_k) \right) + \frac{1}{2} y'_k \left(\tilde{t}_{k,\alpha}^\dagger \tilde{t}_{-k,\alpha}^\dagger + \tilde{t}_{k,\alpha} \tilde{t}_{-k,\alpha} \right) \right], \quad (3.20c)$$

$$\mathcal{H}_1 = N \mathcal{E}(t) d. \quad (3.20d)$$

3.4 Observables

Now, we turn to define the physical observables and expectation values for both phonon and triplon systems. These definitions are based on the terms that appeared in the Hamiltonians and will be included in the derivation of the equations of motion in the next section. The common observables in a phononic system at any time t are

$$q(t) = \left\langle \frac{1}{\sqrt{N}} (b_0^\dagger + b_0) \right\rangle(t), \quad (3.21a)$$

$$p(t) = \left\langle \frac{i}{\sqrt{N}} (b_0^\dagger - b_0) \right\rangle(t), \quad (3.21b)$$

$$n_{\text{ph}}(t) = \left\langle \frac{1}{N} b_0^\dagger b_0 \right\rangle(t), \quad (3.21c)$$

where $q(t)$, $p(t)$ and $n_{\text{ph}}(t)$ respectively is the phonon displacement, phonon momentum and the phonon occupation. For the triplon system, we define

$$u_k(t) = \left\langle \sum_{\alpha} \tilde{t}_{k,\alpha}^\dagger \tilde{t}_{k,\alpha} \right\rangle(t), \quad (3.22a)$$

$$z_k(t) = \left\langle \sum_{\alpha} \tilde{t}_{k,\alpha}^\dagger \tilde{t}_{-k,\alpha}^\dagger \right\rangle(t), \quad (3.22b)$$

where the real variable $u_k(t)$ is the k -component of the triplon occupation, while there is not a descriptive meaning for complex $z_k(t)$; it only counts triplon mode excitations. The complex conjugate of $z_k(t)$ can be defined as well, i.e. the expectation value of the product of two annihilation operators, which emerges in the SPC Hamiltonian.

3.5 Equations of motion

For an arbitrary observable $O(t)$, applying Lindblad quantum master equation to the prototype model of a driven dimerized spin-1/2 chain to include an additional damping term in its equations of motions (EoMs), we provide the conditions under which the NESS is engineered properly for the spin-lattice system via the systems' parameters. One easily uses Eq. (2.56) to deduce

$$\begin{aligned} \frac{d}{dt} \langle O \rangle(t) &= i \langle [\mathcal{H}, O(t)] \rangle + \sum_i \gamma_i \left\langle \underbrace{L_i^\dagger O(t) L_i}_{\frac{1}{2} L_i^\dagger O(t) L_i + \frac{1}{2} L_i^\dagger O(t) L_i} - \frac{1}{2} \{O(t), L_i^\dagger L_i\} \right\rangle \\ &= i \langle [\mathcal{H}, O(t)] \rangle + \frac{1}{2} \sum_i \gamma_i \left\langle [L_i^\dagger, O(t)] L_i + L_i^\dagger [O(t), L_i] \right\rangle, \end{aligned} \quad (3.23)$$

where \mathcal{H} describes the total system's Hamiltonian given by Eq. (3.20), i.e. their final approximated forms. The equation above contains two terms, the first

Heisenberg term and the second Lindblad (damping) term. As mentioned in Sec. 2.7, L_i are the Lindblad operators in the reduced system's Liouville space and γ_i are given in terms of certain correlation functions of the environment and play the role of relaxation rates for different decay modes of the system.

We start with the phonon sector, which behaves similarly as a damped harmonic oscillator [see Sec. 2.7.2]. For $O(t) = \{q(t), p(t), n_{\text{ph}}(t)\}$, $L_i = \{b_0, b_0^\dagger\}$, $\gamma_{\text{ph}1} = \gamma_{\text{ph}}[n(\omega_0) + 1]$, and $\gamma_{\text{ph}2} = \gamma_{\text{ph}}n(\omega_0)$ one achieves [see Appendix C for details]

$$\frac{d}{dt}q(t) = \omega_0 p(t) - \frac{\gamma_{\text{ph}}}{2}q(t), \quad (3.24a)$$

$$\frac{d}{dt}p(t) = -\omega_0 q(t) - 2[\mathcal{E}(t) + g(\mathcal{U}(t) + \mathcal{V}(t))] - \frac{\gamma_{\text{ph}}}{2}p(t), \quad (3.24b)$$

$$\frac{d}{dt}n_{\text{ph}}(t) = -[\mathcal{E}(t) + g(\mathcal{U}(t) + \mathcal{V}(t))]p(t) - \gamma_{\text{ph}}n_{\text{ph}}(t) + \gamma_{\text{ph}}n(\omega_0), \quad (3.24c)$$

in which

$$\mathcal{U}(t) = \frac{1}{N} \sum_k y_k [u_k(t) - 3n(\omega_k)], \quad (3.25a)$$

$$\mathcal{V}(t) = \frac{1}{N} \sum_k y'_k v_k(t). \quad (3.25b)$$

After tedious calculations given in Appendix C, finally, the time evolution of the triplon system's observables is also obtained as

$$\frac{d}{dt}u_k(t) = 2gq(t)y'_k w_k(t) - \gamma_s u_k(t), \quad (3.26a)$$

$$\frac{d}{dt}v_k(t) = -2[\omega_k + gq(t)y_k] w_k(t) - \gamma_s v_k(t), \quad (3.26b)$$

$$\frac{d}{dt}w_k(t) = 2[\omega_k + gq(t)y_k] v_k(t) + 2gq(t)y'_k \left[u_k(t) + \frac{3}{2} \right] - \gamma_s w_k(t), \quad (3.26c)$$

where

$$v_k(t) = \text{Re } z_k(t) \quad \text{and} \quad w_k(t) = \text{Im } z_k(t). \quad (3.27)$$

A detailed analysis of these equations will be given in the following. Concerning the damping terms, there is a point to be discussed here. Here similar to the phonon sector we have considered the spin-non-conserving dissipation operators $L_{1,k,\alpha} = t_{k,\alpha}^\dagger$ and $L_{2,k,\alpha} = t_{k,\alpha}$, i.e. $L_{1,k,\alpha}^\dagger = L_{2,k,\alpha}$ with the corresponding damping parameters $\gamma_{1,k,\alpha} = \gamma_s [n(\omega_k) + 1]$ and $\gamma_{2,k,\alpha} = \gamma_s n(\omega_k)$. In our model, the spin damping can still be treated as weakly damped oscillators since the spins are coupled to a phononic bath. By this consideration, the spin-conservation is easily breakable and for this reason, one may think of the systems with finite spin-orbit coupling as the target materials. However, for systems with weak spin-orbit

couplings, spin conservation requires terms of the general type $L_{kq,\alpha} = t_{k,\alpha}^\dagger t_{q,\alpha}$. In this case, mixed wave-vector states of the triplon system come into play role in the spin-dependent phonon scattering processes and thus lead to a significantly more involved set of EoMs.

Let us concisely comment on the k -independent spin damping γ_s . In general, we are allowed to consider k -dependence of the decay rate, $\gamma_s(k)$, however, the spin chain is a 1D system and it is coupled to a generalized 3D phononic bath, meaning that the weak coupling between the spin sector and the phononic bath allows us to ignore the k -dependence of the spin damping.

It should be stressed that there are no correlations between different modes k and the system is totally symmetric in k , therefore, $3N + 3$ dimension of the ordinary differential equation system can simply be reduced to $3\frac{N}{2} + 3$. Solving Eqs. (3.24) and (3.26), we provide the conditions under which the NESS is engineered properly for the spin sector via the system's parameters. So far, we have formulated a specific way of exciting a quantum driven-dissipative dimerized spin-1/2 chain out of equilibrium – by switching on the laser field and changing the entire Hamiltonian. Nevertheless, it is well-known that the entire system should be in equilibrium at zero temperature, resulting in the initial conditions

$$q(0) = 0, \quad p(0) = 0, \quad n_{\text{ph}}(0) = 0, \quad (3.28a)$$

$$u_k(0) = 0, \quad v_k(0) = 0, \quad w_k(0) = 0. \quad (3.28b)$$

Let us define two following new quantities in the spin system for consistency with the phonon sector, as well as for providing physical meaning of the observables, as

$$n_x(t) = \frac{1}{N} \sum_k u_k(t), \quad (3.29a)$$

$$V(t) = \frac{1}{N} \sum_k v_k(t), \quad (3.29b)$$

respectively the *dressed* triplon number per site and average behavior of the off-diagonal component resulting from Eq. (3.26). Of course, one allows to define $W(t) = \frac{1}{N} \sum_k w_k(t)$. On the other hand, to connect these to the close definitions in Eq. (3.25), we introduce the *bare* triplon number per site

$$n_b(t) = \mathcal{U}(t) + \mathcal{V}(t) + \frac{3}{2N} \sum_k [y_k - 1], \quad (3.30)$$

which can be understood/derived from Eq. (3.11) at zero temperature. The last term in the equation above is the equilibrium expectation value, 0.0285, in the thermodynamic limit, referring to the quantum and/or vacuum fluctuations in equilibrium. Physically, these fluctuations are the main origin of driven phonon-induced modification of the magnetic interaction in the spin-lattice system. However, we have used the new basis to rotate it to 0 to have all \tilde{t} operators in

Eq. (3.11) as the excitations above the vacuum value of 0, resulting in zero values for the initial conditions of the spin sector observables given by Eq. (3.28b).

It is necessary to mention that the most of parameters in the model presented for a dimerized spin-1/2 chain, $\{N, J, J', g, a, \omega_0, \omega, \gamma_{\text{ph}}, \gamma_{\text{s}}\}$, are variable throughout the present thesis. However, phonon damping obviously depends on its coupling to other phonons as well as its energy. Due to the weak coupling of a single Einstein phonon to an ensemble of phonons (bath), we set this damping to be very small, e.g., 2% of the phonon energy $\hbar\omega_0$ [$\hbar = 1$], i.e. $\gamma_{\text{ph}} = 0.02\omega_0$ throughout the thesis. In the majority of our calculations in the solution of the EoMs, we will use $N = 2000$ dimers to ensure that finite-size effects can be empirically ruled out. Also, there is no restriction for the time interval and the quantum spin NESS can be studied from $t = 0$ to ∞ . Additionally, we mostly consider the spin damping smaller than γ_{ph} to stress that the spins coupled to the phononic bath are in general damped weaker than phonons coupled to the bath, i.e. $\gamma_{\text{s}} < \gamma_{\text{ph}}$ holds in general valid. For the amplitude of the laser field, $a = e\mathcal{E}x_0$, considering the maximum displacement $x_0 = \sqrt{\hbar/m_a\omega} \simeq 0.01$ nm with the mass $m_a \lesssim 1$ u of the atoms of the system and $\omega = 2\pi c/L_w$ [L_w being the wavelength of lasers, which are usually of some hundred nanometers], as well as the electric field strength $\mathcal{E} \simeq 2 \times 10^8$ V.m⁻¹ [134], one finds $a \simeq 2$ meV, which for our target material with magnetic interaction $J \simeq 10$ meV, it is experimentally achievable.

It should be noted that the investigation of the average behavior of the observables in the NESS is achieved by

$$\bar{X}(t) = \frac{1}{t - t_0} \int_{t_0}^t X(t') dt', \quad (3.31)$$

for $t > t_0$ where $X(t)$ can be each of the expectation values introduced in both lattice and spin sectors. We use the notation \bar{X}_0 for resonant $\omega = \omega_0$ (between the laser and phonon) and X_0 in the case of off-resonant $\omega \neq \omega_0$ throughout this thesis.

Let us, finally, briefly mention some general information regarding the numerical simulations. We solve the EoMs in C++ employing the GNU Scientific Library [219] and making use of the Runge Kutta 4 algorithm with relative maximum $\epsilon_{\text{rel}} = 0$, absolute maximum $\epsilon_{\text{abs}} = 10^{-6}$ error for the algorithm, initial step size $h_{\text{start}} = 10^{-6}$, and absolute number of data points $N_{\text{data}} = 40000$ [220]. Fourier transforms, however, were calculated utilizing the implemented Fast Fourier Transform in Matlab [221]. Fit functions and plots were also created with Matlab.

3.6 Chapter summary

Starting with the experimental observations on the spin chains, this chapter is devoted to a general understanding of a driven-dissipative dimerized spin-1/2 chain. The model Hamiltonian for such a system is introduced in detail, which comprises of the spin-spin coupling between the nearest- and next-nearest-neighbors, the

driven phonon model, the coupling between the spins and driven phonon, and the coupling between the laser field and the IR-active Einstein phonon. Next, we applied the special approximations to both lattice and spin sectors to make it easier for both analytical and numerical calculations, but still close to the reality. Meanwhile, the Bogoliubov transformation is applied to later calculate the triplon dispersion energy of the spin system.

While the bilinear Hamiltonian neglecting the triplet-trilplet interactions describes the spin Hamiltonian, the mean-field decoupling approximation resembles the SPC to separate the operators acting on the spin and phonon systems. For simplicity, we restrict ourselves to zero temperature and will leave the finite temperature effects for upcoming studies. Finally, we distinguish between the phonon and spin system by defining the physical observables. The dissipation effect which is usually dominated by the many phonons of the lattice system is included within the Lindblad formalism at the operator level. The quantum master equations valid at all times governing the time-evolution of this system and for various sets of real parameters are established.

4. Weak coupling regime: J -model

In this chapter, focusing on the regime of weak SPC, we use the adjoint quantum master equation through the spectral representation of Lindblad formalism [27, 135] to characterize the NESS and their properties in a driven-dissipative dimerized spin-1/2 chain. Section 4.1 focuses on the properties of the obtained NESS from the equations of motions (EoMs) on how the systems' parameters tune this NESS. We then turn to the transient and relaxation processes in Sec. 4.1.1. The influence of driving and SPC are discussed in Sec. 4.1.2. A quantitative analysis of the convergence timescale in the spin NESS is provided in Sec. 4.1.3. The general condition for the existence of NESS is briefly discussed in Sec. 4.1.4. Section 4.2 deals with the harmonic decompositions of the NESS in the presence of a weak SPC. In Sec. 4.3, the energy flow of different parts of the system in the NESS will be discussed, which is helpful for experimental perspectives. It is presented in Sec. 4.4 how the applied approximations can be accepted in reality. The experimental perspectives are given in Sec. 4.5 and, finally, a summary of the chapter is included in Sec. 4.6.

Most of this chapter has been published as a Regular Article in Physical Review B [169].

4.1 NESS in the phonon-driven spin system

In the beginning, we reduce the space of possible driving parameters and restrict our considerations to resonant excitation of the Einstein phonon mode in the presence of a weak SPC, meaning that we select the laser frequency such that $\omega = \omega_0$, i.e. $\mathcal{E}(t) = a \cos(\omega_0 t)$. This is required to find the strongest effects of the

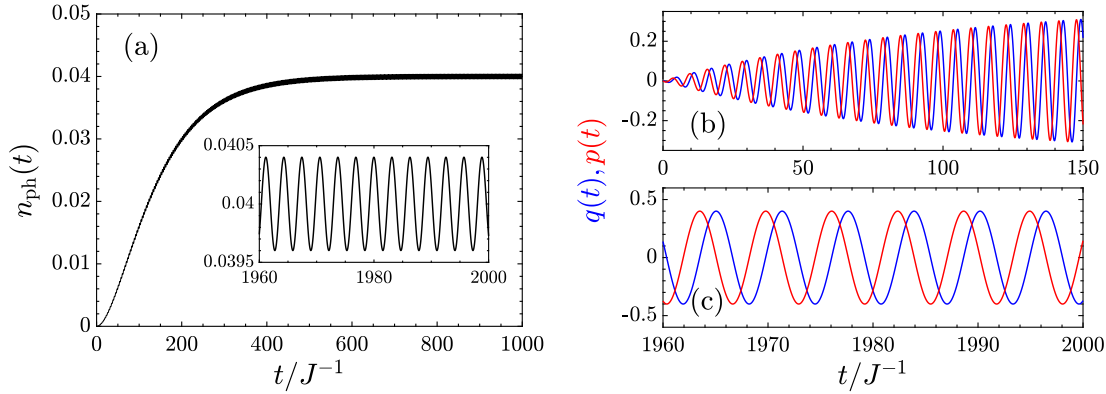


Figure 4.1: Response of the Einstein phonon to a resonant driving field. Here $\omega_0/J = 1$, $a/J = 0.004$, $\gamma_{\text{ph}} = 0.02\omega_0$, and $g = 0$. (a) phonon occupation, $n_{\text{ph}}(t)$ – the inset shows the steady state of the driven phonon system at long times. (b) Phonon displacement, $q(t)$, and momentum, $p(t)$, shown from $t = 0$ and (c) $q(t)$ and $p(t)$ at long times.

driven phonon on the spin system, i.e. when ω_0 matches the triplon excitations. An obvious manifestation is the fact that the typical coupling of the driven phonon to the spin system, g , is weak, thus, the phonon characterized by $q(t)$, $p(t)$ and $n_{\text{ph}}(t)$ can behave as a classical damped driven harmonic oscillator [see Sec. 2.9]. The basic reasoning of this weak SPC strength is founded on the inherent generic weakly locking of the spin and lattice degrees of freedom. The initial step towards establishing a typicality argument is to identify the decisive physical mechanisms or characteristics determining the NESS. The standard recipe to do so is the case of decoupled spin-lattice system, $g = 0$, where the driven phonon is the available system to arrive at a phonon NESS. Once a candidate for the relevant properties is available, we can construct classes of coupled setups that share those characteristics.

In Fig. 4.1(a), the phonon occupation is illustrated that is driven up to a finite average value, and the inset that it oscillates steadily around this finite value for all later times; this is the NESS of the laser-driven phonon system. The timescale for which the NESS is reached is $2/\gamma_{\text{ph}}$ for $n_{\text{ph}}(t)$, which it is understandable from Eq. (3.24) in which $q(t)$ and $p(t)$ serve damping $\gamma_{\text{ph}}/2$, while for the phonon occupation one should additionally calculate the damping effect of the phonon momentum such that $+\frac{\gamma_{\text{ph}}}{2} - \gamma_{\text{ph}} = -\gamma_{\text{ph}}/2$ is the final damping of $n_{\text{ph}}(t)$, too. It is important to pause for a moment and find out the average of the phonon occupation in the decoupled situation, $g = 0$, in the NESS. Let us characterize this average by $\bar{n}_{\text{ph}0}$ following the notation introduced before in Eq. (3.31). As mentioned before, we are allowed to investigate the phonon system as a damped driven harmonic oscillator at $g = 0$. So, from the fundamental relation between the bosonic creation and annihilation operators as well as the displacement and momentum operators, the expectation value of the number operator is linearly proportional to the square of maximum displacement, i.e. $\langle b_0^\dagger b_0 \rangle \propto q_{\text{max}}^2$, where

we noticed that in the resonance condition, $q_{\max} \propto a/\gamma_{\text{ph}}$ [see Sec. 2.9]. Thus the phonon occupation is proportional to $(a/\gamma_{\text{ph}})^2$, addressed by Fermi's golden rule [the flow of energy into the system is proportional to the square of the matrix element], where for fixed $a/\gamma_{\text{ph}} = 0.2$ in our case it yields $\bar{n}_{\text{ph}0} = 0.04$, which is small but it is a macroscopic occupation for a single created and annihilated field excitation (phonon).

In the case $g = 0$, the phonon displacement fulfills the following equation

$$\frac{d^2q(t)}{dt^2} + \frac{\gamma_{\text{ph}}}{2} \frac{dq(t)}{dt} + \omega_0^2 q(t) = -\omega_0 \left[\frac{\gamma_{\text{ph}}}{2} p(t) + 2\mathcal{E}(t) \right], \quad (4.1)$$

describing the displacement of a damped driven harmonic oscillator [222]. The numerical solution of this equation [and the corresponding one for $p(t)$] is shown in Figs. 4.1(b) and 4.1(c), respectively, at short and long times. Both quantities oscillate with time and continuously reach a NESS with the same timescale of $2/\gamma_{\text{ph}}$. Note that, as usual, for the displacement and momentum, a relative $\frac{\pi}{2}$ phase difference [due to $\mathbf{i} = \exp(\mathbf{i}\pi/2)$ difference between Eqs. (3.21a) and (3.21b)] gives rise to the same trend for $p(t)$. The function in the NESS, Fig. 4.1(c), oscillates with a constant maximum amplitude $2(a/\gamma_{\text{ph}})$ and the driving frequency ω_0 . But, the frequency of the oscillations in the driven $n_{\text{ph}}(t)$ is twice that of $q(t)$ and $p(t)$ [see Eq. (3.24c) in which both the laser field and phonon momentum with frequency ω_0 lead to a oscillating phonon occupation with frequency $2\omega_0$]. From the above interpretations, one notices that the averages of $q(t)$ and $p(t)$ in the decoupled NESS are zero. We will only discuss the effects of physical parameters on the phonon occupation for the phonon sector in the following.

In most of the figures, we set the spin damping to a finite value, however, even without a driving criterion, it is worth seeing how NESS formation is treated in both phonon and triplon occupations. Note that the strongest responses of both phonon and spin systems when including the SPC is dedicated to the driving frequencies within the two-triplon band, i.e. at $2\omega_{\min} \leq \omega_0 \leq 2\omega_{\max}$ ($\sqrt{2} \leq \omega_0/J \leq \sqrt{6}$). For our standard parameter $a/\gamma_{\text{ph}} = 0.2$ and weak SPC regime $g/J = 0.05$, Fig. 4.2(a) shows that for the in-band driving at $\omega_0/J = 1.5$ and $\gamma_s/J = 0.01$, a NESS is formed. However, for $\gamma_s/J = 0$, i.e. when the spin-freezing occurs, Fig. 4.2(b) shows how the triplon occupation is pumped rapidly to an unstable regime, leading to an unstable phonon occupation as well. The instability phenomena in both occupations follow the same treatment such that if $n_x(t)$ is not periodic, $n_{\text{ph}}(t)$ is not also periodic. For $\omega_0/J = 3.0$ above the two-triplon band, a NESS emerges even without spin damping, see Fig. 4.2(c). In this case, a phonon is far from the two-triplon band and it can not efficiently drive the spin system, hence, the response of the spin system characterized by the occupation of triplons is weak, while the phonon occupation remains so. It is necessary to mention that there is a direct relationship between the damping effect and the beating type of the envelope function in the responses. In Fig. 4.2(c) the undamped k -components of $n_x(t)$, i.e. $u_k(t)$, leads to such a beating form. In another selection, if the phonon

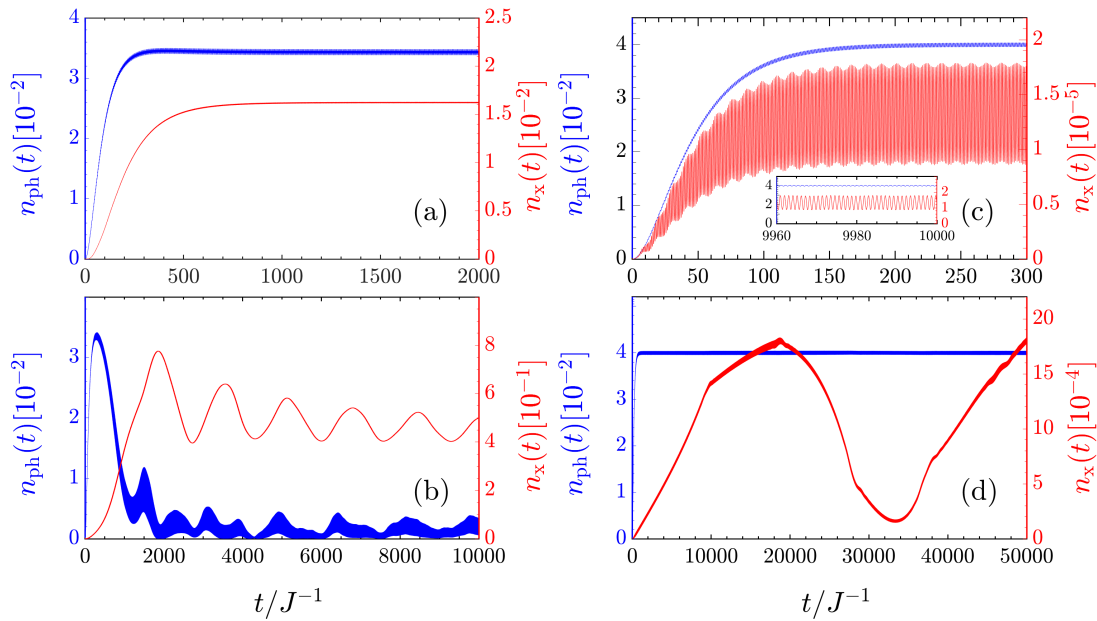


Figure 4.2: Time-dependence of the phonon occupation, $n_{\text{ph}}(t)$, and triplon occupation, $n_x(t)$, shown with $a/\gamma_{\text{ph}} = 0.2$ and $g/J = 0.05$. (a) When $\omega_0/J = 1.5$ and $\gamma_s/J = 0.01$, the system converges to a NESS on a conventional timescale. (b) When $\omega_0/J = 1.5$ and $\gamma_s/J = 0$, $n_x(t)$ increases rapidly, destabilizing the phonon occupation. (c) When $\omega_0/J = 3.0$, the driving frequency lies sufficiently far above the two-triplon band that NESS exist even when $\gamma_s/J = 0$. (d) When $\omega_0/J = 0.75$, the driving frequency lies well below the two-triplon band but the second harmonic, $2\omega_0$, lies within it. In this case, when $\gamma_s/J = 0$ the lattice approximates a NESS, but with this near-constant driving of the spin system a NESS cannot be formed.

frequencies locate below the lower two-triplon band edge, e.g. at $\omega_0/J = 0.75$, the situation is somewhat more complicated since the spin system is more unstable than other frequencies if the spin-phonon coupling is not strong enough. As can be seen in Fig. 4.2(d), the phonon does indeed approach a NESS, but following the weak SPC regime, this essentially steady driving does not create a spin NESS. The difficulty to determine a spin NESS in the adiabatic regime (below the band) is inherent to the instability of the system in this regime.

Given this information, we choose six values of ω_0/J at fixed $g/J = 0.1$ (to get rid of the instability effect in the low-frequency regime, shown in Fig. 4.2(d)) and $\gamma_s/J = 0.01$ depending on the driven phonon frequencies below, in, and above the two-triplon band to study the spin occupation dynamics. Figure 4.3(a) shows that for laser driving at any driving frequency ω_0/J , the spin occupation is “pumped” to a new average value similar to the phonon system, about which it oscillates. It will be discussed in the next subsection 4.1.3 how this average value is determined. It can be seen that for the frequencies far from the two-triplon band, i.e. for $\omega_0/J = 0.5$ and 3.0 , a very weak occupation $\bar{n}_{x0} \lesssim 0.0001$ is produced, while for frequencies near the band, i.e. for $\omega_0/J = 1.5$ and 2.5 , we find states with

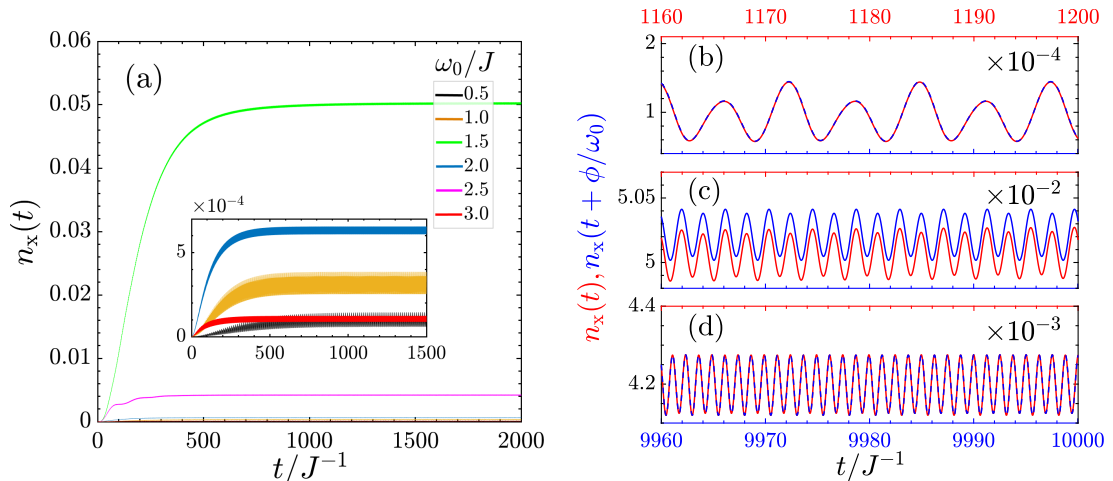


Figure 4.3: (a) Response of the spin system, measured by $n_x(t)$, to the driving phonon frequencies $\omega_0/J = 0.5, 1.0, 1.5, 2.0, 2.5$, and 3.0 at fixed $a/\gamma_{\text{ph}} = 0.2$, $g/J = 0.1$, and $\gamma_s/J = 0.01$. $n_x(t)$ in the spin NESS is shown at (b) $\omega_0/J = 0.5$, (c) $\omega_0/J = 1.5$, and (d) $\omega_0/J = 2.5$, where we compare results in the time window $1160 \leq t \leq 1200$ with those at $9960 \leq t \leq 10000$. All blue long-time traces are shifted by a phase $0 \leq \phi < 2\pi$ to see whether the red and blue states can be mapped to each other – as a characterization for the true NESS.

stronger occupations: $\bar{n}_{x0} \simeq 0.05$ and 0.004 , respectively. As for the band center, $\omega_0/J = 2$, only $\bar{n}_{x0} \simeq 0.0006$ is observed. The weak response of the band center originates from the momentum $k = \pi/2$ [see Fig. 3.3] at which the triplet state couples/excites to/from the driven phonon weaker than other momenta, due to the matrix element y'_k , resulting in a weak response of the spin system. It is worthwhile mentioning that the spin NESS established at frequencies far from the two-triplon band acts as a weak perturbation for the equilibrium state if one compares them with the value of quantum spin fluctuation, i.e. $\bar{n}_{b0} \simeq 0.0285$ in Eq. (3.30). By contrast, for some frequencies in and around the two-triplon band, the quantum spin NESS is almost twice that of \bar{n}_{b0} , which can be interpreted as a direct consequence of the resonance condition $\omega_0 = 2\omega_k$.

Moreover, the timescale over which the spin system reaches its NESS is different at various frequencies, meaning that the spin feedback effect depending on the phonon energy is important. However, it seems that it is 4 to 5 time constants of the spin damping $1/\gamma_s$. For $\omega_0/J = 0.5$, the convergence is associated with the delay because, at this frequency, γ_s is the same as γ_{ph} , meaning that the same timescale as the phonon “switch-on” timescale is needed for the spin system. For other frequencies, the role of phonon damping is also important in determining the convergence timescale due to the SPC process. Among the frequencies, $\omega_0/J = 1.5$ shows a longer process to be converged [we will come to the reason in the next subsection].

Let us zoom in the NESS trends in a time window $1160 \leq t \leq 1200$ in

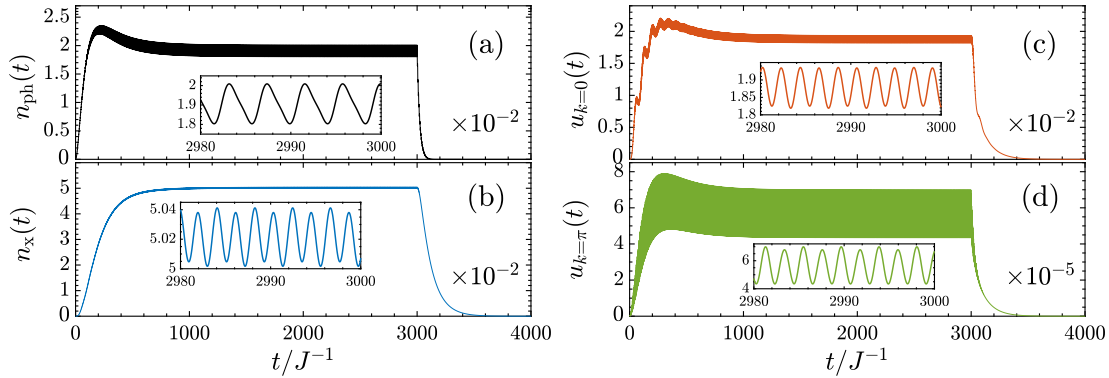


Figure 4.4: Creation of the NESS established with $a/\gamma_{\text{ph}} = 0.2$ and $g/J = 0.1$ for the driving frequency $\omega_0/J = 1.5$ and spin damping $\gamma_s/J = 0.01$; these are also the parameters of the green line in Fig. 4.3(a). (a) $n_{\text{ph}}(t)$, (b) $n_x(t)$, (c) $u_{k=0}$, and (d) $u_{k=\pi}$. Also shown is the relaxation of each variable when the driving is removed after 3000 time steps.

Figs. 4.3(b)-(d) for $\omega_0/J = 0.5, 1.5,$ and 2.5 and compare them with the long-time limit $9960 \leq t \leq 10000$ to demonstrate whether each of the driven states is a true NESS. We see that the spin NESS is proven since identical periodic traces are obtained for arbitrarily long times. Also, it is nice to confirm the NESS at rather short times for frequencies below and above the two-triplon band, Figs. 4.3(b) and 4.3(d), which is important for real applications. However, the trend is not yet a NESS for the in-band frequency, shown in Fig. 4.3(c), because the criterion in the band is not satisfied yet by the present set of parameters, see next subsections. In addition to the above-mentioned points, it can be seen that the NESS at any driving frequency shows a rather complex form, with a definite superposition of different frequency harmonics. This harmonic mixing is stronger at the low-frequency regime than other ones [see Sec. 4.2 for more details].

4.1.1 Switch-on and switch-off processes

In the previous sections, we discussed the convergence process of a NESS and concluded that for the frequencies sufficiently away from the band edges, the convergence is faster than those in the band. To understand the slow convergence process at switch-on in the band, we consider $\omega_0/J = 1.5$, $a/\gamma_{\text{ph}} = 0.2$, $\gamma_s/J = 0.01$, and $g/J = 0.1$ [similar to Fig. 4.3] in Fig. 4.4. Here we have added the phonon occupations in Fig. 4.4(a) in addition to the spin observables to see what happens to $\bar{n}_{\text{ph}0}$ at $g/J \neq 0$. Although the driving strength is the same as before, $n_{\text{ph}}(t)$ does not approach $(a/\gamma_{\text{ph}})^2$, but it first rises towards the plateau value of 0.04 in a time dictated by $1/\gamma_{\text{ph}}$ and pulls down again to a new average value $\bar{n}_{\text{ph}0} \simeq 0.02$ in a timescale of $1/[\gamma_s - f(\omega_0, \omega_k, g, a/\gamma_{\text{ph}})]$. This is a direct consequence of the spin feedback effect so that it absorbs some of the input phonon energy due to the SPC, g . In Fig. 4.4(b), the spin NESS is reached only after approximately 1200 time steps, which means $1/[\gamma_s - f(\omega_0, \omega_k, g, a/\gamma_{\text{ph}})] \approx 3/\gamma_s$. Looking at the

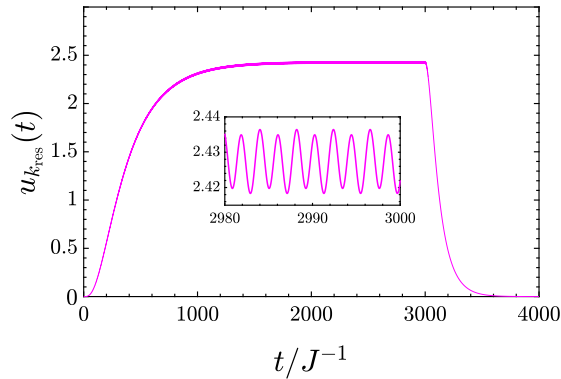


Figure 4.5: The same as Fig. 4.4, but for $u_{k_{\text{res}}}(t)$.

individual k -components in Figs. 4.4(c) and 4.4(d) shows that $k = 0$ and $k = \pi$ components behave the same as the phonon occupation so that they rise first with the timescale of $1/\gamma_s$, while a phonon driving- and SPC-dependent decaying rate is observed. However, it seems that the components at the band edges are not significantly determining the final spin NESS. Of course, it is no surprise to expect that the resonant wave-vector k_{res} satisfying $\omega_0 = 2\omega_{k_{\text{res}}}$ is mostly contributing to the final spin NESS and slow-convergence behavior. For this reason, we plot $u_{k_{\text{res}}}$ in Fig. 4.5, in the same way of Fig. 4.4 to verify this expectation. It is clear that the largest and the most slowly converging component is dedicated to k_{res} , requiring a longer time constant to converge, similar to Fig. 4.4(b) in the total triplon occupation.

Upon turning off the laser field, we remark that the relaxation timescale corresponding to both lattice and spin systems, which is obtained by evaluating either $1/\gamma_{\text{ph}}$ or $1/\gamma_s$ to their equilibrium value, 0, is satisfied with relevant relaxation timescales, meaning that our numerical calculations satisfy the experimental expectations very well. The process of relaxation in the Lindblad quantum master equation is the recovery of thermal equilibrium upon turning off the drive. In our model, the system temperature is initially set to $T = 0$ when the drive is off, and after a while, it should relax back to this state when the drive is off again, as confirmed.

4.1.2 The influence of driving and SPC

Having formulated the goals and laid out our model to tackle the dynamic of driven dimerized spin-1/2 chain, we now specify more concretely the quasi-stationary behavior of the NESS that may be amenable to our theoretical approach. To start with, we focus on the mean phonon occupation, $\bar{n}_{\text{ph}0}$. Figure 4.6(a) addresses the decoupled model (in the absence of SPC) for all driving frequencies in which the average energy in the driven phonon mode rises with the driving power, which is proportional to the square of the normalized electric-field amplitude to the phonon damping. However, the spin system is driven by the pumped phonon through the

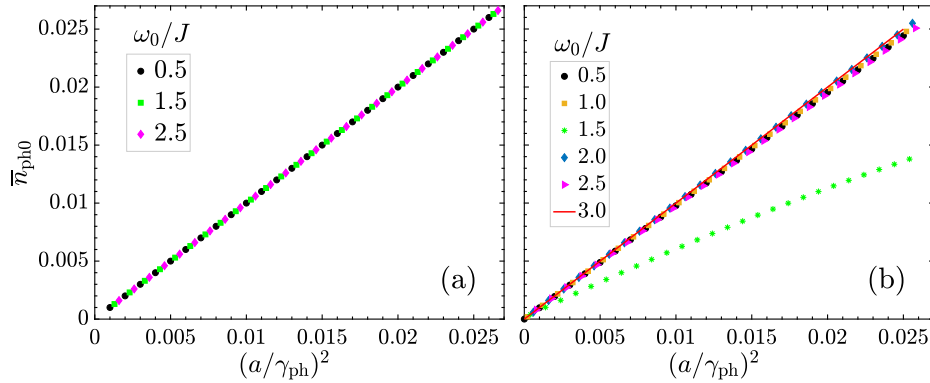


Figure 4.6: Average value of the driven phonon occupation number, \bar{n}_{ph0} , in a NESS, displayed as a function of $(a/\gamma_{ph})^2$ for various driving frequencies at fixed $\gamma_{ph} = 0.02\omega_0$ and $\gamma_s/J = 0.01$. (a) In the decoupled case, $g = 0$, and (b) in the presence of a given SPC, $g/J = 0.1$.

SPC parameter, g . When allowing g to come into play in the dynamic responses, the spin system is driven as well indirectly by the external laser field. We fix it to a generic value here, $g/J = 0.1$, and will discuss the weak and strong regimes in Fig. 4.7 and more in the next chapter. Additionally, spin damping is now possible to be included; here we fix it to $\gamma_s/J = 0.01$. In the absence of spin damping, somehow a spin freezing occurs for the resonant coupling between the phonon and triplons [see Fig. 4.2]. In Fig. 4.6(b), it is evident that the induced changes to the spin system from the damped driven phonons are small at most frequencies, except $\omega_0/J = 1.5$ for which the changes are significant along with a strong deviation from $(a/\gamma_{ph})^2$. This can again be traced back to the spin conservation in our model [see Eq. (3.4)] for which two spins are excited by the driven phonon. From this point, $\omega_0/J = 1.5$ shows a special suppression behavior and occupations can be exchanged between resonant states.

Having made sure that the results from the temporal behaviors as well as that the joint system will usually relax to a new (thermal) equilibrium state, we proceed with the spin system. We can then ask how the late-time behavior of the spin system is modified when changing some parameter of that Hamiltonian. To gain further insights on the dependency of triplon occupation on the power of laser a^2 and SPC g , we stick to Fig. 4.7. In Fig. 4.7(a), we show the dependence of the average triplon occupation, \bar{n}_{x0} , on a^2 in the NESS for various driving frequencies below, in, and above the two-triplon band. In the weak SPC regime, the dependence is linear over the full range of $(a/\gamma_{ph})^2$ for all frequencies except $\omega_0/J = 0.5$ [sufficiently away from the band] and 1.5 [in the band]. This linear response is expected from the elementary electrodynamics in which this power is proportional to the squared amplitude of the laser field. In these special frequencies, a saturation shown as \bar{n}_{x0} is driven towards unphysical values at very large a . We call these values unphysical because we have applied many

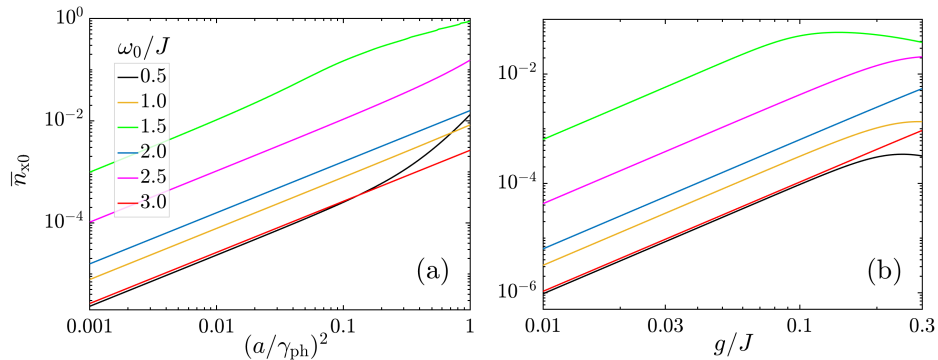


Figure 4.7: (a) Dependence of the average triplon occupation, \bar{n}_{x0} , in the NESS on the fluence, shown as $(a/\gamma_{\text{ph}})^2$, at driving phonon frequencies $\omega_0/J = 0.5, 1.0, 1.5, 2.0, 2.5,$ and 3.0 . The fixed system parameters are $g/J = 0.1$, $\gamma_{\text{ph}} = 0.02\omega_0$, and $\gamma_s/J = 0.01$. Only the $\omega_0/J = 0.5$ and 1.5 phonons at very high fluences show deviations from a linear form. (b) Dependence of \bar{n}_{x0} on the SPC constant, g , for driving phonons of the same six frequencies at fixed $a/\gamma_{\text{ph}} = 0.2$. A well-defined g^2 dependence at all small couplings gives way to a suppression of \bar{n}_{x0} at larger g values whose onset depends on ω_0 .

approximations to model the system properly while maintaining it to be soluble. Although the hard-core nature of the dimer spin states sets an absolute upper limit of $\bar{n}_{x0} = 1$ on the triplon occupation, the approximations allow us to set it to a lower value such as 0.2 to be physical. Note that this corresponds to the least favorable setup considered for $a/\gamma_{\text{ph}} = 0.2$ in the previous temporal results to assess the validity in the linear regime of driving. This justifies $\omega_0/J = 1.5$, while for $\omega_0/J = 0.5$, non-linear behavior of \bar{n}_{x0} at strong electric fields still makes it unphysical, originating from the instability of the system in the low-frequency regime. Coming back to Fig. 4.2, we noticed that an instability of the system below the two-triplon band occurs at late times for the spin system, conforming with the non-linear trends at $\omega_0/J = 0.5$.

Another interesting case arises if the SPC in the reference system is variable. Figure 4.7(b) aims at the dependence of the driven triplon occupation on the SPC, g , for the same six driving frequencies. As can be observed, at low values of g , the triplon occupation shows a g^2 form that is directly analogous to its dependence on a^2 . However, a suppression emerges for \bar{n}_{x0} at high g [where non-linearity treatment starts to appear], which is stronger for $\omega_0/J = 0.5$ and 1.5 than other driving frequencies. This suppression happened before in Fig. 4.6(b) for $\omega_0/J = 1.5$. So, we define the “weak” SPC regime corresponding to the linear behavior of \bar{n}_{x0} with g and the “strong” SPC regime corresponding to the non-linear trends. However, as mentioned before, for the purposes of the present analysis in this chapter, which is to discuss the properties of a generic driven quantum magnet, we will focus on the weak-coupling regime. This stems from the fact that most magnetic quantum materials do not show strong SPC

at equilibrium. After bringing them into contact employing sufficiently weak coupling, $g/J = 0.08$ is the point where these regimes are distinguished, but we adopt the value $g/J = 0.05$ hereafter to be representative of the class of magnetic materials. We will study the strong-coupling regime in the next chapter.

4.1.3 Quantitative analysis of the convergence timescale in the spin NESS

In the previous paragraphs, we briefly mentioned that there exist the driving parameters suitable for the formation of NESS. We noticed that for the in-band phonon frequencies, every aspect is different than beneath and above the two-triplon band. For the logic applications, one may need the “start-on” behaviors. So, we need to analyze the convergence process and identify a further effective timescale arising from the driving rather than $1/\gamma_{\text{ph}}$ and $1/\gamma_s$. Thereby, before turning to the next investigations, here we present a quantitative analysis of the convergence timescale in the spin NESS on both in- and out-of-band drivings. We approximate the phonon oscillations in the NESS as sinusoidal for weak SPCs with a fixed amplitude [see the inset panel in Fig. 4.1(a)]. Simply, the phonon displacement which is valid for the weak-coupling regime of SPC [for the strong regime of SPC, a more complex waveform is formed and a simple sinusoidal function does no longer describe it; see the next chapter for strong SPC effects] can be written as

$$q(t) = 2 \frac{a}{\gamma_{\text{ph}}} \sin(\omega_0 t) = 2 \frac{DJ}{g} \sin(\omega_0 t), \quad (4.2)$$

defining a dimensionless effective driving parameter for the spin system, $D = ga/J\gamma_{\text{ph}}$. After tedious calculations, for the resonant condition $\omega_0 = 2\omega_{k_{\text{res}}}$ where k_{res} is called the resonant momentum, we finally find [see Appendix D for details of the calculations] the following solutions for the EoM of triplon occupation

$$u_{k_{\text{res}}}(t) = \frac{3}{4} \Gamma_{k_{\text{res}}} \left[\frac{1 - e^{-(\gamma_s - \Gamma_{k_{\text{res}}})t}}{\gamma_s - \Gamma_{k_{\text{res}}}} - \frac{1 - e^{-(\gamma_s + \Gamma_{k_{\text{res}}})t}}{\gamma_s + \Gamma_{k_{\text{res}}}} \right], \quad (4.3)$$

with

$$\Gamma_{k_{\text{res}}} = \left| \frac{y'_{k_{\text{res}}} \omega_0 J_1 \left(\frac{4DJy_{k_{\text{res}}}}{\omega_0} \right)}{y_{k_{\text{res}}}} \right|, \quad (4.4a)$$

$$y_{k_{\text{res}}} = \frac{J + \frac{\omega_0^2}{4J}}{\omega_0}, \quad y'_{k_{\text{res}}} = \frac{J - \frac{\omega_0^2}{4J}}{\omega_0}, \quad (4.4b)$$

where $J_1(4DJy_{k_{\text{res}}}/\omega_0)$ is the Bessel function of the first kind.

This solution provides good agreements with the numerical responses of \bar{u}_{k0} and \bar{n}_{x0} in the resonant NESS. Equation (4.3) shows that $\gamma_s - \Gamma_{k_{\text{res}}}$ should be positive to have a true convergence, i.e. $\gamma_s > \Gamma_{k_{\text{res}}}$ has to hold. From this point, we define the true convergence rate, or excitation rate, as

$$\tilde{\gamma}_s = \gamma_s - \Gamma_{k_{\text{res}}}, \quad (4.5)$$

which should be positive to avoid an exponential divergence in the resonant triplon occupation $u_{k_{\text{res}}}(t)$. The long-time limit of Eq. (4.3) is given by

$$\lim_{t \rightarrow \infty} u_{k_{\text{res}}}(t) = \frac{3}{4} \Gamma_{k_{\text{res}}} \left[\frac{1}{\gamma_s - \Gamma_{k_{\text{res}}}} - \frac{1}{\gamma_s + \Gamma_{k_{\text{res}}}} \right] = \frac{3}{2} \frac{\Gamma_{k_{\text{res}}}^2}{\gamma_s^2 - \Gamma_{k_{\text{res}}}^2}, \quad \gamma_s > \Gamma_{k_{\text{res}}}. \quad (4.6)$$

For $\omega_0/J = 1.5$, $g/J = 0.1$, and $a/\gamma_{\text{ph}} = 0.2$ [see Fig. 4.3(c)], $\Gamma_{k_{\text{res}}} \simeq 0.0116$ can be found, which is larger than the fixed $\gamma_s/J = 0.01$. So, one expects no true convergence for this frequency and this resonance mode, which is confirmed in Fig. 4.3(c) through the non-matched short- and long-time NESSs originating from this resonance mode. It should be pointed out that although this divergence affects the final treatment of the NESS, it only happens for a certain mode and other modes in the band may lead to a final convergence treatment. While for another in-band resonant frequency $\omega_0/J = 2.0$, a true NESS can be obtained since $\Gamma_{k_{\text{res}}}$ approaches zero and satisfies the criterion $\gamma_s > \Gamma_{k_{\text{res}}}$. In this case, the average value of $u_{k_{\text{res}}}(t)$ in the NESS approaches zero if we sum over all resonance momenta, as confirmed by the blue curve (but for all excitations) in Fig. 4.3(a).

So far, we focused on the resonant case, however, for completeness of quantitative purposes it is necessary to consider the effect of driving at frequency ω_0 on the modes at $k \neq k_{\text{res}}$, meaning the action of the driving phonon as a ‘‘detuned’’ pump of all other triplon modes. We use the same strategy and allow $2\omega_k$ to differ from ω_0 . Let us define

$$\delta = 2\omega_k - \omega_0, \quad (4.7)$$

meaning that the excited mode k is detuned from the driving assuming $|\delta| < \omega_0$, i.e. we assume that the detuning is small compared to the driving, which δ can be positive or negative. By this, the k -component of triplon occupation $u_k(t)$ in the detuned phase is given by [see Appendix E for details]

$$u_k(t) = \frac{3}{2} \frac{\Gamma_k^2}{\tilde{\Gamma}_k(\gamma_s^2 - \tilde{\Gamma}_k^2)} \left(\tilde{\Gamma}_k [1 - e^{-\gamma_s t} \cosh(\tilde{\Gamma}_k t)] - \gamma_s e^{-\gamma_s t} \sinh(\tilde{\Gamma}_k t) \right), \quad \Gamma_k > |\delta|, \quad (4.8a)$$

$$u_k(t) = \frac{3}{2} \frac{\Gamma_k^2}{\tilde{\mathcal{G}}_k(\gamma_s^2 + \tilde{\mathcal{G}}_k^2)} \left(\tilde{\mathcal{G}}_k [1 - e^{-\gamma_s t} \cos(\tilde{\mathcal{G}}_k t)] - \gamma_s e^{-\gamma_s t} \sin(\tilde{\mathcal{G}}_k t) \right), \quad \Gamma_k < |\delta|, \quad (4.8b)$$

where $\Gamma_k = \frac{y'_k \omega_0}{y_k} J_1(4DJy_k/\omega_0)$ and

$$\tilde{\Gamma}_k^2 = \Gamma_k^2 - \delta^2, \quad \tilde{\mathcal{G}}_k^2 = \delta^2 - \Gamma_k^2. \quad (4.9)$$

The long-time limit of Eq. (4.8) is given by

$$\lim_{t \rightarrow \infty} u_k(t) = \frac{3}{2} \frac{\Gamma_k^2}{\gamma_s^2 - \tilde{\Gamma}_k^2}, \quad \Gamma_k > |\delta|, \quad (4.10a)$$

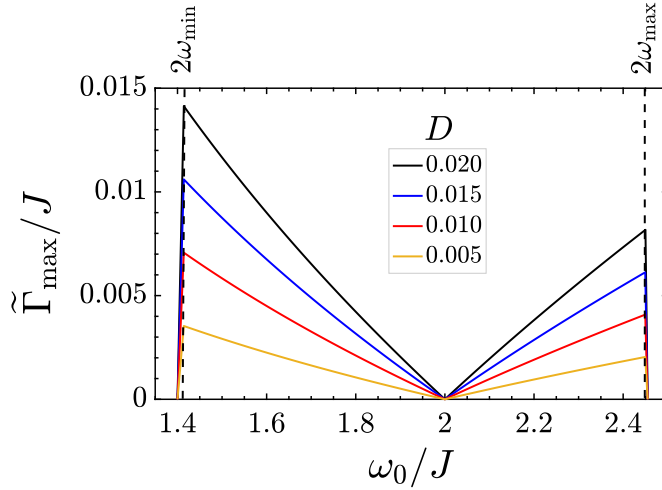


Figure 4.8: Dependence of $\tilde{\Gamma}_{\max}$ on the phonon frequency ω_0/J for four values of the driving strength, $D = ga/J\gamma_{\text{ph}}$ on the weak-coupling regime.

$$\lim_{t \rightarrow \infty} u_k(t) = \frac{3}{2} \frac{\Gamma_k^2}{\gamma_s^2 + \tilde{\mathcal{G}}_k^2}, \quad \Gamma_k < |\delta|. \quad (4.10b)$$

Accordingly, it is time to conclude that for frequencies sufficiently away from the two-triplon band, a rather fast convergence with the timescale $\frac{1}{\gamma_s - \tilde{\Gamma}_k} > \frac{1}{\gamma_s}$ is expected to a NESS. This has been confirmed/observed in Fig. 4.3(a) for $\omega_0/J = 0.5, 1.0$ and 3.0 .

In the resonant case, Eq. (4.3) will provide the highest threshold value, making $\tilde{\Gamma}_{\max} = \Gamma_{k_{\text{res}}}$, however, for frequencies outside but close to the two-triplon band, detuned driving comes into play. In Fig. 4.8, we look at $\tilde{\Gamma}_{\max}$ as a function of ω_0 . It shows an almost linear rise with frequency towards the two band edges along with the zero value at the band center $\omega_0/J = 2$ due to the zero element $y'_k|_{k=\pi/2} = 0$. Various tested D values show that $\tilde{\Gamma}_{\max}$ linearly alters with D . Due to the detuned driving, one expects a finite value for $\tilde{\Gamma}_{\max}$ as well beyond the band edges. Interestingly, most of the chosen set of parameters are proper for a true spin NESS and satisfy the above analytical expressions.

It is the time now to look at the k -components to see which values of k are selected by the phonon driving. To do so, for the full range of ω_0 , we in Fig. 4.9 show \bar{u}_{k0} for a few selected k across the Brillouin zone. As well-known up until now from the resonance $\omega_0 = 2\omega_{k_{\text{res}}}$, $k = 0$ and $k = \pi$ should present the strongest respective peaks at the band edges, respectively, at $2\omega_{\min}$ and $2\omega_{\max}$. For other in-band components $k = \pi/4, \pi/2 + \epsilon$ [$\epsilon = \pi/N$ is an offset from the band center, where $u_{k=\pi/2} = 0$] and $k = 3\pi/4$, the peaks appear at respective frequencies meeting the resonance condition $\omega_0 = 2\omega_k$. Thus k -selection on the basis of the driving energy is rather accurate and it is well justified to believe in a “resonant” wave vector, k_{res} from $\omega_0 = 2\omega_{k_{\text{res}}}$. Gathering all of these resonant wave vectors leads to the black squares u_{k0}^{\max} . The results are in agreement with the analytical expressions provided in Eqs. (4.6) and (4.10), as presented by dotted red lines

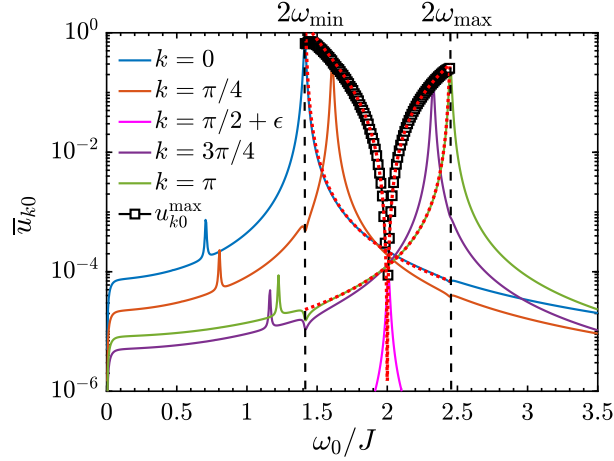


Figure 4.9: Average k -component of triplon occupation, \bar{u}_{k0} , in the NESS at fixed parameters $\gamma_{\text{ph}} = 0.02\omega_0$, $a/\gamma_{\text{ph}} = 0.2$, $g/J = 0.05$, and $\gamma_s/J = 0.01$ shown as a function of the driving frequency, ω_0 , for $k = 0, \pi/4, \pi/2 + \epsilon, 3\pi/4$, and π ; $\epsilon = \pi/N$ is an offset from the band center, where $u_{k=\pi/2} = 0$. Black squares show the maxima, u_{k0}^{\max} , of the \bar{u}_{k0} functions referring to different wave vectors k_{res} across the Brillouin zone. At all frequencies below the two-triplon band, $\omega_0 < 2\omega_{\min}$, the strongest peak is found in $u_{k=0}$ and at $\omega_0 > 2\omega_{\max}$ in $u_{k=\pi}$. The analytical results provided in Eqs. (4.6) and (4.10) are shown with dotted red lines in the band. The discrepancy observed at the band edges between the analytic and numeric results originates from detuning effects.

in the band. Also, outside the two-triplon band, one may notice that each \bar{u}_{k0} shows a pronounced below-band two-phonon process; the smaller peaks below $2\omega_{\min}$. Averaging over all the peaks of k -components below the band minimum leads to the peak at $\omega_0 = \omega_{\min}$ in \bar{n}_{x0} .

4.1.4 A systematic study of the existence of NESS

Moreover, the collection of information from the obtained results can be improved systematically and by generating multiple spin damping by restricting the triplon occupation. Keeping the driving continuously would lead to heating of the system on a finite timescale. In the case of the phonon sector, the Lindemann criterion in Sec. 2.8 easily establishes that the lattice melting due to phonon driving would become an issue for average phonon mode occupancies on the order of 10. On the other side, we fix a criterion for the triplon occupation, $n_x^{\max} = 0.2 < 1$, due to the applied approximations. So, we should find the driving parameters systematically such that the convergence of the coupled system does not hold anymore. In other words, we intend to discuss the conditions under which a NESS can exist over long driving times.

We begin with this criterion in Fig. 4.10 in which we show the threshold value of the driving strength, $(a/\gamma_{\text{ph}})_t$, as functions of spin damping and driving frequency, required to drive the triplon occupation of the spin NESS below 0.2. From the plot, it can be seen that when a small fraction of the leading magnetic interaction

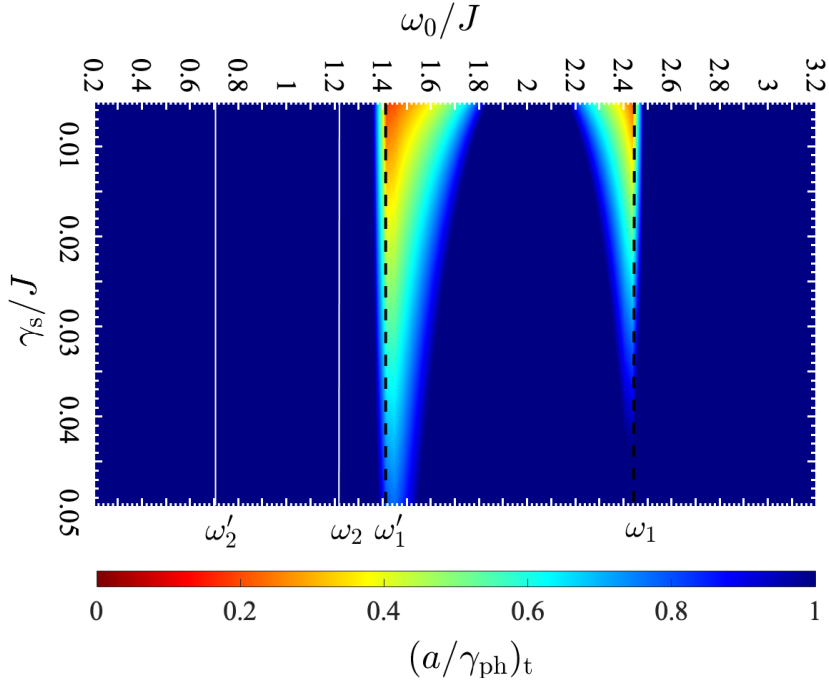


Figure 4.10: Threshold value, $(a/\gamma_{\text{ph}})_t$, of the normalized laser electric field strength required to achieve the maximum steady-state triplon occupation of $n_x = 0.2$, shown as a function of γ_s/J and ω_0/J for fixed $g/J = 0.05$ and $\gamma_{\text{ph}} = 0.02\omega_0$. We draw attention to the three regimes of behavior below, in, and above the two-triplon bands, $\omega'_1 = 2\omega_{\text{min}}$ and $\omega_1 = 2\omega_{\text{max}}$. Also one-triplon band is shown by the frequencies $\omega'_2 = \omega_{\text{min}}$ and $\omega_2 = \omega_{\text{max}}$, where unlike Fig. 4.9 no additional structure is visible in $(a/\gamma_{\text{ph}})_t$.

is damped to the bath (small spin dampings γ_s/J), the small driving $(a/\gamma_{\text{ph}})_t$ is adequate at driving frequencies corresponding to the lower and upper edges of the two-triplon band to meet the efficient triplon occupation ≤ 0.2 . However, strong driving is needed for the frequencies near the band center, below, and above the band at the same spin dampings. The actually required reason for these behaviors is interpreted by the direct relation of driving and damping effects in such coupled systems. Moreover, in contrast to Fig. 4.9, $(a/\gamma_{\text{ph}})_t$ does not reflect the presence of the two-phonon response feature around $\omega_0 = \omega_{\text{min}}$, underlining that the \bar{n}_{x0} values arising due to these processes are indeed small.

4.2 Harmonic decompositions of the spin NESS

From Fig. 4.3(b), we found a complex superposition of frequencies present in the NESS. To deeply interpret the harmonic content of the spin NESS signal, it is easy to apply the Fourier transform (FT) for understanding harmonic components. Employing the following Fourier series for any observable $O(t)$ appearing in a NESS driven by any frequency ω ,

$$O(t) = \sum_m O_m e^{im\omega t}, \quad (4.11)$$

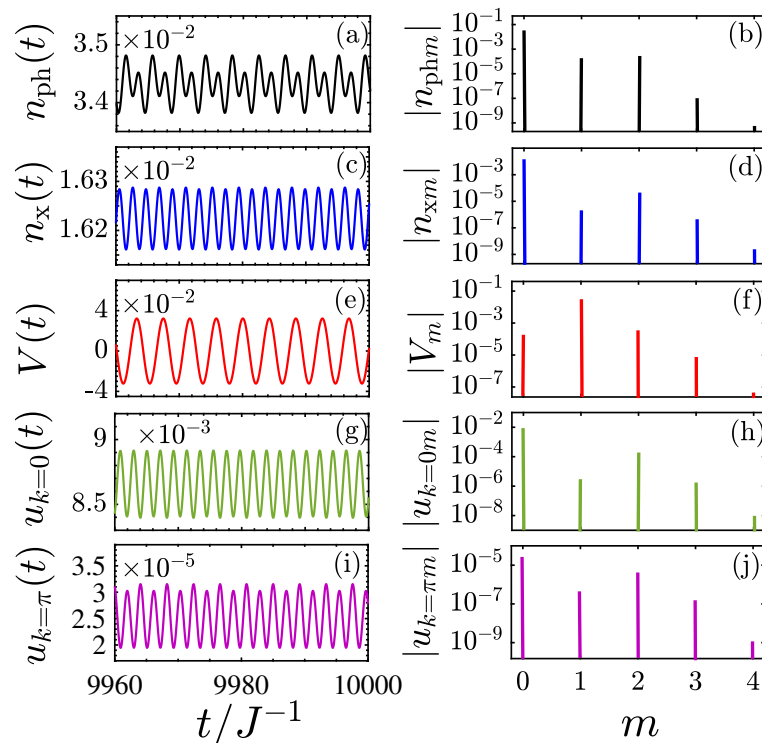


Figure 4.11: The temporal behavior of quantities (a) $n_{\text{ph}}(t)$, (c) $n_x(t)$, (e) $V(t)$, (g) $u_{k=0}(t)$, and (i) $u_{k=\pi}(t)$ in the NESS at fixed $a/\gamma_{\text{ph}} = 0.2$, $g/J = 0.05$, $\gamma_s/J = 0.01$, and $\omega_0/J = 1.5$. Juxtaposed in the right panels (b), (d), (f), (h), and (j) show the corresponding Fourier decompositions.

one finds delta peaks in the FTs properly up to the m -th harmonic. Note that we refer to only one cycle of the NESS signal in our interpretation and those with $m = 0$ are all real numbers, while any quantity with an integer subscript denotes a Fourier component with real and imaginary parts. However, we here plot the absolute value of all these components for meaningful descriptions.

In Fig. 4.11, we show in the left panels the temporal behavior of observables in the NESS at $\omega_0/J = 1.5$, while juxtaposed in the right panels show the corresponding harmonic decompositions. It can be seen that $n_{\text{ph}}(t)$, $n_x(t)$, $u_{k=0}(t)$, and $u_{k=\pi}(t)$ are dominated by the even Fourier components $m = 0$ and 2 , while $V(t)$ is dominated by $m = 1$. The main reason can be traced back to the Eq. (3.26). We noticed that in our model, the phonon displacement $q(t)$ is a sinusoidal function oscillating with frequency ω_0 in the weak SPC regime, which is the same as the frequency of oscillations in $v_k(t)$ and $w_k(t)$. So, $m = 1$ is the dominant component in $v_k(t)$ and by extension in $V(t)$. However, the leading order response in $u_k(t)$ oscillates at frequency $2\omega_0$ associated with a constant offset. By extension, $n_x(t)$ shows harmonic components primarily at $m = 0$ and $m = 2$. It is expected to see different response amplitudes for different k -components depending on the driving frequency $\omega = \omega_0$. For the case of $\omega_0/J = 1.5$, near the two-triplon band minimum $2\omega_{\text{min}} = \sqrt{2}$, $m = \{0, 2\}$ harmonics are expected to be larger in the

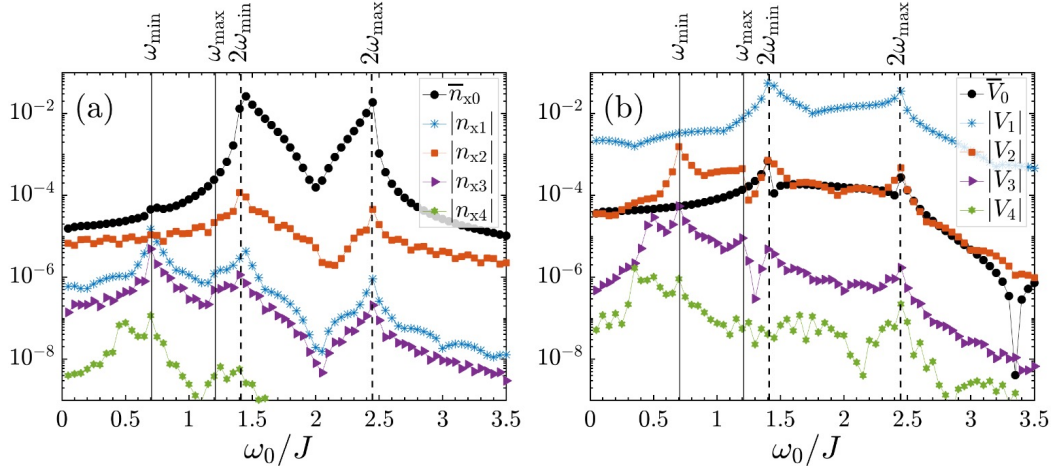


Figure 4.12: Coefficients of the Fourier transforms of (a) $n_x(t)$ and (b) $V(t)$ in the NESS at fixed $\gamma_{\text{ph}} = 0.02\omega_0$, $a/\gamma_{\text{ph}} = 0.2$, $g/J = 0.05$, and $\gamma_s/J = 0.01$ shown as a function of the driving phonon frequency, $\omega = \omega_0$.

$k = 0$ component than $k = \pi$ one. This happens in the opposite manner if one considers $\omega_0/J = 2.5$, near the two-triplon band maximum $2\omega_{\text{max}} = \sqrt{6}$.

Although in $n_{\text{ph}}(t)$, $m = 0$ and 2 are still dominant harmonics, it is observed that $m = 1$ is also so close to $m = 2$ and one may argue that the phonon occupation is dominated by $m = 0, 1$ and 2 harmonics at some point. This is a direct consequence of strong feedback from the spin system, where in Eq. (3.24c) the term $g\mathcal{U}(t)p(t)$ includes both $2\omega_0$ and ω_0 oscillations respectively for $\mathcal{U}(t)$ and $p(t)$.

In the previous figure, we focused on a special driving frequency $\omega_0/J = 1.5$. In Fig. 4.12, to investigate the effect of the driving phonon frequency, the coefficients of $n_x(t)$ and $V(t)$ from $m = 0$ to 4 are shown systematically as a function of ω_0/J ranging from 0.05 to 3.5 covering all regimes below, in and above the two-triplon band. Figure 4.12(a) is nicely confirming what we already claimed. \bar{n}_{x0} and $|n_{x2}|$ are indeed the dominant components of the triplon occupation for all frequencies, except $\omega_0 = \omega_{\text{min}}$. On the other hand, in Fig. 4.12(b), the $|V_1|$ component is dominant. As expected from the resonance condition $\omega_0 = 2\omega_k$, the coefficients show peaks at band edges $2\omega_{\text{min}}$ and $2\omega_{\text{max}}$. Also, around $\omega_0 = \omega_{\text{min}}$, which is far from a direct resonance, a number of the harmonic components present a peak.

As Eqs. (3.26b) and (3.26c) show, the oscillations are indeed induced at $2\omega_0$ because $q(t)$ is multiplied by $v_k(t)$ and $w_k(t)$. So, $v_k(t)$ and $w_k(t)$ are strongly enhanced when the second harmonic satisfies the resonance condition. This, in turn, induces stronger first and third harmonic components in $u_k(t)$ [see Eq. (3.26a)], in which $w_k(t)$ is multiplied by $q(t)$ where it acts as a driving term at frequencies $(2 \pm 1)\omega_0$. This is sort of a harmonic mixing, in which $|n_{x1}|$ exceeds $|n_{x2}|$ around $\omega_0 = \omega_{\text{min}}$ as well as $|n_{x3}|$ is also strongly enhanced. This is the case for $|V_2|$ and $|V_3|$ around this frequency, where the peak of $|V_2|$ approaches $|V_1|$. All these

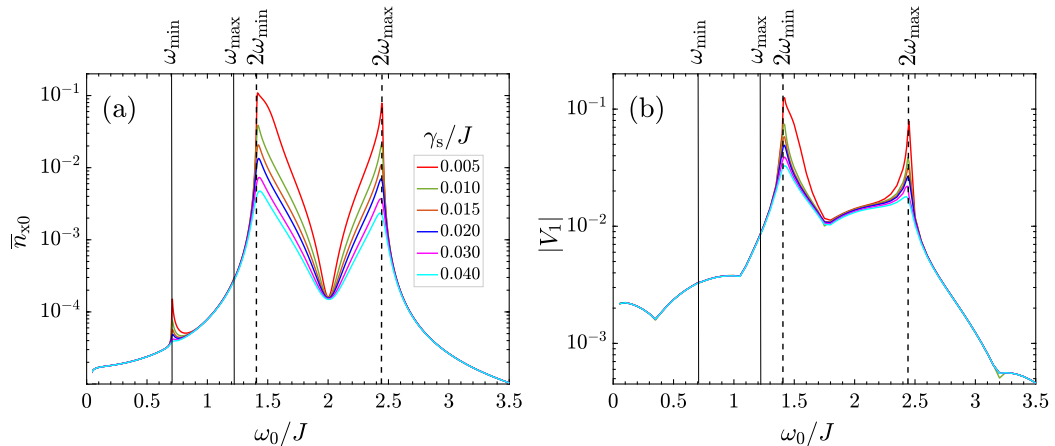


Figure 4.13: (a) Average triplon occupation, \bar{n}_{x0} , in the NESS at fixed $\gamma_{\text{ph}} = 0.02\omega_0$, $a/\gamma_{\text{ph}} = 0.2$, and $g/J = 0.05$ as a function of ω_0 for different values of γ_s . The band-edge features become increasingly prominent as γ_s decreases, as does the peak at $\omega_0 = \omega_{\min}$, but for most other phonon frequencies far from the band edges and ω_{\min} , \bar{n}_{x0} is insensitive to the spin damping. (b) Corresponding off-diagonal response, shown by the dominant component $|V_1|$.

justify the reason why the temporal behavior of the spin NESS displays more and different features at below-band frequencies around $\omega_0/J = 0.5$ in Fig. 4.3(b).

From the above explanations, we conclude that the existing “frequency-doubling” effects enhance the Fourier components around $\omega_0 = \omega_{\min}$. It should be noted that the oscillation response at $2\omega_0$ in $n_x(t)$ is not a doubling phenomenon because this is an effect induced by the driven phonon and finally other triplon degrees of freedom $u_k(t)$, $v_k(t)$ and $w_k(t)$. However, those around $\omega_0 = \omega_{\min}$ for the phonon and those around $\omega_0 = 2\omega_{\min}$ for the triplon are real doubling phenomena.

4.2.1 The influence of spin damping

It is possible to generate ensembles of spin dampings without approximately prescribed small $\gamma_s < \gamma_{\text{ph}}$. To investigate the effect of the spin damping γ_s on the dominant responses in both \bar{n}_{x0} and $|V_1|$, we plot Fig. 4.13. To allow NESS formation at all frequencies for the chosen driving parameters, we set $n_x^{\text{max}} = 0.2$ discussed before [less than the hard-core nature of $n_x = 1$ due to the applied approximations]. By this fixing of the triplon occupation, the lowest considered spin damping is set to 0.005. From the results, it can be reported that at frequencies far from a resonance with the edges of the band, \bar{n}_{x0} in Fig. 4.13(a) is insensitive to γ_s and it strongly decreases with γ_s around $\omega_0 = \omega_{\min}$ and two-triplon band edges. In Fig. 4.13(b), it is also clear that $|V_1|$ is insensitive to the spin damping outside the two-triplon band. In contrast to \bar{n}_{x0} , $|V_1|$ does not show any response to γ_s close to $\omega_0 = \omega_{\min}$ since $V(t)$ is generically chosen as the off-diagonal diagnostic and it is a primary driving term in Eq.(3.26) rather than a driven term. For the

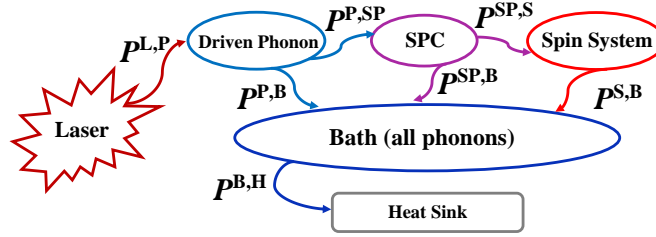


Figure 4.14: A schematic representation of energy flows in the driven spin-lattice system coupled to the phononic bath. All the energies are defined to be positive in the direction of the arrows.

kinks at $\omega_0/J \simeq 0.35$ and 1.06 of Fig. 4.13(b), we just need to look at EoMs corresponding to $v_k(t)$ and $w_k(t)$, i.e. Eqs.(3.26b) and (3.26c). Interestingly, the kinks located at these driving frequencies are respectively the maximum values of y_k and y'_k at $k = 0$ of the one-triplon band [see Fig. 3.3], i.e. at $\omega_0 = \omega_{\min}$, where the density of states are subdominant. These maximum values are symmetrically located around ω_{\min} in Fig. 3.3, which is also the case here; we see that the kinks symmetrically appear around $\omega_0 = \omega_{\min}$. So, the main origin of these kinks comes from the corresponding subdominant density of states.

4.3 Energy flow

While dynamical properties express that the SPC is an origin of energy transfer between the driven phonon and spin sectors, it does make sense to focus on the energy flows of individual parts for a fixed set of parameters. The energy flow through the spin-lattice system is of interest for both conceptual and practical purposes. If a true NESS is formed, the rate of energy power should be constant in all stages of interaction from the driving to the dissipation. More precisely, starting from the true Hamiltonian \mathcal{H} of the actual system of interest, in Fig. 4.14, a schematic of energy flows is represented. Accordingly, the input power is the uptake of laser energy by the driven phonon, $P^{L,P}$. Part of this input energy goes into the SPC part, $P^{P,SP}$, and part of which flows directly to the bath $P^{P,B}$. On the one side, the energy flow from SPC divides into two parts, one into the spin system, $P^{SP,S}$, and another one to the bath, $P^{SP,B}$. On the other hand, the induced energy to the spin system flows into the bath, $P^{S,B}$. The lattice is the modeled bath in this project and energy entering the bath from phonon, SPC, and spin parts is crucially important in determining the temperature of the system. This temperature is controlled by a large virtual modeled conducting heat sink. Finally, the energy flow entering the heat sink after leaving the entire system is $P^{B,H}$. All these processes, indeed, mean that the sum rules between these energies should be preserved in the end.

From Fig. 4.14 and Eq. (3.24), the energy flow from the laser into the Einstein phonon, from this phonon to the bath and the SPC part at zero temperature can

be found, respectively, as [169]

$$P^{\text{L,P}}(t) = -\mathcal{E}(t)\omega_0 p(t), \quad (4.12a)$$

$$P^{\text{P,B}}(t) = \gamma_{\text{ph}}\omega_0 n_{\text{ph}}(t), \quad (4.12b)$$

$$P^{\text{P,SP}}(t) = g\omega_0 [\mathcal{U}(t) + \mathcal{V}(t)] p(t), \quad (4.12c)$$

resulting in the sum rule $\overline{P}_0^{\text{L,P}} = \overline{P}_0^{\text{P,B}} + \overline{P}_0^{\text{P,SP}}$ for the temporal averages of each power in the NESS.

The energy flow from the SPC part to the bath is expected to be a combination of the phonon and spin dampings. For this reason, we are allowed to stick to Eq. (3.17) to simply deduce

$$\langle \mathcal{H}_{\text{sp}} \rangle (t) = gq(t) [\mathcal{U}(t) + \mathcal{V}(t)]. \quad (4.13)$$

It is known that power is the rate at which energy is transferred in time. So, after pretty simple calculations [see Appendix G], we end up with

$$\frac{\partial}{\partial t} \langle \mathcal{H}_{\text{sp}} \rangle (t) = P^{\text{P,SP}}(t) - P^{\text{SP,S}}(t) - P^{\text{SP,B}}(t), \quad (4.14)$$

in which

$$P^{\text{SP,S}}(t) = \frac{2gq(t)}{N} \sum_k y'_k \omega_k w_k(t), \quad (4.15a)$$

$$P^{\text{SP,B}}(t) = gq(t) \left(\frac{\gamma_{\text{ph}}}{2} + \gamma_s \right) [\mathcal{U}(t) + \mathcal{V}(t)]. \quad (4.15b)$$

It satisfies our expectation on the energy flow from the SPC to the bath above-mentioned: This energy flow balances the sum rule $\overline{P}_0^{\text{P,SP}} = \overline{P}_0^{\text{SP,S}} + \overline{P}_0^{\text{SP,B}}$.

Due to the SPC term, the spin system receives some energy. The energy flow from the SPC part into the spin system and from the spin system into the bath can again be extracted from Fig. 4.14 and Eq. (3.26) at zero temperature, given, respectively, by $P^{\text{SP,S}}(t)$ in Eq. (4.15a) and

$$P^{\text{S,B}}(t) = \frac{\gamma_s}{N} \sum_k \omega_k u_k(t), \quad (4.16)$$

leading to the energy conservation $\overline{P}_0^{\text{SP,S}} = \overline{P}_0^{\text{S,B}}$ on the time-averaged values in the NESS. Moreover, after damping and transferring the input energy through the above-formulated ways, the energy flow leaving the entire system and going into the heat sink is equal to the energy flows entering the bath, i.e. the last sum rule in the NESS can be met as $\overline{P}_0^{\text{P,B}} + \overline{P}_0^{\text{SP,B}} + \overline{P}_0^{\text{S,B}} = \overline{P}_0^{\text{B,H}}$.

Figure 4.15 shows how the energy flows behave with the driving frequency $\omega = \omega_0$. From Fig. 4.15(a), we observe that the majority of the laser energy flows directly to the bath [see the dashed-red and solid-blue lines], while $\overline{P}_0^{\text{P,SP}}$ as the energy flow towards the spin system via the driven phonon is always relatively

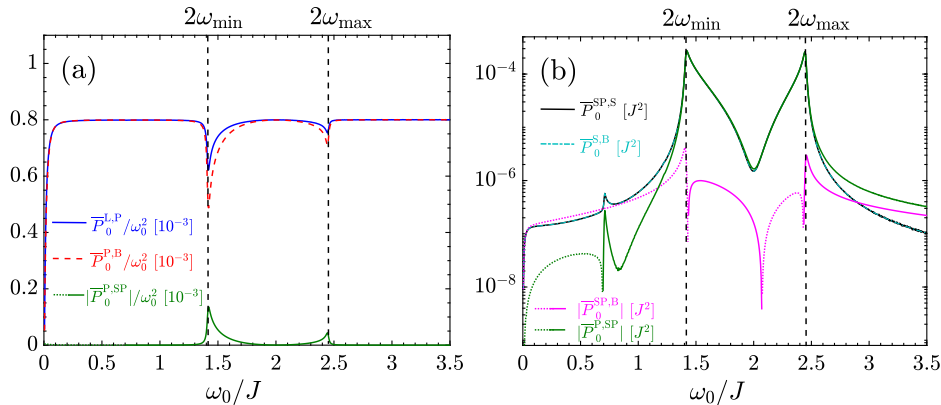


Figure 4.15: Average energy flows through the driven spin-lattice system coupled to the phononic bath, depicted in Figs. 3.2 and 4.14, as a function of $\omega = \omega_0$ at fixed $\gamma_{\text{ph}} = 0.02\omega_0$, $a/\gamma_{\text{ph}} = 0.2$, $g/J = 0.05$, and $\gamma_s/J = 0.01$. (a) Power absorbed by the driving phonon from the laser field ($\overline{P}_0^{L,P}$), power dissipated directly to the bath from this driven phonon ($\overline{P}_0^{P,B}$) and the power transferred towards the SPC part from this phonon ($\overline{P}_0^{P,SP}$). For clarity the powers are normalized to ω_0^2 and the solid (dotted) line in $\overline{P}_0^{P,SP}$ stands for for a positive (negative) power. (b) Once more power transferred towards the SPC part ($\overline{P}_0^{P,SP}$), power delivered to the spin system from SPC part ($\overline{P}_0^{SP,S}$), power entered the bath by the SPC part ($\overline{P}_0^{SP,B}$), and power dissipated by the effect of the bath on the spin system ($\overline{P}_0^{S,B}$).

small. The solid blue line in Fig. 4.15(a) shows that the absorption peak is actually suppressed when ω_0 lies in the spin band, most strongly so for phonons resonant with $2\omega_{\min}$ and $2\omega_{\max}$. This phenomenon is called a “giant self-blocking” effect [see next chapter for more details], which appears initially to be in contrast to common-sense expectation, as one might expect stronger absorption when more system degrees of freedom are at resonance with the incoming laser. However, it should be pointed out that the spin system is not coupled directly to the light, being only coupled to/excited by the driven phonon. This situation, in turn, introduces the spin system just as an extra “inertia” in the coupled spin-lattice system to force the driven phonon to move. It is not contributing to weakening the self-blocking effect. The reason can be understood from Eq. (3.26c) in which the spin system acts against $\mathcal{E}(t)$ through the SPC, not directly through the laser field itself, making it more difficult for the phonon to draw energy from the laser electric field. This process blocks most of the input energy from the laser in the lattice part and a few percent of the input energy is transferred to the spin system through the SPC.

To compare the energies flowing into and out of the SPC term, we show once more $\overline{P}_0^{P,SP}$ in Fig. 4.15(b). From the second sum rule $\overline{P}_0^{P,SP} = \overline{P}_0^{SP,S} + \overline{P}_0^{SP,B}$, the difference between $\overline{P}_0^{P,SP}$ and $\overline{P}_0^{SP,S}$ is $\overline{P}_0^{SP,B}$. While at very low and very high driving phonon frequencies, $|\overline{P}_0^{SP,B}|$ becomes a more significant fraction of the energy in the spin system, it remains at the percent level for all driving

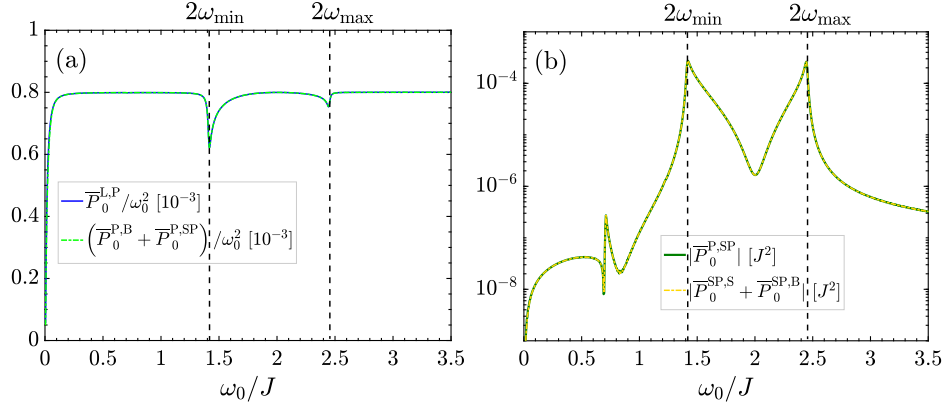


Figure 4.16: (a) The first sum rule, $\bar{P}_0^{L,P} = \bar{P}_0^{P,B} + \bar{P}_0^{P,SP}$, and (b) the second sum rule, $\bar{P}_0^{P,SP} = \bar{P}_0^{SP,S} + \bar{P}_0^{SP,B}$, as a function of $\omega = \omega_0$ at fixed $\gamma_{\text{ph}} = 0.02\omega_0$, $a/\gamma_{\text{ph}} = 0.2$, $g/J = 0.05$, and $\gamma_s/J = 0.01$.

frequencies within the two-triplon band, meaning that the SPC part of the system does not act to store significant energy at non-resonant frequencies, but in essence transmits it from the phonon to the spin system as expected physically. In general, this energy is, in turn, a very small fraction of the total (laser) energy flowing through the system, which in turn, means that the SPC term as a perturbation in the mean-field approach is well justified and neglecting the higher spin-phonon correlations is not an issue. Having all these energy flows, the total output energy flows $\bar{P}_0^{B,H}$ can simply be calculated. Finally, it is valuable to mention that in Figs. 4.13(a) and 4.10 an asymmetrical behavior could be observed for the spin responses around the band edges, however, in the case of respective energies, $\bar{P}_0^{SP,S}$ and $\bar{P}_0^{SP,B}$, in Fig. 4.15(b), an almost symmetrical behavior emerges. This originates from the extra symmetrical factor triplon dispersion ω_k in Eqs. (4.15a) and (4.16).

The sum rule results can also be checked separately by summing up the related energies. Note that the results of the third sum rule, i.e. $\bar{P}_0^{SP,S} = \bar{P}_0^{S,B}$, is already established in Fig. 4.15(b). However, in Fig. 4.16, we use Eqs. (4.12) and (4.15) to showcase the validity of the first and second sum rules with the same parameters used in Fig. 4.15. To facilitate comparisons, we use the same colors as in Fig. 4.15. As discussed before, we nicely achieve an excellent agreement between the energy flows in satisfying the physical sum rules between different parts of the coupled system. Further information and more involved treatments with SPC can be found in the next chapter.

In an absorption experiment, $P_0^{L,P}$ (as mentioned before, we use the notation X_0 in the case of off-resonant $\omega \neq \omega_0$) is mostly measured since it is the fluence taken up by the coupled spin-lattice system. So, for experimental interests, we would pump the system at all frequencies beyond the resonance condition, i.e. at $\omega \neq \omega_0$, to see how the input power reacts to the phonon coupled to the spin system. However, we still expect the dominant absorption at $\omega = \omega_0$. For

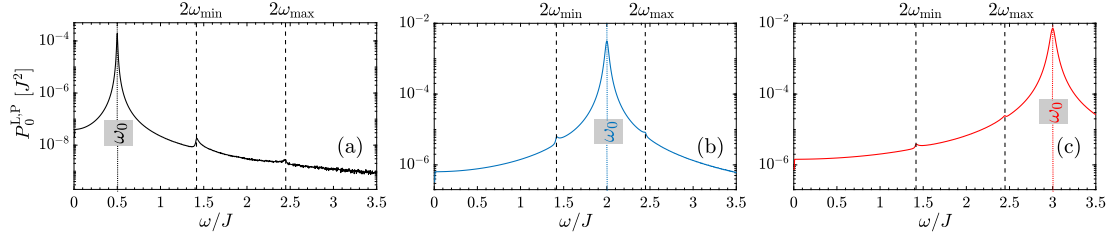


Figure 4.17: $P_0^{L,P}$ shown as a function of ω for $\gamma_{\text{ph}} = 0.02\omega_0$, $a/\gamma_{\text{ph}} = 0.2$, $g/J = 0.1$, and $\gamma_s/J = 0.01$, for systems with one phonon at a frequency (a) $\omega_0/J = 0.5$, (b) $\omega_0/J = 2.0$, and (c) $\omega_0/J = 3.0$.

$\omega_0/J = 0.5, 2.0, \text{ and } 3.0$, Fig. 4.17 satisfies this expectation associated with the fingerprints of the responses at band edges, which are not as strong as before due to sufficiently far phonons from the band edges as well as due to weak SPC. It should be shortly discussed that in our model, there is no probing field and delay time of extra probe driving in the NESS – pumping is the only field driving system into the non-equilibrium. Further suggestions or experimental realizations of an effective pump-probe situation will be departed in chapter 7 from what we had so far and we will introduce the probing field as well for practical investigations.

4.4 Discussion on the heating issue

We come back to the issue already mentioned in the discussion of driving strength, namely the fact that keeping continuous driving unavoidably leads to heating of the system. For this reason, remediation is necessary to avoid destroying the coherence of the system. To get a quantitative understanding of how the energy distribution can be tuned, we provide a rough estimate of the heating of the sample subjected to the applied continuous laser field. In this estimation, the target material is the inorganic compound CuGeO_3 [see Fig. 3.1 and Sec. 3.1] with a large SPC. Although the SPC is large in this material, our estimation would still be valid for the weak-coupling regime we considered up until now. As mentioned before, the leading magnetic exchange constant J in CuGeO_3 is around 10 meV [159]. We assume that a phonon driving the system near $2\omega_{\text{min}}$ of the two-triplon band also has this order of magnitude energy to modulate the dimerization, i.e. $\hbar\omega_0 = 10 \text{ meV} \approx 2.4 \text{ THz}$. In Fig. 4.15, we understood that the most of input energy is absorbed by the phononic bath, so, to estimate the dumped power per spin dimer (because the phonon is coupled to two spins in a dimer), it is reasonable to use $\bar{P}_0^{\text{P,B}} = \gamma_{\text{ph}}\omega_0\bar{n}_{\text{ph}0}$. Considering the fixed parameters $a/\gamma_{\text{ph}} = 0.2$ ($\bar{n}_{\text{ph}0} \simeq 0.04$ for decoupled and weak-coupling situation) and $\gamma_{\text{ph}} = 0.02\omega_0$, one finds [$1 \text{ s} = 10^{12} \text{ THz}^{-1} = 2.5 \times 10^{12} \hbar/J$]

$$\bar{P}_0^{\text{P,B}} = 1.93 \times 10^{-11} \text{ J} \cdot \text{s}^{-1} \text{ per dimer}, \quad (4.17a)$$

$$\frac{\bar{P}_0^{\text{P,B}} N_a}{2} = 5.81 \times 10^{12} \text{ W per mole of spins}, \quad (4.17b)$$

where $N_a = 6.022 \times 10^{23} \text{ mol}^{-1}$ is Avogadro's constant. In the above estimate, we have taken two spins per dimer into account, i.e. a mole of CuGeO_3 comprises only half a mole spin dimers. Also, $2\pi\omega_0$ is considered to include the frequency of the optical phonon.

To heat up the sample from $T_i = 0$ or 2 K up to $T_{\max} = 20$ K [considering it as the maximum temperature after which the quantum coherence of spin processes is destroyed], the time required for the driven system before destroying the coherence in the absence of any cooling apparatus is given by

$$\bar{P}_0^{\text{P,B}} t_h = \int_{T_i}^{T_{\max}} C_{\text{ph}} dT, \quad (4.18a)$$

$$t_h = \frac{\beta}{4\bar{P}_0^{\text{P,B}}} [T_{\max}^4 - T_i^4], \quad (4.18b)$$

where $C_{\text{ph}} = \beta T^3$ is the pure-phonon low-temperature specific heat of CuGeO_3 with $\beta \approx 0.3 \text{ mJ}/(\text{mol K}^4)$ [223]. Thus, the time required to reach T_{\max} is $t_h \approx 2.06 \times 10^{-12} \text{ s}$, or $5.16 \hbar/J$, which corresponds to only 5 cycles of the driving phonon and is fairly too short by a factor of several hundreds when compared with our results. This, in turn, means that the system melts if we keep driving, which is outside the scope of present experimental goals, see the first chapter of this thesis. So, we turn to a mechanism to make the sample cool by the heat sink.

To address the effect of the heat sink, the sample dimensions and the thermal conductivities to remove heat from the sample need to be introduced. We consider a thin sample with a thickness of $d = 20 \text{ nm}$. It is not hard to find the mass per mole formula unit of 184 g for the compound CuGeO_3 according to the periodic table of elements, which corresponds to 1 mole of spins. Also, one immediately deduces the mass density of 5.11 g.cm^{-3} [224]. For a sample of area $A = 1 \text{ mm}^2$ and the molar density $\rho = 5.11/184 = 28 \times 10^{-3} \text{ mol.cm}^{-3}$, the required laser power to be transported through this area of the sample to the heat sink is given by

$$P_{\text{laser}} = A d \rho \bar{P}_0^{\text{P,B}} = 3.25 \text{ kW}. \quad (4.19)$$

On the other hand, for the rate at which heat leaves the sample (the rate of heat loss), one needs the thermal conductivity of CuGeO_3 , which an approximate value for the cross-chain direction at low-temperature is $\kappa = 0.1 \text{ W.K.cm}^{-1}$ [225]. By these, we calculate

$$P_{\kappa} = \kappa A \frac{T_{\max} - T_i}{d} = 9 \text{ kW}. \quad (4.20)$$

These show that the heat sink should be a highly conducting metal able to remove the input power efficiently, see Fig. 4.18, and thus no bottleneck should arise due to its thermal contact or the thermal conductivity. However, metals are not known to have a high heat capacity, and thus we estimate the thermal energy that could

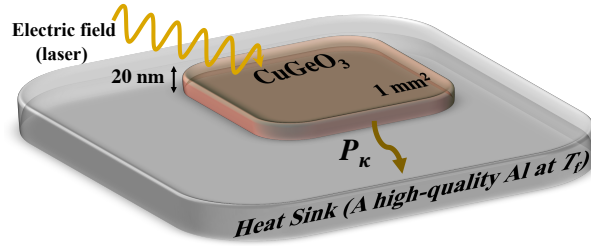


Figure 4.18: Proposition of a simple experimental setup for the effect of a high-quality Al heat sink at temperature T_f with a sample (CuGeO_3) thickness and area, respectively, 20 nm and 1 mm^2 .

be taken up by a metal block. To this end, we consider a high-quality Al (residual resistivity ratio $\text{RRR} = 30$) with $k_{\text{Al}} = 1 \text{ W.K.cm}^{-1}$ and the low-temperatures specific heat of $C_{\text{Al}} = 0.05 T \text{ J. K}^{-2}.\text{kg}^{-1}$ [226]. Thus for a block of Al with the mass $m = 1.35 \text{ g}$ [226], the time to overheating of the block by increasing the temperature from $T_i = 0$ or 2 K to the temperature of the heat sink $T_f = 5 \text{ K}$ is given by

$$P_{\text{laser}} t_{\text{sink}} = m \int_{T_i}^{T_f} C_{\text{Al}} dT = 0.025 m [T_f^2 - T_i^2] \text{ J. K}^{-2}.\text{kg}^{-1}, \quad (4.21)$$

leading to

$$t_{\text{sink}} = 2.1 \times 10^{-7} \text{ s} \approx 5.4 \times 10^5 \hbar/J, \quad (4.22)$$

which corresponds to over half a million cycles of the 2.4 THz driving phonon. Thus, an Al heat sink has plenty of reserve capacity for the purposes of a NESS experiment and the computed long-time behavior is readily observable. So, experiments of the type we discuss to establish and to control bulk quantum spin NESS are possible in real magnetic materials if one prepares the system with a thickness in the range of tens of nanometres.

4.5 Experimental perspectives

Although in most of the analysis for the real applications and estimations, we used the inorganic compound CuGeO_3 , another excellent example realizing quasi-1D alternating spin-1/2 chains is $\text{Cu}(\text{NO}_3)_2$ [166], which anisotropy is absent in this compound, the SPC is not strong, and the second-neighbor interactions are negligible. However, the magnetic energy scales in this material are lower by a factor of 20 than the test-case numbers presented before. This, in turn, means that a different balance of slower heating rates, slower convergence to NESS, and altered damping ratios come up.

Considering the spin sector alone, our present formalism can readily be extended to alternating chains with different gap-to-bandwidth ratios, e.g. 1D gapped spin system of even-leg spin-1/2 ladders and Haldane (spin-1) chains. Also, Sr_2CuO_3

and SrCuO₂ cuprates are described by the spin-1/2 large- J Heisenberg spin chains with weak SPCs at $T \ll J$ [107, 227–229]. 1D Heisenberg spin-1/2 chain compound Ca₂CuO₃ can also be another candidate in this regard [230]. More complex spin sectors include anisotropic systems such as Ising and XY models without magnetic order, gapless spin chains, and gapped or gapless non-ordered states in higher dimensions. Here the challenge is not only to find a suitable framework in which a complex correlated spin sector can be described, especially if this is changed by using laser driving to push it across a magnetic quantum phase transition, but also to deal with the situation where the excitations of the spin system extend to arbitrarily low energies, thus interacting strongly with even the acoustic phonons. Also, accurate lattice dynamics calculations are necessary to obtain the phonon modes and frequencies, and the corresponding oscillator strengths.

4.6 Chapter summary

In this chapter, the quantum NESS of a driven-dissipative gapped dimerized spin-1/2 chain under continuous driving, is investigated. In summary, we have been involved with special treatments for the laser (weak driving), for both lattice and spin sectors (weak SPC), for the quantum master equation method (thermal bath without memory), the fast and slow convergence processes to the NESS in the entire system (adiabatic, resonant and antidiabetic regimes), the exchange coupling strengths (the dimerized chain), the mode occupations (low triplon occupation and the Lindemann criterion), and the low-temperature system (heat sink).

The transient behavior at switch-on and relaxation at switch-off are studied. At switch-on, a complex phenomenology is found where even the weakly-coupled system can be driven close to thresholds, in triplon occupation and rate of excitation, at which its characteristic timescales are renormalized strongly. The NESS amplitude shows a dramatic sensitivity to the frequency of the driving phonon, peaking strongly at the upper and lower edges of the two-triplon band. Additionally, the spin NESS and its k -components response to the driving electric field, to the lattice and spin damping coefficients, and to the SPC, causing a rapid onset of strong mutual feedback between sectors, are studied.

The Fourier transform is employed to analyze the components of the spin NESS appearing at different harmonics of the driving frequency even in the weak-coupling regime. The energy flows through the coupled spin-lattice system associated with different dissipation effects are computed, highlighting the giant self-blocking effect, whereby the lattice system absorbs most of the laser power. Finally, heating timescales and the practical requirements are discussed in the form of sample geometry and cooling capacity via a conducting heat sink.

5. Strong coupling regime: J -model

In this chapter, the weak-coupling regime is extended to involve more degrees of freedom in the system and to obtain additional physics, which all are also described by the same derived EoMs. This, in turn, renders the opportunity to observe new phenomena and provides a first testing ground for the application of the regime in possible materials. The strong SPC makes the dynamics more intricate, since it comes into play role in blocking some flowing energies in different frequency regimes and in significantly showing the spin feedback effects. The interplay between *strong SPC*, driving parameters, and dissipative dynamics in tuning the stability of nonequilibrium order and in determining novel different types of hybrid states in both lattice and spin sectors are the overarching themes of this chapter.

We, in Sec. 5.1, will first look into the behavior of the system occupations at switch-on and switch-off processes in the presence of both weak and strong SPCs, focusing on their temporal behavior and universal properties. This distinguishes the weak- and strong-coupling regimes in another way compared to the previous chapter. Also, a systematic study of occupations as functions of SPC including both weak and strong couplings will be provided. In Sec. 5.2, the giant resonant self-blocking effect between the driven phonon and spin excitation frequencies will be presented. In Sec. 5.3, the SPC-induced frequency shifts in both lattice and spin systems are included due to the lattice vibrations (phonon displacement). This includes a description of the hybrid states, SPC dependence of triplon mode, and multiphonon (still weak) processes. In Sec. 5.4, the strong SPC effects on the input energy flow will be addressed. Finally, a chapter summary will be given in Sec. 5.5. Most of this chapter has been submitted as a Letter Article to Physical

Review Letters [170].

Before delving into the analysis of the results, we briefly review the set of parameters, see the details in Ref. [169] and the previous chapter. Due to the weak coupling of a single Einstein phonon to an ensemble of phonons (bath), we set the phonon damping to a very small value, e.g., 2% of the phonon energy $\hbar\omega_0$, i.e. $\gamma_{\text{ph}} = 0.02\omega_0$. Further, the spins are in general damped to the bath weaker than Einstein phonon, i.e. $\gamma_s < \gamma_{\text{ph}}$ holds valid, thus we set $\gamma_s/J = 0.01$. For the amplitude of the laser field, for our systems under consideration with magnetic interaction $J \simeq 10$ meV, $a \simeq 2$ meV to 4 meV is experimentally achievable [134]. So, we set the reliable $a/\gamma_{\text{ph}} = 0.2$ to be weak enough to avoid lattice melting as well [185]. To ensure that the laser excites the phonon, we first apply the pumping field setting $\omega_0 = \omega$ and then set $\omega_0 \neq \omega$ to figure out what happens to both phonon and spin-band frequencies. Here it should be mentioned that we still use the notation \bar{X}_0 for average quantities at $\omega_0 = \omega$ to distinguish the resonant and off-resonant (X_0) responses in the NESS. As for the SPC strength, the upper limit of $g = J/2 \simeq 5$ meV is considered, consistent with CuGeO_3 and $(\text{VO})_2\text{P}_2\text{O}_7$ compounds [157, 159–165].

5.1 Characterization of strong coupling regime

Shown in Figs. 5.1(a) and 5.1(b) are respectively $n_{\text{ph}}(t)$ and $n_x(t)$ for different SPCs. Here, the switches on and off of the drive field are thought to happen instantaneously with the driving beginning at time $t = 0$ and relaxing at $t/J^{-1} = 1500$ (when the laser field is switched off). Although the responses of the resonant regime between the driven phonon and spin excitations, $\omega_0 = 2\omega_k$, will be dominated by the density of spin states and the leading harmonics, the fingerprints of the low-frequency regimes on the responses in the presence of strong SPCs are of interest as well. We set $\omega_0 = \omega_{\text{min}}$ to see the harmonic mixing hiding in the complex waveforms in the NESS signal. Both quantities oscillate with time and continuously reach a NESS. From the previous chapter, we learned that the timescale for which the NESS is reached is $2/\gamma_{\text{ph}}$ for all quantities in the phonon sector. However, the timescale is 4 to 5 times larger than $1/\gamma_s$ expected from Eq. (3.26a) for $n_x(t)$, which stems from the fact that the phonon momentum comes into play role in pumping the spin system and an extra damping from the phonon is induced to the spins, shown by the function $f(ga/\gamma_{\text{ph}}, \omega_0, \omega_k) < \gamma_s$ in the figure. This timescale manifests itself in the number of cycles for which the NESS is reached such that at $g/J = 0.3$ one cycle, while a few numbers of cycles are required for the convergence at a stronger $g/J = 0.5$.

If we set another $\omega_0 = 2\omega_{\text{min}}$ in Figs. 5.1(c) and 5.1(d) with the same set of parameters, the same phenomenon emerges as g is increased, but the delay time is much shorter in this driving frequency because of extreme strong suppression of phonon occupation (it is difficult to have different occupations corresponding

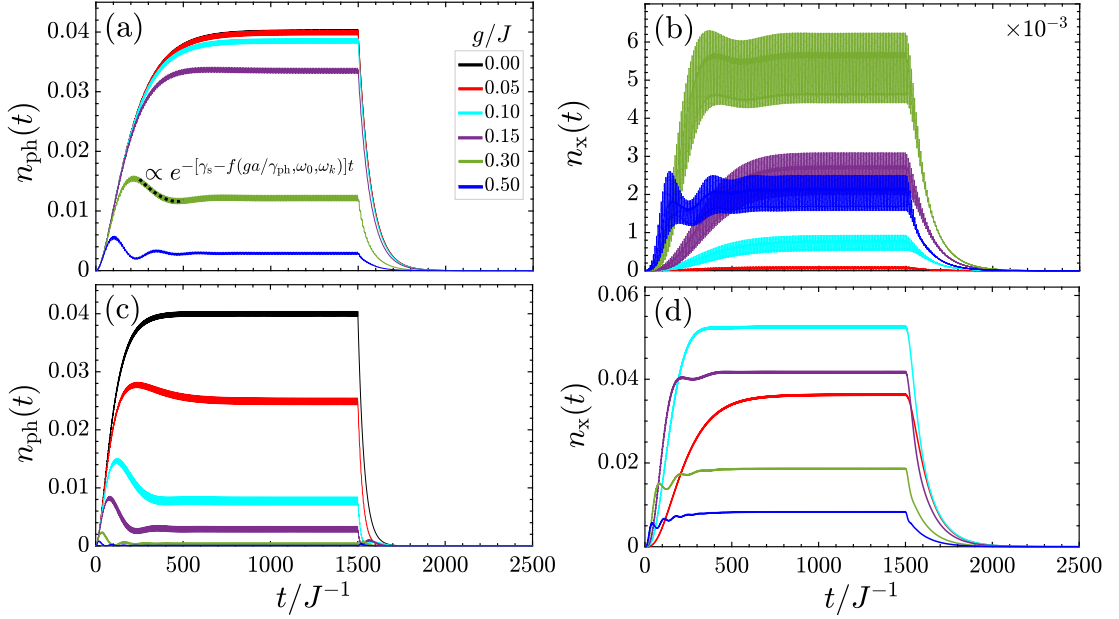


Figure 5.1: Time evolution of the (a) phonon occupation $n_{\text{ph}}(t)$ and (b) triplon occupation $n_x(t)$ with the driving turning on at time $t = 0$ and turning off at $t/J^{-1} = 1500$. The set of parameters: $N = 2000$, $\gamma_{\text{ph}} = 0.02\omega_0$, $a/\gamma_{\text{ph}} = 0.2$, $\gamma_s/J = 0.01$, and $\omega_0 = \omega_{\text{min}}$. The same for $\omega_0 = 2\omega_{\text{min}}$ in panels (c) and (d).

to various SPCs at the same scale). Accordingly, much more cycles are required to converge the NESS in both sectors due to the mutual feedback effects.

We note that, when the driving is removed after 1500 time steps (or at another arbitrary step) in the NESS signal, the systems back to their initial states, i.e. their equilibrium state, with the same timescales aforementioned. There is an interesting physics in the transient process when weak and strong g is considered, that needs to be discussed. In the language of strong SPC, there exists a strong feedback effect from the phonon-driven spins such that the phonon occupation after a specific time step pulls down first and departs significantly to a new NESS then [not to the square of maximum displacement $(a/\gamma_{\text{ph}})^2$]. In fact, $n_{\text{ph}}(t)$ intends to catch $(a/\gamma_{\text{ph}})^2$, but it is suppressed by the driven triplon modes. On the other hand, the specific time step above-mentioned decreases with g , leading to fast convergence to the NESS associated with new short-time oscillatory behaviors. Moreover, from Fig. 5.1(a), one can see that the phonon occupation in general decreases with g , which can be understood from the fact that $n_{\text{ph}}(t)$ reflects the driving of the phonon momentum $p(t)$ [see Eq. (3.24c)] and the bonding between phonons and spins increases as the SPC is increased because the spin acts as an extra inertia (perturbation) for the laser-driven phonon, leading to the reduction of phonon momentum and eventually phonon occupation.

One allows to conclude that the decreasing transient trend for phonon occupation occurs after a critical g value, which depends on the driving frequency. This critical SPC divides the weak and strong regimes of the SPC depending on

the low, intermediate, and high frequency regimes. Similar to the phonon sector, the spin sector transient is also affected by strong SPCs, resulting in short-time oscillatory behaviors, as represented in Fig. 5.1(b), and a suppression of $n_x(t)$. The main reason of such a complex behavior can be explored from the existing higher harmonics in the strong SPC regime, which will be addressed in the next figures. In other words, the spin system is going to be blockade at strong SPCs due to its stronger negative feedback effect (known as the giant self-blocking effect in the following) on the laser-driven phonon and by this the spin system approaches its behavior in the equilibrium case.

It is important to pause for a moment and find out the timescale for which $n_{\text{ph}}(t)$ starts to pull down due to the spin feedback effects. The fitting function shows that the phonon occupation decays as $1/[\gamma_s - f(ga/\gamma_{\text{ph}}, \omega_0, \omega_k)]$, at relatively short times, see the representative fitting dotted curve. This function can be characterized numerically, however, we here provide our physical expectations on the functionality of f . As explained before, the phonon occupation pulls down after a critical SPC due to the feedback effect from the driven spin system, thus, f should be a function of ga/γ_{ph} , i.e. of the driving amplitude of the spin system. On the other hand, the driving frequency ω_0 exhibits a high sensitivity of the phonon sector to the resonance exciting, resulting in a ω_0 -dependent f . In particular, the SPC varies the background, on top of which the resonance phonons become more or less bonded. Following the spin feedback effect, the triplon modes k also play crucial roles in recognizing the decaying rate. Involving the simultaneous emission of several Einstein phonons due to the coupling to the spins can strongly reduce the phonon lifetime manifesting itself in a decay process. Note that this process is not a directly laser-induced process in the present work and only the SPC is responsible for the multiphonon transition rate. All these together lead to the general expression $f(ga/\gamma_{\text{ph}}, \omega_0, \omega_k)$. In special cases, this function agrees perfectly with the presented analytical solutions in the previous chapter, while in the generic case, comparison with our numerically NESS, yields equivalence. Another straightforward remark on f refers to its envelope oscillatory behavior at short times at strong g values, consistent with the reported Bessel function of the first kind in the above-mentioned special case [169]. This function is typically accompanied by the extra γ_s in the decaying rate, which is again present due to the direct reflection of the spin system.

5.1.1 Late-time behavior of signals in the NESS

We henceforth return to the question raised in the introduction: What is the effect of strong SPC on the observed NESS? To obtain the steady state situation, we focus on the long-time oscillations of both $n_{\text{ph}}(t)$ and $n_x(t)$ deduced by their average value in the NESS, $\bar{n}_{\text{ph}0}$ and \bar{n}_{x0} , thus all curves are symmetrized around zero in Figs. 5.2(a) and 5.2(b). For simplicity, we present only strong g values compared to a weaker one $g/J = 0.05$. There are two important points about

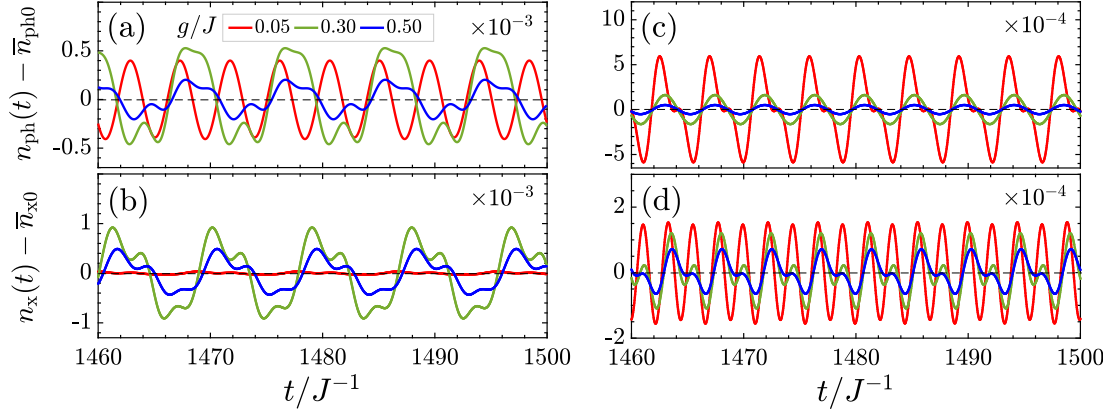


Figure 5.2: Long-time behavior of the (a) phonon occupation $n_{\text{ph}}(t)$ and (b) triplon occupation $n_x(t)$ deduced respectively by their average $\bar{n}_{\text{ph}0}$ and \bar{n}_{x0} in the NESS at $N = 2000$, $\gamma_{\text{ph}} = 0.02\omega_0$, $a/\gamma_{\text{ph}} = 0.2$, $\gamma_s/J = 0.01$, and $\omega_0 = \omega_{\text{min}}$. The same for $\omega_0 = 2\omega_{\text{min}}$ in panels (c) and (d).

the formed NESSs in the presence of strong SPC as general principles. First is similarity in the oscillation frequency of both weak and strong SPCs such that both sector observables oscillate with the frequency $2\omega_0$ stemming from the phonon momentum multiplied by the laser field [see Eq. (3.24c)]. Thus, the frequency-doubling effect after driving occurs. However, there is a shift in the long-time oscillations in the presence of SPCs such that $[2\omega_0 t + \varphi]$ is the new argument in both $n_{\text{ph}}(t)$ and $n_x(t)$ with phase $0 \leq \varphi < 2\pi$, implying that the cycles are not started at the same points. These SPCs and frequency $\omega_0 = \omega_{\text{min}}$ are probably good descriptions for highlighting these points, however; other frequencies can be systematically addressed because the shift above-mentioned can be different in other frequency regimes. Second point immediately refers to the complex NESS signals in time reflecting the stronger multiple harmonic effects in the strong SPC regime compared to the weak regime, meaning that the responses are dealing with complex non-sinusoidal functions. It is necessary to mention that the detailed analysis of the SPC effect on the harmonic components is needed for a deeper understanding of the physics behind the behaviors. This can be done by performing Fourier transform of the NESS signal, see Fig. 5.17. It would be useful for experimentalists to stress that the quantum NESS is reached at sort of short times, which in turn, means that it is not needed to drive the system long-enough to meet the NESS. With up to 10000 dimers, we have checked that the current set of reliable parameters have no finite-size effects, allowing us to obtain the NESS in the thermodynamic limit. The same arguments are valid for a resonant frequency $\omega_0 = 2\omega_{\text{min}}$ in Figs. 5.2(c) and 5.2(d).

It is also worth establishing the existence of a pure NESS signal looking at NESS at different time steps. In doing so, we compute Fig. 5.3 where $\bar{n}_{\text{ph}0}$ is obtained by averaging during its time evolution towards a NESS up to seven digits accuracy over different time intervals, namely Δt_i with $i \in \{1, 2, 3, 4, 5\}$,

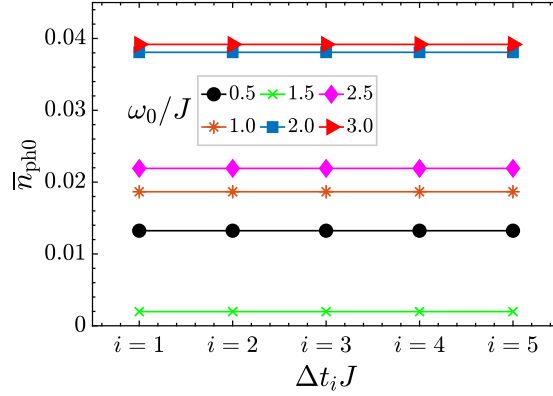


Figure 5.3: Averaged phonon occupation in the NESS signal, $\bar{n}_{\text{ph}0}$, for five Δt_i with $i \in \{1, 2, 3, 4, 5\}$, corresponding respectively to the time intervals $[900, 1000]$, $[4900, 5000]$, $[11900, 12000]$, $[24900, 25000]$, and $[49900, 50000]$ at $N = 2000$, $a/\gamma_{\text{ph}} = 0.2$, $\gamma_{\text{s}}/J = 0.01$, $g/J = 0.3$, $\gamma_{\text{ph}} = 0.02\omega_0$ and different driving frequencies ω_0/J .

corresponding respectively to the time steps $[900, 1000]$, $[4900, 5000]$, $[11900, 12000]$, $[24900, 25000]$, and $[49900, 50000]$. For comparison, we also consider different driving frequencies at the same set of parameters as Fig. 5.2(a) and at a strong SPC, $g/J = 0.3$. The true NESS is corroborated by reasonably good data lines independent of the time interval, hence these simulated lines correspond to a “true” NESS response profile.

5.1.2 NESS occupations in the strong SPCs

Following this scheme, it is now the time to determine the critical ω_0 -dependent SPC characterizing the weak and strong SPC regimes. To do so, we plot the resonant average occupations $\bar{n}_{\text{ph}0}$ and $\bar{n}_{\text{x}0}$ in the NESS as functions of g/J in Fig. 5.4. We focus on below, in, and above the two-triplon band frequencies. Although after the critical $g_c \simeq 0.08J$ (except at $\omega_0/J = 1.5$, which is related to the giant resonant responses or self-blocking effect; see next section), the phonon

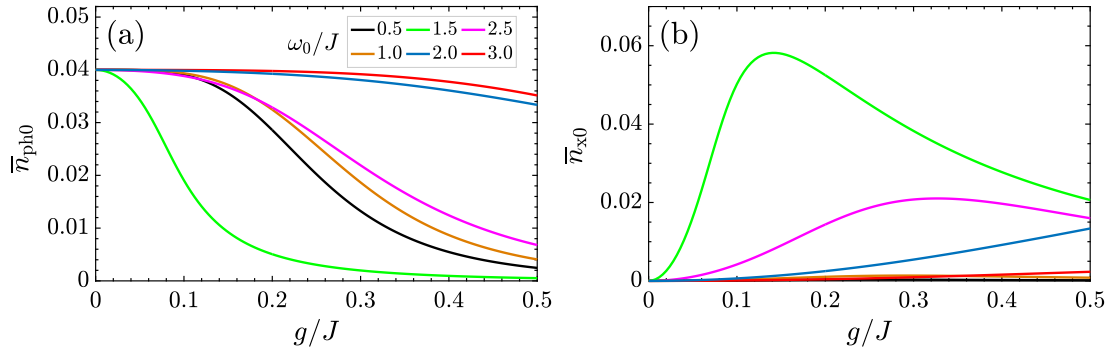


Figure 5.4: (a) Phonon and (b) triplon occupation response at fixed $N = 2000$, $\gamma_{\text{ph}} = 0.02\omega_0$, $a/\gamma_{\text{ph}} = 0.2$, and $\gamma_{\text{s}}/J = 0.01$ as a function of g/J for various frequencies ω_0/J .

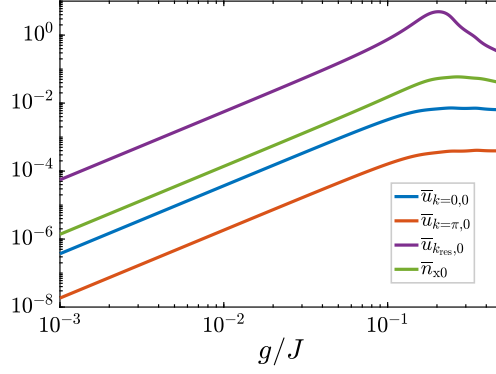


Figure 5.5: Average $k = 0$, π and k_{res} -component of the dressed triplon occupation, \bar{n}_{x0} response at fixed $a/\gamma_{\text{ph}} = 0.2$, $\gamma_s/J = 0.01$, $N = 2000$, and $\gamma_{\text{ph}} = 0.02\omega_0$ as a function of g/J at $\omega_0/J = 1.7$.

sector displays the strong (nonlinear) SPC regime, which is approximately a good scaling independent of the driving frequency, the trend strongly depends on the driving frequency in the spin sector and can not be generalized. This treatment of the spin sector will be understood in the next figures from the strong coupling to the Einstein phonon for which the strong responses and/or self-blocking effect results in an irregular behavior of the triplon occupation over a wide range of phonon frequencies. In fact, the strong and/or nonlinear regime of the SPC is dedicated to the *intense deviation* from the linear trends at which both phonon and triplon occupations are strongly suppressed. As expected from the resonant condition $\omega_0 = 2\omega_k$, the phonon frequency $\omega_0/J = 1.5$, which is so close to the lower limit of the band, shows the strongest suppression in $\bar{n}_{\text{ph}0}$ and strongest increase in \bar{n}_{x0} for $g/J \leq 0.2$ among all other cases.

To stress once more that the resonant momentum is mostly contributing to the spin response, we plot Fig. 5.5 for $k = 0$, $k = \pi$ and $k = k_{\text{res}}$ components at an arbitrary driving frequency inside the band, $\omega_0/J = 1.7$, and at the same set of parameters as Fig. 5.2. The $k = 0$ component is larger than $k = \pi$ because the triplon frequency corresponding to this mode, $2\omega_{\text{min}}$, is closer to the considered driving frequency $\omega_0/J = 1.7$. However, the resonance mode $k_{\text{res}} \simeq 0.313\pi$ corresponding to $\omega_0/J = 1.7$ shows the maximum response compared to other modes. The main reason of the peak in $\bar{u}_{k_{\text{res}},0}$ originates from the nonlinear behaviors of both sectors at strong SPCs, namely the giant resonant self-blocking effect, see below.

5.2 Giant resonant self-blocking effect

Figure 5.6 presents the resonant $\omega = \omega_0$ dependence of $\bar{n}_{\text{ph}0}$ in the NESS at $a/\gamma_{\text{ph}} = 0.2$ and $\gamma_s/J = 0$ (0.01) for $g = 0$ ($g \neq 0$). We once more stress that the strongest responses of both phonon and spin systems to $g/J \neq 0$ is dedicated to the driving frequencies within the two-triplon band, i.e. at $2\omega_{\text{min}} \leq \omega_0 \leq 2\omega_{\text{max}}$.

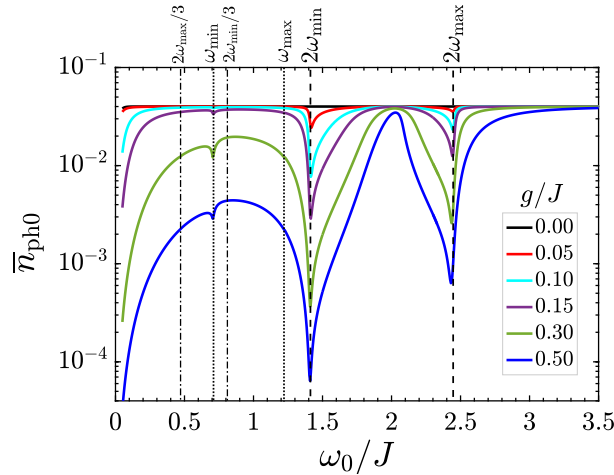


Figure 5.6: Average phonon occupation response to the resonant driving frequency $\omega = \omega_0$ for different SPCs at fixed $N = 2000$, $\gamma_{\text{ph}} = 0.02\omega_0$, $a/\gamma_{\text{ph}} = 0.2$, and $\gamma_s/J = 0.01$.

In the low-frequency (below two-triplon band) limit, the suppression of $\bar{n}_{\text{ph}0}$ at ω_{min} in the strong SPC regime manifests itself with a small kink, which is stronger than the one at ω_{max} , originating from the DOS features [see Fig. 3.3(b)]. This is also the case for respectively $2\omega_{\text{min}}$ and $2\omega_{\text{max}}$; the resulting suppression is stronger at $2\omega_{\text{min}}$. For the in-band frequencies, it exhibits the expected strongest responses corresponding to the resonance frequencies $\omega_0 = 2\omega_k$. However, the band's mean frequency $\omega_0/J = 2$ is seen to get close to the NESS in the decoupled phase, $\bar{n}_{\text{ph}0} = (a/\gamma_{\text{ph}})^2 = 0.04$, provided that the triplon mode is replaced by $k = \pi/2$ at this frequency, where the spin feedback effect stemming from this perpendicular triplon mode is quite weak. Thus, one expects 0.04 for the phonon occupation at this frequency, however, the main reason of $\bar{n}_{\text{ph}0} < 0.04$ at this frequency for $g/J > 0.3$ backs to the prefactor y_k [see Eq. (3.12)], which is not zero at $k = \pi/2$ and takes a role associated with the SPC in the EoMs. In the high-frequency (above band) limit, referred to as Floquet limit, the occupation of the triplon mode excitations is negligible and there is no substantial excitation affecting the phonons. For this reason, the results start to fall in 0.04 at $\omega_0 > 2\omega_{\text{max}}$.

Nevertheless, it is somewhat remarkable that the suppression of phonon occupation at strong SPCs provides a *strong self-blocking effect*. Small phonon occupation (about three orders of magnitude) is the sign of this effect. As explained before, this effect can be associated with the energy flows physics such that the laser field forces the Einstein phonon to move by inducing the energy power $-\mathcal{E}(t)\omega_0 p(t)$ [see the first term of Eq. (3.24c)]. On the other hand, the output energy from the driven phonon to the bath due to the damping is measured by $\gamma_{\text{ph}}\omega_0 n_{\text{ph}}(t)$ [see the third term of Eq. (3.24c)]. This is unexpected so far as strong SPC is always in the strong-perturbation regime for the step driving and more degrees of freedoms should be involved in the theory, whereas spin system acts

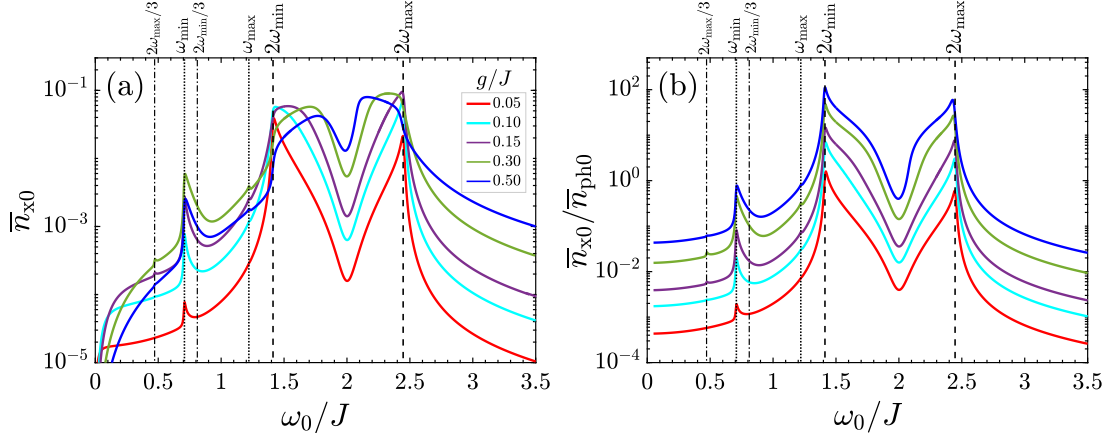


Figure 5.7: (a) Average triplon occupation response to the resonant driving frequency $\omega = \omega_0$ for different SPCs at fixed $N = 2000$, $\gamma_{\text{ph}} = 0.02\omega_0$, $a/\gamma_{\text{ph}} = 0.2$, and $\gamma_s/J = 0.01$. The normalized \bar{n}_{x0} to $\bar{n}_{\text{ph}0}$ is presented in (b).

as a perturbation (extra inertia) and the coupling to the spin system forces the driven phonon to move anyway during the coupling protocol, which leads to a finite value for the temporal average of phonon displacement (and/or momentum) [see chapter 7 for more details]. However, the input energy does not deliver to the spin system through this coupling and a percent level of the laser power is transferred into the spin system; most of it is already absorbed by the lattice sector. This, in turn, is expected to block parts of the input energy by the phonons at the spin-band edges. Thus, the spin system itself is the main origin of blocking of the uptake energy from the driven phonon; that's why we call it a self-blocking effect. With referring to the mean-field approximation, see the second term of Eq. (3.24c), part of the input power which is the uptake of laser energy by the driven phonon drives the spin sector through the effect of SPC. This part is quite small at strong SPCs in the adiabatic limit $\omega_0 < 2\omega_{\min}$, which the properties of the system may be rarely affected by phonon dynamics, resulting in strong deviations from $\bar{n}_{\text{ph}0} = 0.04$, the so-called off-resonant self-blocking effect. In addition to the mean-field approximation effect, the two-phonon process at a low-frequency limit satisfying $2\omega_0 \simeq 2\omega_{\min}$ comes into play role in determining the response of the system. Thus, the explicit validity analysis for the off-resonant self-blocking effect belongs to the favorable effect of low frequencies at small perturbation, and for large perturbations, intermediate and high frequencies are the proper ones.

To integrate out the response of both phonon and spin sectors, with the same set of parameters similar to Fig. 5.6, the average of the triplon occupation in the NESS is represented in Fig. 5.7(a) as a function of the driving frequency for different SPCs. In the band, the response is conventional: two large-amplitude shoulders around the band edge frequencies correspond to two-spin excitations, balanced by a few small peaks at below band frequencies $\{\omega_{\max}, \omega_{\min}, 2\omega_{\max}/3\}$. The latter is an outcome of the multiphonon process [which is not strong except at

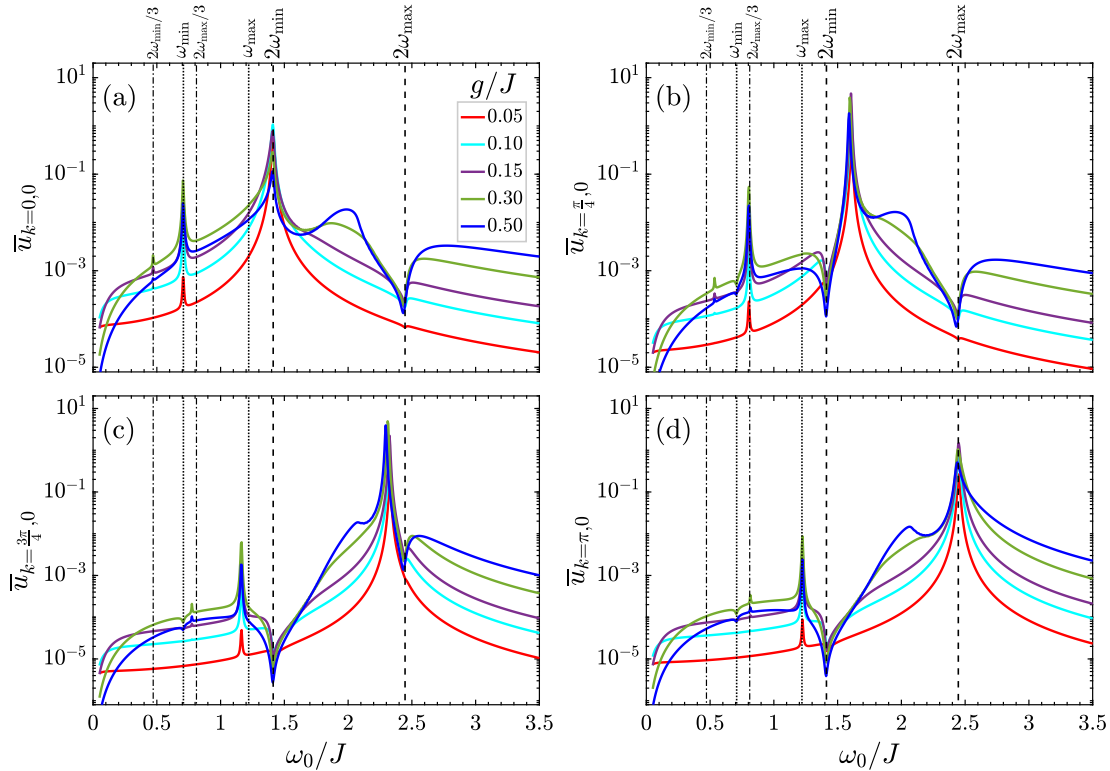


Figure 5.8: Average (a) $k = 0$, (b) $\pi/4$, (c) $3\pi/4$ and (d) π -component of the triplon occupation at fixed $a/\gamma_{\text{ph}} = 0.2$, $\gamma_{\text{s}}/J = 0.01$, $N = 2000$, and $\gamma_{\text{ph}} = 0.02 \omega_0$ as a function of driving frequency ω_0/J for different SPCs.

ω_{min} where the two-phonon process becomes strong with SPC] induced to the spin sector by the driven phonon. On the other hand, the response below the band regime displays a striking qualitative change at $\omega_0 = \omega_{\text{min}}$ as $g/J = 0.3$ crosses over other SPCs. Again, the nontrivial large behavior of the spin responses in the adiabatic limit originates from the mean-field decoupling approximation, for which the phonon dynamics is not important at strong SPCs and the two-phonon process occurs for which the response of the system tries to satisfy the condition $2\omega_0 \simeq 2\omega_{\text{min}}$. However, it is important to realize that the instability in the position of peaks at band edges arises at strong coupling. Without referring to any approximation, it is clear that it is due to the self-blocking effect that emerged in $\bar{n}_{\text{ph}0}$, unbalancing the energies and eventually responses in the two-triplon band.

To confirm the latter interpretation, we proceed now with the normalized triplon occupation to the phonon occupation in the resonance condition, i.e. to $\bar{n}_{\text{ph}0}$ shown in Fig. 5.6. In this case, Fig. 5.7(b) shows that when the self-blocking effect is removed, as the system is described by the triplon occupation only, the nontrivial behaviors are gone and $\bar{n}_{\text{x}0}$ is gradually increased by g ; the origin comes from the unimportant phonon dynamics at strong SPCs such that the triplon system plays the main role in the dynamics. The resulting picture shows then the strongest responses at band edges without any instability in the position

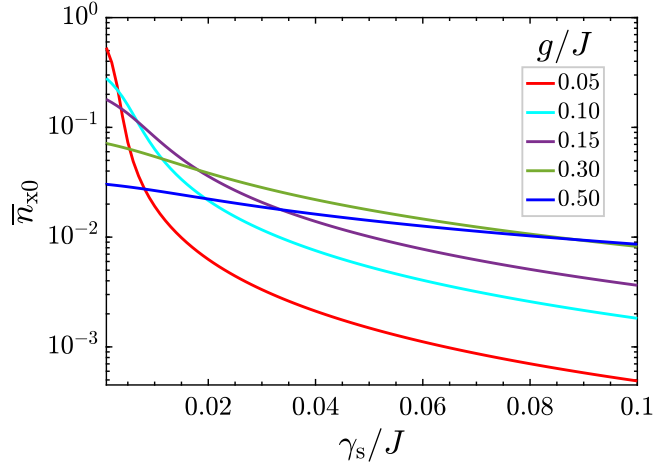


Figure 5.9: Average triplon occupation, \bar{n}_{x0} , response at fixed $a/\gamma_{\text{ph}} = 0.2$, $\omega_0 = 2\omega_{\text{max}}$, $N = 2000$, and $\gamma_{\text{ph}} = 0.02\omega_0$ as a function of spin damping γ_s/J for different SPCs.

of peaks. Compared to \bar{n}_{x0} itself in Fig. 5.7(a), it can be concluded that both weak and strong coupling regimes behave similarly in the resonant responses, however, the strong g in the presence of the self-blocking effect is responsible for spreading the resonant response to a wider range of frequencies. Intriguingly, the density profile presented suggests that the system at strong-enough SPCs in the steady-state spontaneously proposes symmetry between the responses in the lower and upper band edges. The origin of this proposed symmetry lies in the triplon dispersion-dependent factors y_k and y'_k [see Eq. (3.12)] in Eq. (3.26), which become important at strong SPCs in the regions of the Brillouin zone.

As n_{x0} comprises many modes k , the response of four selected components $k = 0, \pi/4, 3\pi/4$, and π , respectively corresponding to resonant phonon frequencies $\omega_0 = 2\omega_{\text{min}}, \simeq 1.61, \simeq 2.32$, and $\simeq 2\omega_{\text{max}}$, are shown in Fig. 5.8. The agreement between these frequencies and the strongest response are dictated by the sharp peaks at the band edges [Figs. 5.8(a) and 5.8(d)] and in the band [Figs. 5.8(b) and 5.8(c)]. Following the self-blocking effect at band edges due to suppressed phonon occupation, in both $k = \pi/4$ and $3\pi/4$ modes, a dip appears at both band edges, while this occurs at upper (lower) band edge at $k = 0$ (π). Notice that the sharpness of dips for the phonons in the band depends strongly on their proximity to the band edges. For $k = 3\pi/4$, one expects a weaker suppression at upper band edge since it is close to $2\omega_{\text{max}}$. This is nicely the case for the lower band edge if one chooses a mode like $k = \pi/4$. For the adiabatic and antiadiabatic regimes respectively below and above the two-triplon band, one finds the dominant response of $g/J = 0.3$ below the band at $\omega_{\text{min}}, 2\omega_{\text{min}}/3, \simeq 0.97\omega_{\text{max}}$, and ω_{max} for $k = 0, \pi/4, 3\pi/4$, and π . The shoulders for the strong SPCs in the center of band demonstrate that the system intends to forget the suppression of the phonon occupation for a possible strong response.

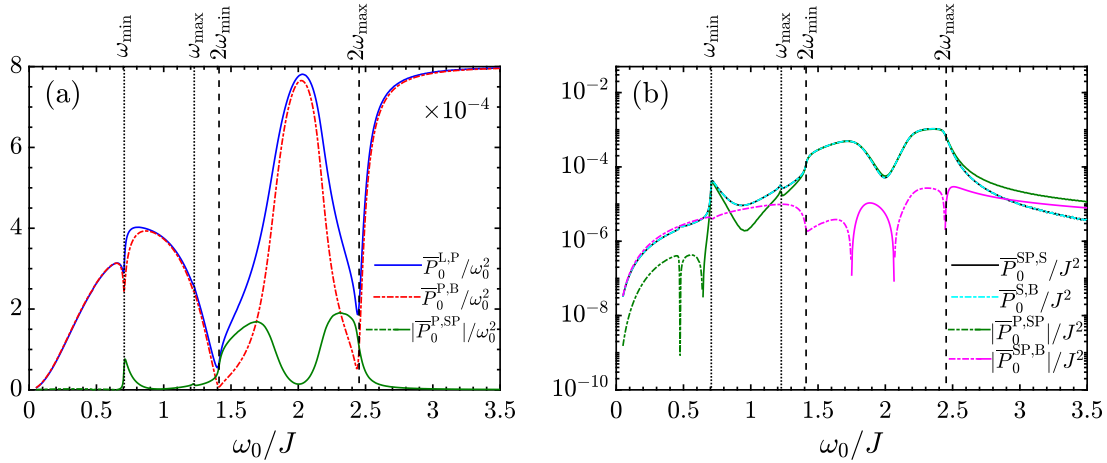


Figure 5.10: (a) and (b) Average energy flows through the driven spin-lattice system coupled to the phononic bath as a function of $\omega = \omega_0$ at fixed $\gamma_{\text{ph}} = 0.02\omega_0$, $a/\gamma_{\text{ph}} = 0.2$, a large SPC $g/J = 0.3$, and $\gamma_s/J = 0.01$. For clarity the powers are normalized to ω_0^2 and the solid (dashed) line in $\bar{P}_0^{\text{P,SP}}$ and $\bar{P}_0^{\text{SP,B}}$ stands for for a positive (negative) power.

We also provide some information in Fig. 5.9 about the spin damping effect, although it was fixed at $\gamma_s/J = 0.01$ up until now. For this purpose, we choose triplon occupation, \bar{n}_{x0} , response to the spin damping for various SPCs. In Fig. 4.13 we found that the responses decrease gradually with γ_s in the weak coupling regime at band edges. That also happens for a strong coupling regime but is accompanied by a slower slope. Thereby, one would expect a constant occupation with γ_s at the strong-enough coupling. The main reason for this can be understood from the self-blocking effect for which the spin system gets involved in the driving hardly and the unexpected spin-freezing somehow happens. Thus, the spin damping to the bath cannot be then so important. It should be pointed out that we have chosen the upper band edge in this interpretation because the self-blocking effect is the strongest at band edges. One can also choose the lower band edge for smaller occupations.

5.2.1 Energy flows in the presence of a strong SPC

Before delving into the details of another main topic of the present chapter, as expected from the previous results, we can roughly expect a different type of behavior for the energy flows in the presence of strong SPCs. In fact, the expressions and sum rules in Sec. 4.3 can be applied by using a larger g . In other words, they allow for a host of analytic expressions. In this subsection, we recall those expressions and discuss the results of the strong SPC effect on them.

Figure 5.10 shows all energy flows for a fixed $g/J = 0.3$ with the set of parameters: $\gamma_{\text{ph}} = 0.02\omega_0$, $a/\gamma_{\text{ph}} = 0.2$, and $\gamma_s/J = 0.01$. In the two panels, an analog of Fig. 4.15 of the chapter 4 is reproduced. It can be seen in panel (a) that at band edges and around it, the majority of input energy flows to the SPC

part, but this does not guarantee that it eventually flows to the spin system, see panel (b). Interestingly, the damping of the phonon to the bath, i.e. $\bar{P}_0^{\text{P,B}}$ is nearly zero at the lower band edge, meaning that almost all the power is dumped to the bath through the spin system in this regime, in contrast to what we saw in the weak coupling regime [see Fig. 4.15]. However, $\bar{P}_0^{\text{SP,B}}$ is still much smaller than the others in Fig. 5.10(b). Also, the energy entering the spin system through the driven phonon, $\bar{P}_0^{\text{SP,S}}$, is still small and this, in turn, confirms the strong self-blocking effect. All these together help to conclude that the mean-field decoupling approximation is not broken down and thus, we do not seem to get into an anomalous energy-flow regime at strong resonant self-blocking, while this is still the case at a very-low-frequency regime. On the other hand, getting away from the band edges, we again see that $\bar{P}_0^{\text{P,B}}$ is dominated as in the weak-coupling regime, which does not matter because here we are looking for the fraction of the input energy flowing to the spin system at strong SPCs, where the self-blocking takes place, i.e. at band edges. Furthermore, still, as measured by \bar{n}_{ph0} , self-blocking is 10 times weaker at the upper band edge compared to the lower band edge, which can be understood from the nominally asymmetrical spin density of states due to matrix elements.

5.3 Strong SPC-induced magnetic-phononic hybrid states

Up to now, all considerations were focused on the out-of-equilibrium alternatives for the determination of the SPC effect on the physical observables in the NESS at $\omega = \omega_0$, i.e. at the resonance condition between the laser and the driven phonon. We henceforth turn to the case of $\omega \neq \omega_0$, which is more meaningful in the experiment, to see how the strong g modifies the spin-lattice system. By this, we first drive the system with frequency ω at a given phonon frequency ω_0 different than ω and in the next step, we scan the responses to the driving frequency ω in both phonon and spin sectors for various SPCs.

We first provide the off-resonance response of the phonon occupation to the laser field in Fig. 5.11. Setting $N = 2000$, $\gamma_{\text{ph}} = 0.02 \omega_0$, $a/\gamma_{\text{ph}} = 0.2$, $\gamma_{\text{s}}/J = 0.01$, and $g/J = 0.3$ for three different phonon frequencies, namely $\omega_0/J = 1, 2, \text{ and } 3$, respectively below, in and above the two-triplon band we plot \bar{n}_{ph0} as a function of driving frequency ω/J . We emphasize the following: The maximum occupation $\bar{n}_{\text{ph0}} = 0.04$ encapsulates the strong responses at $\omega = \omega_0$, i.e. it determines the dominant processes at the resonance frequency. This process can be regarded as the light-matter analogy for which it signals a transition between optical bands in condensed-matter systems. Moreover, by direct inspection, we see that the driving frequencies at band edges are responsible for the small peaks in the response stemming from the spin feedback effects (two-spin excitations). We expect a converged dynamical response for the phonon frequencies in the case of low and high driving frequencies (it is clear for the low frequencies) that their

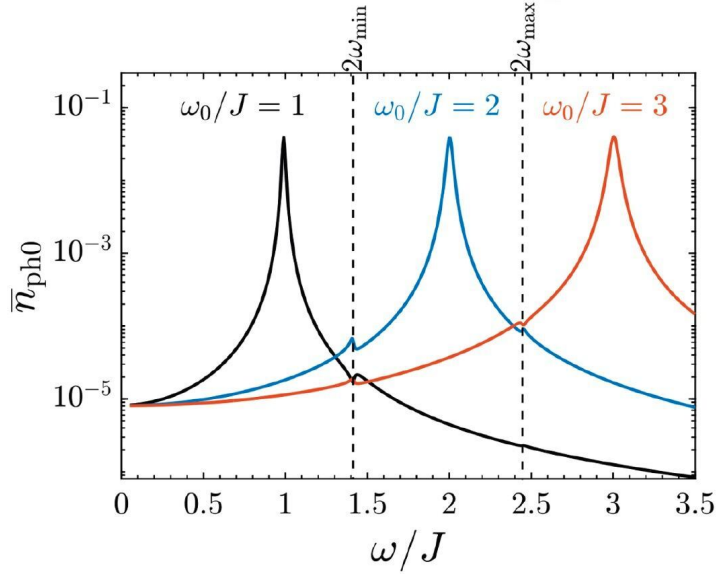


Figure 5.11: Phonon occupation response at fixed $N = 2000$, $\gamma_{\text{ph}} = 0.02\omega_0$, $a/\gamma_{\text{ph}} = 0.2$, $\gamma_{\text{s}}/J = 0.01$, and $g/J = 0.3$ to the driving frequency ω/J in off-resonance with the phonon frequency for three different $\omega_0/J = 1, 2$ and 3 respectively below, in, and above the two-triplon band.

time-dependent fluctuations are intrinsically the same due to respectively weak dynamical response and strong regime.

Due to the insignificant responses away from the phonon frequency and band edges, we mostly in what follows show the close-ups of responses in the vicinity of band edges and ω_0 values. For a basic understanding, we consider four phonon frequencies; two in-band ($\omega_0/J = 1.45$ and 2.4) and two out-of-band ($\omega_0/J = 1.35$ and 2.5). With this knowledge, as a first quantity, we consider $\bar{n}_{\text{ph}0}$ in the NESS in Fig. 5.12 to provide a qualitative statement about the strong SPC effects. For $\omega_0/J = 1.35$, in Fig. 5.12(a), stronger SPCs weaken the phononic excitation associated with a shift to the lower driving frequencies. It should be pointed out that the initial phononic NESSs are not destroyed by this weakening in the presence of strong SPCs, but new set of states are just formed by distributing the purely initial phononic states to magnetic-phononic states. This mainly stems from the level repulsion effect between our coupled harmonic oscillators (phonons and triplons) such that the phonon frequency at $\omega_0/J = 1.35$ as the lower one decreases when the coupling strength between the phonon and triplons increases, while the triplon frequency at the lower band edge as the higher one increases. However, this is in another way for phonons with higher energies than triplons, i.e. for $\omega_0/J = 1.45$ in Fig. 5.12(b), the damping of responses with g is stronger and the phononic peak is also driven to the higher ω frequencies inside the two-triplon band. For the in-band phonons, there is an extra peak at the lower band edge $2\omega_{\text{min}}$ which comes up at $g/J = 0.1$ and becomes more visible to the lower ω frequencies outside the two-triplon band as g is increased. For the phonons close to the upper

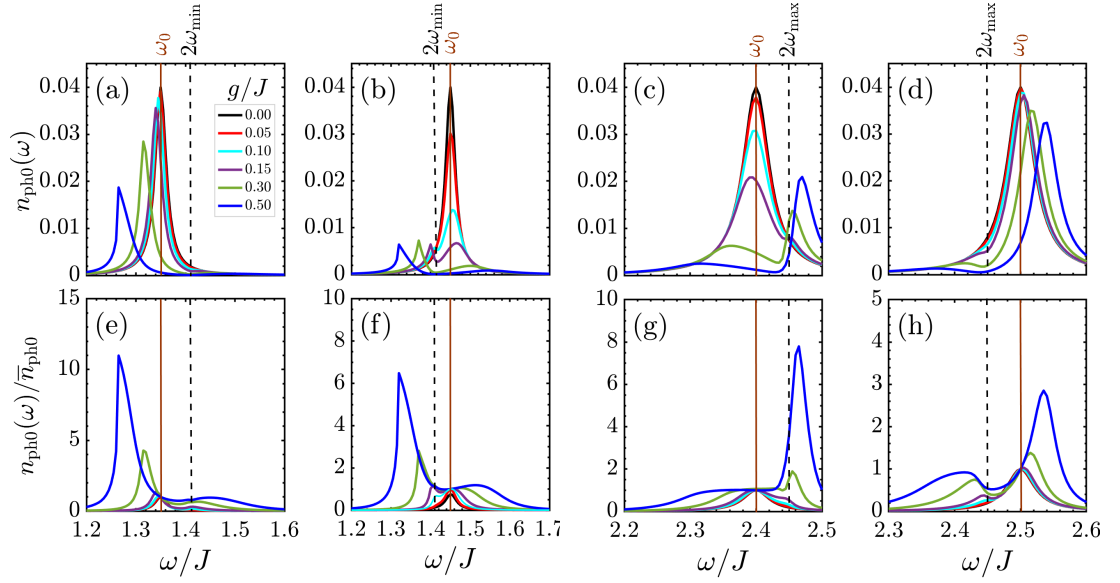


Figure 5.12: Average phonon occupation response in the NESS to the driving frequency ω/J in off-resonance with the phonon frequency at fixed $N = 2000$, $\gamma_{\text{ph}} = 0.02 \omega_0$, $a/\gamma_{\text{ph}} = 0.2$, and $\gamma_s/J = 0.01$ for (a) $\omega_0/J = 1.35$, (b) $\omega_0/J = 1.45$, (c) $\omega_0/J = 2.40$, and (d) $\omega_0/J = 2.50$. Corresponding normalized average phonon occupations in off-resonance $\omega \neq \omega_0$ to the average phonon occupation in resonance $\omega = \omega_0$ in the NESS as a function of the driving frequency ω/J are shown in (e)-(h).

two-triplon band edge, Figs. 5.12(c) and 5.12(d), the same features appear with different broadening and sharpening peaks originating from the differences in matrix elements. Again, for phonon inside the band, the second peak comes up in Fig. 5.12(c) at $2\omega_{\text{max}}$ and $g/J = 0.1$ accompanied by the repulsion from the upper band edge to the higher driving frequencies. But, for the phonon outside the band, although no second strong peak appears, the repulsion occurs towards the higher ω values.

The origin of the extra peak above-mentioned for the phonons inside the band is not ambiguous; they are more aptly referred to as the outcome of the self-blocking effect due to the suppressed phononic response at $2\omega_{\text{min}}$ and $2\omega_{\text{max}}$. However, in addition to the introduced giant self-blocking effect, there exists a level repulsion between phonon and spins accompanied by the in-band and out-of-band *hybrid states*. This is an interesting and expecting result since we are creating magnetic states outside the two-triplon band. In Figs. 5.12(e)-(h), we remove the self-blocking effect to first confirm its impact and second, to highlight the roles of level repulsion and phonon frequency shift effects, which manifest themselves in the hybrid states. By this, we find the significance of the self-blocking effect in creating the peaks in-band and one out-of-band at strong SPCs. However, the self-blocking is not the only reason for new extra peaks at band edges and the level repulsion resulting in the magnetic-phononic states is more significant in determining new responses outside the band. At first glance, it is seen that by

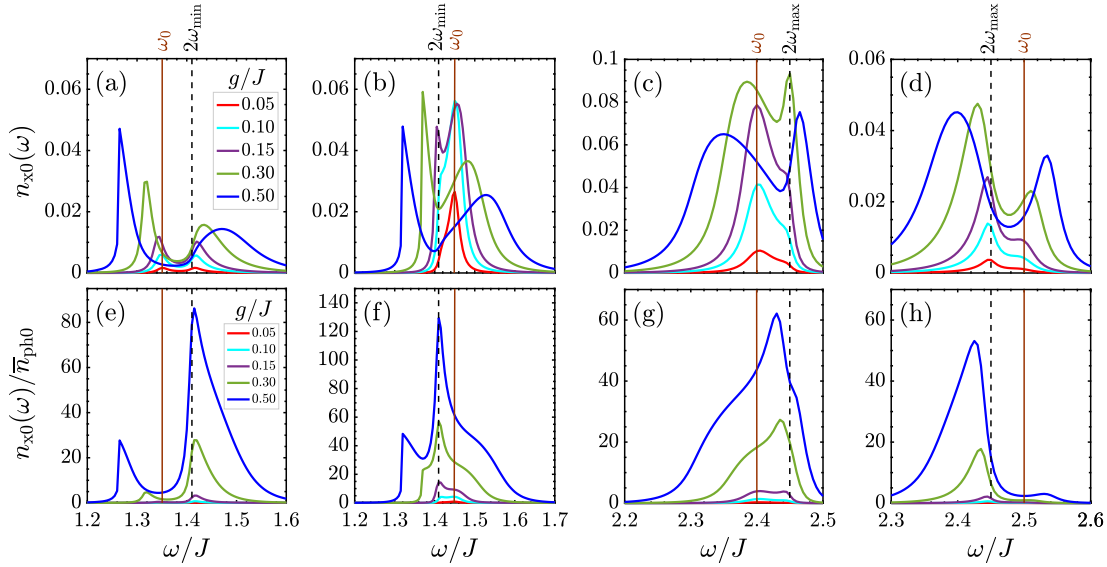


Figure 5.13: The same as Fig. 5.12, but for the average triplon occupation.

removing the self-blocking effect, the height of peaks outside the band becomes larger, confirming the strong role of the self-blocking effect at band edges. However, the responses in-band and out-of-band are mainly connected to the hybrid states such that the peaks and the corresponding shifts are still present at the same energies after removing the self-blocking effect. Interestingly, it is much easier to conclude that without self-blocking the responses dramatically increase with g outside the band, while they are still dampening inside the band with g .

For improved consistency with $\bar{n}_{\text{ph}0}$, we use the same parameters for $\bar{n}_{\text{x}0}$ in Fig. 5.13 as reference ones. As a general observation, in contrast to $\bar{n}_{\text{ph}0}$ with weak peaks (invisible in Fig. 5.12) for phonons inside the spin band in both weak- and strong-coupling regimes, $\bar{n}_{\text{x}0}$ appears with strong peaks in the band since we are looking at the spin characters here with weaker dissipation. Similarly, the shifts of peaks and the presence of valleys are the consequences of the combined effect of the self-blocking effect and the level repulsion effect (hybrid states). However, the irregular behavior of the peaks, which also affects the position of peaks inside and outside the two-triplon band, with SPC stems only from the self-blocking effect, as confirmed by removing this effect in Figs. 5.13(e)-(h). Although one realizes a strong response out-of-band with SPC in Figs. 5.13(a)-(d), we still from the normalized triplon occupations believe that the strongest responses in both resonance and off-resonance conditions belong to the band edges. Moreover, it becomes obvious that responses confirm once more the dominant contribution of $2\omega_{\text{min}}$, i.e. Figs. 5.13(a), 5.13(b), 5.13(e), and 5.13(f).

The contribution of lattice and spin degrees of freedom in forming such hybrid states should be seen simultaneously outside the spin-band, shown in Figs. 5.14(a) and 5.14(c) for respectively $\omega_0/J = 0.6$ and 3. For both phonons away from the spin band, there is a slight shift to the driving frequencies outside the band in

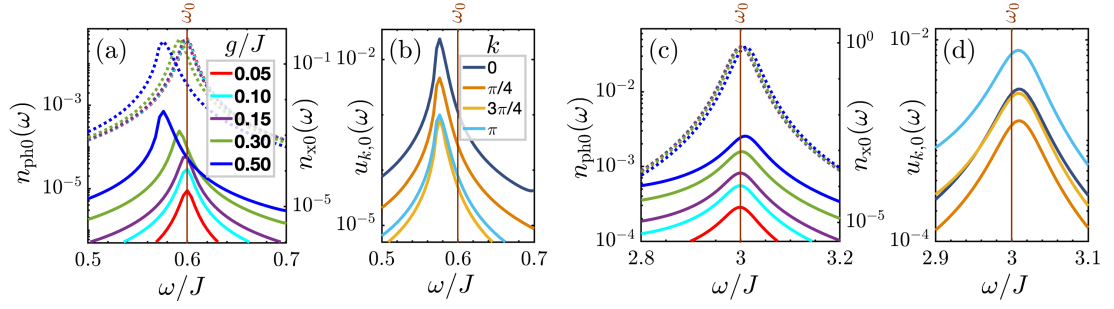


Figure 5.14: Average occupations in off-resonance $\omega \neq \omega_0$ in the NESS as a function of the driving frequency ω/J at fixed $N = 2000$, $\gamma_{\text{ph}} = 0.02\omega_0$, $a/\gamma_{\text{ph}} = 0.2$, and $\gamma_{\text{s}}/J = 0.01$ for (a) phonon occupation (dotted lines) and triplon occupation (solid lines) for various SPCs and (b) k -components of the spin response at $\omega_0/J = 0.6$ and $g/J = 0.5$ far from the two-triplon band edges. The same for $\omega_0/J = 3$ in panels (c) and (d).

both phonon (dotted lines) and spin (solid lines) systems. However, the peaks take place at the same positions in both systems, confirming the formed hybrid states between the phonon and triplet states. So, here this hybridization causes a phononic mode stemming from the SPC. Moreover, the average k -components of the triplon occupation are plotted at these phonon frequencies in Figs. 5.14(b) and 5.14(d) for selected $k = 0, \pi/4, 3\pi/4$, and π . From these plots, one can conclude that no component is destroyed through this hybridization (localized phononic mode formation) and all components show a response. It is no surprise that for $\omega_0/J = 0.6$ below the lower band edge, the $k = 0$ component is dominant, while it is the case for $k = \pi$ around the upper band edge at $\omega_0/J = 3$.

In short, we see that the SPC dependence of the giant self-blocking effect and level repulsion phenomenon shows a typical phenomenon related to both phononic and magnetic states: the SPC-induced frequency shifts caused by driving. Being the frequency corresponding to the highest occupation in this phenomenon, we will refer to it from now on as ω^{hyb} and identify it for various SPCs. The SPC-induced phonon frequency shifts obtained in this way are plotted versus g/J in Figs. 5.15(a) and 5.15(b). It is expected to meet $\omega^{\text{hyb}} = \omega_0$ in the decoupled case $g/J = 0$. The values shown denote the relative shift compared to $g/J = 0$. Before turning to the quantitative analysis of the results, we would like to list the SPC-induced shifts of both sectors to build up the Fig 5.15. Generically, in Fig 5.15(a), we have, for peaks around both lower and upper band edges,

- close gray circle – phononic, peaks outside the band
- close magenta diamond – magnetic, peaks outside the band
- open gray circle – phononic, peaks inside the band
- open magenta diamond – magnetic, peaks inside the band
- close orange rectangle – phononic, peaks inside the band

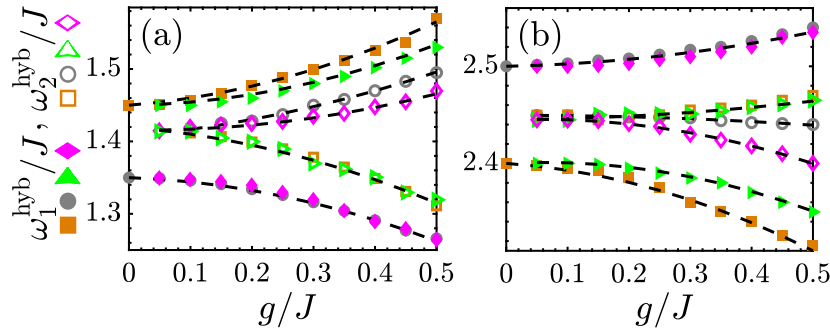


Figure 5.15: The characteristic frequencies of phonon and spin occupations are taken from Figs. 5.12 and 5.13 for phonon frequencies around the (a) lower and (b) upper band edge. For the symbols, see the text.

- close green triangle – magnetic, peaks inside the band
- open orange rectangle – phononic, peaks outside the band
- open green triangle – magnetic, peaks outside the band

In this language, “phononic” and “magnetic” states are characterized by the frequency ω_0/J and $2\omega_{\min/\max}/J$, respectively. However, to estimate the strength of hybridized states due to the SPC and driving, we define a dimensionless hybridization parameter $h = g/|\omega_0 - 2\omega_{\min/\max}|$. While $h < 1$ refers to the weakly hybridized magnetic-phononic states, e.g. see Fig. 5.14(a), $h \gg 1$ refers to the strongly ones with 50:50 contribution of both lattice and spin sectors, e.g. see Figs. 5.12 and 5.13. In the language of the quasiparticles, we would propose “phonon-bitriplons” since two bosons are produced by a single boson as the hybrid states are formed in the presence of strong SPCs.

The out-of-band peak in the adiabatic limit ($\omega < 2\omega_{\min}$) shows a decrease of the frequency with increasing SPC, while the out-of-band one in the antidiabetic limit ($\omega > 2\omega_{\max}$) shows an increased treatment. It can be seen that both phononic and magnetic states (see respectively close gray and magenta symbols below $2\omega_{\min}$ and above $2\omega_{\max}$) obey the same treatment beyond the resonance $\omega_0 = 2\omega_k$. In the resonance case, different matrix elements avoid the same treatment. However, for the in-band peaks, the phonon frequency close to the lower (upper) band edge shows an increase (a decrease) shift with g/J , which is accompanied by different phononic and magnetic responses as expected since the two mutually repelling excitations are much stronger in the two-triplon band than outside the band (see respectively close orange and green symbols getting away from $\omega_0/J = 1.45$ and $\omega_0/J = 2.4$ as well as the corresponding open symbols at band edges). In all these shifts, there is a general scale for which the level of repulsion scales with it. That the general trend can be qualitatively explained with the simple dashed fitting

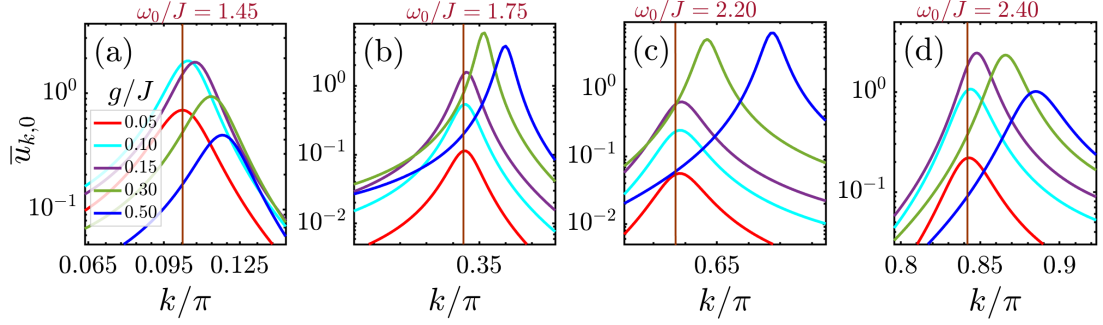


Figure 5.16: The response of the average k -component of the triplon occupation in the NESS to the triplon mode k at $\omega = \omega_0$ for (a) $\omega_0/J = 1.45$, (b) $\omega_0/J = 1.75$, (c) $\omega_0/J = 2.20$ and (d) $\omega_0/J = 2.40$ at various SPCs at fixed $N = 3000$, $\gamma_{\text{ph}} = 0.02\omega_0$, $a/\gamma_{\text{ph}} = 0.2$, and $\gamma_{\text{s}}/J = 0.01$.

function of

$$\omega^{\text{hyb}}(g) = \omega_0 + \frac{g^2}{\pm\omega_0 \mp 2\omega_{\text{min/max}}} \mathcal{C}, \quad (5.1)$$

where the upper and lower signs in the denominator stands respectively for $\omega_0 < 2\omega_{\text{min/max}}$ and $\omega_0 > 2\omega_{\text{min/max}}$. An important mechanism that justifies the phonon frequency shift can be expected from ordinary perturbation theory, which expects a square of g because in particular, the SPC can be treated as a perturbation for both phonon and spin systems. From the SPC Hamiltonian, it is not far from the fact that the coefficient \mathcal{C} in the fitting function of the shifted frequency is proportional to the spin correlations given by $\text{avg}(\mathcal{U}_0 + \mathcal{V}_0)$ where the average is taken over the values of $(\mathcal{U}_0 + \mathcal{V}_0)$ for different g/J . Physically, it is reasonable because g is only coupled to magnetic interaction J and the correlation between two spins is responsible for the phonon and/or spin frequency shifts with the SPC. This correlation, as we know, is described by $[\langle \vec{S}_1 \cdot \vec{S}_2 \rangle - \langle \vec{S}_1 \cdot \vec{S}_2 \rangle_{\text{eq}}]$ as understandable from Eq. (3.4) which the equilibrium value is not important out of equilibrium and we certainly would argue that the coefficient \mathcal{C} can be well-described by $\text{avg}(\mathcal{U}_0 + \mathcal{V}_0)$.

5.3.1 Triplon mode dependence of SPC

In Sec. 5.3, we have seen that the SPC-induced frequency shift depends on the spin correlations. Among the triplon modes, one would expect to see the most pronounced SPC effects for the in-plane modes. So, the phonon displacement would be the most sensitive quantity to magnetic correlations with in-plane modes, as they directly alter the exchange integral between the in-plane noninteracting modes. Therefore, among all in-plane modes, the ones corresponding to the phonon frequency should show the strongest SPC-induced shifts. For a comparison, the relative triplon mode dependency of SPC shift is plotted in Fig. 5.16 through \bar{u}_{k0} . For a better accurate measurement of the shifts, we set the system size to

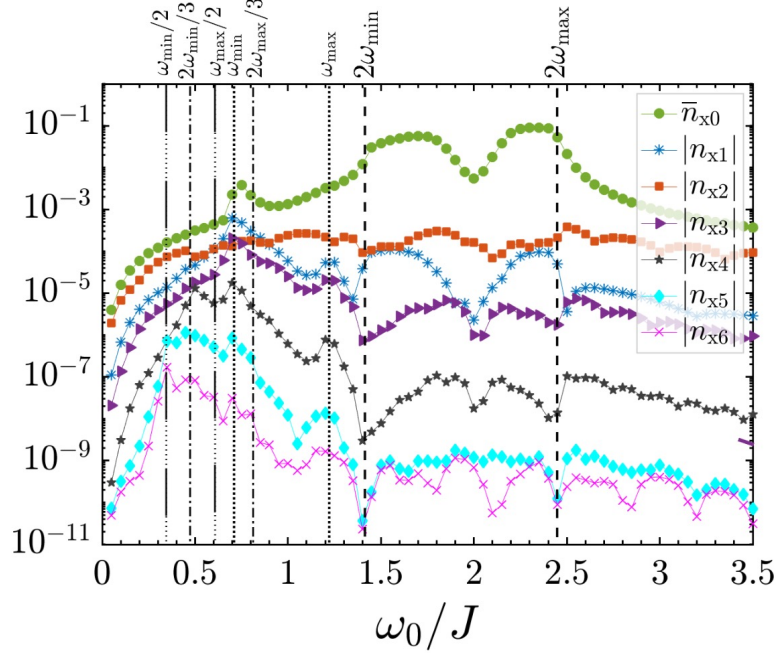


Figure 5.17: Comparison between the coefficients of the Fourier transforms of $n_x(t)$ at fixed $N = 2000$, $\gamma_{\text{ph}} = 0.02 \omega_0$, $a/\gamma_{\text{ph}} = 0.2$, $\gamma_s/J = 0.01$, and $g/J = 0.3$ for below, in, and above the band regime, and $\gamma_{\text{ph}} = 0.02 \omega_0$.

$N = 3000$. This figure shows four different phonon frequencies (two near and two away from the band edges) and their corresponding mode shifts with SPC, which corresponds to $k(\omega_0)$ plus a constant shift. Several new modes appear in this configuration, the most intense of which is different depending on ω_0 and g . For $\omega_0/J = 1.45$ in Fig. 5.16(a), the dominant contribution of the self-blocking effect leads to a damped response with g . The same happens around the upper band edge, i.e. for $\omega_0/J = 2.4$ in Fig. 5.16(d). However, for the phonons inside the two-triplon band, i.e. for $\omega_0/J = 1.75$ and $\omega_0/J = 2.2$ in Figs. 5.16(b) and 5.16(c), the self-blocking effect is weak compared to two others and the SPC results in an enhancement of responses.

5.3.2 SPC-induced harmonic decompositions

As a direct consequence of this observation (triplon mode renormalization), one can conclude that harmonic phonons are used to control magnetic exchange-type interactions, i.e. a magnetophononic driving effect. However, it is worth mentioning that this cannot be the case for the phonons close to or at the band edges because the giant resonant self-blocking effect at the band edges stops their action. In order to deeply interpret the SPC effects on the NESS signal, it is easy to apply the FT for understanding harmonic components. Let $n_x(t)$ takes the role of $O(t)$ in Eq. (4.11). As well-known from the basic principles of the FT, the average of the NESS signal is equivalent to the zeroth component. For this reason, we keep the absolute value of the zeroth component as before, \bar{n}_{x0} , while

other components are characterized explicitly by $|n_{xm}|$ to be different than the zeroth one. Figure 5.17 shows the results of FT for $n_x(t)$ at a fixed strong SPC, $g/J = 0.3$, up to the sixth harmonic, carried out with the same set of parameters as Fig. 5.7. While obtaining the zeroth component as the dominant one results from average of the original NESS signal in order to fully verify the green curve in Fig. 5.7, the second harmonic regarding dynamical properties is the next dominant component in the sense that $u_k(t)$ oscillates at $2\omega_0$ due to the oscillation of both $q(t)$ and $w_k(t)$ at ω_0 in Eq. (3.26a). Following this, one expects to see the first component in $w_k(t)$ (or $v_k(t)$) as the dominant component [not shown here but it is well-confirmed in the previous chapter]. However, this dominance in $n_x(t)$ is unstable around a region $[\omega_{\max}/2, 2\omega_{\max}/3]$ for which the first harmonic (and third harmonic at ω_{\min}) becomes dominant. The reason can be understood from the fact that $w_k(t)$ in Eq. (3.26c), leads to a driving frequency term for $u_k(t)$ as $(2 \pm 1)\omega_0$. So, one immediate result would be nontrivial behaviors of $u_k(t)$ and eventually $n_x(t)$ below the band regime [see Figs. 5.1 and 5.7] at $\omega_0 = \omega_{\min}$ compared to other low frequencies. In the general case, a decreasing function of $m \geq 1$ can be treated for $|n_{xm}|$ far from the special region above-mentioned.

To reinforce the above considerations, we zoom in the low-frequency limit responses for higher harmonics to be more effective in highlighting the multiphonon process effect when SPC is strong. Indeed, we observe that more small peaks and dips are developing in the low-frequency limit where the strong SPC shows its impact. The peaks at frequencies $\{2\omega_{\min}/3, \omega_{\min}\}$, $\{\omega_{\min}/2, 2\omega_{\min}/3, \omega_{\min}\}$ and $\{\omega_{\min}/2, 2\omega_{\min}/3, \omega_{\min}, 2\omega_{\max}/3\}$ corresponding respectively to $m = 4, 5$ and 6 confirm the importance of multiphonon process effect when SPC is strong (but still very small and negligible). In contrast to the shoulders around the two-triplon band edges for \bar{n}_{x0} , the self-blocking effect mentioned before in the phonon occupation is rooted in the harmonic components $m \geq 3$, leading to strong dips at band edges.

5.4 Off-resonant SPC-induced input energy flow

Apart from the above arguments, together with the EoMs, it is customary to define the energy flows entering to the Einstein phonon, transferring and/or distributing to the SPC and spin parts, and dissipating to the bath [169] when $\omega \neq \omega_0$, i.e. in the off-resonance condition. However, we only focus on the energy flow entering the Einstein phonon, which is of interest in the experiment:

$$P^{\text{L,P}}(t) = -\omega_0 \mathcal{E}(t) p(t). \quad (5.2)$$

Like before, the average of $P^{\text{L,P}}(t)$ and its normalized version to $\bar{n}_{\text{ph}0}$ in the NESS are drawn in Fig. 5.18 for $\{(a),(e)\}$ $\omega_0/J = 1.35$, $\{(b),(f)\}$ $\omega_0/J = 1.45$, $\{(c),(g)\}$ $\omega_0/J = 2.40$ and $\{(d),(h)\}$ $\omega_0/J = 2.50$ and the same set of parameters as before. Similar to the phonon and spin occupations, in the decoupled phase, a single

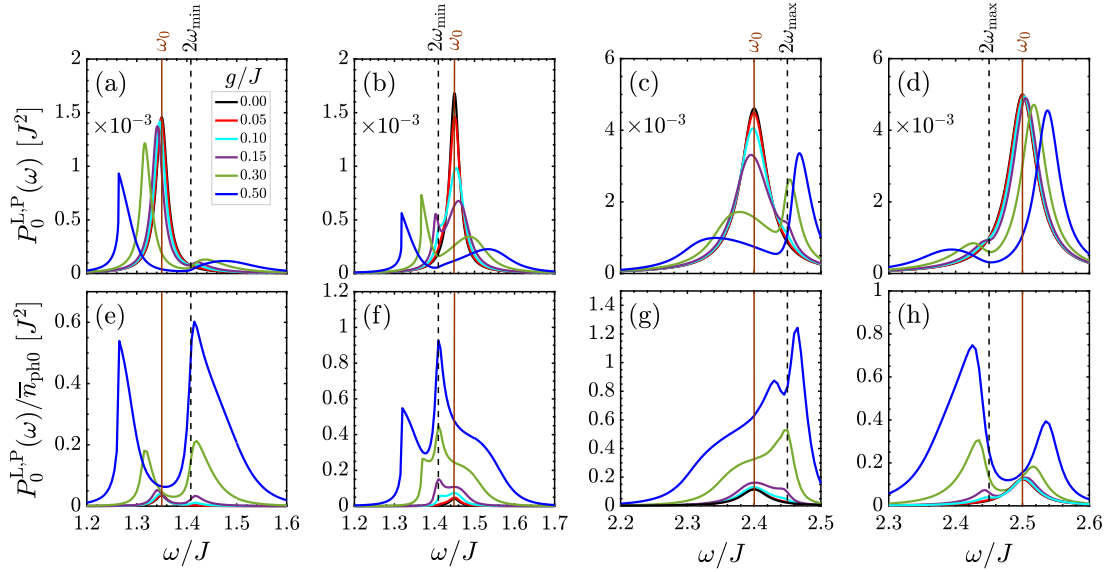


Figure 5.18: Average input energy response in the NESS to the driving frequency ω/J in off-resonance with the phonon frequency at fixed $N = 2000$, $\gamma_{\text{ph}} = 0.02\omega_0$, $a/\gamma_{\text{ph}} = 0.2$, and $\gamma_s/J = 0.01$ for (a) $\omega_0/J = 1.35$, (b) $\omega_0/J = 1.45$, (c) $\omega_0/J = 2.40$ and (d) $\omega_0/J = 2.50$. Normalized average triplon occupations in off-resonance $\omega \neq \omega_0$ to the average phonon occupation in resonance $\omega = \omega_0$ in the NESS as a function of the driving frequency ω/J are represented in (e)-(h), respectively.

peak can be observed at $\omega = \omega_0$ independent of the phonon frequency. With the increasing SPC in Fig. 5.18(a)-(d), induced by the incorporation of more and more of the level repulsion and the self-blocking effect, the single peak converts into two peaks inside and outside of the two-triplon band. This is the analogous effect like in $\bar{n}_{\text{ph}0}$ and \bar{n}_{x0} and in all of them, the position of peaks is identical. This graph shows that the values of $P_0^{L,P}$ decrease with SPC on average. It stands to reason that this is related to the presence of the SPC part which absorbs most of the input energy at band edges through the small phonon momentum or displacement as the origins of dynamical responses. However, integrating over the power curve, expects that suppressing and shifting the peaks with g at the different phonon frequencies do not significantly affect the area under the curve, as expected from the energy conservation. Removing the self-blocking effect leads to the same behaviors as for n_{x0} , represented in Figs. 5.18(e)-(h), for which the level repulsion effect acts as the main origin of the remaining peaks.

5.5 Chapter summary

In this chapter, we have particularly focused on the strong coupling effects between the lattice dynamics and magnetic correlations, the so-called strong SPC regime, to explore novel insights by examination of the physical observables in the NESS that make up the contribution to the nonequilibrium physics. For a systematic

analysis, we have considered the standard parameter space of the model including a sufficient magnitude of dissipation in both spin and lattice sectors.

Notably, we observed the strong self-blocking effect along with the low phonon occupation, the phonon and spin-band frequency shifts, and the magnetic-phononic hybrid states (proposing new quasiparticles called phonon-bitriplons), which are the result of the mediation of the exchange integral caused mainly by the lattice vibrations. In other words, we have dealt with a quantum magnetophononic effect in which the spin sector is modulated through the lattice excitations and a new set of hybrid states is formed at strong SPCs. The observations made on the strong SPC effect can be supported by possible materials CuGeO_3 and $(\text{VO})_2\text{P}_2\text{O}_7$ compounds with strong SPCs.

6. Coupling based on J' -model

In the chapters 4 and 5 we saw that a dimerized spin chain in contact with a laser-driven phonon and a phononic bath experiences novel physical insights in the presence of both weak and strong SPCs. In both regimes, the phonon was coupled to the leading magnetic interaction in the spin chain, however, the dynamical properties in such systems can also be tuned with a different structured SPC Hamiltonian. In this part of the thesis, we aim to develop another picture of the problem on the level of the SPC Hamiltonian by introducing the J' -model, beyond the coupling of laser-driven phonon to the J exchange interaction (J -model) presented in Eq. (3.4). This procedure will enable us to show how the next-nearest-neighbor encodes the dynamical properties and magnetophonics associated with the dimerization of the spin chains.

A short part of this chapter is based on submitted results in Ref. [170]. In Sec. 6.1 we derive the EoMs in the J' -model. Thereafter, we will turn to the energy flows from these EoMs. The numerical results for both quantitative and qualitative comparisons between the models will be presented in Sec. 6.2. Finally, we conclude with a discussion in Sec. 6.3.

6.1 J' -model

In this model, the spin Hamiltonian, the phonon Hamiltonian, the laser-phonon coupling Hamiltonian, and the dissipation effects (as an assumption we consider the same phonon damping of J' -model as the J -model, i.e. we assume that $\gamma'_{\text{ph}} = \gamma_{\text{ph}}$) are kept unchanged and the only change comes from the SPC part. Thus, we stick to the coupling of the phonon and next-nearest-neighbor magnetic

exchange coupling J' in the spin system with strength g' [see Fig. 6.1] as

$$\mathcal{H}_{\text{sp}}^{J'} = \sum_{i=1}^N g' (b_i + b_i^\dagger) \left(\vec{S}_{2,i} \cdot \vec{S}_{1,i+1} - \langle \vec{S}_{2,i} \cdot \vec{S}_{1,i+1} \rangle_{\text{eq}} \right), \quad (6.1)$$

in which $\langle \vec{S}_{2,i} \cdot \vec{S}_{1,i+1} \rangle_{\text{eq}}$ is again the equilibrium value to set the vacuum state as the ground state of both lattice and spin systems, and $(b_i + b_i^\dagger)$ is that of the phonon displacement. From Eq. (A.9), we have

$$\sum_{i=1}^N \vec{S}_{2,i} \cdot \vec{S}_{1,i+1} = -\frac{1}{4} \sum_{k,\alpha} \cos(k) \left(2t_{k,\alpha}^\dagger t_{k,\alpha} + t_{k,\alpha} t_{-k,\alpha} + t_{k,\alpha}^\dagger t_{-k,\alpha}^\dagger + 3 \right). \quad (6.2)$$

Plugging Eq. (6.2) into Eq. (6.1) and applying the mean-field approximation, we obtain

$$\mathcal{H}_{\text{sp,s}}^{J'} = -\frac{g'}{4} \langle d \rangle \sum_{k,\alpha} \cos(k) \left(2t_{k,\alpha}^\dagger t_{k,\alpha} + t_{k,\alpha} t_{-k,\alpha} + t_{k,\alpha}^\dagger t_{-k,\alpha}^\dagger - 2n(\omega_k) \right), \quad (6.3)$$

where $n(\omega_k) = \langle t_{k,\alpha}^\dagger t_{k,\alpha} \rangle_{\text{eq}}$. Employing the Bogoliubov transform with the help of Eqs. (B.1), (B.3) and (B.4) as well as Eqs. (B.6e) and (3.12), we calculate [the equilibrium value is neglected henceforth since it is not important in the commutators later]

$$\begin{aligned} \mathcal{H}_{\text{sp,s}}^{J'} &= -\frac{g'}{4} \langle d \rangle \sum_{k,\alpha} \cos(k) \left(2\tilde{t}_{k,\alpha}^\dagger \tilde{t}_{k,\alpha} + \tilde{t}_{k,\alpha} \tilde{t}_{-k,\alpha} + \tilde{t}_{k,\alpha}^\dagger \tilde{t}_{-k,\alpha}^\dagger \right) \\ &\quad \underbrace{\left(\cosh(2\theta_k) + \sinh(2\theta_k) \right)}_{e^{2\theta_k} = 1/\sqrt{1 - \frac{J'}{J} \cos(k)}} + \underbrace{2 \sinh^2(\theta_k) + \sinh(2\theta_k)}_{\text{constant}} \\ &= -\frac{g'}{4} \langle d \rangle \sum_{k,\alpha} \underbrace{\frac{\cos(k)}{\sqrt{1 - \frac{J'}{J} \cos(k)}}}_{2Jy'_k/J'} \left(2\tilde{t}_{k,\alpha}^\dagger \tilde{t}_{k,\alpha} + \tilde{t}_{k,\alpha} \tilde{t}_{-k,\alpha} + \tilde{t}_{k,\alpha}^\dagger \tilde{t}_{-k,\alpha}^\dagger \right) + \text{constant} \\ &= -\frac{g'J}{2J'} \langle d \rangle \sum_{k,\alpha} y'_k \left(2\tilde{t}_{k,\alpha}^\dagger \tilde{t}_{k,\alpha} + \tilde{t}_{k,\alpha} \tilde{t}_{-k,\alpha} + \tilde{t}_{k,\alpha}^\dagger \tilde{t}_{-k,\alpha}^\dagger \right) + \text{constant}. \end{aligned} \quad (6.4)$$

While the above formulation works for an arbitrary value of g' , it is necessary to point out that g' should always be smaller than g since the interdimer coupling J' is always smaller than the intradimer (leading) coupling J . From this point, the maximum value we can adopt it for g' would be again 50% of the interdimer coupling, i.e. $g'_{\text{max}} = 0.5J'$ or $g'_{\text{max}} = 0.25J$.

6.1.1 Equations of motion

Following the useful commutators in Eq. (C.7) and the spin observables $u_q(t) = \langle \sum_\alpha \tilde{t}_{q,\alpha}^\dagger \tilde{t}_{q,\alpha} \rangle(t)$ and $z_q(t) = \langle \sum_\alpha \tilde{t}_{q,\alpha}^\dagger \tilde{t}_{-q,\alpha}^\dagger \rangle(t)$, we find

$$[\mathcal{H}_s, u_q(t)] = 0, \quad (6.5a)$$

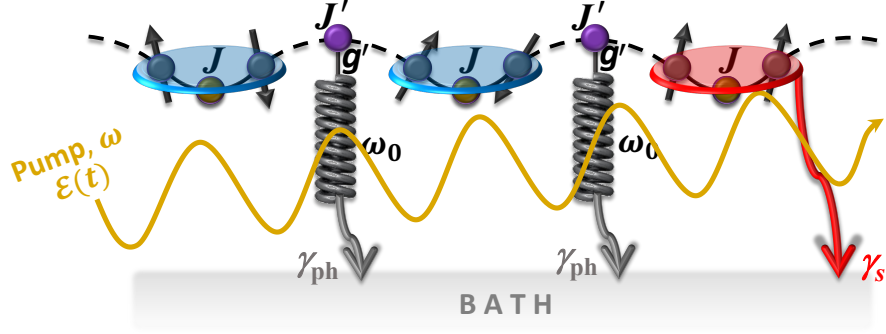


Figure 6.1: Schematic of a driven-dissipative quantum magnet based on the J' -model under study consisting of the spin system, driven Einstein phonon, laser field, and the bath. The spin-spin coupling, interdimer coupling, the SPC, phonon damping, and spin damping are described respectively by $J = 10$ meV, $J'/J = 1/2$, g' , γ_{ph} , and γ_s . The laser continuously pumps energy into the system and then drives it out of equilibrium. Blue ellipses display dimer singlets, while the red one shows a triplon excitation, which is the excitation considered in the present thesis.

$$[\mathcal{H}_{\text{sp,s}}^{J'}, u_q(t)] = 2i \frac{g'J}{J'} q(t) y'_k w_k(t), \quad (6.5b)$$

$$[\mathcal{H}_s, z_q(t)] = 2\omega_k z_k(t), \quad (6.5c)$$

$$[\mathcal{H}_{\text{sp,s}}^{J'}, z_q(t)] = -2 \frac{g'J}{J'} q(t) y'_k \left(z_k(t) + u_k(t) + \frac{3}{2} \right), \quad (6.5d)$$

resulting in the following EoMs for the triplon system when the laser-driven phonon is coupled to the J' bond

$$\frac{d}{dt} u_k(t) = -2 \frac{g'J}{J'} q(t) y'_k w_k(t) - \gamma_s u_k(t), \quad (6.6a)$$

$$\frac{d}{dt} z_k(t) = 2i\omega_k z_k(t) - 2i \frac{g'J}{J'} q(t) y'_k \left(z_k(t) + u_k(t) + \frac{3}{2} \right) - \gamma_s z_k(t). \quad (6.6b)$$

From the definition of the complex quantity $z_k(t) = v_k(t) + iw_k(t)$, we ultimately obtain the following EoMs for the magnetic part of the system

$$\frac{d}{dt} u_k(t) = -2 \frac{g'J}{J'} q(t) y'_k w_k(t) - \gamma_s u_k(t), \quad (6.7a)$$

$$\frac{d}{dt} v_k(t) = -2 \left[\omega_k - \frac{g'J}{J'} q(t) y'_k \right] w_k(t) - \gamma_s v_k(t), \quad (6.7b)$$

$$\frac{d}{dt} w_k(t) = 2 \left[\omega_k - \frac{g'J}{J'} q(t) y'_k \right] v_k(t) - 2 \frac{g'J}{J'} q(t) y'_k \left[u_k(t) + \frac{3}{2} \right] - \gamma_s w_k(t). \quad (6.7c)$$

Accordingly, we calculate the EoMs for the phonon system with the new form of SPC Hamiltonian. Most of commutator relations presented in Appendix C remain unchanged. However, we need to recalculate

$$[\mathcal{H}_{\text{sp,s}}^{J'}, p(t)] = -i \frac{g'J}{2J'N} \underbrace{\langle [b_0^\dagger + b_0, b_0^\dagger - b_0] \rangle}_2 \sum_k y'_k [2u_k(t) + \underbrace{z_k(t) + z_k^*(t)}_{2\text{Re}z_k(t)}]$$

$$= -2i \frac{g'J}{J'} [\mathbb{U}(t) + \mathcal{V}(t)], \quad (6.8a)$$

$$[\mathcal{H}_{\text{sp,s}}^{J'}, n_{\text{ph}}(t)] = -i \frac{g'J}{J'} p(t) [\mathbb{U}(t) + \mathcal{V}(t)], \quad (6.8b)$$

where this time we have $\mathbb{U}(t) = \frac{1}{N} \sum_k y'_k u_k(t)$ instead of Eq. (3.25a) at zero temperature, $n(\omega_k) = 0$. Thus, we end up with the following EoMs for the lattice part of the coupled system

$$\frac{d}{dt} q(t) = \omega_0 p(t) - \frac{\gamma_{\text{ph}}}{2} q(t), \quad (6.9a)$$

$$\frac{d}{dt} p(t) = -\omega_0 q(t) - 2 \left[\mathcal{E}(t) - \frac{g'J}{J'} (\mathbb{U}(t) + \mathcal{V}(t)) \right] - \frac{\gamma_{\text{ph}}}{2} p(t), \quad (6.9b)$$

$$\frac{d}{dt} n_{\text{ph}}(t) = - \left[\mathcal{E}(t) - \frac{g'J}{J'} (\mathbb{U}(t) + \mathcal{V}(t)) \right] p(t) - \gamma_{\text{ph}} n_{\text{ph}}(t). \quad (6.9c)$$

6.1.2 Energy flow

In chapter 4, Sec. 4.3, we started a discussion on the energy flows in all stages of the driven-dissipative spin-phonon system for the J -model (i.e. when the phonon was coupled to the J bond). We introduced the uptake of laser energy by the driven phonon, $P^{\text{L,P}}$, the energy going into the SPC part, $P^{\text{P,SP}}$, the energy going into the bath $P^{\text{P,B}}$, the energy flow from SPC into the spin system, $P^{\text{SP,S}}$, the energy flow from SPC into the bath, $P^{\text{SP,B}}$, the induced energy to the spin system flowing into the bath, $P^{\text{S,B}}$, and finally the energy flow entering the heat sink after removing from the entire system, $P^{\text{B,H}}$ [see Fig. 4.14]. Now, we calculate the same quantities for the J' -model. Note that the sum rules still hold valid. For the laser-phonon-bath part, we have

$$P^{\text{L,P}}(t) = -\mathcal{E}(t) \omega_0 p(t), \quad (6.10a)$$

$$P^{\text{P,B}}(t) = \gamma_{\text{ph}} \omega_0 n_{\text{ph}}(t), \quad (6.10b)$$

$$P^{\text{P,SP}'}(t) = -\frac{g'J}{J'} \omega_0 [\mathbb{U}(t) + \mathcal{V}(t)] p(t). \quad (6.10c)$$

For the SPC part, we obtain

$$P^{\text{SP,S}'}(t) = -\frac{2g'J}{J'N} q(t) \sum_k y'_k \omega_k w_k(t), \quad (6.11a)$$

$$P^{\text{SP,B}'}(t) = -\frac{g'J}{J'} q(t) \left(\frac{\gamma_{\text{ph}}}{2} + \gamma_{\text{s}} \right) [\mathbb{U}(t) + \mathcal{V}(t)]. \quad (6.11b)$$

And for the energy flow from the spin system into the bath, we still have the same relation

$$P^{\text{S,B}}(t) = \frac{\gamma_{\text{s}}}{N} \sum_k \omega_k u_k(t). \quad (6.12)$$

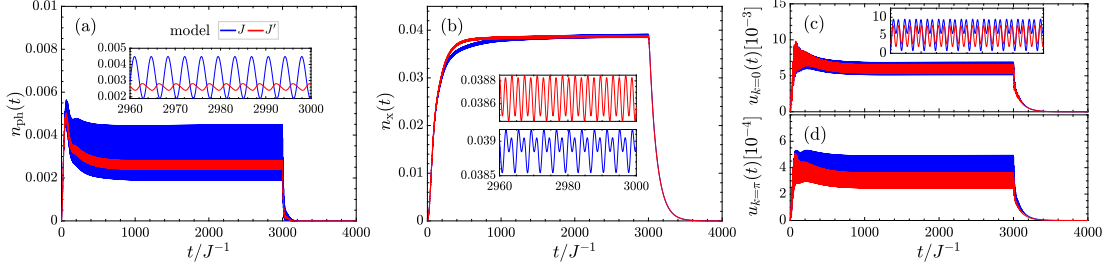


Figure 6.2: A comparison between the J and J' models through temporal behaviors of (a) phonon occupation, (b) triplon occupation, (c) $k = 0$ component, and (d) $k = \pi$ component of the triplon occupation at fixed $N = 2000$, $\omega_0/J = 1.7$, $\gamma_{\text{ph}} = 0.02\omega_0$, $a/\gamma_{\text{ph}} = 0.2$, and $\gamma_s/J = 0.01$. In the case of J -model, we fix $g/J = 0.5$, while $g'/J = 0.25$ is fixed for the J' -model. The driving field is turned off at $t/J^{-1} = 3000$ to approach the NESS to its equilibrium state.

6.2 Numerical comparisons between the J - and J' -model

Ultimately, we are going to obtain dynamics valid for system-bath coupling within the J' -model via the same set of parameters as the J -model required for achieving a coherent NESS. We mainly focus on the occupations in both sectors here. Moreover, we are interested in the strong regime (large SPCs) of resonant coupling between the driven phonon and triplons (phonon in the two-triplon band) for strong triplon excitations. However, we show the main previously findings in a compact form here to avoid repetition.

We start the numerical results of this chapter with a brief comparison between the two models originating from the spin-phonon configuration. The important difference of EoMs in the J' -model compared with the J -model is based on different terms found in the matrix elements. This implies that if we compare Eq. (3.26) with Eq. (6.7), we have the changes of $\{g \rightarrow g'J/J', y_k \rightarrow y'_k\}$ and a negative sign behind y'_k in EoMs within the J' -model. We again are able to address the comparisons at resonant $\omega = \omega_0$ and off-resonant $\omega \neq \omega_0$ conditions.

6.2.1 Resonant $\omega = \omega_0$

Note that we are sure of the coherent NESS in both models since the above changes do not affect the coherency of steady states far from equilibrium. As mentioned before, $g \rightarrow g'J/J'$ and $y_k \rightarrow y'_k$ and a negative sign behind y'_k in the EoMs are the main differences between the J and J' models. This allows us to see if the relation $y'_k < y_k$ setting $g'J/J' = g$, because y_k is almost 4-5 times larger than y'_k , can lead to the close responses in both J and J' models. To confirm this, we plot Fig. 6.2 for (a) phonon occupation and (b) triplon occupation of both models at fixed $\omega_0/J = 1.7$, $\gamma_{\text{ph}} = 0.02\omega_0$, $a/\gamma_{\text{ph}} = 0.2$, $g/J = 0.5$, and $g'/J = 0.25$. Because of $g = g'J/J'$ in the J and J' models, all responses in the coupled spin-lattice system are expected to be close to each other. We have chosen the above phonon frequency to be between the lower band edge and the

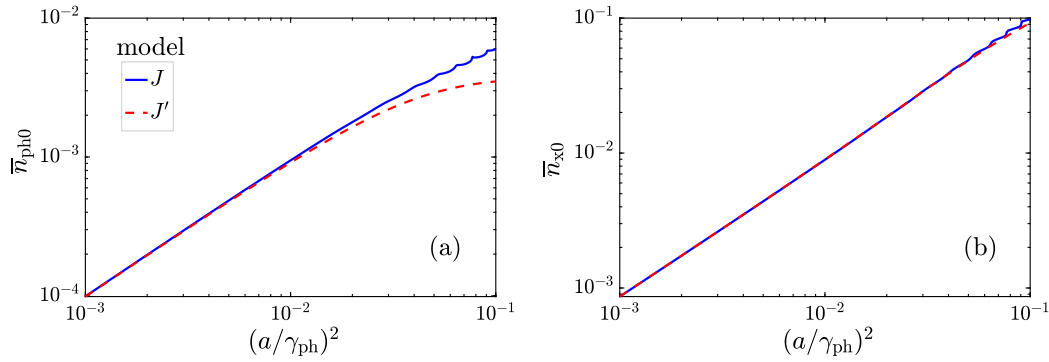


Figure 6.3: A comparison between the J and J' models through time-average behaviors of (a) phonon occupation and (b) triplon occupation at fixed $N = 2000$, $\omega_0/J = 1.7$, $\gamma_{\text{ph}} = 0.02\omega_0$, $a/\gamma_{\text{ph}} = 0.2$, and $\gamma_s/J = 0.01$. In the case of SPC, we again fix $g/J = 0.5$ and $g'/J = 0.25$ for the J and J' models, respectively.

band center because of their specific responses (we could choose another phonon between the band center and the upper band edge, but the symmetry between the band edges does not make a big discrepancy between the interpretations). We also turn off the laser field at $t/J^{-1} = 3000$ to drive back the system to its initial equilibrium state. The decaying timescales are similar in both models since the dissipation effect is not affected by the model. Another point refers to the oscillations in the NESS. In both models, we observe almost the same oscillations in the inset panels of Fig. 6.2(a), however, there is a slight shift in the NESS oscillations in the case of J' -model due to a different matrix element. We also show Figs. 6.2(c) and 6.2(d) to once more confirm that different matrix elements manifest themselves first in the k -components and then directly in the phonon occupation. Furthermore, it is notable to mention that strong suppression of responses relates to the strong SPC strengths $g/J = 0.5$ and $g'/J = 0.25$.

We refrain from discussing more details of temporal plots here, while a general statement of NESS features will be given in the following.

Impact of driving

Solutions for the driving, a/γ_{ph} , effect can also be found in the J' -model for strong spin-lattice coupling and a moderate phonon frequency. Let us again fix $N = 2000$, $\omega_0/J = 1.7$, $\gamma_{\text{ph}} = 0.02\omega_0$, $a/\gamma_{\text{ph}} = 0.2$, and $\gamma_s/J = 0.01$. We also fix $g/J = 0.5$ and $g'/J = 0.25$ for the J and J' models, respectively. Here, the existence of strong a/γ_{ph} leads to different NESS averages and gives more involved nonlinearity with respect to Fermi's golden rule which expects a linear expression for the responses versus $(a/\gamma_{\text{ph}})^2$. In particular, one finds a dependence on higher orders of $(a/\gamma_{\text{ph}})^2$ in both models, which indicate that for large drivings, the Fermi's golden rule is broken down. The NESS values also become qualitatively incorrect above this threshold, referred to as nonlinear effects, which mostly are unphysical due to the lattice melting issue. So, this again confirms that the fixed

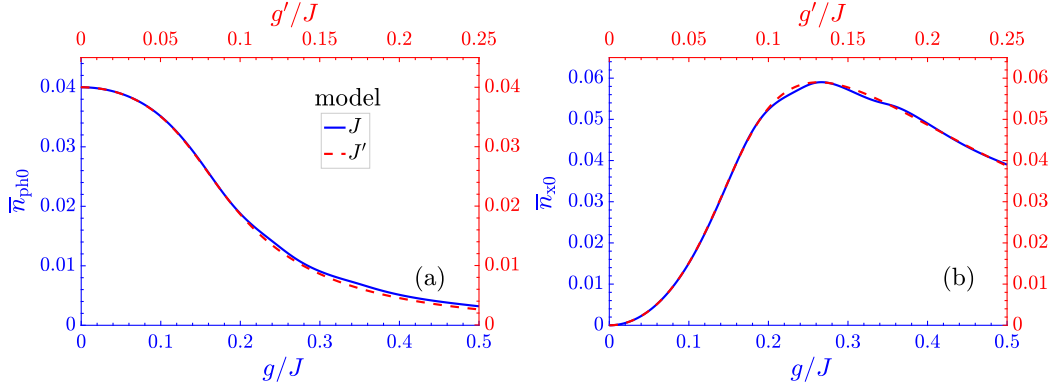


Figure 6.4: A comparison between the J and J' models through the time-average behaviors of (a) phonon occupation and (b) triplon occupation at fixed $N = 2000$, $\omega_0/J = 1.7$, $\gamma_{\text{ph}} = 0.02\omega_0$, $a/\gamma_{\text{ph}} = 0.2$, and $\gamma_s/J = 0.01$. The relation $y'_k < y_k$ and the difference factor J/J' in the SPCs in the models makes the observed discrepancies and one expects the same trends shown at $g'J/J' = g$.

$a/\gamma_{\text{ph}} = 0.2$ was a proper choice in most parts of this thesis since close responses in J and J' models to the same contribution of y'_k after setting $g'J/J' = g$, also mostly belong to the regime of weak driving.

Impact of SPC

Next, we are going to compare the J and J' models for weak-to-strong SPC regime in Fig. 6.4 with the same set of parameters as Fig. 6.3. As investigated in Fig. 6.2, one expects to observe close trends both qualitatively and quantitatively if we set $g'J/J' = g$. Of course, for other couplings, different treatments emerge. The dynamics of the spin-lattice model is determined by the influence of g/J and g'/J in J and J' models, respectively, which encodes the effect of different couplings on the behavior of the coupled damped system. For a driven spin chain, the phonon occupation is strongly suppressed in both models similarly as discussed before. As for the spin system, the strongest response also appears at weaker $g'/J \simeq 0.13$ in the J' -model compared to $g/J \simeq 0.26$ in the J -model with a difference factor $J/J' = 2$. However, not-perfect match of data of models in the strong SPCs is due to different matrix elements when the phonon ($\omega = \omega_0 = 1.7J$) resides on the two-triplon band. Also, it is evident that the phonon occupation is strongly suppressed at large SPCs, $g/J = 0.5$ and $g'/J = 0.25$, originating from the resonant self-blocking effect.

Impact of driving frequency

By expanding frequencies over a wide range from adiabatic to in band and to antiadiabatic, the response of the systems are given by Fig. 6.5 setting the same parameters: $N = 2000$, $\gamma_{\text{ph}} = 0.02\omega_0$, $a/\gamma_{\text{ph}} = 0.2$, and $\gamma_s/J = 0.01$. Also, $g/J = 0.5$ and $g'/J = 0.25$ for the J and J' models, respectively. First, we are again faced with the similar behaviors of J and J' models over all driving

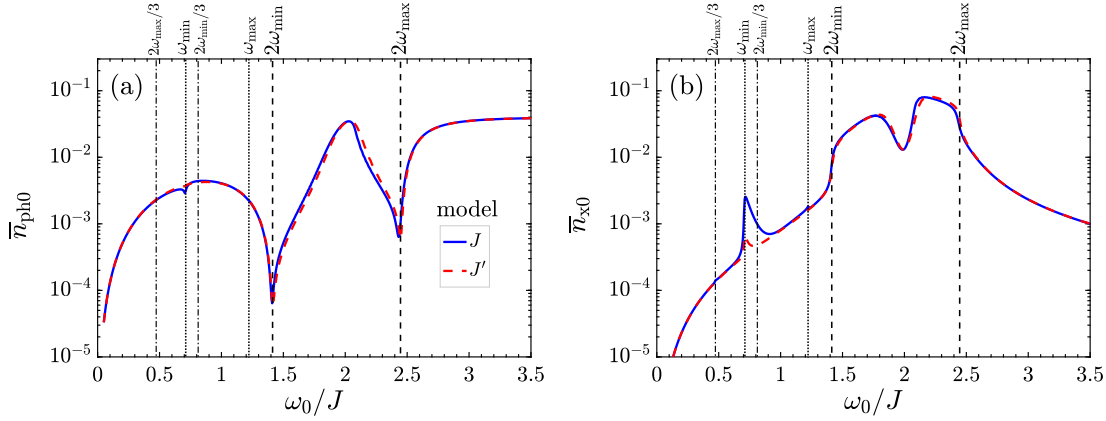


Figure 6.5: A comparison between the J and J' models through time-average behaviors of (a) phonon occupation and (b) triplon occupation as a function of driving phonon frequency at fixed $N = 2000$, $\gamma_{\text{ph}} = 0.02\omega_0$, $a/\gamma_{\text{ph}} = 0.2$, and $\gamma_{\text{s}}/J = 0.01$. In the case of J (J') model, we have fixed $g/J = 0.5$ ($g'/J = 0.25$).

frequencies and our previously conclusion between these two models was not limited to only a single phonon frequency. And, in both phonon and spin responses, again, the total action in J' -model can be well understood from the difference factor J/J' . Second, we again stress that the spin system itself merely produces a force to move the driven phonon which appears as strong as possible at below the band and at the band edges asymmetrically. Also, the expression $\bar{n}_{x0}/\bar{n}_{\text{ph}0}$ directly justifies the self-blocking effect at band edges in both models [very strong peaks restored at band edges appear] because by this we avoid the response spreading over a wider range of in-band frequencies, however, we do not show it here. The resonant self-blocking at band edges is clearly understandable from the previous chapters, however, we note that the two-phonon process is still present at low-frequency regime in J and J' models which the mean-field approximation helps to understand the off-resonant self-blocking far from the band edges. Third, here, we have a tiny discrepancy in the responses of J' -model at $\omega = \omega_0 = \omega_{\text{min}}$ and in the two-triplon band due to the difference in the matrix elements $\{y_k, y'_k\}$.

We comment on the difference factor J/J' in the SPCs of the models where the same responses hold. This argument is valid for all J/J' strengths, not only $J/J' = 2$, which means that the perturbation theory behind the master equation treatments is valid. Also, it means that the above argument is independent of the geometrical frustration [174]. In particular, we have a coupling g/J larger than the normal g'/J which makes the responses virtually different. To generalize this claim, we use the broad range of phonons below, in, and above the two-triplon band for two other $\lambda = J'/J = 0.3$ and 0.7 to be different than the selected $J'/J = 0.5$. We again set $g'J/J' = g$ in Fig. 6.6. Simply, we confirm that the subdominant role of y'_k in the matrix elements makes it an auxiliary factor for proving this claim, as well as, the results for different models we discussed above fall into this factor J/J' . In the same vein, we also intend to adopt an argument by describing the band

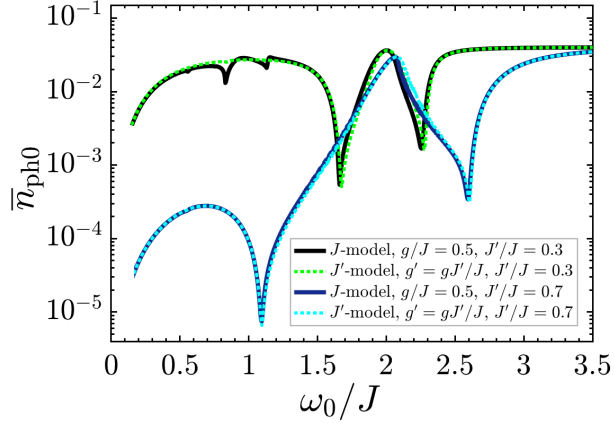


Figure 6.6: Illustration of the comparison between the J and J' models over a wide range of phonon frequencies at fixed $N = 2000$, $\gamma_{\text{ph}} = 0.02\omega_0$, $a/\gamma_{\text{ph}} = 0.2$, and $\gamma_{\text{s}}/J = 0.01$.

dispersion which becomes narrower and broader, respectively, for $\lambda = J'/J = 0.3$ and 0.7 . However, the case of $\lambda = J'/J = 0.7$ poses additional challenges since the upper edge of the one-triplon band lies inside the two one-triplon-band and multiphonon processes become complicated. But, we will not tackle this challenge in the present thesis.

Energy flow

We utilize the same driving-damping protocol as shown in Fig. 4.14. The effect of bath damping prior to energy transfer into the SPC and spin parts is then the main aim of comparison between the two models. In order to find an explicit comparison, we consider the same fixed parameters for J' -model as the J -model in the presence of strong SPCs, i.e. $\gamma_{\text{ph}} = 0.02\omega_0$, $a/\gamma_{\text{ph}} = 0.2$, $\gamma_{\text{s}}/J = 0.01$, and $g'/J = 0.25$. It is now a straightforward matter to report the close responses of J and J' models in order to avoid repetition. Despite the fact that the sum rules between the energy flows hold true in all parts of the system, we state that most of the uptake energy from the laser by the phonon at strong SPCs should still be delivered to the bath in the J' -model which was also the case for the J -model, when the phonon is inside the two-triplon band, i.e. when the strongest excitation takes place. On the other hand, like before, the mean-field decoupling approximation can be justified by the small values of $\bar{P}_0^{\text{SP},\text{B}^{J'}}$ in the band. Therefore, the effect of coupling to J' bond is not adding new information about the energy flow than the J bond.

6.2.2 Off-resonant $\omega \neq \omega_0$

As outlined in previous chapters, the EoMs allow us to obtain the dynamics for a wide range of parameters. In the same chapter, we presented numerical results for the specific case of resonant conditions between the laser field and the driving phonon. In the following, we evaluate the results for the case of off-resonant

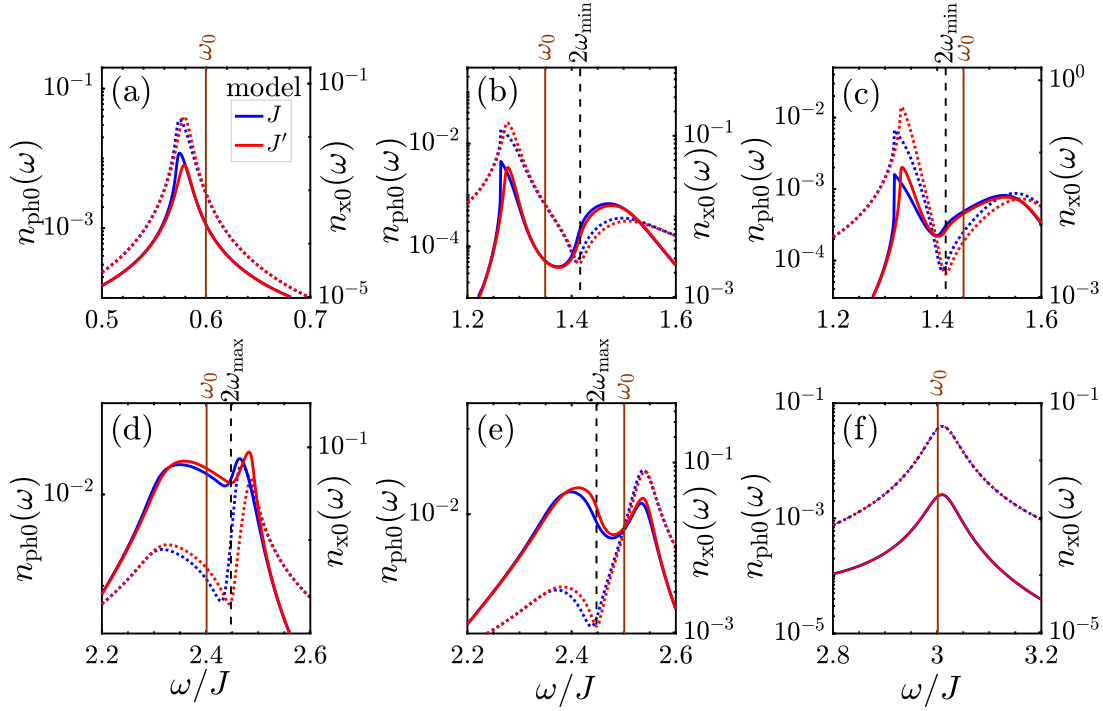


Figure 6.7: A comparison between (left y -axis, dotted lines) phonon and (right y -axis, solid lines) triplon occupation of the J and J' models as a function of driving laser frequency in off-resonant condition $\omega \neq \omega_0$ at fixed $\gamma_{\text{ph}} = 0.02\omega_0$, $a/\gamma_{\text{ph}} = 0.2$, $g/J = 0.5$ (J -model), $g'/J = 0.25$ (J' -model) for (a) $\omega_0/J = 0.6$, (b) 1.35, (c) 1.45, (d) 2.40, (e) 2.50, and (f) 3.0.

$\omega \neq \omega_0$ and only include the strong SPCs in the models. Comparison with the J -model then allows us to make statements about the impact of a driven spin chain for the coupling strength J' .

We again look at the dynamics for the phonon and triplon occupations. In this part of the thesis we use the forms of two-sided plots in Fig. 6.7; dotted (solid) lines refer to the phonon (triplon) occupation. The same SPC strengths in the J - and J' -model makes them equivalent, as confirmed before in various ways. However, the role of matrix elements y_k and y'_k comes into play in determining different peak positions for the responses in the J - and J' -model when scanning the driving frequency out-of-resonance with the phonon driving frequency. Nevertheless, we have included many phonons outside and inside the two-triplon band to only check the shift rate of strong responses characterized by the peaks in the occupations. At first glance, one can observe that hybrid states introduced before in Sec. 5.3 with phononic and magnetic responses take place at a bit different phonon frequencies in J' -model, independent of phonon frequency. This is a direct consequence of matrix element effect in the models. Similar to the J -model, only the phonons far from the band show a weakly hybridized phononic mode. A general relationship between the SPCs and the models can also be derived on the basis of the peak positions as Fig. 5.15, where we expect a

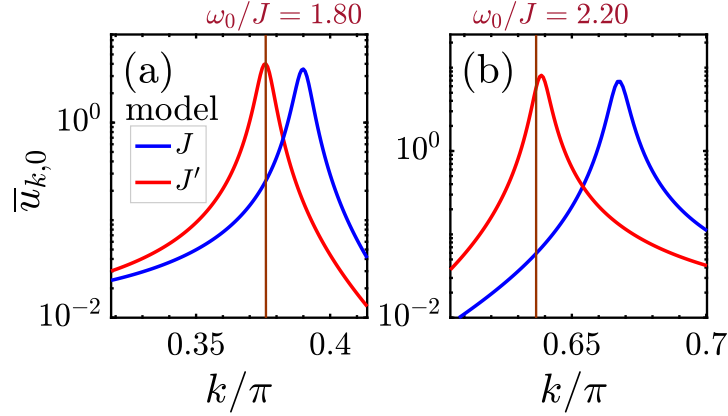


Figure 6.8: A comparison between the J and J' models through time-average behaviors of k -components of the spin system at (a) $\omega = \omega_0 = 1.8$ and (b) $\omega = \omega_0 = 2.20$ at fixed $N = 3000$, $\gamma_{\text{ph}} = 0.02\omega_0$, $a/\gamma_{\text{ph}} = 0.2$, and $\gamma_{\text{s}}/J = 0.01$. In the case of J (J') model, we fix $g/J = 0.5$ ($g'/J = 0.25$).

quadratically shifts with respect to g/J or g'/J . However, Fig. 6.7 is based on the simplest aim, that is, shift contribution of models and it is unnecessary to look at the hybrid frequencies here.

Let us give the third quantity behavior for completeness, i.e. $\bar{u}_{k,0}$ versus k/π at strong SPCs in Fig. 6.8. We are free to choose the phonon frequency. This time, we stick to two cases around the band center, $\omega = \omega_0 = 1.80$ and $\omega = \omega_0 = 2.20$ in resonance. The parameters of the results are $N = 3000$, $\gamma_{\text{ph}} = 0.02\omega_0$, $a/\gamma_{\text{ph}} = 0.2$, $\gamma_{\text{s}}/J = 0.01$. In the case of J (J') model, we fix $g/J = 0.5$ ($g'/J = 0.25$). Therein, the peak positions are renormalized modes k_{max} and depend on the SPC and phonon frequency trivially. These modes ensure that the triplon dispersion has the right shifts. We observe the insignificant of the SPC-induced triplon mode shift in the J' -model: Specifically, we can see that the peak is nearly unchanged by the strong SPC. This means that in the red curve at both arbitrary phonon frequencies, they directly relate the strong SPC effect to the weak shift of responses compared to the J -model and include the weaker responses. Confronted with such a weak response in the J' -model even though $g'/J/J' = g$ is set, we would immediately declare this to be the direct result of small matrix element y'_k , which directly manifest itself in the triplon modes.

Before summarizing, we would briefly mention that the results of the energy flow in the J' -model when the laser is in off-resonance with the phonon frequency can be analyzed within the same manner as Fig. 6.7 and there is no significant impact of matrix elements or the difference factor J/J' rather than those provided before. We, therefore, avoid repetition.

6.3 Chapter summary

In this part of the thesis, first, we have successfully rederived the EoMs when coupling the spins to the driven phonons in terms of next-nearest-neighbor magnetic interaction, so-called the J' -model. Then, we have proceeded to compare them with the J -model (valid for coupling the spins to the driven phonons in terms of leading magnetic interaction) presented in chapters 4 and 5. The dynamics determined by the J' -model shows the same self-blocking behavior with a standard SPC strength, which emerges from the same matrix element in the theory. However, our analyses from the triplon mode dependency of responses found that strong SPCs in the J' -model weaken the shift of resonant modes compared to the J -model, that is, the magnetophononic features are weak in the J' -model.

7. Spin-band renormalization

The by now presented results in the previous chapters provide a quite profound understanding of how an open quantum magnetic system brings into a NESS in the long run in the presence of both weak and strong coupling regimes. It furthermore asserts, the eventually reached NESS can generically lead to amazing giant self-blocking effect and correspondingly to modulation of hybrid states. However, much less attention is paid to the driving protocol about the band-engineering on which the probe of the system out of equilibrium takes place, and even scarcer are general principles or predictions describing the competition between the pump and probe fields (e.g. the self-hybrid effect or static effects) of the strong coupling regime. So, the modulation of magnetic interactions through the laser-driven phonons formalizes the goals in this chapter. The principal question we aim to attack is then: Provided that we know the dynamics of the spin-lattice system in a given setup, can we obtain the behavior of the triplon dispersion under similar circumstances? This problem of characterizing the new triplon dispersion poses modulated magnetic interactions. We make an artificial language for the presence of driving fields. From the probe driving point of view, we analyze the static and dynamic spin-band shifts in the absence and presence of probe driving, respectively.

In this chapter, we will develop such a prediction for both J and J' models formulated before under the influence of SPC. The main physical results are contained in the ensuing two sections: an analytical prediction of the spin-band renormalization induced by the single pump driving field, static, and the phonon displacement in the strong coupling regime in Sec. 7.1 and then the dynamic spin-band renormalization of the considered models in Sec. 7.2. The language

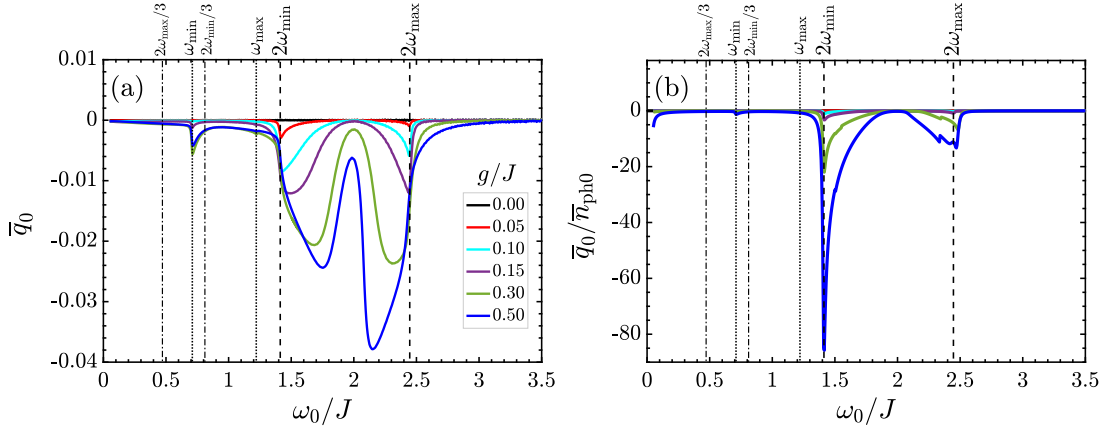


Figure 7.1: (a) Average phonon displacement \bar{q}_0 in the NESS for various SPCs at fixed $N = 2000$, $\gamma_{\text{ph}} = 0.02 \omega_0$, $a/\gamma_{\text{ph}} = 0.2$, and $\gamma_s/J = 0.01$. The \bar{q}_0 normalized to $\bar{n}_{\text{ph}0}$, Fig. 5.6, is shown in (b).

of “static” and “dynamic” stems from the probe point of view. If it is in the effective electric field, we call it a dynamic spin-band renormalization, otherwise it is static. This latter result, in particular, will be illustrated by means of various phonon frequencies. Both sections will be examined by the various driving fields in Sec. 7.3. Finally, in Sec. 7.4, we will end the chapter with a summary. The most results presented in this chapter have not been published yet and parts of them have been included in the submitted results of Ref. [170].

7.1 Static spin-band renormalization

The general setting to be investigated in the following involves the spin and spin-phonon Hamiltonians in Eq. (3.1).

7.1.1 J -model

In the following, to tackle this problem by means of the same Hamiltonians in the J -model, one easily can rewrite them as $\mathcal{H}_s + \mathcal{H}_{\text{sp}} = \sum_{i=1}^N [J + g(b_i + b_i^\dagger)] \vec{S}_{1,i} \cdot \vec{S}_{2,i} + J' \vec{S}_{2,i} \cdot \vec{S}_{1,i+1} - g(b_i + b_i^\dagger) \langle \vec{S}_{1,i} \cdot \vec{S}_{2,i} \rangle_{\text{eq}}$. It is obvious that the magnetic interaction J is modulated to $J + g\bar{q}_0$ in the presence of SPC, where \bar{q}_0 is the average phonon displacement in the NESS. We call it a static phonon displacement since the probe driving field is not turned on yet and it only originates from the pump driving field. In the J -model, J' remains unchanged with SPC. By this, the dimerization of the spin system which is determined by $\lambda = J'/J$ is changed to

$$\tilde{\lambda} = \frac{J'}{J + g\bar{q}_0}. \quad (7.1)$$

Accordingly, a renormalized triplon dispersion,

$$\tilde{\omega}_k = \tilde{J} \sqrt{1 - \frac{J'}{\tilde{J}} \cos(k)}, \quad (7.2)$$

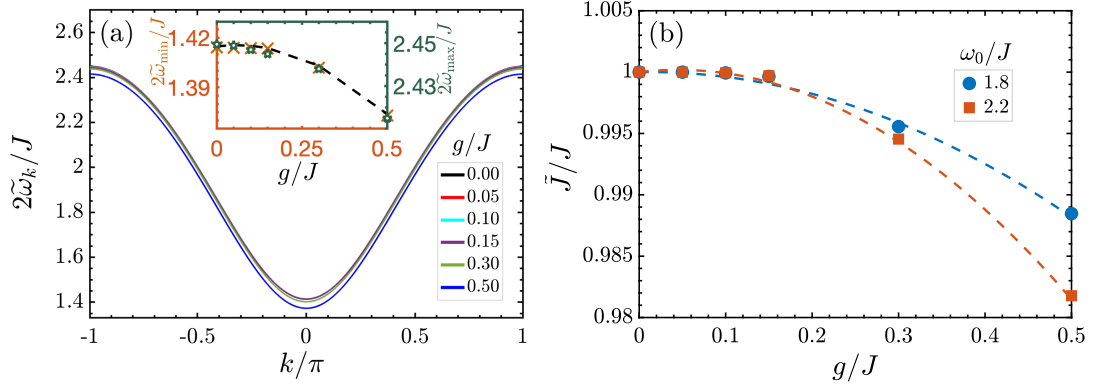


Figure 7.2: (a) SPC-induced spin-band frequency shift, Eq. (7.2), for various SPCs at $\omega = \omega_0 = 2.2J$ at fixed $N = 2000$, $\gamma_{\text{ph}} = 0.02\omega_0$, $a/\gamma_{\text{ph}} = 0.2$, and $\gamma_s/J = 0.01$. Panel (b) shows the change of modulated leading magnetic interaction $\tilde{J} = J + g\bar{q}_0$ with g for two arbitrary frequencies $\omega_0/J = 1.8$ and 2.2 around the band center.

is acquired to describe triplons [see Appendix F for details] where $\tilde{J} = J + g\bar{q}_0$. This equation can be evaluated right away by measuring \bar{q}_0 for whether the frequencies $\omega = \omega_0$ or $\omega \neq \omega_0$. We focus on the former one.

For each phonon frequency, ω_0 , a special \bar{q}_0 is obtained. Thereby, we first plot \bar{q}_0 to address the aspect of spin-band frequency shift. Following this, in Fig. 7.1(a), the value of \bar{q}_0 relative to the SPC-dependent ω_0 is adopted setting the same set of parameters as Figs. 5.6 and 5.7. We remark that the phonon displacement is the origin of the dynamical response of the triplon occupation, which can be understood from Eq. (3.26a). Thus, following \bar{n}_{x0} trends, one expects to see the same behaviors for \bar{q}_0 in the band, too. In Sec. 5.2, we learned that the self-blocking effect can be associated with the physics behind the energy flows such that the laser field forces Einstein phonon to move by inducing the energy power $-\mathcal{E}(t)\omega_0 p(t)$ [see the first term of Eq. (3.24c)]. So, a negative small finite value for the temporal average of phonon displacement (and/or momentum) is needed to make the output energy non-zero and positive. This finite value stems from the coupling to the spin system, which acts as an extra perturbation for the lattice sector and forces the driven phonon to move anyway. Nicely, our results satisfy this expectation. On the other hand, to achieve a quantitative understanding of the self-blocking effect on the properties of the system characterized by \bar{q}_0 , we evaluate the phonon displacement renormalized by the phonon occupation (Fig. 5.6) in Fig. 7.1(b). Like before, the spreading of the displacements in the band is a direct result of the giant resonant self-blocking effect, which is gone as soon as the self-blocking effect is excluded.

Next, we strive to achieve a quantitative understanding of the negative \bar{q}_0 on the cosine spin-band in Fig. 7.2(a), by evaluating the SPC-induced spin-band frequency shift from Eq. (7.2). To do this, we consider the driving frequency

g/J	$\tilde{k}_{\text{res}}/\pi$	k_{max}/π
0.05	0.6379751807	0.6379999997
0.10	0.6380561040	0.6380954907
0.15	0.6384287351	0.6384588730
0.30	0.6465140745	0.6467771828
0.50	0.6671716308	0.6670636617

Table 7.1: A comparison between \tilde{k}_{res} and k_{max} [taken from Fig. 5.16(c)] for various SPCs in the J -model at fixed $N = 3000$, $\omega = \omega_0 = 2.2J$, $\gamma_{\text{ph}} = 0.02\omega_0$, $a/\gamma_{\text{ph}} = 0.2$, and $\gamma_s/J = 0.01$.

$\omega = \omega_0 = 2.2J$ from Fig. 7.1(a) and plug its corresponding \bar{q}_0 into Eq. (7.2). It is already obvious in the plot of \bar{q}_0 that the phonon frequency plays a role in the dispersion of the triplons. The results show that the effects of the weak SPCs may be small compared to the overall triplon dispersion, but are not negligible. Due to the renormalization of triplon dispersion, the dimerization parameter $\Delta\lambda = \tilde{\lambda} - \lambda = -g\lambda\bar{q}_0/[J + g\bar{q}_0]$ becomes larger as it is already established to change with g (see Fig. 7.2(b) for $\tilde{J} = J + g\bar{q}_0$ vs. g). The spin-band shift of the lower and upper band edges with g is the same due to symmetrical matrix elements, as shown in the inset panel of Fig. 7.2(a).

The corresponding wave-vectors of g -dependent peaks in \bar{u}_{k_0} provided by Fig. 5.16 are identical to resonant wave-vectors k_{res} satisfying $\omega_0 = 2\tilde{\omega}_{k_{\text{res}}}$ in Eq. (7.2). So, these shifts are in agreement with the SPC-dependent triplon mode extracted from Eq. (7.2) in which the resonance mode changes with SPC. Despite the different intensities in the presence of SPCs for various driving frequencies, which stems from the phonon displacement, similar elongation patterns can be observed far from the shifted modes. Let us compare \tilde{k}_{res} and k_{max} taken from Fig. 5.16(c) for $\omega_0 = 2\tilde{\omega}_{k_{\text{res}}}$ in Tab. 7.1. These renormalized triplon modes should be in excellent agreement with each other. This, in turn, means that the triplon dispersion provided in Eq. (7.2) is strongly valid for all mode components. Thus, we expect to see that the band-edge responses in all SPCs move toward lower frequencies, i.e. toward the same frequencies provided in Fig. 7.2.

7.1.2 J' -model

Before evaluating the static spin-band renormalization through the mode equality $k_{\text{max}} = \tilde{k}_{\text{res}}$ which determines the effective triplon mode according to $\omega_0 = 2\tilde{\omega}_{k_{\text{res}}}$, we remember the insignificant shift of the SPC-induced triplon mode in the J' -model from the previous results: Specifically, we can see that the peak in Fig. 6.8 is nearly unchanged with the strong SPC. This means that in the red curve at both arbitrary phonon frequencies, they directly relate the strong SPC effect to the weak shift of responses compared to the J -model and include the weaker

responses. This result merely reformulates the conclusions drawn in Sec. 6.2 of this thesis on the SPC-induced spin-band renormalization.

Implementing the new EoMs (6.7) and (6.9), we would derive the renormalized spin-band through the phonon displacement in the J' -model to see how the dimerization is changed. To start with, we again look at the Hamiltonian parts with the new SPC part, Eq. (6.4):

$$\begin{aligned} \mathcal{H}_s = & \underbrace{-\frac{3}{4}JN - \frac{3}{4}J' \sum_k \cos(k)}_{\mathcal{H}_0} + J \sum_{k,\alpha} t_{k,\alpha}^\dagger t_{k,\alpha} \\ & - \frac{1}{4}J' \sum_{k,\alpha} \cos(k) \left(2t_{k,\alpha}^\dagger t_{k,\alpha} + t_{k,\alpha} t_{-k,\alpha} + t_{k,\alpha}^\dagger t_{-k,\alpha}^\dagger \right), \end{aligned} \quad (7.3a)$$

$$\langle \mathcal{H}_p \rangle = \omega_0 \langle b_0^\dagger b_0 \rangle = \frac{N\omega_0}{4} \bar{q}_0^2 = \mathcal{E}_{\text{ph}}, \quad (7.3b)$$

$$\mathcal{H}_{\text{sp,s}}^{J'} = -\frac{g'}{4} \langle d \rangle \sum_{k,\alpha} \cos(k) \left(2t_{k,\alpha}^\dagger t_{k,\alpha} + t_{k,\alpha} t_{-k,\alpha} + t_{k,\alpha}^\dagger t_{-k,\alpha}^\dagger - 2n(\omega_k) \right), \quad (7.3c)$$

and

$$\begin{aligned} \mathcal{H}_{\text{eff}}^{J'} &= \mathcal{H}_s + \langle \mathcal{H}_p \rangle + \mathcal{H}_{\text{sp,s}} \\ &= \sum_{k,\alpha} \mathbb{A}_k t_{k,\alpha}^\dagger t_{k,\alpha} + \frac{1}{2} \mathbb{B}_k \left(t_{k,\alpha} t_{-k,\alpha} + t_{k,\alpha}^\dagger t_{-k,\alpha}^\dagger \right) + \text{constant}, \end{aligned} \quad (7.4)$$

where the constant term refers to the ground state energy, $\mathbb{A} = J - \frac{J'}{2} \cos(k) - \frac{g'}{2} \bar{q}_0^{J'} \cos(k)$ and $\mathbb{B}_k = -\frac{J'}{2} \cos(k) - \frac{g'}{2} \bar{q}_0^{J'} \cos(k)$. Following the same procedure presented in Eq. (F.7), we obtain

$$\tilde{\omega}_k^{J'} = \sqrt{\mathbb{A}_k^2 - \mathbb{B}_k^2} = J \sqrt{1 - \frac{J' + g' \bar{q}_0^{J'}}{J} \cos(k)}. \quad (7.5)$$

Therefore, the next-nearest-neighbor J' is modulated to $J' + g' \bar{q}_0^{J'}$, where $\bar{q}_0^{J'}$ denotes the phonon displacement in the J' -model.

For the present case, the phonon displacement is especially important as we investigate a range of different values for the resonant driving frequency. So, first, we compare the average \bar{q}_0 in both models. Using the same parameters as Fig. 6.8 together with \bar{q}_0 from Fig. 7.1, we obtain the results shown in Fig. 7.3(a) for both models. We obtain a full agreement for the phonon displacement in the J' -model with the behavior of y'_k before and after the band center [see Fig. 3.3(d) where it is positive (negative) below (above) the mode center at $k/\pi = 1/2$]. However, the impact of strong SPC, $g'/J = 0.25$, in the J' -model is comparably small in all driving frequencies. This, in turn, means that there is no considerable effect on the band renormalization in the J' -model, as also confirmed by the way of peak positions in Fig. 6.8. Thus, SPC has a strong effect only on the spin-band in the

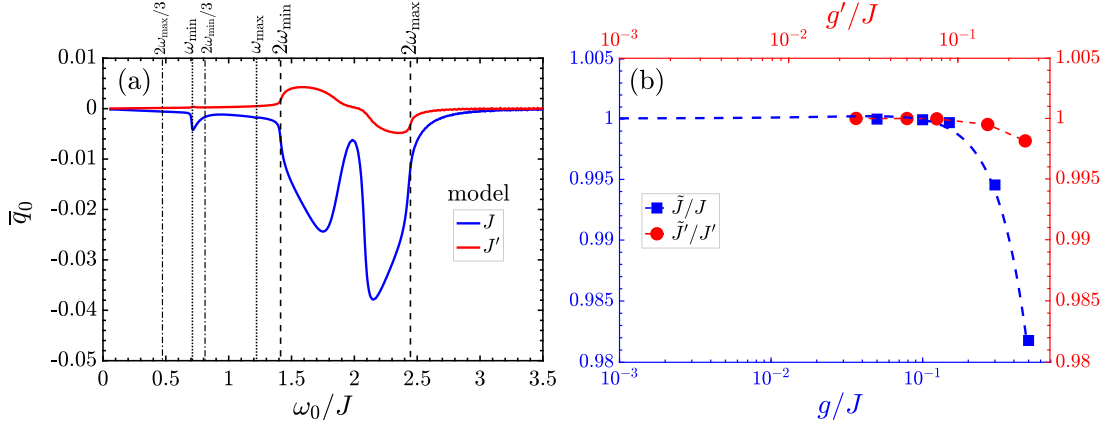


Figure 7.3: (a) A comparison between two models through time-average behaviors of phonon displacement at fixed $N = 2000$, $\gamma_{\text{ph}} = 0.02\omega_0$, $a/\gamma_{\text{ph}} = 0.2$, and $\gamma_{\text{s}}/J = 0.01$. In the case of J (J') model, we have fixed $g/J = 0.5$ ($g'/J = 0.25$). (b) A comparison between J and J' models to indicate the change of modulated leading magnetic interaction $\tilde{J} = J + g\bar{q}_0$ with g as well as modulated next-nearest magnetic interaction $\tilde{J}' = J' + g'\bar{q}'_0$ with g' for phonon frequency $\omega_0/J = 2.2$.

effective J -model. This can also be confirmed by Fig. 7.3(b) in which the shift with SPC becomes so sluggish that any physical SPC cannot strongly change the next-nearest-neighbor magnetic interaction J' because the result is always close to one within a reasonable pristine frame.

The former relation for the resonance triplon mode in the J -model becomes different in the J' -model as

$$\tilde{k}_{\text{res}}^{J'} = \cos^{-1} \left(\frac{J}{J' + g'\bar{q}'_0} \left[1 - \frac{\omega_0^2}{4J^2} \right] \right). \quad (7.6)$$

The former agreements between k_{max} , the position of shifted peaks in k -component occupations, and the obtained \tilde{k}_{res} were done for various SPCs in the J -model, however, here we have already chosen large SPCs. It is, therefore, useful to compare results for larger SPC strengths in Tab. 7.2. The most evident result of this table is a complete agreement between the modes extracted from different ways in both models up to three digits. All these together ensure us that the renormalized spin-band relations provided in Eqs. (7.2) and (7.5) are valid for all resonance modes of both models, especially $k = 0$ and π of the band edges.

g/J	g'/J	$\tilde{k}_{\text{res}}/\pi$	k_{max}/π
0.50	–	0.6671716308	0.6670636617
–	0.25	0.6382399127	0.6384674237

Table 7.2: A comparison between \tilde{k}_{res} and k_{max} for various SPCs and two models J ($g/J = 0.5$) and J' ($g'/J = 0.25$) at fixed $N = 3000$, $\omega = \omega_0 = 2.2J$, $\gamma_{\text{ph}} = 0.02\omega_0$, $a/\gamma_{\text{ph}} = 0.2$, and $\gamma_{\text{s}}/J = 0.01$.

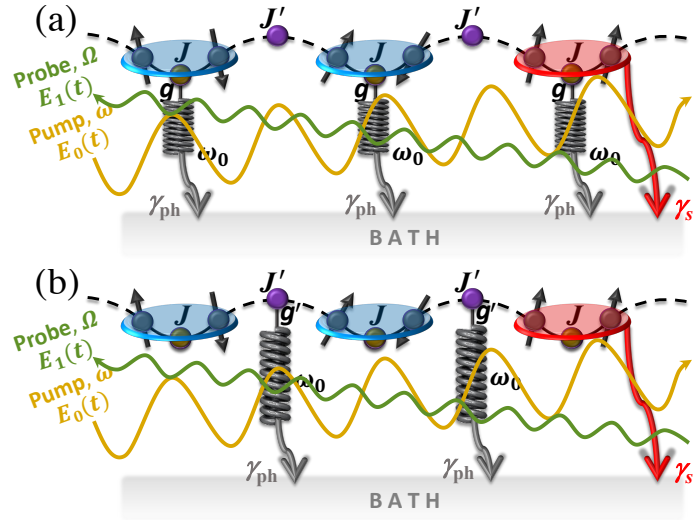


Figure 7.4: A new picture of (a) J -model and (b) J' -model with the probe driving field $E_1(t)$. The probe beam is addressed with the frequency Ω .

7.2 Dynamic spin-band renormalization

Similarly, as in the previous section, we intend to investigate the spin-band renormalization under the influence of weak-to-strong coupling, meaning that the spin-band is modulated with g and g' . Contrary to the static way, however, we now allow the probe driving field to be turned on and this means a dynamic feature from the probe field point of view, hence the total laser field is composed of two parts: a pump and a probe, both of which are again steady driving, and the pump field exhibit basically the same properties as before, while the probe features can be explored in detail. One of the more exciting things is that the pump-probe protocol can distinguish the various things going on inside a material that are normally mixed up.

We sketch the new models including the probe driving field in Fig. 7.4. As before, we study the dynamics in terms of expectation values of the system's observables. This pump-probe driving will provide a better accurate measurement of the spin-band renormalization. We first send a pump field to excite the system at $\omega = \omega_0$. Second, a weaker probe field with amplitude a_{pr} and frequency Ω is sent right after the first one to measure the effect of the first excitations. By this, we drive the system at $\omega = \omega_0$ and scan the spin response in a wide range of probe frequency Ω with increasing SPCs to the nearest- and next-nearest-neighbor magnetic interactions to see if the observed static SPC-induced frequency shifts can be captured. It is well-known that by changing the interval between the first and second fields, the evolution of the excitation in the course of time can be reconstructed, however, the time delay between the fields is neglected for simplicity in this protocol. Let us still call it a *pump-probe* protocol of laser driving even without the time delay. So, we introduce the laser field $\mathcal{E}(t) = a \cos(\omega t) + a_{pr} \cos(\Omega t)$ this time [see Fig. 7.4 in which $E_0(t) = a \cos(\omega t)$

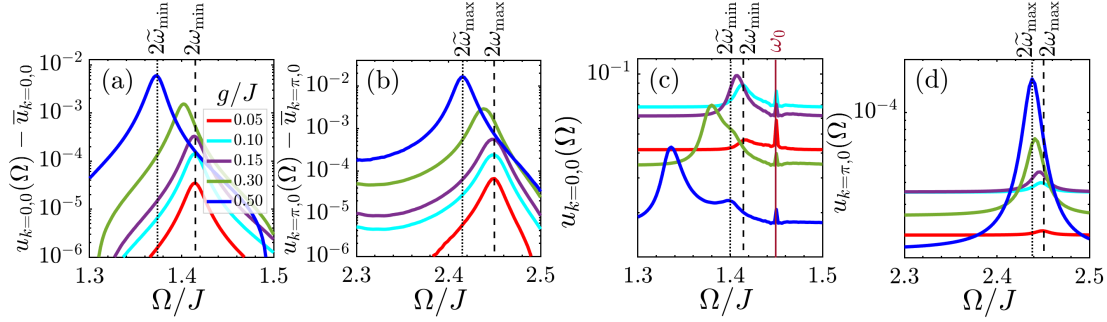


Figure 7.5: Average value of (a) $k = 0$ and (b) $k = \pi$ component of the spin response in the J -model, deducted by their resonant values for a better resolution of peaks, as a function of the probe frequency, Ω/J , at $N = 2000$, $\gamma_{\text{ph}} = 0.02\omega_0$, $a/\gamma_{\text{ph}} = 0.2$, $\gamma_{\text{s}}/J = 0.01$, and $a_{\text{pr}}/a = 0.2$ for various SPCs and driving frequency $\omega = \omega_0 = 2.2J$ far from the band edges. The dotted vertical lines show the driving-renormalized two-triplon bands at strong SPCs. Panels (c) and (d) investigate the same treatments (without any deduction this time) at another driving frequency $\omega = \omega_0 = 1.45J$ close to the lower band edge.

and $E_1(t) = a_{\text{pr}} \cos(\Omega t)$]. Here we fix the probe amplitude around 20% of the pump field, i.e. $a_{\text{pr}}/a = 0.2$, and then will apply various weaker probe fields later to see how the shifts are affected.

The starting point is again sticking to the k -components of the triplon occupation. The overall goal of this section is again very similar to the previous one: Considering both models, we aim to engineer the spin-band shifts of the coupled system through the pump-probe protocol. We start with the J -model.

7.2.1 J -model

Illustrated in Figs. 7.5(a) and 7.5(b) are the corresponding results of pump-probe calculations at the same driving frequency $\omega = \omega_0 = 2.2J$ away from the band edges as Fig. 7.2(a) [for a clear comparison] for $k = 0$ and $k = \pi$ components of the spin response deducted by their resonant values for a better resolution of peaks. Interestingly, as expected, the response in these components moves toward lower probe frequencies, i.e. toward the same frequencies provided in Fig. 7.2(a) for strong SPCs. The dotted vertical lines indicate respectively the renormalized lower and upper band edge at $g/J = 0.5$. It should be pointed out that at this driving frequency, the hybridization effect is not so strong and for this reason, we can believe in the shifted lower and upper band edges, which are in excellent agreement with previously founded shifts. It can be observed that there is a small difference between the peak positions and the dotted vertical lines for both band edges. To achieve the same dimerization parameters, one needs to completely resolve this discrepancy. This discrepancy will be addressed in detail later in the same section.

Another important example of SPC-dependent spin-band engineering that

can be looked at it is driving frequency $\omega = \omega_0 = 1.45J$ so close to the lower band edge. In this case, which constitutes strong phononic-magnetic hybrid states due to a stronger self-blocking effect at and around the band edges, the large peaks of the responses can not be labeled anymore as the new band edges because strong hybridizations associated with the level repulsion are commonly assumed to happen instantaneously, i.e. the corresponding band shifts are taken to occur in a hidden way. In fact, this shift will obviously be carried out in a possibly small way. The sign of this small shift comes up with some *shoulders* around the lower band edge, see Fig. 7.5(c). As long as the phonon is far from the upper band edge, the hybridization effect is still weak and the large peaks are purely located at the new band edges, see Fig. 7.5(d). By comparison with the results of Eq. (7.2) we can thus discern how the SPC affects the spin-band. Our present framework is especially suited to show that there is also a resonance between the probe frequency Ω and driving frequency $\omega = \omega_0 = 1.45J$, shown as small spikes.

7.2.2 J' -model

Starting from the same driving frequencies and keeping the set of parameters fixed, any of these band engineering can be assessed by means of the predictions from Sec. 7.1.2 and Fig. 6.8 and suitably combined to obtain a better estimate of the band shifts in the J' -model.

Contrary to the J -model in which only the phonons far from the two-triplon band constitute the weak self-hybrid states (strong spin-band shift) due to the dominant role of y_k element (not significant in the spin-excitations) in EoMs in comparison to the y'_k (mainly responsible for the spin-excitations), the hybridization effect is weak in the J' -model for a range of phonons below, in and above the two-triplon band. The reason is that the maximal level excitation in the coupled system usually occurs with the pair operators accompanied by the small y'_k factor in the EoMs. Since the given EoMs in the J' -model is therefore described by the individual presence of this element as the main factor of spin-band excitations, the hybrid states are weakly formed for all phonons. Under physically reasonable assumptions about the coupled system, the effect of driving frequencies on the band shifts for $\omega = \omega_0 = 1.45J$ is also assessed with the shoulders in the J' -model.

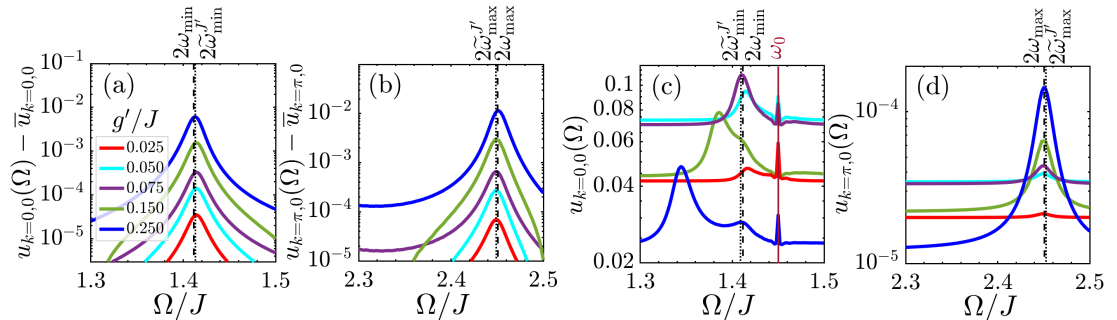


Figure 7.6: As Fig. 7.5 but in the J' -model.

We remark that the latter prediction between the true and the observed dynamics is exact, provided that in Fig. 7.6 for both phonons at $\omega = \omega_0 = 1.45J$ and $\omega = \omega_0 = 2.2J$, respectively, close and far from the band edges, the responses appear weakly and the large peaks are originated from the weak hybrid states (level repulsion effect). Since the density of states is still high at the band edges independent of the model, the resolution of peaks for the phonons around the band edges are higher than those away from the band edges. Note that the parameter J/J' , which was used to control the models has now been absorbed into the effective shift profile, meaning that yet the agreement between the models setting $g'J/J' = g$ will turn out to be useful for phonons so close to the band edges [see e.g. Fig. 6.6] and for those in the band, the matrix elements y_k and y'_k compete, which the better resolution of this competition can be provided via the pump-probe protocol, though the responses are not matched perfectly in the band even without probe driving field, as confirmed in Figs. 6.2 and 6.6.

The phonon displacement in the J' -model, which required a positive (negative) intensity before (after) the band center, does also reflect its trend in the dynamic band shifts such that sufficiently weak perturbations for the driven system expect a band-narrowing and a band-broadening at $\omega = \omega_0 = 2.2J$ and $\omega = \omega_0 = 1.45J$, respectively, due to the extra negative sign in corresponding EoMs, see Eq. (6.7).

Here, the static (in the absence of probe field) and dynamic (in the presence of probe field) band shifts are again not perfectly consistent with each other and a discrepancy is remained between the position of the peaks and the dotted lines corresponding to the new static band edges. We have two reasons behind this discrepancy between static and dynamic shifts in both models: Phonon displacement mechanism and static effects.

The first origin of this sensitivity of triplon modes in the J' -model is a sort of phonon displacement mechanism, whereby the weaker interplay of many largely independent modes appears practically weak in \bar{q}_0 and the contribution of phonon displacement to the SPC for possible spin excitations and then for possible magnetic interaction modulation can thus be understood as a second-order correction whose value depends on the first component of the Fourier transform of $q(t)$. Thereby, let us first shortly compare the Fourier decompositions of $q(t)$ in both models in Fig. 7.7 with the help of Eq. (4.11). Taking into account the three first coefficients of the Fourier transforms of phonon displacement in the (a) J -model with $g/J = 0.5$ and (b) J' -model with $g'/J = 0.25$ in Fig. 7.7 at fixed $N = 2000$, $\omega = \omega_0 = 2.2J$, $\gamma_{\text{ph}} = 0.02\omega_0$, $a/\gamma_{\text{ph}} = 0.2$, and $\gamma_s/J = 0.01$, we exploit that the difference between the zeroth and first components in the J' -model is extensive with a factor of 10 compared to the J -model. This can be understood from the late-time steady states of phonon displacements as well such that the amplitude of oscillations in the J' -model is larger than that of the J -model, see the inset panels. By this, we argue that the role of second-order correction of $q(t)$ is more extensive in the J' -model. Hence, one needs to include the second-order correction

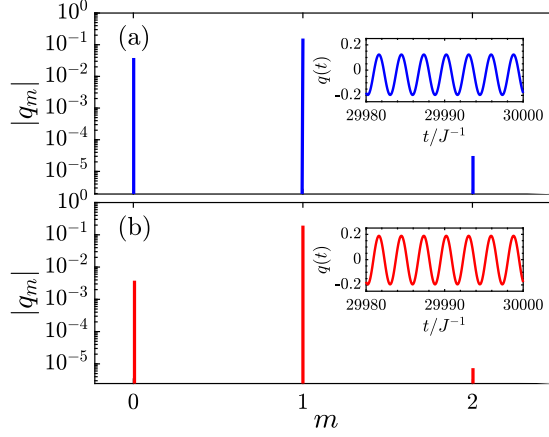


Figure 7.7: Three first coefficients of the Fourier transform of phonon displacement in the (a) J -model with $g/J = 0.5$ and (b) J' -model with $g'/J = 0.25$ at fixed $N = 2000$, $\omega = \omega_0 = 2.2J$, $\gamma_{\text{ph}} = 0.02\omega_0$, $a/\gamma_{\text{ph}} = 0.2$, and $\gamma_s/J = 0.01$. The inset panels indicate the late-time evolution of the phonon displacements.

in the models to try to compensate the discrepancies.

In our model, we are allowed to rewrite the phonon displacement as

$$q(t) = \langle d \rangle(t) = q_0 + Q_p \cos(\omega t), \quad (7.7)$$

where Q_p is related to the absolute value of first coefficient of Fourier transform, $|q_1|$. To find the relationship between them, we once more look at the SPC Hamiltonians in both models at zero temperature, i.e.

$$\mathcal{H}_{\text{sp},s}^J = g \langle d \rangle \sum_{k,\alpha} \left[y_k \tilde{t}_{k,\alpha}^\dagger \tilde{t}_{k,\alpha} + \frac{1}{2} y'_k (\tilde{t}_{k,\alpha}^\dagger \tilde{t}_{-k,\alpha}^\dagger + \tilde{t}_{k,\alpha} \tilde{t}_{-k,\alpha}) \right], \quad (7.8a)$$

$$\mathcal{H}_{\text{sp},s}^{J'} = -\frac{g'J}{2J'} \langle d \rangle \sum_{k,\alpha} y'_k \left[2 \tilde{t}_{k,\alpha}^\dagger \tilde{t}_{k,\alpha} + \tilde{t}_{k,\alpha}^\dagger \tilde{t}_{-k,\alpha}^\dagger + \tilde{t}_{k,\alpha} \tilde{t}_{-k,\alpha} \right]. \quad (7.8b)$$

Since the laser field indirectly excites spins through the lattice, the main contribution of second-order correction of phonon displacement originates from the pair creation and annihilation operators. Therefore, in this formulation, we have

$$Q_p^J = g q_1^J y'_k / 2, \quad (7.9a)$$

$$Q_p^{J'} = -g' J q_1^{J'} y'_k / 2J', \quad (7.9b)$$

for J - and J' -model, respectively.

We now lay the foundation of the calculations of second-order correction to the phonon displacement via the Magnus expansion with the help of Eq. (2.27), see Sec. 2.5.1. Similar to two coupled harmonic oscillators, for the second-order correction to the band edges, we here have

$$\Delta^{(2)}\omega_k = 2 \frac{Q_p^2 \omega_k}{\omega_0^2 - 4\omega_k^2}. \quad (7.10)$$

In the J -model, at $\omega = \omega_0 = 2.2J$, we have $Q_p^J \simeq -0.0134$ and 0.0077 for the lower $2\omega_{k=0} = \sqrt{2}$ and upper $2\omega_{k=\pi} = \sqrt{6}$ band edge, respectively. Following the above relation, we respectively obtain $\Delta^{(2)}\omega_{k=0} \simeq 8.94 \times 10^{-5}$ and $\Delta^{(2)}\omega_{k=\pi} \simeq -1.25 \times 10^{-4}$. In the J' -model, respectively, $Q_p^{J'} \simeq 0.0163$ and -0.0093 result in $\Delta^{(2)}\omega_{k=0} \simeq 1.32 \times 10^{-4}$ and $\Delta^{(2)}\omega_{k=\pi} \simeq -1.82 \times 10^{-4}$. From the order of these corrections, in turn, one notices that the nonlinear mechanism in the J' -model is stronger than the J -model for which the time-dependent perturbation of the spin Hamiltonian in the J' -model created by this phonon-induced modulation can be expressed as a Taylor expansion and the effective second-order approximation of the phonon displacement can be extracted.

These corrections try to make both peak positions and dotted lines closer, but not significantly. Thus, we need to stick to the second origin, i.e. static effects included in the weak probe driving effects.

7.3 Driving effects on the spin-band

Before scrutinizing the consequences of both pump and probe driving effects on both the static and dynamic band renormalization generated by strong SPCs, we shortly mention that the idea is to seek stronger band shifts with the SPC: This idea structurally originates from Fermi's golden rule [see Sec. 2.4] in which employing stronger driving fields in the underlying basic perturbation can efficiently enhance the responses.

7.3.1 Pump driving effect

Static band renormalization

As explained in Sec. 7.1, we intend to adopt the theoretical predictions from the phonon displacement \bar{q}_0 to the dynamics generated by the SPC. For this to be valid, the displacements should thus be calculated for other pump driving strengths. We choose $a/\gamma_{\text{ph}} = 0.1$ and 0.4 to be different than the fixed one before at fixed $N = 2000$, $\omega = \omega_0 = 2.2J$, $\gamma_{\text{ph}} = 0.02\omega_0$, $g/J = 0.5$, $g'/J = 0.25$, and $\gamma_s/J = 0.01$. And it should be mentioned that the probe field changes simultaneously with the pump one following the relation $a_{\text{pr}}/a = 0.2$. In the case of the J - and J' -model, respectively, the leading and next-nearest-neighbor magnetic interaction is calculated by the means of $\tilde{J} = J + g\bar{q}_0^J$ and $\tilde{J}' = J' + g'\bar{q}_0^{J'}$. After inserting the corresponding displacements from Fig. 7.8 into these modulated interactions for $a/\gamma_{\text{ph}} = 0.1$ to 0.4 at $\omega = \omega_0 = 2.2J$, we find Tab. 7.3. From Fig. 7.8, we understand the responses are no longer in the exact $(a/\gamma_{\text{ph}})^2$ regime when increasing the driving strength, as already confirmed by Fig. 6.3, and clearly the responses are decreasing as the driving increases. This is a direct consequence of strong perturbation effects.

We already expected stronger band shifts with increasing the pump driving field. Since the quantities $2\tilde{\omega}_{\text{min}}$ and $2\tilde{\omega}_{\text{max}}$ are in direct correspondence to the

a/γ_{ph}	\tilde{J}/J	$2\tilde{\omega}_{\text{min}}^J$	$2\tilde{\omega}_{\text{max}}^J$	\tilde{J}'/J'	$2\tilde{\omega}_{\text{min}}^{J'}$	$2\tilde{\omega}_{\text{max}}^{J'}$
0.0	1.0	1.41421356	2.44948974	1.0	1.41421356	2.44948974
0.1	0.995818	1.40533909	2.44095267	0.99960	1.41449460	2.44932745
0.2	0.981775	1.37549213	2.41227664	0.99816	1.41550768	2.44874212
0.4	0.954315	1.31690488	2.35616181	0.99406	1.41840403	2.44706559

Table 7.3: A comparison between J and J' models for various pump driving strengths a/γ_{ph} at fixed $N = 2000$, $\omega = \omega_0 = 2.2J$, $\gamma_{\text{ph}} = 0.02\omega_0$, $g/J = 0.5$, $g'/J = 0.25$, and $\gamma_s/J = 0.01$.

magnetic interactions, the band shifts (stronger in the J -model) at both the lower and upper band edges move towards the lower energy levels with a/γ_{ph} . In the case of J' -model, however, the behavior is not the same with a/γ_{ph} such that the lower band edge moves to the higher levels and the upper band edge moves slightly to the lower levels, resulting in narrower spin-band [see Tab. 7.3].

Generally speaking, the band shifts to the lower energy levels with a/γ_{ph} in the J -model independent of the driving frequency. While we do not exploit a general description for the shifts in the J' -model since the phonon displacement does not offer a constant sign and remnants of driving frequencies below the band center propose a broader spin-band in the final prediction.

Dynamic band renormalization

The pump-probe driving field suggests that predicting the band shifts generated by the SPC by means of probe frequency scan should yield constant offsets for various pump fields, meaning that individual pump driving without probing does not need any further discussion. If the effective $\mathcal{E}(t)$ is unprobed in the sense that $E_1(t)$ vanishes, then $E_0(t)$ does not show any response from the spin excitations via the probe driving or SPC. However, the influence of pump field at a constant probe field ($a_{\text{pr}} = 0.2a$) is more subtle. We thus additionally require a strong

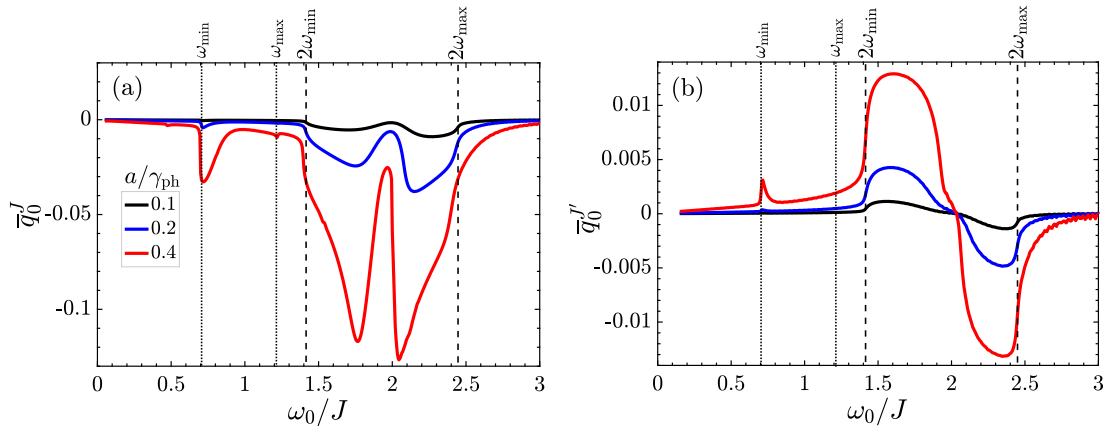


Figure 7.8: Pump driving effect on the phonon displacement in the (a) J -model and (b) J' -model at fixed $N = 2000$, $\gamma_{\text{ph}} = 0.02\omega_0$, $g/J = 0.5$, $g'/J = 0.25$, and $\gamma_s/J = 0.01$.

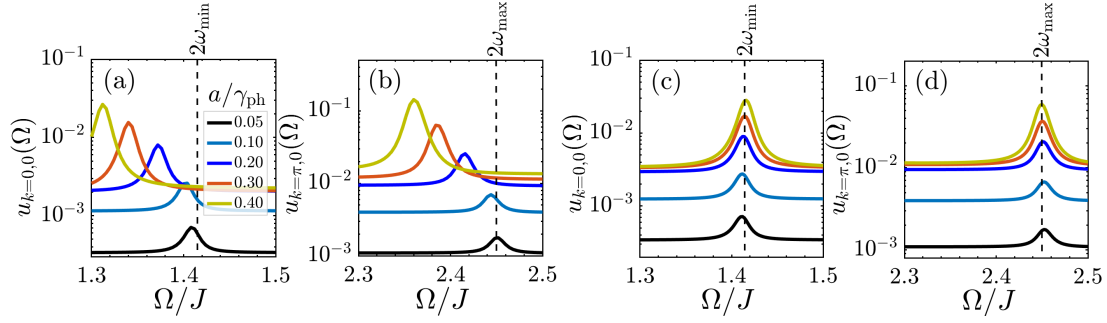


Figure 7.9: Pump driving effect on the dynamic spin-band renormalization in the $\{(a),(b)\}$ J -model and $\{(c),(d)\}$ J' -model at fixed $N = 2000$, $\omega = \omega_0 = 2.2J$, $\gamma_{\text{ph}} = 0.02\omega_0$, $g/J = 0.5$, $g'/J = 0.25$, and $\gamma_s/J = 0.01$.

SPC at least to see the effects. We again use $g/J = 0.5$ and $g'/J = 0.25$ in both models at the same used parameters to control the dynamical responses.

By inspection of various pump amplitudes a/γ_{ph} in Fig. 7.9 for a representative driving frequency $\omega = \omega_0 = 2.2J$ in both J and J' models, we understand that the effective band shift strength as mediated by the driving phonon is grown with the pump field, meaning that the spin-band renormalization strength translates into a corresponding driving prerequisite. Moreover, the occupations increase with driving amplitude. We remark that, in the J -model, the somewhat trivial limit of extremely weak and strong drivings are reflected correctly: If the pump driving is weak-enough, $a/\gamma_{\text{ph}} = 0.1$, then the perturbation profile is somehow mapped back onto the case of decoupled case and the tiny percent of shift is observed for the new band edge formation. As with the strong perturbation profile, large shifts happen for $a/\gamma_{\text{ph}} = 0.4$. On the other hand, in the J' -model, the band becomes narrower with driving a/γ_{ph} at the driving frequency $\omega = \omega_0 = 2.2J$ [and a broader spin-band is expected for $\omega = \omega_0 = 1.8J$ due to $\bar{q}_0 > 0$ in the J' -model]. Since the static and dynamic predictions are not expected to reach different shifts, comparing the new energy levels at, for instance, $a/\gamma_{\text{ph}} = 0.1$ and 0.4 of Fig. 7.9 (a) and (b) produces the same shifts as, respectively, 1.405 and 1.316 for the lower band edge and 2.440 and 2.356 for the upper band edge of J -model, consistent with third and fourth columns of Tab. 7.3. We achieve, considering the second-order correction discussed in Eq. (7.10) in the case of J' -model, respectively, 1.414 and 1.418 for the lower band edge and 2.449 and 2.447 for the upper band edge, again consistent with sixth and seventh columns of Tab. 7.3.

7.3.2 Probe driving effect

For the purpose of a perfect match between static and dynamic shifts, we temporarily switch off the pump driving by setting $a = 0$ to get a qualitative understanding of how the band dispersion changes under the probe diving. This means that the only available driving field in the models is the *very weak* probe fields, namely $a_{\text{pr}}/\gamma_{\text{ph}} = 0.001, 0.002, 0.003, 0.004, 0.006, \text{ and } 0.008$ for the experimental pur-

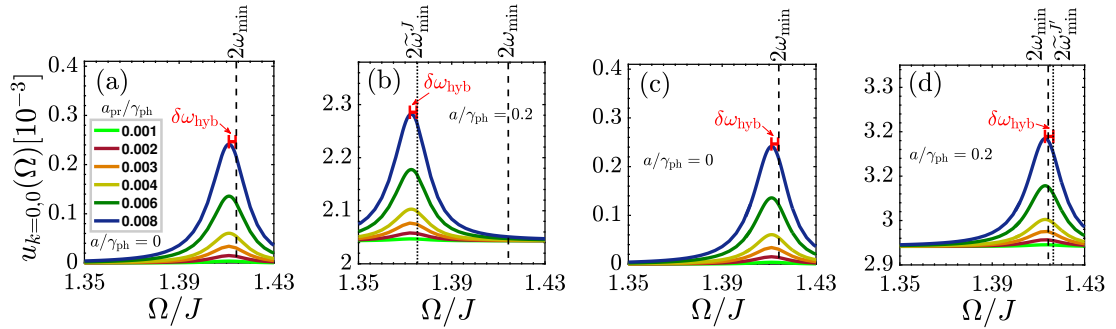


Figure 7.10: Probe driving effect on the dynamic spin-band renormalization in the $\{(a),(b)\}$ J -model and $\{(c),(d)\}$ J' -model at fixed $N = 2000$, $\omega = \omega_0 = 2.2J$, $\gamma_{\text{ph}} = 0.02\omega_0$, $g/J = 0.5$, $g'/J = 0.25$, and $\gamma_s/J = 0.01$. In panels (b) and (d) the pump driving field is turned on, $a/\gamma_{\text{ph}} = 0.2$. In the panels $\delta\omega_{\text{hyb}}$ refers to the energy difference between the peak positions and the bare band edges induced by the probe driving field and/or self-hybrid effect.

poses. Note that the damping energy is also already weak – around 2% of the phonon energy which is $\gamma_{\text{ph}} = 0.044J$ for the phonon frequency $\omega = \omega_0 = 2.2J$ – for instance. Thus, in these weak-enough probe fields, the system is almost undriven (static limits) and no laser energy indirectly/directly should be transferred into the coupled system. In general, we expect that the SPC-induced phononic-magnetic hybrid states are approximately not formed as time progresses. Thus, the spin-band shift must approach zero for these weak fields, meaning that the weak-enough probe driving ensures that the modifications of the spin-band are persistent on the relevant SPCs and do not change significantly with SPC. If this result is not met, we call the states *directly resonant self-hybrid* originating from the static effects and the inherent band shift with probe field is the second origin (significant) of discrepancy between static and dynamic shifts. For the sake of the pump driving absence, we focus on the dynamic band renormalizations in the following. Moreover, we may think of only the lower band edge since the symmetry between the lower and upper band edges expects the same arguments.

As plotted in Figs. 7.10(a) and 7.10(c), respectively, for the J - and J' -model, the generally emerging picture is thus as follows: Occupations can be shifted with SPC even when the probe driving is very weak which should not be the case, meaning that the system displays a self-hybrid effect. In a sufficiently generic setting, almost the energy level of all self-hybrid states will remain unchanged with probe driving as well as both models show almost the same responses because of the same matrix elements in the absence of pump field. However, this effect is weak in both models, implying that the peaks are not far from the bare band edges with the sole role of probe driving field. This, in turn, is not the case when the pump driving field is switched on. In this case, having made sure that the y'_k matrix elements are mainly responsible for spin excitations in both models, the sensitivity criteria of models to the perturbations can only be collected via this

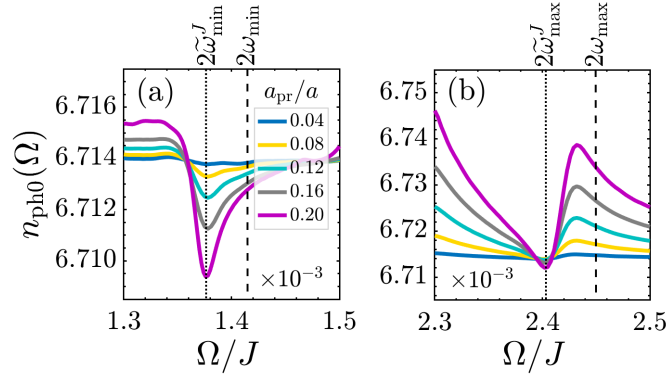


Figure 7.11: Probe driving effect on the phonon spectrum around the (a) lower and (b) upper band edge in the J -model at fixed $N = 2000$, $\omega = \omega_0 = 2.2J$, $\gamma_{\text{ph}} = 0.02\omega_0$, $g/J = 0.5$, $g'/J = 0.5$, and $\gamma_s/J = 0.01$.

element. Additionally, the occupations increase with the probe driving amplitude, similar to the pump one.

Note that the second-order correction of phonon displacement is already included in the dotted lines, however, the discrepancy between static and dynamic shifts is still there. Let us concentrate on the band edge shifts here and the hybridization effects which are mainly dedicated to the large peaks. Under the same assumptions and conditions, we turn on the pump field, $a/\gamma_{\text{ph}} = 0.2$ in both models, see Figs. 7.10(b) and 7.10(d). Altogether, occupations show the energy level of blue lines in Figs. 7.9(a) and 7.9(c). From Fig. 7.10(b), one can conclude that the probe driving field and/or the self-hybrid effect does shift the band edge which can be characterized by $\delta\omega_{\text{hyb}} \neq 0$ as the difference between the peak positions and the bare band edges. By this the discrepancy mentioned before is resolved. Thus, $(2\tilde{\omega}_k + \Delta^{(2)}(2\omega_k))|_{\text{static}} = (\Omega_{\text{max}} + \delta\omega_{\text{hyb}})|_{\text{dynamic}}$ holds true.

Finally, we come back to the self-blocking effect mentioned in chapter 5 in the discussion of strong SPC effect, namely the fact that the spin system acts as a perturbation and extra inertia by pushing the phonons to move, which in turn leads to more (less) energy absorption by the phonons (triplons). And, it eventually blocks the input energies to the spin system itself. The strong suppression at the band edges of the two-triplon band directly relates to this self-blocking effect and for the new band edges engineered by the pump-probe protocol, significant suppression of phonon occupation must only occur at the energy levels of new band edges. Naturally, the phonon occupation receives a correction from the modified triplon band and, nevertheless, the general mechanism remains the same to satisfy the resonance condition $\tilde{\omega}_0 = 2\tilde{\omega}_k$ in both models. For instance, at $\omega = \omega_0 = 2.2J$ and the same set of parameters, in the J -model, the phonon occupation is suppressed at the new band edges [Fig. 7.11(a) and 7.11(b)] around both band edges. The same argument is valid in the J' -model, not shown here. In this way, we also show the spin-band renormalization.

7.4 Chapter summary

This chapter's study of spin-band renormalization in a driven-dissipative quantum spin-1/2 chain dealt with two types of method accompanying the SPC effect. The first type of setup is focused on the two-triplon band modulation through the single pump driving field and phonon displacement. While the second method as the general setup starts a pump-probe protocol prepared in a non-equilibrium state, followed by another periodic probe protocol (in addition to the pump driving field) during which it evolves the dynamics weakly under the same conditions.

In the spirit of J and J' models, we applied these methods by suitable parameters, calculated the band edge frequencies at both weak and strong SPC regimes, calculated the average value of $k = 0$ and $k = \pi$ components of triplon occupations in the NESS, and showed that the individually observed behavior of spin-band edges with SPC under both these methods is not practically indistinguishable from each other. A detailed test of our analytical calculations against numerical simulations of a pump-probe protocol revealed good agreement, notably only with second-order approximation of the phonon displacement and inherent static effects. In the latter, changing perspectives, individual extremely weak probe protocols lead to an inherent feature of the system, called self-hybrid effect due to the static effects, i.e. a setup in which some external weak control parameter can be manipulated such that coupled spin-lattice system answers to the strong SPC regime. Another noteworthy aspect of these numerical verifications is that the giant resonant self-blocking effect can be seen in the new modulated band edges. These, in turn, promote the pump-probe protocol to a measurement for the spin-band engineering in magnetophononically driven quantum magnets.

8. Summary and outlook

In this dissertation, we have investigated some aspects of the non-equilibrium dynamics of open quantum magnetic systems. The central subject matter of this thesis was to find simple descriptions for the behavior of quantum magnetic systems out-of-equilibrium based on the well-verified theoretical modeling of their constituents. In particular, we have considered those non-equilibrium situations which are generated by the presence of time-dependent stationary driving fields. Yet the detailed observable behavior of spin systems out-of-equilibrium is not well-established. For instance, as expounded in chapter 2, the inclusion of the damping effects in the open quantum systems may lead to the stationary states for the observable expectation values at long times; the stationary states coincide with the calculations in the current thesis for a dimerized driven-dissipation spin-1/2 chain (chapter 3).

More precisely, our primary interest was to describe the dynamical properties of spin-1/2 chain that are finally far from the equilibrium state under the influence of weak-to-moderate perturbations: How do the driven lattice and spin degrees of freedom reach the NESS, preserve it, and relax towards the equilibrium (chapter 4)? Can we tune the reached NESS with the driving parameters, weak spin-phonon coupling, and damping energy? How does this NESS emerge in the experiment? Can we find novel physical insights with the strong spin-phonon coupling (chapter 5)? How does the coupling of the lattice to different spin-bonds affect the subsystem responses (chapter 6)? And how the spin-band can be renormalized through the vibrations and pump-probe protocols (chapter 7)? For this setup, we have answered these questions for the time evolution of expectation values of driven damped spin-lattice system in two distinct but related models.

In the first step, the dynamical properties generated by a laser-frequency modulation in a dimerized driven-dissipation spin-1/2 chain have been solved with mainly Lindbladian adjoint quantum master equation within the Markovian approximation. This is a common procedure to derive the time evolution of observables in open quantum systems with much slow decay of bath correlations/excitations. The general idea of this equation is thus to individually couple the system sectors with the fact that the weak interaction with many atoms is supposed to simulate the coupling to a thermal bath with temperature T and for this, the rates of Lindblad operators must be related to each other by a Maxwell-Boltzmann factor. Conceptionally, this exploits the phenomenological dissipation effects well.

In chapter 3 we reviewed the experimental observations of a target material CuGeO_3 , an alternating gapped spin-1/2 chain, and modeled the whole driven damped spin-lattice system, which can be split into four parts: a spin sector for which we assume an antiferromagnetic Heisenberg Hamiltonian comprising of intra- and inter-dimer couplings, an infrared-active dispersionless phonon, a spin-phonon coupling part as developed in the context of mean-field decoupling approximation, and a laser-phonon coupling Hamiltonian employed based on the mechanism that the time-varying electrical dipole moment of phonons is coupled to the time-dependent steady laser field. The physical observables of the entire system were then introduced. Finally, the equations of motion of these observables were derived through the Lindblad quantum master equation.

In chapter 4, we studied the dynamical properties of driven damped, but weakly coupled spin-lattice system in detail. Achieving the coherent phonon and spin NESS was the primary result for a wide range of applicable parameters, which is important for experimental purposes. In the context of many-body systems, the perturbation theory states that the response of occupations for weak perturbations and late times is proportional to the square of laser amplitude as well as to the square of spin-phonon coupling. Not least, this was the case in our model because arguably the standard method using ordinary perturbation theory is usually limited to small dense spectra. Besides describing the relaxation towards equilibrium, the theory also provides a description of the energy flows in various parts of the system. As in most studies, in the last part of this chapter, the experimental possibilities for the ultrafast running of such systems were provided.

In chapter 5, we investigated the strong coupling regime of the spin-lattice system, which allows us to quantify the spin feedback effects in terms of occupations. The general procedure works as follows: The strong spin-lattice coupling regime is prepared in a NESS and at this point, an effective *negative* spin feedback effect is appeared as an extra inertia/perturbation for the laser-driven phonon – a giant resonant self-blocking effect in the spin system associated with the suppressed phonon occupation. The dependence of response of the occupations to a strong coupling regime leads to hybrid phononic-magnetic states and to introducing

quasiparticles *phonon-bitriplons*. We assessed to what extent the hybrid states manifest themselves in the triplon modes, looking at the k -components of the triplon occupation.

In chapter 6, we developed another model. By analogy with the coupling to the leading magnetic interaction J , the J' -model where the phonon is coupled to the next-nearest-neighbor J' coupling was regarded as a new scenario for a sensitive dependency of self-blocking and hybrid states on the strong spin-lattice coupling regime. The matrix elements pertaining to the spin excitations as well as the prefactor $1/\lambda = J/J'$ are the main differences in the models, to cover the weaker responses in the J' -model.

In chapter 7, for the spin-band renormalization, we analytically calculated the band edge shifts and formulated a pump-probe setup with very weak probe driving fields to compare the obtained results from the analytical ones. Analytical solutions were obtained for special driving frequencies, notably for sufficiently away from the band edges. Interestingly, the results resemble common shifts for the band edges which are nonlinear with the spin-lattice coupling. These demonstrated that the good agreement is not the latest finding. In single very weak probe driving examples, the spin-lattice system was expected to remain almost decoupled with a strong coupling regime, but *self-hybrid effects* appeared as an inherent property of this system.

Regarding the reliable approximations adopted and employed in this thesis during the derivations and analyses, even though the model and EoMs are applicable to a large variety of different regimes, it also suffers from some limitations.

The discussion in the present thesis is restricted to spin-1/2 objects. Higher values for the spins would result in larger local Hilbert spaces, but this should not affect most aspects of the qualitative physics of this model. Whereas the model presented here treats the weak-to-strong SPC dependence of dynamics well, it does make limitations and approximations in other respects. The use of a Heisenberg model to describe inorganic dimerized spin chain compounds misses the anisotropy terms as well as the interaction between different triplon modes. Clearly, further research and theoretical input are needed to fully include these terms into this system, which can lead to an overestimate of the spin gap.

As the inter-dimer coupling, λ , is changed with SPC, the approximation that we treat the triplons as bosons may no longer be strictly valid. In this case, triplons can be treated as hard-core bosons especially when the triplet-triplet interaction is taken into account in the dynamics. However, as our triplon occupation in the NESS has shown, the quantitative densities are small and one may still keep the approximation.

In the implementation of the Lindblad formalism, we assumed that Lindblad operators for triplons are spin nonconserving and can be approximately treated as damped oscillators. This is consistent with the weak damping of spin excitations. Inclusion of generic spin-conserving operators $\mathcal{L}_{kq} = t_k^\dagger t_q$ gives extra dissipation

channels and eventually new corrections to the EoMs, which our calculation does account for in the future works. It is also well-known that the system temperature is mainly controlled by the phonons and employing a thermal phonon occupation or temperature-dependent bath operators in the Lindblad formalism may extend the current study to the finite temperature situation.

The laser driving field is steady in the present work. However, our formalism can also be used to study the non-equilibrium physics of quantum magnetic materials subjected to various driving sources like Gaussian pulses instead of steady driving.

In addition, it would naturally be desirable to look at the interaction between the triplons in the spin system through the retarded Green's functions to see how the observables are affected by each other after a time-lapse. These functions can be taken into account when they are important in spectral density or optical studies.

A. Spin Hamiltonian

To derive the Hamiltonian for the spin system, we start with the Sachdev's bond operator representation given in Sec. 2.3, to calculate both terms of intra- and inter-dimer interactions given by Eq. (3.2). So, we have

$$\vec{S}_{1,i} \cdot \vec{S}_{2,i} = \sum_{\alpha} S_{\alpha,i}^1 S_{\alpha,i}^2, \quad (\text{A.1a})$$

$$\begin{aligned} &= -\frac{1}{4} \sum_{\alpha} \left(\underbrace{s_i^{\dagger} t_{\alpha,i} s_i^{\dagger} t_{\alpha,i}}_{s_i^{\dagger} t_{\alpha,i}} + \underbrace{s_i^{\dagger} t_{\alpha,i} t_{\alpha,i}^{\dagger} s_i}_{s_i^{\dagger} s_i + s_i^{\dagger} s_i t_{\alpha,i}^{\dagger} t_{\alpha,i}} + \underbrace{t_{\alpha,i}^{\dagger} s_i s_i^{\dagger} t_{\alpha,i}}_{t_{\alpha,i}^{\dagger} t_{\alpha,i} + s_i^{\dagger} s_i t_{\alpha,i}^{\dagger} t_{\alpha,i}} + \underbrace{t_{\alpha,i}^{\dagger} s_i t_{\alpha,i}^{\dagger} s_i}_{t_{\alpha,i}^{\dagger} s_i} \right) \\ &\quad - \frac{i}{4} \sum_{\alpha,\beta,\zeta} \underbrace{\epsilon_{\alpha\beta\zeta} s_i^{\dagger} t_{\alpha,i} t_{\beta,i}^{\dagger} t_{\zeta,i}}_{\checkmark} - \frac{i}{4} \sum_{\alpha,\beta,\zeta} \underbrace{\epsilon_{\alpha\beta\zeta} t_{\alpha,i}^{\dagger} s_i t_{\beta,i}^{\dagger} t_{\zeta,i}}_{\times} \\ &\quad + \frac{i}{4} \sum_{\alpha,\beta,\zeta} \underbrace{\epsilon_{\alpha\beta\zeta} t_{\beta,i}^{\dagger} t_{\zeta,i} s_i^{\dagger} t_{\alpha,i}}_{\checkmark} + \frac{i}{4} \sum_{\alpha,\beta,\zeta} \underbrace{\epsilon_{\alpha\beta\zeta} t_{\beta,i}^{\dagger} t_{\zeta,i} t_{\alpha,i}^{\dagger} s_i}_{\times} \\ &\quad - \frac{1}{4} \sum_{\alpha,\beta,\zeta,\beta',\zeta'} \epsilon_{\alpha\beta\zeta} \epsilon_{\alpha\beta'\zeta'} t_{\beta,i}^{\dagger} t_{\zeta,i} t_{\beta',i}^{\dagger} t_{\zeta',i}, \end{aligned} \quad (\text{A.1b})$$

$$\begin{aligned} &= -\frac{1}{4} \sum_{\alpha} \left(s_i^{\dagger} s_i^{\dagger} t_{\alpha,i} t_{\alpha,i} + 2s_i^{\dagger} s_i t_{\alpha,i}^{\dagger} t_{\alpha,i} + t_{\alpha,i}^{\dagger} t_{\alpha,i}^{\dagger} s_i s_i + s_i^{\dagger} s_i + t_{\alpha,i}^{\dagger} t_{\alpha,i} \right) \\ &\quad + \frac{i}{4} \sum_{\alpha,\beta,\zeta} \epsilon_{\alpha\beta\zeta} \left[\underbrace{s_i^{\dagger} \left(t_{\beta,i}^{\dagger} t_{\zeta,i} t_{\alpha,i} - t_{\alpha,i} t_{\beta,i}^{\dagger} t_{\zeta,i} \right)}_{\checkmark} + \underbrace{s_i \left(t_{\beta,i}^{\dagger} t_{\zeta,i} t_{\alpha,i}^{\dagger} - t_{\alpha,i}^{\dagger} t_{\beta,i}^{\dagger} t_{\zeta,i} \right)}_{\times} \right] \\ &\quad - \frac{1}{4} \sum_{\beta,\zeta,\beta',\zeta'} (\delta_{\beta,\beta'} \delta_{\zeta,\zeta'} - \delta_{\beta,\zeta'} \delta_{\zeta,\beta'}) t_{\beta,i}^{\dagger} t_{\zeta,i} t_{\beta',i}^{\dagger} t_{\zeta',i}. \end{aligned} \quad (\text{A.1c})$$

It is again simple to see the role of three first terms in the first line of Eq. (A.1c) in any arbitrary state is zero. Thus,

$$\begin{aligned}
\vec{S}_{1,i} \cdot \vec{S}_{2,i} &= -\frac{1}{4} \sum_{\alpha} \left(s_i^{\dagger} s_i + t_{\alpha,i}^{\dagger} t_{\alpha,i} \right) \\
&+ \frac{i}{4} \sum_{\alpha,\beta,\zeta} \epsilon_{\alpha\beta\zeta} s_i^{\dagger} \left(t_{\beta,i}^{\dagger} t_{\zeta,i} t_{\alpha,i} - t_{\beta,i}^{\dagger} t_{\zeta,i} t_{\alpha,i} - \delta_{\alpha,\beta} t_{\zeta,i} \right) \\
&+ \frac{i}{4} \sum_{\alpha,\beta,\zeta} \epsilon_{\alpha\beta\zeta} s_i \left(t_{\beta,i}^{\dagger} t_{\zeta,i} t_{\alpha,i}^{\dagger} - t_{\beta,i}^{\dagger} t_{\zeta,i} t_{\alpha,i}^{\dagger} - \delta_{\alpha,\zeta} t_{\beta,i}^{\dagger} \right) \\
&- \frac{1}{4} \sum_{\beta,\zeta} t_{\beta,i}^{\dagger} t_{\zeta,i} t_{\beta,i}^{\dagger} t_{\zeta,i} + \frac{1}{4} \sum_{\beta,\zeta} t_{\beta,i}^{\dagger} t_{\zeta,i} t_{\zeta,i}^{\dagger} t_{\beta,i}, \tag{A.2a}
\end{aligned}$$

$$\begin{aligned}
&= -\frac{3}{4} s_i^{\dagger} s_i - \frac{1}{4} \sum_{\alpha} t_{\alpha,i}^{\dagger} t_{\alpha,i} - \frac{1}{4} \sum_{\beta,\zeta} t_{\beta,i}^{\dagger} t_{\beta,i}^{\dagger} t_{\zeta,i} t_{\zeta,i} - \frac{1}{4} \sum_{\beta,\zeta} t_{\beta,i}^{\dagger} t_{\zeta,i} \delta_{\beta,\zeta} \\
&+ \frac{1}{4} \sum_{\beta,\zeta} \underbrace{t_{\beta,i}^{\dagger} t_{\zeta,i}^{\dagger} t_{\zeta,i} t_{\beta,i}}_{t_{\beta,i}^{\dagger} t_{\beta,i} t_{\zeta,i}^{\dagger} t_{\zeta,i} - t_{\beta,i}^{\dagger} t_{\zeta,i} \delta_{\beta,\zeta}} + \frac{1}{4} \sum_{\beta,\zeta} t_{\beta,i}^{\dagger} t_{\beta,i}, \tag{A.2b}
\end{aligned}$$

$$\begin{aligned}
&= -\frac{3}{4} s_i^{\dagger} s_i - \frac{1}{4} \sum_{\alpha} t_{\alpha,i}^{\dagger} t_{\alpha,i} - \frac{1}{4} \sum_{\alpha} t_{\alpha,i}^{\dagger} t_{\alpha,i} + \frac{1}{4} \underbrace{\sum_{\beta,\zeta} t_{\beta,i}^{\dagger} t_{\beta,i} t_{\zeta,i}^{\dagger} t_{\zeta,i}}_{\sum_{\beta} t_{\beta,i}^{\dagger} t_{\beta,i} \sum_{\zeta} t_{\zeta,i}^{\dagger} t_{\zeta,i}} \\
&- \frac{1}{4} \sum_{\alpha} t_{\alpha,i}^{\dagger} t_{\alpha,i} + \frac{3}{4} \sum_{\alpha} t_{\alpha,i}^{\dagger} t_{\alpha,i}, \tag{A.2c}
\end{aligned}$$

$$\begin{aligned}
&= -\frac{3}{4} \underbrace{s_i^{\dagger} s_i}_{1 - \sum_{\alpha} t_{\alpha,i}^{\dagger} t_{\alpha,i}} + \frac{1}{4} \sum_{\alpha} t_{\alpha,i}^{\dagger} t_{\alpha,i}, \tag{A.2d}
\end{aligned}$$

$$= -\frac{3}{4} + \sum_{\alpha} t_{\alpha,i}^{\dagger} t_{\alpha,i}. \tag{A.2e}$$

Using the Fourier transformation the operators can be transferred into the momentum space

$$t_{\alpha,i} = \frac{1}{\sqrt{N}} \sum_k t_{k,\alpha} e^{ikr_i}, \tag{A.3a}$$

$$t_{\alpha,i}^{\dagger} = \frac{1}{\sqrt{N}} \sum_k t_{k,\alpha}^{\dagger} e^{-ikr_i}, \tag{A.3b}$$

leading to

$$\sum_{i=1}^N \vec{S}_{1,i} \cdot \vec{S}_{2,i} = -\frac{3}{4} N + \sum_{k,\alpha} t_{k,\alpha}^{\dagger} t_{k,\alpha}, \tag{A.4}$$

which is that of Eq. (3.8a).

Turning to the second term of Eq. (3.2), we calculate

$$\vec{S}_{2,i} \cdot \vec{S}_{1,i+1} = \sum_{\alpha} S_{\alpha,i}^2 S_{\alpha,i+1}^1, \tag{A.5a}$$

$$\begin{aligned}
&= -\frac{1}{4} \sum_{\alpha} \left(s_i^{\dagger} t_{\alpha,i} + t_{\alpha,i}^{\dagger} s_i + i \sum_{\beta,\zeta} \epsilon_{\alpha\beta\zeta} t_{\beta,i}^{\dagger} t_{\zeta,i} \right) \\
&\cdot \left(s_{i+1}^{\dagger} t_{\alpha,i+1} + t_{\alpha,i+1}^{\dagger} s_{i+1} - i \sum_{\beta',\zeta'} \epsilon_{\alpha\beta'\zeta'} t_{\beta',i+1}^{\dagger} t_{\zeta',i+1} \right), \quad (\text{A.5b}) \\
&= -\frac{1}{4} \sum_{\alpha} \left(s_i^{\dagger} t_{\alpha,i} s_{i+1}^{\dagger} t_{\alpha,i+1} + s_i^{\dagger} t_{\alpha,i} t_{\alpha,i+1}^{\dagger} s_{i+1} + t_{\alpha,i}^{\dagger} s_i s_{i+1}^{\dagger} t_{\alpha,i+1} \right. \\
&+ \left. t_{\alpha,i}^{\dagger} s_i t_{\alpha,i+1}^{\dagger} s_{i+1} \right) + \frac{i}{4} \sum_{\alpha,\beta,\zeta} \epsilon_{\alpha\beta\zeta} s_i^{\dagger} t_{\alpha,i} t_{\beta,i+1}^{\dagger} t_{\zeta,i+1} \\
&+ \frac{i}{4} \sum_{\alpha,\beta,\zeta} \epsilon_{\alpha\beta\zeta} t_{\alpha,i}^{\dagger} s_i t_{\beta,i+1}^{\dagger} t_{\zeta,i+1} - \frac{i}{4} \sum_{\alpha,\beta,\zeta} \epsilon_{\alpha\beta\zeta} t_{\beta,i}^{\dagger} t_{\zeta,i} s_{i+1}^{\dagger} t_{\alpha,i+1} \\
&- \frac{i}{4} \sum_{\alpha,\beta,\zeta} \epsilon_{\alpha\beta\zeta} t_{\beta,i}^{\dagger} t_{\zeta,i} t_{\alpha,i+1}^{\dagger} s_{i+1} - \frac{1}{4} \sum_{\alpha,\beta,\zeta,\beta',\zeta'} \epsilon_{\alpha\beta\zeta} \epsilon_{\alpha\beta'\zeta'} t_{\beta,i}^{\dagger} t_{\zeta,i} t_{\beta',i}^{\dagger} t_{\zeta',i}. \quad (\text{A.5c})
\end{aligned}$$

At this stage, to make the calculations easier, we stick to the triplon operator representation given in Sec. 2.3.2 in which the singlet state is defined as the vacuum state, meaning that one sets $s = 1$, leading to

$$\begin{aligned}
\vec{S}_{2,i} \cdot \vec{S}_{1,i+1} &= -\frac{1}{4} \sum_{\alpha} \left(t_{\alpha,i} t_{\alpha,i+1} + t_{\alpha,i} t_{\alpha,i+1}^{\dagger} + t_{\alpha,i}^{\dagger} t_{\alpha,i+1} + t_{\alpha,i}^{\dagger} t_{\alpha,i+1}^{\dagger} \right) \\
&+ \frac{i}{4} \sum_{\alpha,\beta,\zeta} \epsilon_{\alpha\beta\zeta} t_{\alpha,i} t_{\beta,i+1}^{\dagger} t_{\zeta,i+1} + \frac{i}{4} \sum_{\alpha,\beta,\zeta} \epsilon_{\alpha\beta\zeta} t_{\alpha,i}^{\dagger} t_{\beta,i+1}^{\dagger} t_{\zeta,i+1} \\
&- \frac{i}{4} \sum_{\alpha,\beta,\zeta} \epsilon_{\alpha\beta\zeta} t_{\beta,i}^{\dagger} t_{\zeta,i} t_{\alpha,i+1} - \frac{i}{4} \sum_{\alpha,\beta,\zeta} \epsilon_{\alpha\beta\zeta} t_{\beta,i}^{\dagger} t_{\zeta,i} t_{\alpha,i+1}^{\dagger} \\
&- \frac{1}{4} \sum_{\beta,\zeta} t_{\beta,i}^{\dagger} t_{\zeta,i} t_{\beta,i+1}^{\dagger} t_{\zeta,i+1} + \frac{1}{4} \sum_{\beta,\zeta} t_{\zeta,i}^{\dagger} t_{\beta,i} t_{\beta,i+1}^{\dagger} t_{\zeta,i+1}. \quad (\text{A.6})
\end{aligned}$$

Again, taking only bilinear terms into account, we only keep the first term

$$\sum_{i=1}^N \vec{S}_{2,i} \cdot \vec{S}_{1,i+1} = -\frac{1}{4} \sum_{i=1}^N \sum_{\alpha} \left(t_{\alpha,i} t_{\alpha,i+1} + t_{\alpha,i} t_{\alpha,i+1}^{\dagger} + t_{\alpha,i}^{\dagger} t_{\alpha,i+1} + t_{\alpha,i}^{\dagger} t_{\alpha,i+1}^{\dagger} \right). \quad (\text{A.7})$$

Following Eq. (A.3) and the Dirac delta definition

$$\delta_{k,k'} = \frac{1}{N} \sum_{i=1}^N e^{i(k-k')r_i}, \quad (\text{A.8})$$

one finds

$$\begin{aligned}
\sum_{i=1}^N \vec{S}_{2,i} \cdot \vec{S}_{1,i+1} &= -\frac{1}{4} \sum_{i=1}^N \sum_{\alpha} \left(t_{\alpha,i} t_{\alpha,i+1} + t_{\alpha,i} t_{\alpha,i+1}^{\dagger} + t_{\alpha,i}^{\dagger} t_{\alpha,i+1} + t_{\alpha,i}^{\dagger} t_{\alpha,i+1}^{\dagger} \right), \quad (\text{A.9a}) \\
&= -\frac{1}{4N} \sum_{i=1}^N \sum_{k,k',\alpha} \left(t_{k,\alpha} t_{k',\alpha} e^{i(k+k')r_i} e^{ik'} + t_{k,\alpha} t_{k',\alpha}^{\dagger} e^{i(k-k')r_i} e^{-ik'} \right)
\end{aligned}$$

$$+ t_{k,\alpha}^\dagger t_{k',\alpha} e^{i(k'-k)} e^{ik'} + t_{k,\alpha}^\dagger t_{k',\alpha}^\dagger e^{i(-k-k')} e^{-ik'} , \quad (\text{A.9b})$$

$$= -\frac{1}{4} \sum_{k,\alpha} \left(t_{k,\alpha} t_{-k,\alpha} e^{-ik} + t_{k,\alpha} t_{k,\alpha}^\dagger e^{-ik} + t_{k,\alpha}^\dagger t_{k,\alpha} e^{ik} + t_{k,\alpha}^\dagger t_{-k,\alpha}^\dagger e^{ik} \right) , \quad (\text{A.9c})$$

$$= -\frac{1}{4} \sum_{k,\alpha} \left(t_{k,\alpha} t_{-k,\alpha} e^{-ik} + 2t_{k,\alpha}^\dagger t_{k,\alpha} e^{ik} + t_{k,\alpha}^\dagger t_{-k,\alpha}^\dagger e^{ik} + e^{-ik} \right) , \quad (\text{A.9d})$$

$$= -\frac{1}{8} \sum_{k,\alpha} \left(t_{k,\alpha} t_{-k,\alpha} (e^{ik} + e^{-ik}) + 2t_{k,\alpha}^\dagger t_{k,\alpha} (e^{ik} + e^{-ik}) \right. \\ \left. + t_{k,\alpha}^\dagger t_{-k,\alpha}^\dagger (e^{ik} + e^{-ik}) \right) - \frac{1}{8} \sum_{k,\alpha} (e^{ik} + e^{-ik}) , \quad (\text{A.9e})$$

$$= -\frac{1}{4} \sum_{k,\alpha} \cos(k) \left(2t_{k,\alpha}^\dagger t_{k,\alpha} + t_{k,\alpha} t_{-k,\alpha} + t_{k,\alpha}^\dagger t_{-k,\alpha}^\dagger + 3 \right) . \quad (\text{A.9f})$$

Thus, the spin Hamiltonian considering both terms in Eqs. (A.4) and (A.9) can be obtained as

$$\mathcal{H}_s = -\frac{3}{4} J N - \frac{3}{4} J' \sum_k \cos(k) + J \sum_{k,\alpha} t_{k,\alpha}^\dagger t_{k,\alpha} \\ - \frac{1}{4} J' \sum_{k,\alpha} \cos(k) \left(2t_{k,\alpha}^\dagger t_{k,\alpha} + t_{k,\alpha} t_{-k,\alpha} + t_{k,\alpha}^\dagger t_{-k,\alpha}^\dagger \right) . \quad (\text{A.10})$$

B. Triplon dispersion relation

Here we intend to derive the triplon dispersion relation (3.14). To do so, we start with the Bogoliubov transform via

$$t_{k,\alpha} = \tilde{t}_{k,\alpha} \cosh(\theta_k) + \tilde{t}_{-k,\alpha}^\dagger \sinh(\theta_k), \quad (\text{B.1a})$$

$$t_{k,\alpha}^\dagger = \tilde{t}_{k,\alpha}^\dagger \cosh(\theta_k) + \tilde{t}_{-k,\alpha} \sinh(\theta_k). \quad (\text{B.1b})$$

resulting in the following transformed terms appeared in the spin Hamiltonian (3.9) [we omit the triplon flavor index α hereafter where necessary for simplicity]

$$2t_k^\dagger t_k = 2\tilde{t}_k^\dagger \tilde{t}_k \cosh^2(\theta_k) + 2\tilde{t}_k^\dagger \tilde{t}_{-k}^\dagger \cosh(\theta_k) \sinh(\theta_k) + 2\tilde{t}_{-k} \tilde{t}_k \cosh(\theta_k) \sinh(\theta_k) + 2\tilde{t}_{-k} \tilde{t}_{-k}^\dagger \sinh^2(\theta_k), \quad (\text{B.2a})$$

$$t_k t_{-k} = \tilde{t}_k \tilde{t}_{-k} \cosh^2(\theta_k) + \tilde{t}_k \tilde{t}_k^\dagger \cosh(\theta_k) \sinh(\theta_k) + \tilde{t}_{-k}^\dagger \tilde{t}_{-k} \cosh(\theta_k) \sinh(\theta_k) + \tilde{t}_{-k}^\dagger \tilde{t}_k^\dagger \sinh^2(\theta_k), \quad (\text{B.2b})$$

$$t_k^\dagger t_{-k}^\dagger = \tilde{t}_k^\dagger \tilde{t}_{-k}^\dagger \cosh^2(\theta_k) + \tilde{t}_k^\dagger \tilde{t}_k \cosh(\theta_k) \sinh(\theta_k) + \tilde{t}_{-k} \tilde{t}_{-k}^\dagger \cosh(\theta_k) \sinh(\theta_k) + \tilde{t}_{-k} \tilde{t}_k \sinh^2(\theta_k). \quad (\text{B.2c})$$

Given that the expressions are invariant due to $\cos(-k) = \cos(k)$, we exchange $-k$ by k in the above equations, leading to

$$2t_k^\dagger t_k = 2\tilde{t}_k^\dagger \tilde{t}_k \left(\cosh^2(\theta_k) + \sinh^2(\theta_k) \right) + \left(\tilde{t}_k^\dagger \tilde{t}_{-k}^\dagger + \tilde{t}_{-k} \tilde{t}_k \right) \sinh(2\theta_k) + 2 \sinh^2(\theta_k), \quad (\text{B.3a})$$

$$t_k t_{-k} = \tilde{t}_k \tilde{t}_k \sinh(2\theta_k) + \tilde{t}_{-k} \tilde{t}_k \cosh^2(\theta_k) + \tilde{t}_k^\dagger \tilde{t}_{-k}^\dagger \sinh^2(\theta_k) + \frac{1}{2} \sinh(2\theta_k), \quad (\text{B.3b})$$

$$t_k^\dagger t_{-k}^\dagger = \tilde{t}_k^\dagger \tilde{t}_k \sinh(2\theta_k) + \tilde{t}_{-k} \tilde{t}_k \sinh^2(\theta_k) + \tilde{t}_k^\dagger \tilde{t}_{-k}^\dagger \cosh^2(\theta_k) + \frac{1}{2} \sinh(2\theta_k) . \quad (\text{B.3c})$$

Thus, we obtain the spin Hamiltonian as

$$\mathcal{H}_s = J \sum_{k,\alpha} t_{k,\alpha}^\dagger t_{k,\alpha} - \frac{1}{4} J' \sum_{k,\alpha} \cos(k) \left(2 t_{k,\alpha}^\dagger t_{k,\alpha} + t_{k,\alpha} t_{-k,\alpha} + t_{k,\alpha}^\dagger t_{-k,\alpha}^\dagger \right) , \quad (\text{B.4a})$$

$$\begin{aligned} &= \sum_{k,\alpha} \tilde{t}_{k,\alpha}^\dagger \tilde{t}_{k,\alpha} \underbrace{\left(J \cosh(2\theta_k) - \frac{1}{2} \cos(k) [\cosh(2\theta_k) + \sinh(2\theta_k)] \right)}_{\omega_k} \\ &+ \left(\tilde{t}_{-k,\alpha} \tilde{t}_{k,\alpha} + \tilde{t}_{k,\alpha}^\dagger \tilde{t}_{-k,\alpha}^\dagger \right) \left(\frac{1}{2} J \sinh(2\theta_k) - \frac{1}{4} J' \cos(k) [\cosh(2\theta_k) \right. \\ &\quad \left. + \sinh(2\theta_k)] \right) \\ &+ \underbrace{2 \sinh^2(\theta_k) + \sinh(2\theta_k)}_{\text{constant}} . \end{aligned} \quad (\text{B.4b})$$

This Hamiltonian is expected to be diagonal as

$$\mathcal{H}_s = \sum_{k,\alpha} \omega_k \tilde{t}_{k,\alpha}^\dagger \tilde{t}_{k,\alpha} + \text{constant} . \quad (\text{B.5})$$

Thereby, the following term given in the second line of Eq. (B.4b) should be zero, resulting in

$$\frac{1}{2} J \sinh(2\theta_k) - \frac{1}{4} J' \cos(k) [\cosh(2\theta_k) + \sinh(2\theta_k)] = 0 , \quad (\text{B.6a})$$

$$\sinh(\theta_k) \cosh(2\theta_k) = \frac{1}{4} \frac{J'}{J} \cos(k) [\sinh(\theta_k) + \cosh(\theta_k)]^2 , \quad (\text{B.6b})$$

$$\left(e^{\theta_k} - e^{-\theta_k} \right) \left(e^{\theta_k} + e^{-\theta_k} \right) = \frac{J'}{J} \cos(k) e^{2\theta_k} , \quad (\text{B.6c})$$

$$1 - e^{-4\theta_k} = \frac{J'}{J} \cos(k) , \quad (\text{B.6d})$$

$$e^{-2\theta_k} = \sqrt{1 - \frac{J'}{J} \cos(k)} . \quad (\text{B.6e})$$

Now, it is time to find ω_k :

$$\omega_k = J \cosh(2\theta_k) - \frac{1}{2} \cos(k) [\cosh(2\theta_k) + \sinh(2\theta_k)] , \quad (\text{B.7a})$$

$$= \frac{J}{2\sqrt{1 - \frac{J'}{J} \cos(k)}} \left[2 - \frac{J'}{J} \cos(k) \right] - \frac{J' \cos(k)}{2\sqrt{1 - \frac{J'}{J} \cos(k)}} , \quad (\text{B.7b})$$

$$= \frac{1}{2\sqrt{1 - \frac{J'}{J} \cos(k)}} (2J - 2J' \cos(k)) , \quad (\text{B.7c})$$

$$= J \sqrt{1 - \frac{J'}{J} \cos(k)} , \quad (\text{B.7d})$$

where defining $\lambda = J'/J$, the one-triplon dispersion relation is determined by

$$\omega_k = J\sqrt{1 - \lambda \cos(k)}. \quad (\text{B.8})$$

C. Equations of motion

Here we deduce the equations of motion for all defined observables in Sec. 3.4. In the absence of damping effects, we only deal with the Heisenberg term, i.e. the first term of the Lindblad equation. In the beginning, we provide some useful relations

$$[A, B] = -[B, A], \quad (\text{C.1a})$$

$$[cA, B] = c[A, B], \quad (\text{C.1b})$$

$$[AB, C] = A[B, C] + [A, C]B, \quad (\text{C.1c})$$

$$[A, BC] = [A, B]C + B[C, A], \quad (\text{C.1d})$$

$$[AB, CD] = [A, C]BD + C[A, D]B + A[B, C]D + CA[B, D]. \quad (\text{C.1e})$$

where A , B , C and D are operators and c is a complex number.

We start with the phonon sector observables defined by Eq. (3.21), i.e. $q(t) = \langle (b_0^\dagger + b_0)/\sqrt{N} \rangle(t)$, $p(t) = \langle i(b_0^\dagger - b_0)/\sqrt{N} \rangle(t)$ and $n_{\text{ph}}(t) = \langle b_0^\dagger b_0/N \rangle(t)$. Thus, we obtain

$$\begin{aligned} [\mathcal{H}, q(t)] &= [\mathcal{H}_p, q(t)] = \left\langle \frac{\omega_0}{\sqrt{N}} (b_0^\dagger [b_0, b_0^\dagger] + [b_0^\dagger, b_0] b_0) \right\rangle(t) \\ &= \left\langle \frac{\omega_0}{\sqrt{N}} (b_0^\dagger - b_0) \right\rangle(t) = -i\omega_0 p(t), \end{aligned} \quad (\text{C.2a})$$

$$\begin{aligned} [\mathcal{H}, p(t)] &= [\mathcal{H}_p, p(t)] + [\mathcal{H}_{\text{sp,s}}, p(t)] + [\mathcal{H}_1, p(t)] \\ &= \left\langle i \frac{\omega_0}{\sqrt{N}} \underbrace{(b_0^\dagger [b_0, b_0^\dagger] - [b_0^\dagger, b_0] b_0)}_{b_0^\dagger + b_0} \right\rangle(t) \\ &\quad + i \frac{g}{N} \underbrace{\langle [b_0^\dagger + b_0, b_0^\dagger - b_0] \rangle}_2 \sum_k \left(y_k [u_k(t) - 3n(\omega_k)] \right) \end{aligned}$$

$$\begin{aligned}
& + \frac{1}{2} y'_k \left[\underbrace{z_k(t) z_k^*(t)}_{2\text{Re}z_k(t)} \right] (t) + i\mathcal{E}(t) \langle \underbrace{[b_0^\dagger + b_0, b_0^\dagger - b_0]}_2 \rangle (t) \\
& = i\omega_0 q(t) + 2i (\mathcal{E}(t) + g[\mathcal{U}(t) + \mathcal{V}(t)]) , \tag{C.2b}
\end{aligned}$$

$$\begin{aligned}
[\mathcal{H}, n_{\text{ph}}(t)] &= [\mathcal{H}_{\text{sp},s}, p(t)] + [\mathcal{H}_l, p(t)] \\
&= \langle \frac{g}{\sqrt{N}} \underbrace{[b_0^\dagger + b_0, b_0^\dagger b_0]}_{-b_0^\dagger + b_0} \rangle (t) [\mathcal{U}(t) + \mathcal{V}(t)] + \frac{\mathcal{E}(t)}{\sqrt{N}} \langle \underbrace{[b_0^\dagger + b_0, b_0^\dagger b_0]}_{-b_0^\dagger + b_0} \rangle (t) \\
&= i (\mathcal{E}(t) + g[\mathcal{U}(t) + \mathcal{V}(t)]) p(t) , \tag{C.2c}
\end{aligned}$$

where

$$\mathcal{U}(t) = \frac{1}{N} \sum_k y_k [u_k(t) - 3n(\omega_k)] , \tag{C.3a}$$

$$\mathcal{V}(t) = \frac{1}{N} \sum_k y'_k v_k(t) , \tag{C.3b}$$

and $v_k(t) = \text{Re} z_k(t)$.

Now, we employ the Lindblad formalism to take the damping into account for each of $q(t)$, $p(t)$ and $n_{\text{ph}}(t)$. To do so, as mentioned in the Sec. 2.7.2, the only possible Lindblad (jump) operators are $L_i = b_0$ and b_0^\dagger because it is clear from Eq. (2.59) that for $L_i = b_0^\dagger b_0$ or $b_0 b_0^\dagger$ at zero temperature, $n(\omega_0) = 0$, the damping effect is zero. Following Eq. (3.23), we make use of the commutators

$$[b_0^\dagger, q(t)] = \langle \frac{1}{\sqrt{N}} [b_0^\dagger, b_0^\dagger + b_0] \rangle (t) = -\frac{1}{\sqrt{N}} , \tag{C.4a}$$

$$[q(t), b_0] = \langle \frac{1}{\sqrt{N}} [b_0^\dagger + b_0, b_0] \rangle (t) = -\frac{1}{\sqrt{N}} , \tag{C.4b}$$

$$[b_0^\dagger, p(t)] = \langle \frac{i}{\sqrt{N}} [b_0^\dagger, b_0^\dagger - b_0] \rangle (t) = \frac{i}{\sqrt{N}} (t) , \tag{C.4c}$$

$$[p(t), b_0] = \langle \frac{i}{\sqrt{N}} [b_0^\dagger - b_0, b_0] \rangle (t) = -\frac{i}{\sqrt{N}} , \tag{C.4d}$$

$$[b_0^\dagger, n_{\text{ph}}(t)] = \langle \frac{1}{N} [b_0^\dagger, b_0^\dagger b_0] \rangle (t) = -\frac{b_0^\dagger}{N} , \tag{C.4e}$$

$$[n_{\text{ph}}(t), b_0] = \langle \frac{1}{N} [b_0^\dagger b_0, b_0] \rangle (t) = -\frac{b_0}{N} . \tag{C.4f}$$

Inserting these relations in Eq. (3.23) and using Eq. (C.2) at zero temperature, we obtain

$$\begin{aligned}
\frac{d}{dt} q(t) &= i[\mathcal{H}, q(t)] - \frac{1}{2} \gamma_{\text{ph}} (n(\omega_0) + 1) \langle \frac{b_0 + b_0^\dagger}{\sqrt{N}} \rangle (t) \\
&\quad + \frac{1}{2} \gamma_{\text{ph}} n(\omega_0) \langle \frac{b_0^\dagger + b_0}{\sqrt{N}} \rangle (t) \\
&= \omega_0 p(t) - \frac{\gamma_{\text{ph}}}{2} q(t) , \tag{C.5a}
\end{aligned}$$

$$\begin{aligned}
\frac{d}{dt}p(t) &= i[\mathcal{H}, p(t)] - \frac{1}{2}\gamma_{\text{ph}}(n(\omega_0) + 1)\langle \frac{b_0 - b_0^\dagger}{\sqrt{N}} \rangle(t) \\
&\quad + \frac{1}{2}\gamma_{\text{ph}}n(\omega_0)\langle \frac{b_0^\dagger - b_0}{\sqrt{N}} \rangle(t) \\
&= -\omega_0q(t) - 2\left(\mathcal{E}(t) + g[\mathcal{U}(t) + \mathcal{U}(t)]\right) - \frac{\gamma_{\text{ph}}}{2}p(t), \tag{C.5b}
\end{aligned}$$

$$\begin{aligned}
\frac{d}{dt}n_{\text{ph}}(t) &= i[\mathcal{H}, n_{\text{ph}}(t)] - \frac{1}{2}\gamma_{\text{ph}}(n(\omega_0) + 1)\langle \frac{2b_0^\dagger b_0}{N} \rangle(t) \\
&\quad + \frac{1}{2}\gamma_{\text{ph}}n(\omega_0)\langle \frac{2b_0 b_0^\dagger}{N} \rangle(t) \\
&= -\left(\mathcal{E}(t) + g[\mathcal{U}(t) + \mathcal{U}(t)]\right)p(t) - \gamma_{\text{ph}}n_{\text{ph}}(t). \tag{C.5c}
\end{aligned}$$

where γ_{ph} refers to the phonon damping parameter. Thus, in summary, the following EoMs should be solved for the phonon sector:

$$\frac{d}{dt}q(t) = \omega_0p(t) - \frac{\gamma_{\text{ph}}}{2}q(t), \tag{C.6a}$$

$$\frac{d}{dt}p(t) = -\omega_0q(t) - 2[\mathcal{E}(t) + g(\mathcal{U}(t) + \mathcal{V}(t))] - \frac{\gamma_{\text{ph}}}{2}p(t), \tag{C.6b}$$

$$\frac{d}{dt}n_{\text{ph}}(t) = -[\mathcal{E}(t) + g(\mathcal{U}(t) + \mathcal{V}(t))]p(t) - \gamma_{\text{ph}}n_{\text{ph}}(t). \tag{C.6c}$$

As for the spin sector, we use the definitions $u_k(t) = \langle \sum_{\alpha} \tilde{t}_{k,\alpha}^\dagger \tilde{t}_{k,\alpha} \rangle(t)$ and $z_k(t) = \langle \sum_{\alpha} \tilde{t}_{k,\alpha}^\dagger \tilde{t}_{-k,\alpha}^\dagger \rangle(t)$. Also, the diagonalized spin Hamiltonian given by $\mathcal{H}_s = \sum_{q,\beta} \omega_q \tilde{t}_{q,\beta}^\dagger \tilde{t}_{q,\beta}$ fits the notation. We first would list some useful commutators in the following

$$[\tilde{t}_{k,\alpha}^\dagger \tilde{t}_{-k,\alpha}^\dagger, \tilde{t}_{q,\beta}^\dagger \tilde{t}_{q,\beta}] = -\delta_{k,q} \delta_{\alpha\beta} \tilde{t}_{q,\beta}^\dagger \tilde{t}_{-k,\alpha}^\dagger - \delta_{-k,q} \delta_{\alpha\beta} \tilde{t}_{q,\beta}^\dagger \tilde{t}_{k,\alpha}^\dagger = -2\tilde{t}_{k,\alpha}^\dagger \tilde{t}_{-k,\alpha}^\dagger, \tag{C.7a}$$

$$[\tilde{t}_{k,\alpha} \tilde{t}_{-k,\alpha}, \tilde{t}_{q,\beta}^\dagger \tilde{t}_{q,\beta}] = +\delta_{k,q} \delta_{\alpha\beta} \tilde{t}_{-k,\alpha} \tilde{t}_{q,\beta} + \delta_{-k,q} \delta_{\alpha\beta} \tilde{t}_{k,\alpha} \tilde{t}_{q,\beta} = +2\tilde{t}_{-k,\alpha} \tilde{t}_{k,\alpha}, \tag{C.7b}$$

$$[\tilde{t}_{k,\alpha}^\dagger \tilde{t}_{k,\alpha}, \tilde{t}_{q,\beta}^\dagger \tilde{t}_{-q,\beta}^\dagger] = +\delta_{k,q} \delta_{\alpha\beta} \tilde{t}_{k,\alpha}^\dagger \tilde{t}_{-q,\beta}^\dagger + \delta_{k,-q} \delta_{\alpha\beta} \tilde{t}_{q,\beta}^\dagger \tilde{t}_{k,\alpha}^\dagger = +2\tilde{t}_{k,\alpha}^\dagger \tilde{t}_{-k,\alpha}^\dagger, \tag{C.7c}$$

$$\begin{aligned}
[\tilde{t}_{k,\alpha} \tilde{t}_{-k,\alpha}, \tilde{t}_{q,\beta}^\dagger \tilde{t}_{-q,\beta}^\dagger] &= \delta_{k,q} \delta_{\alpha\beta} \tilde{t}_{-k,\alpha} \tilde{t}_{-q,\beta}^\dagger + \delta_{k,-q} \delta_{\alpha\beta} \tilde{t}_{q,\beta}^\dagger \tilde{t}_{-k,\alpha} \\
&\quad + \delta_{-k,q} \delta_{\alpha\beta} \tilde{t}_{k,\alpha} \tilde{t}_{-q,\beta}^\dagger + \delta_{-k,-q} \delta_{\alpha\beta} \tilde{t}_{q,\beta}^\dagger \tilde{t}_{k,\alpha} \\
&= 2 + 2\tilde{t}_{-k,\alpha} \tilde{t}_{-k,\alpha} + 2\tilde{t}_{k,\alpha}^\dagger \tilde{t}_{k,\alpha}. \tag{C.7d}
\end{aligned}$$

We then calculate (at zero temperature $n(\omega_k) = 0$)

$$[\mathcal{H}_s, u_q(t)] = \langle [\sum_{k,\alpha} \omega_k \tilde{t}_{k,\alpha}^\dagger \tilde{t}_{k,\alpha}, \sum_{\beta} \tilde{t}_{q,\beta}^\dagger \tilde{t}_{q,\beta}] \rangle(t) = 0, \tag{C.8a}$$

$$\begin{aligned}
[\mathcal{H}_{\text{sp,s}}, u_q(t)] &= gq(t) \langle [\sum_{k,\alpha} y_k \tilde{t}_{k,\alpha}^\dagger \tilde{t}_{k,\alpha} \\
&\quad + \frac{1}{2}y'_k(\tilde{t}_{k,\alpha}^\dagger \tilde{t}_{-k,\alpha}^\dagger + \tilde{t}_{k,\alpha} \tilde{t}_{-k,\alpha}), \sum_{\beta} \tilde{t}_{q,\beta}^\dagger \tilde{t}_{q,\beta}] \rangle(t)
\end{aligned}$$

$$\begin{aligned}
&= \frac{gq(t)}{2} \langle \sum_{k,\alpha,\beta} y'_k [\tilde{t}_{k,\alpha}^\dagger \tilde{t}_{-k,\alpha}^\dagger, \tilde{t}_{q,\beta}^\dagger \tilde{t}_{q,\beta}] + y'_k [\tilde{t}_{k,\alpha} \tilde{t}_{-k,\alpha}, \tilde{t}_{q,\beta}^\dagger \tilde{t}_{q,\beta}] \rangle (t) \\
&= gq(t) \langle y'_k \underbrace{(z_k(t) - z_k^*(t))}_{2i\text{Im}z_k(t)} \rangle \\
&= 2igq(t) y'_k w_k(t), \tag{C.8b}
\end{aligned}$$

$$[\mathcal{H}_s, z_q(t)] = \langle [\sum_{k,\alpha} \omega_k \tilde{t}_{k,\alpha}^\dagger \tilde{t}_{k,\alpha}, \sum_{\beta} \tilde{t}_{q,\beta}^\dagger \tilde{t}_{-q,\beta}^\dagger] \rangle (t) = 2\omega_k z_k(t), \tag{C.8c}$$

$$\begin{aligned}
[\mathcal{H}_{\text{sp},s}, z_q(t)] &= gq(t) \langle \sum_{k,\alpha,\beta} y_k [\tilde{t}_{k,\alpha}^\dagger \tilde{t}_{k,\alpha}, \tilde{t}_{q,\beta}^\dagger \tilde{t}_{-q,\beta}^\dagger] + \frac{1}{2} y'_k [\tilde{t}_{k,\alpha} \tilde{t}_{-k,\alpha}, \tilde{t}_{q,\beta}^\dagger \tilde{t}_{-q,\beta}^\dagger] \rangle (t) \\
&= 2gq(t) \left(y_k z_k(t) + y'_k [u_k(t) + \frac{3}{2}] \right), \tag{C.8d}
\end{aligned}$$

where in Eq. (C.8b), we have used the definition $w_k(t) = \text{Im} z_k(t)$.

Next, the damping effect is taken into account employing the Lindblad formalism. In the spin sector, the Lindblad operators are again chosen as single operators due to the same reason mentioned in the phonon sector at zero temperature. So, we choose $L_i = \tilde{t}_{k,\alpha}$ and $\tilde{t}_{k,\alpha}^\dagger$. By this, we need the following relations

$$[\tilde{t}_{k,\alpha}^\dagger, u_k(t)] = [\tilde{t}_{k,\alpha}^\dagger, \sum_{\beta} \tilde{t}_{q,\beta}^\dagger \tilde{t}_{q,\beta}] = - \sum_{\alpha} \tilde{t}_{k,\alpha}^\dagger, \tag{C.9a}$$

$$[u_k(t), \tilde{t}_{k,\alpha}] = [\sum_{\beta} \tilde{t}_{q,\beta}^\dagger \tilde{t}_{q,\beta}, \tilde{t}_{k,\alpha}] = - \sum_{\alpha} \tilde{t}_{k,\alpha}, \tag{C.9b}$$

$$[\tilde{t}_{k,\alpha}^\dagger, z_k(t)] = [\tilde{t}_{k,\alpha}^\dagger, \sum_{\beta} \tilde{t}_{q,\beta}^\dagger \tilde{t}_{-q,\beta}^\dagger] = 0, \tag{C.9c}$$

$$[z_k(t), \tilde{t}_{k,\alpha}] = [\sum_{\beta} \tilde{t}_{q,\beta}^\dagger \tilde{t}_{-q,\beta}^\dagger, \tilde{t}_{k,\alpha}] = -2 \sum_{\alpha} \tilde{t}_{-k,\alpha}^\dagger. \tag{C.9d}$$

Inserting these relations in Eq. (3.23) and using Eq. (C.8), we obtain

$$\begin{aligned}
\frac{d}{dt} u_k(t) &= i[\mathcal{H}, u_k(t)] - \frac{1}{2} \gamma_s \langle \sum_{\alpha} 2\tilde{t}_{k,\alpha}^\dagger \tilde{t}_{k,\alpha} \rangle (t) \\
&= 2gq(t) y'_k w_k(t) - \gamma_s u_k(t), \tag{C.10a}
\end{aligned}$$

$$\begin{aligned}
\frac{d}{dt} z_k(t) &= i[\mathcal{H}, z_k(t)] - \frac{1}{2} \gamma_s \langle \sum_{\alpha} 2\tilde{t}_{k,\alpha}^\dagger \tilde{t}_{-k,\alpha}^\dagger \rangle (t) \\
&= 2i\omega_k z_k(t) + 2igq(t) \left(y_k z_k(t) + y'_k [u_k(t) + \frac{3}{2}] \right) - \gamma_s z_k(t), \tag{C.10b}
\end{aligned}$$

where γ_s is the spin damping parameter. As previously defined, $z_k(t) = v_k(t) + iw_k(t)$ is a complex operator with the EoM given by Eq. (C.10b). However, we separate real and imaginary parts for simplicity to have

$$\begin{aligned}
\frac{d}{dt} [v_k(t) + iw_k(t)] &= 2i\omega_k [v_k(t) + iw_k(t)] \\
&\quad + 2igq(t) \left(y_k [v_k(t) + iw_k(t)] + y'_k [u_k(t) + \frac{3}{2}] \right) - \gamma_s [v_k(t) + iw_k(t)], \tag{C.11a}
\end{aligned}$$

$$\frac{d}{dt} v_k(t) = -2\omega_k w_k(t) - 2gq(t) y_k w_k(t) - \gamma_s v_k(t), \tag{C.11b}$$

$$\frac{d}{dt}w_k(t) = 2\omega_k v_k(t) + 2gq(t) \left(y_k v_k(t) + y'_k \left[u_k(t) + \frac{3}{2} \right] \right) - \gamma_s w_k(t). \quad (\text{C.11c})$$

Thus, for the spin sector the following EoMs are obtained:

$$\frac{d}{dt}u_k(t) = 2gq(t) y'_k w_k(t) - \gamma_s u_k(t), \quad (\text{C.12a})$$

$$\frac{d}{dt}v_k(t) = -2 [\omega_k + gq(t) y_k] w_k(t) - \gamma_s v_k(t), \quad (\text{C.12b})$$

$$\frac{d}{dt}w_k(t) = 2 [\omega_k + gq(t) y_k] v_k(t) + 2gq(t) y'_k \left[u_k(t) + \frac{3}{2} \right] - \gamma_s w_k(t). \quad (\text{C.12c})$$

D. Resonant triplon criterion

In this appendix, we derive the resonant triplon criterion to find the driving parameters suitable for the formation of NESS; those causing the spin system to inhibit NESS formation. In general, we deal with the EoMs given by Eqs. (3.26a)-(3.26c) in the triplon system and the phonon displacement $q(t) = 2\frac{a}{\gamma_{\text{ph}}} \sin(\omega_0 t) = 2\frac{DJ}{g} \sin(\omega_0 t)$ as follows

$$\frac{d}{dt}u_k(t) = 2gq(t)y'_k \text{Im}z_k(t) - \gamma_s u_k(t), \quad (\text{D.1a})$$

$$\frac{d}{dt}z_k(t) = 2i\omega_k z_k(t) + 2igq(t) \left(y_k z_k(t) + y'_k [u_k(t) + \frac{3}{2}] \right) - \gamma_s z_k(t). \quad (\text{D.1b})$$

To find $u_k(t)$ solution quantitatively, one needs $z_k(t)$ as well. Let us call in $z_k(t)$

$$f_k(t) = 4DJ \sin(\omega_0 t) y'_k [u_k(t) + \frac{3}{2}], \quad (\text{D.2})$$

leading to

$$\frac{d}{dt}z_k(t) = \underbrace{2i[\omega_k + 2DJ \sin(\omega_0 t) y_k]}_{i \frac{d}{dt} h_k(t)} z_k(t) + i f_k(t) - \gamma_s z_k(t), \quad (\text{D.3})$$

in which we have defined

$$h_k(t) = 2 \int [\omega_k + 2DJ \sin(\omega_0 t) y_k] dt = 2\omega_k t - \frac{4DJ y_k}{\omega_0} \cos(\omega_0 t), \quad (\text{D.4})$$

allowing the solution of Eq. (D.3) to be expressed in the form

$$\frac{d}{dt}z_k(t) - i \left[\frac{d}{dt} h_k(t) \right] z_k(t) + \gamma_s z_k(t) = i f_k(t), \quad (\text{D.5a})$$

$$\frac{d}{dt}[z_k(t)e^{-ih_k(t)+\gamma_s t}]e^{+ih_k(t)-\gamma_s t} = \mathbf{i}f_k(t), \quad (\text{D.5b})$$

$$\frac{d}{dt}[z_k(t)e^{-ih_k(t)+\gamma_s t}] = \mathbf{i}f_k(t)e^{-ih_k(t)+\gamma_s t}, \quad (\text{D.5c})$$

$$z_k(t) = \mathbf{i}e^{+ih_k(t)-\gamma_s t} \int_0^t f_k(t')e^{-ih_k(t')+\gamma_s t'} dt'. \quad (\text{D.5d})$$

It is clear that we should do something to get rid of the integral in the r.h.s of Eq. (D.5d) to have $z_k(t)$ and finally $u_k(t)$. Let us perform one more simplification. From the previous results, we noticed that the dominant triplon occupation is the one at the resonant condition, $\omega_0 = 2\omega_{k_{\text{res}}}$, where k_{res} is called the resonant momentum. Substituting Eq. (D.2) into Eq. (D.5d), we would rewrite $z_{k_{\text{res}}}(t)$ as

$$z_{k_{\text{res}}}(t) = \mathbf{i}e^{+ih_{k_{\text{res}}}(t)-\gamma_s t} \int_0^t \left(4DJ \sin(\omega_0 t') y'_{k_{\text{res}}}[u_{k_{\text{res}}}(t') + \frac{3}{2}] \right) e^{-ih_{k_{\text{res}}}(t')+\gamma_s t'} dt', \quad (\text{D.6a})$$

$$= 4\mathbf{i}DJ y'_{k_{\text{res}}} e^{+ih_{k_{\text{res}}}(t)-\gamma_s t} \int_0^t \left(\sin(\omega_0 t') e^{-ih_{k_{\text{res}}}(t')} [u_{k_{\text{res}}}(t') + \frac{3}{2}] \right) e^{\gamma_s t'} dt'. \quad (\text{D.6b})$$

We average over one period $T_0 = 2\pi/\omega_0$ to get rid of fast oscillations and use Eq. (D.4) to calculate

$$\frac{1}{T_0} \int_0^{T_0} \sin(\omega_0 t') e^{-\mathbf{i}[2\omega_{k_{\text{res}}} t' - \frac{4DJ y_{k_{\text{res}}}}{\omega_0} \cos(\omega_0 t')]} dt' = \frac{\omega_0}{4DJ y_{k_{\text{res}}}} J_1\left(\frac{4DJ y_{k_{\text{res}}}}{\omega_0}\right), \quad (\text{D.7})$$

where $J_1(4DJ y_{k_{\text{res}}}/\omega_0)$ is the Bessel function of the first kind. By this, we obtain

$$z_{k_{\text{res}}}(t) = \mathbf{i} \frac{y'_{k_{\text{res}}}}{y_{k_{\text{res}}}} \omega_0 J_1\left(\frac{4DJ y_{k_{\text{res}}}}{\omega_0}\right) e^{+ih_{k_{\text{res}}}(t)-\gamma_s t} \int_0^t [u_{k_{\text{res}}}(t') + \frac{3}{2}] e^{+\gamma_s t'} dt'. \quad (\text{D.8})$$

Going back to Eq. (D.1a) to calculate $u_{k_{\text{res}}}(t)$, we use $2\mathbf{i}\text{Im}z_k(t) = z_k(t) - z_k^*(t)$

$$\frac{d}{dt}u_{k_{\text{res}}}(t) + \gamma_s u_{k_{\text{res}}}(t) = -2\mathbf{i}DJ \sin(\omega_0 t) y'_{k_{\text{res}}}[z_{k_{\text{res}}}(t) - z_{k_{\text{res}}}^*(t)], \quad (\text{D.9a})$$

$$\frac{d}{dt}[u_{k_{\text{res}}}(t)e^{\gamma_s t}]e^{-\gamma_s t} = -2\mathbf{i}DJ \sin(\omega_0 t) y'_{k_{\text{res}}}[z_{k_{\text{res}}}(t) - z_{k_{\text{res}}}^*(t)], \quad (\text{D.9b})$$

$$u_{k_{\text{res}}}(t)e^{\gamma_s t} = -2\mathbf{i}DJ y'_{k_{\text{res}}} \int_0^t \sin(\omega_0 t') e^{+\gamma_s t'} [z_{k_{\text{res}}}(t') - z_{k_{\text{res}}}^*(t')] dt'. \quad (\text{D.9c})$$

It is not hard to deduce

$$e^{+\gamma_s t'} [z_{k_{\text{res}}}(t') - z_{k_{\text{res}}}^*(t')] = \mathbf{i} \frac{y'_{k_{\text{res}}}}{y_{k_{\text{res}}}} \omega_0 J_1\left(\frac{4DJ y_{k_{\text{res}}}}{\omega_0}\right) [e^{+ih_{k_{\text{res}}}(t'')} + e^{-ih_{k_{\text{res}}}(t'')}] \cdot \int_0^{t'} [u_{k_{\text{res}}}(t'') + \frac{3}{2}] e^{+\gamma_s t''} dt'', \quad (\text{D.10})$$

wherein the integral term is a real quantity. Thus, we have

$$u_{k_{\text{res}}}(t)e^{\gamma_s t} = 2DJ \frac{y_{k_{\text{res}}}^{\prime 2}}{y_{k_{\text{res}}}} \omega_0 J_1\left(\frac{4DJ y_{k_{\text{res}}}}{\omega_0}\right) \int_0^t \sin(\omega_0 t') \underbrace{[e^{ih_{k_{\text{res}}}(t')} + e^{-ih_{k_{\text{res}}}(t')}]}_{2\text{Re}[e^{+ih_{k_{\text{res}}}(t')}] \cdot \left(\int_0^{t'} [u_{k_{\text{res}}}(t'') + \frac{3}{2}] e^{+\gamma_s t''} dt'' \right) dt', \quad (\text{D.11})$$

where we again average over one period T_0 via Eq. (D.7), yielding

$$u_{k_{\text{res}}}(t)e^{\gamma_s t} = \underbrace{\left[\frac{y'_{k_{\text{res}}}\omega_0}{y_{k_{\text{res}}}} J_1\left(\frac{4DJy_{k_{\text{res}}}}{\omega_0}\right) \right]^2}_{\Gamma_{k_{\text{res}}}} \text{Re} \int_0^t \left(\int_0^{t'} [u_{k_{\text{res}}}(t'') + \frac{3}{2}] e^{\gamma_s t''} dt'' \right) dt'. \quad (\text{D.12})$$

Taking the second derivative of the l.h.s of equation above into account,

$$\frac{d^2}{dt^2}[u_{k_{\text{res}}}(t)e^{\gamma_s t}] = \left(\frac{d^2}{dt^2}u_{k_{\text{res}}}(t) + 2\gamma_s \frac{d}{dt}u_{k_{\text{res}}}(t) + \gamma_s^2 u_{k_{\text{res}}}(t) \right) e^{\gamma_s t}, \quad (\text{D.13})$$

the EoM for $u_{k_{\text{res}}}(t)$ is obtained as

$$\frac{d^2}{dt^2}u_{k_{\text{res}}}(t) + 2\gamma_s \frac{d}{dt}u_{k_{\text{res}}}(t) + (\gamma_s^2 - \Gamma_{k_{\text{res}}}^2)u_{k_{\text{res}}}(t) - \frac{3}{2}\Gamma_{k_{\text{res}}}^2 = 0. \quad (\text{D.14})$$

This differential equation can readily be solved with the relevant initial conditions, $u_{k_{\text{res}}}(0) = 0$ and $\text{ddt}u_{k_{\text{res}}}(0) = 0$ through the Mathematica software or whatever. Therefore, the final expression for $u_{k_{\text{res}}}(t)$ is given by

$$u_{k_{\text{res}}}(t) = \frac{3}{4}\Gamma_{k_{\text{res}}} \left[\frac{1 - e^{-(\gamma_s - \Gamma_{k_{\text{res}}})t}}{\gamma_s - \Gamma_{k_{\text{res}}}} - \frac{1 - e^{-(\gamma_s + \Gamma_{k_{\text{res}}})t}}{\gamma_s + \Gamma_{k_{\text{res}}}} \right]. \quad (\text{D.15})$$

Following Eq. (D.8), $z_{k_{\text{res}}}(t)$ can be found as well.

E. Detuned triplon criterion

In this appendix, we derive the detuned triplon criterion to find the driving parameters suitable for the formation of NESS. In this case, the driving phonon acts as a “detuned” pump of all other triplon modes. Let us define

$$\delta = 2\omega_k - \omega_0, \quad (\text{E.1})$$

meaning that the excited mode k is detuned from the driving assuming $|\delta| < \omega_0$, i.e. we assume that the detuning is small compared to the driving, which δ can be positive or negative. We repeat the calculations in the Appendix D up to Eq. (D.5d):

$$z_k(t) = \mathbf{i} e^{+\mathbf{i}h_k(t) - \gamma_{\text{st}} t} \int_0^t f_k(t') e^{-\mathbf{i}h_k(t') + \gamma_{\text{st}} t'} dt', \quad (\text{E.2a})$$

$$h_k(t) = 2\omega_k t - \frac{4DJy_k}{\omega_0} \cos(\omega_0 t), \quad (\text{E.2b})$$

$$f_k(t) = 4DJ \sin(\omega_0 t) y'_k [u_k(t) + \frac{3}{2}], \quad (\text{E.2c})$$

where in Eq. (E.2b), we have $2\omega_k = \delta + \omega_0$ this time. By this and averaging over one period $T_0 = 2\pi/\omega_0$, one calculates

$$\frac{1}{T_0} \int_0^{T_0} \sin(\omega_0 t') e^{-\mathbf{i}[(\delta + \omega_0)t' - \frac{4DJy_k}{\omega_0} \cos(\omega_0 t')]} dt' = \frac{\omega_0 e^{-\mathbf{i}\delta t}}{4DJy_k} J_1\left(\frac{4DJy_k}{\omega_0}\right), \quad (\text{E.3})$$

resulting in

$$z_k(t) = \mathbf{i} \frac{y'_k}{y_k} \omega_0 J_1\left(\frac{4DJy_k}{\omega_0}\right) e^{+\mathbf{i}h_k(t) - \gamma_{\text{st}} t} \int_0^t [u_k(t') + \frac{3}{2}] e^{+\gamma_{\text{st}} t'} e^{-\mathbf{i}\delta t'} dt', \quad (\text{E.4})$$

and

$$u_k(t)e^{\gamma_s t} = \Gamma_k^2 \operatorname{Re} \int_0^t e^{+i\delta t'} \underbrace{\left(\int_0^{t'} [u_k(t'') + \frac{3}{2}] e^{\gamma_s t''} e^{-i\delta t''} dt'' \right)}_{Q(t')} dt', \quad (\text{E.5})$$

where $\Gamma_k = \frac{y'_k \omega_0}{y_k} J_1(4DJy_k/\omega_0)$. For simplicity we define $\tilde{u}_k(t) = u_k(t)e^{\gamma_s t}$, so

$$\tilde{u}_k(t) = \Gamma_k^2 \operatorname{Re} \int_0^t e^{+i\delta t'} Q(t') dt'. \quad (\text{E.6})$$

Taking the second derivative of $\tilde{u}_k(t)$ as before, one yields

$$\frac{d^2}{dt^2} \tilde{u}_k(t) = \Gamma_k^2 \operatorname{Re} \left(i\delta e^{+i\delta t} Q(t) + [\tilde{u}_k(t) + \frac{3}{2} e^{\gamma_s t}] \right). \quad (\text{E.7})$$

This equation contains the imaginary parts of $e^{+i\delta t} Q(t)$ and one needs to take one further derivative,

$$\frac{d^3}{dt^3} \tilde{u}_k(t) = (\Gamma_k^2 - \delta^2) \frac{d}{dt} \tilde{u}_k(t) + \frac{3}{2} \gamma_s \Gamma_k^2 e^{\gamma_s t}. \quad (\text{E.8})$$

Let us define

$$\tilde{\Gamma}_k^2 = \Gamma_k^2 - \delta^2, \quad (\text{E.9})$$

leading, considering $\mathcal{X}_k(t) = \frac{d}{dt} \tilde{u}_k(t)$ to

$$\frac{d^2}{dt^2} \mathcal{X}_k(t) - \tilde{\Gamma}_k^2 \mathcal{X}_k(t) - \frac{3}{2} \gamma_s \Gamma_k^2 e^{\gamma_s t} = 0, \quad (\text{E.10})$$

with the initial conditions $\mathcal{X}_k(0) = \frac{d}{dt} \tilde{u}_k(0) = 0$ and $\frac{d}{dt} \mathcal{X}_k(0) = \frac{d^2}{dt^2} \tilde{u}_k(0) = \frac{3}{2} \Gamma_k^2$ [see Eq. (E.7)]. It is well-known that this equation possesses the superposition of the homogeneous and the particular solution as follows

$$\mathcal{X}_{k_h}(t) = \frac{1}{\tilde{\Gamma}_k} \sinh(\tilde{\Gamma}_k t), \quad \tilde{\Gamma}_k \geq 0, \quad (\text{E.11a})$$

$$\mathcal{X}_{k_p}(t) = \frac{3\Gamma_k^2 \gamma_s}{4\tilde{\Gamma}_k} \left(\frac{e^{+\gamma_s t} - e^{+\tilde{\Gamma}_k t}}{\gamma_s - \tilde{\Gamma}_k} - \frac{e^{+\gamma_s t} - e^{-\tilde{\Gamma}_k t}}{\gamma_s + \tilde{\Gamma}_k} \right). \quad (\text{E.11b})$$

Thus, the total solution for $\Gamma_k > |\delta|$ is given by

$$\mathcal{X}_k(t) = \frac{d}{dt} \mathcal{X}_k(0) \mathcal{X}_{k_h}(t) + \mathcal{X}_{k_p}(t), \quad (\text{E.12a})$$

$$= \frac{3\Gamma_k^2}{2\tilde{\Gamma}_k} \sinh(\tilde{\Gamma}_k t) + \frac{3\Gamma_k^2 \gamma_s}{4\tilde{\Gamma}_k} \left(\frac{e^{+\gamma_s t} - e^{+\tilde{\Gamma}_k t}}{\gamma_s - \tilde{\Gamma}_k} - \frac{e^{+\gamma_s t} - e^{-\tilde{\Gamma}_k t}}{\gamma_s + \tilde{\Gamma}_k} \right). \quad (\text{E.12b})$$

However, this is the solution of $\frac{d}{dt} \tilde{u}_k(t) = \mathcal{X}_k(t)$. To find $\tilde{u}_k(t)$, we simply perform the following integration

$$\tilde{u}_k(t) = \int_0^t \mathcal{X}_k(t') dt' = \frac{3}{2} \frac{\Gamma_k^2}{\tilde{\Gamma}_k (\gamma_s^2 - \tilde{\Gamma}_k^2)} \left(\tilde{\Gamma}_k [e^{\gamma_s t} - \cosh(\tilde{\Gamma}_k t)] - \gamma_s \sinh(\tilde{\Gamma}_k t) \right), \quad (\text{E.13})$$

and finally using the relation $\tilde{u}_k(t) = u_k(t)e^{\gamma_s t}$ we obtain

$$u_k(t) = \frac{3}{2} \frac{\Gamma_k^2}{\tilde{\Gamma}_k(\gamma_s^2 - \tilde{\Gamma}_k^2)} \left(\tilde{\Gamma}_k [1 - e^{-\gamma_s t} \cosh(\tilde{\Gamma}_k t)] - \gamma_s e^{-\gamma_s t} \sinh(\tilde{\Gamma}_k t) \right). \quad (\text{E.14})$$

Furthermore, having the triplon occupation $u_k(t)$, the complex off-diagonal number $z_k(t)$ can easily be calculated through the integrations in Eq. (E.4). However, we don't need $z_k(t)$ much in the present paper and we omit the presentation of its final lengthy-expression.

Note that for $\tilde{\Gamma}_k < 0$, i.e. when $\Gamma_k < |\delta|$, $\mathcal{X}_{k_h}(t)$ switches to an oscillatory sinusoidal function and we simply obtain

$$u_k(t) = \frac{3}{2} \frac{\Gamma_k^2}{\tilde{\mathcal{G}}_k(\gamma_s^2 + \tilde{\mathcal{G}}_k^2)} \left(\tilde{\mathcal{G}}_k [1 - e^{-\gamma_s t} \cos(\tilde{\mathcal{G}}_k t)] - \gamma_s e^{-\gamma_s t} \sin(\tilde{\mathcal{G}}_k t) \right), \quad (\text{E.15})$$

where $\tilde{\mathcal{G}}_k^2 = \delta^2 - \Gamma_k^2$.

F. Renormalized triplon dispersion

In this appendix, we derive the renormalized two-triplon dispersion through the phonon displacement \bar{q}_0 . To start, we use the spin, phonon, and spin-phonon Hamiltonians

$$\begin{aligned} \mathcal{H}_s = & \underbrace{-\frac{3}{4}JN - \frac{3}{4}J' \sum_k \cos(k)}_{\mathcal{H}_0} + J \sum_{k,\alpha} t_{k,\alpha}^\dagger t_{k,\alpha} \\ & - \frac{1}{4}J' \sum_{k,\alpha} \cos(k) \left(2t_{k,\alpha}^\dagger t_{k,\alpha} + t_{k,\alpha} t_{-k,\alpha} + t_{k,\alpha}^\dagger t_{-k,\alpha}^\dagger \right), \end{aligned} \quad (\text{F.1a})$$

$$\langle \mathcal{H}_p \rangle = \omega_0 \langle b_0^\dagger b_0 \rangle = \frac{N\omega_0}{4} \bar{q}_0^2 = \mathcal{E}_{\text{ph}}, \quad (\text{F.1b})$$

$$\mathcal{H}_{\text{sp,s}} = g \bar{q}_0 \sum_{k,\alpha} \left[t_{k,\alpha}^\dagger t_{k,\alpha} - \langle t_{k,\alpha}^\dagger t_{k,\alpha} \rangle_{\text{eq}} \right], \quad (\text{F.1c})$$

where we have used the definition $\bar{q}_0 = \langle d \rangle$. The effective Hamiltonian versus the phonon displacement \bar{q}_0 is given by

$$\begin{aligned} \mathcal{H}_{\text{eff}} = \mathcal{H}_s + \langle \mathcal{H}_p \rangle + \mathcal{H}_{\text{sp,s}} = & \sum_{k,\alpha} t_{k,\alpha}^\dagger t_{k,\alpha} \underbrace{\left(J - \frac{J'}{2} \cos(k) + g\bar{q}_0 \right)}_{\mathcal{A}_k} \\ & + \frac{1}{2} \sum_{k,\alpha} \left(t_{k,\alpha} t_{-k,\alpha} + t_{k,\alpha}^\dagger t_{-k,\alpha}^\dagger \right) \underbrace{\left(-\frac{J'}{2} \cos(k) \right)}_{\mathcal{B}_k} \\ & - g \bar{q}_0 \underbrace{\sum_{k,\alpha} \langle t_{k,\alpha}^\dagger t_{k,\alpha} \rangle_{\text{eq}}}_{\frac{3}{2} \sum_k [y_k - 1]} + \mathcal{E}_{\text{ph}} + \mathcal{H}_0, \end{aligned}$$

where we have applied Eq. (3.30) for the equilibrium triplon occupation with $y_k = \frac{1 - \frac{\lambda}{2} \cos(k)}{\sqrt{1 - \lambda \cos(k)}}$. Thus, we obtain

$$\mathcal{H}_{\text{eff}} = \sum_{k,\alpha} \mathcal{A}_k t_{k,\alpha}^\dagger t_{k,\alpha} + \frac{1}{2} \mathcal{B}_k \left(t_{k,\alpha} t_{-k,\alpha} + t_{k,\alpha}^\dagger t_{-k,\alpha}^\dagger \right) - \frac{3}{2} g \bar{q}_0 \sum_k [y_k - 1] + \mathcal{E}_{\text{ph}} + \mathcal{H}_0. \quad (\text{F.2})$$

Inspiring the Bogoliubov transformation, Eqs. (B.1) and (B.2), we find the ground state energy through

$$\begin{aligned} \mathcal{H}_{\text{eff}} = & \sum_{k,\alpha} \tilde{t}_{k,\alpha}^\dagger \tilde{t}_{k,\alpha} \underbrace{\left[\mathcal{A}_k \left(\cosh^2 \theta_k + \sinh^2 \theta_k \right) + \mathcal{B}_k \sinh 2\theta_k \right]}_{\tilde{\omega}_k} \\ & + \sum_{k,\alpha} \left(\tilde{t}_{k,\alpha} \tilde{t}_{-k,\alpha} + \tilde{t}_{k,\alpha}^\dagger \tilde{t}_{-k,\alpha}^\dagger \right) \left[\frac{1}{2} \mathcal{A}_k \sinh 2\theta_k + \frac{1}{2} \mathcal{B}_k \left(\cosh^2 \theta_k + \sinh^2 \theta_k \right) \right] \\ & + 3 \underbrace{\sum_k \left(\mathcal{A}_k \sinh^2 \theta_k + \frac{1}{2} \mathcal{B}_k \sinh 2\theta_k \right) - \frac{3}{2} g \bar{q}_0 \sum_k [y_k - 1] + \mathcal{E}_{\text{ph}} + \mathcal{H}_0}_{\mathcal{E}_{\text{ground}}}. \end{aligned} \quad (\text{F.3})$$

This Hamiltonian is expected to be diagonal as

$$\mathcal{H}_{\text{eff}} = \sum_{k,\alpha} \tilde{\omega}_k \tilde{t}_{k,\alpha}^\dagger \tilde{t}_{k,\alpha} + \mathcal{E}_{\text{ground}}, \quad (\text{F.4})$$

implying that the second line in Eq. (F.3) should be zero, resulting in

$$e^{-2\theta_k} = \sqrt{\frac{\mathcal{A}_k + \mathcal{B}_k}{\mathcal{A}_k - \mathcal{B}_k}}, \quad (\text{F.5})$$

and hence, leading to the following ground-state energy

$$\mathcal{E}_{\text{ground}} = \frac{3}{2} \sum_k \left(\sqrt{\mathcal{A}_k^2 - \mathcal{B}_k^2} - \mathcal{A}_k \right) - \frac{3}{2} g \bar{q}_0 \sum_k [y_k - 1] + \mathcal{E}_{\text{ph}} + \mathcal{H}_0. \quad (\text{F.6})$$

For the two-triplon band through the phonon displacement \bar{q}_0 , we use first line of Eq. (F.3) and (F.5) to obtain

$$\tilde{\omega}_k = \sqrt{\mathcal{A}_k^2 - \mathcal{B}_k^2} = Jx \sqrt{1 - \frac{\lambda}{x} \cos(k)} = (J + g \bar{q}_0) \sqrt{1 - \frac{J'}{J + g \bar{q}_0} \cos(k)}. \quad (\text{F.7})$$

G. Energy flow $P^{\text{SP},\text{B}}(t)$

To obtain the physical sum rule in the entire system considered in Fig. 3.2 and Fig. 4.14, it is necessary to consider in detail the SPC term. To do so, we use Eq. (3.17) to calculate the flow of energy from the SPC towards the bath, $P^{\text{SP},\text{B}}(t)$. It is easy to read from Eq. (3.17)

$$\langle \mathcal{H}_{\text{sp}} \rangle (t) = gq(t) [\mathcal{U}(t) + \mathcal{V}(t)] , \quad (\text{G.1})$$

and hence the time derivative

$$\frac{d}{dt} \langle \mathcal{H}_{\text{sp}} \rangle (t) = g \frac{d}{dt} q(t) [\mathcal{U}(t) + \mathcal{V}(t)] + gq(t) \frac{d}{dt} [\mathcal{U}(t) + \mathcal{V}(t)] , \quad (\text{G.2})$$

wherein one uses Eqs. (3.24a), (3.26a) and (3.26b) to have

$$\frac{d}{dt} q(t) = \omega_0 p(t) - \frac{\gamma_{\text{ph}}}{2} q(t) , \quad (\text{G.3a})$$

$$\begin{aligned} \frac{d}{dt} \mathcal{U}(t) &= \frac{1}{N} \sum_k y_k \frac{d}{dt} u_k(t) \\ &= \frac{1}{N} \sum_k y_k \left(2gq(t) y'_k w_k(t) - \gamma_s [u_k(t) - 3n(\omega_k)] \right) , \end{aligned} \quad (\text{G.3b})$$

$$\begin{aligned} \frac{d}{dt} \mathcal{V}(t) &= \frac{1}{N} \sum_k y'_k \frac{d}{dt} v_k(t) \\ &= \frac{1}{N} \sum_k y'_k \left(-2 [\omega_k + gq(t) y_k] w_k(t) - \gamma_s v_k(t) \right) , \end{aligned} \quad (\text{G.3c})$$

leading to [see Eqs. (3.25)]

$$\frac{d}{dt} [\mathcal{U}(t) + \mathcal{V}(t)] = -\frac{2}{N} \sum_k y'_k \omega_k w_k(t) - \gamma_s [\mathcal{U}(t) + \mathcal{V}(t)] . \quad (\text{G.4})$$

Thus, Eq. (G.2) can be rewritten as [see Eqs. (4.12c) and (4.15a)]

$$\begin{aligned}
\frac{d}{dt} \langle \mathcal{H}_{\text{sp}} \rangle (t) &= \underbrace{g\omega_0 [\mathcal{U}(t) + \mathcal{V}(t)] p(t)}_{P^{\text{P,SP}}(t)} - g \frac{\gamma_{\text{ph}}}{2} q(t) [\mathcal{U}(t) + \mathcal{V}(t)] \\
&\quad - \underbrace{\frac{2gq(t)}{N} \sum_k y'_k \omega_k w_k(t)}_{P^{\text{SP,S}}(t)} - gq(t) \gamma_s [\mathcal{U}(t) + \mathcal{V}(t)] \\
&= P^{\text{P,SP}}(t) - P^{\text{SP,S}}(t) - \underbrace{gq(t) \left(\gamma_s + \frac{\gamma_{\text{ph}}}{2} \right) [\mathcal{U}(t) + \mathcal{V}(t)]}_{P^{\text{SP,B}}(t)},
\end{aligned} \tag{G.5}$$

where the last term refers to the dissipation of the SPC part of the system. Finally, we obtain

$$P^{\text{SP,B}}(t) = gq(t) \left(\gamma_s + \frac{\gamma_{\text{ph}}}{2} \right) [\mathcal{U}(t) + \mathcal{V}(t)] . \tag{G.6}$$

List of Figures

2.1	The singlet and triplet states of two spin-1/2 particles in a dimer.	21
2.2	Schematic illustration of an open quantum system and its environment that together constitute a closed quantum system.	28
3.1	(a) The octahedral crystal structure of CuGeO_3 constructed of CuO_2 ribbons connected to each other via GeO_4 tetrahedra. (b) and (c) CuO_2 ribbons projected in the a,b-c, and a-b plane, respectively. The nearest and next-nearest neighbor exchange constant corresponds respectively to the path Cu-O2-Cu and dashed line in (b) [202, 203].	38
3.2	Schematic of the system under study consisting of the spin system, driven Einstein phonon, laser field, and the bath. The intradimer spin-spin coupling, interdimer spin-spin coupling, the SPC, phonon damping, and spin damping are described respectively by $J = 10$ meV, J' , g , γ_{ph} , and γ_{s} . The laser continuously pumps energy into the system and then drives it out of equilibrium. Blue ellipses display dimer singlets and the red one a triplon excitation.	40
3.3	(a) One-triplon band spectrum and (b) corresponding density of states (in arbitrary units) of a dimerized spin-1/2 chain, respectively. The triplon mode-dependent prefactors y_k and y'_k are presented respectively in (c) and (d).	44
4.1	Response of the Einstein phonon to a resonant driving field. Here $\omega_0/J = 1$, $a/J = 0.004$, $\gamma_{\text{ph}} = 0.02\omega_0$, and $g = 0$. (a) phonon occupation, $n_{\text{ph}}(t)$ – the inset shows the steady state of the driven phonon system at long times. (b) Phonon displacement, $q(t)$, and momentum, $p(t)$, shown from $t = 0$ and (c) $q(t)$ and $p(t)$ at long times.	54

4.2 Time-dependence of the phonon occupation, $n_{\text{ph}}(t)$, and triplon occupation, $n_{\text{x}}(t)$, shown with $a/\gamma_{\text{ph}} = 0.2$ and $g/J = 0.05$. (a) When $\omega_0/J = 1.5$ and $\gamma_{\text{s}}/J = 0.01$, the system converges to a NESS on a conventional timescale. (b) When $\omega_0/J = 1.5$ and $\gamma_{\text{s}}/J = 0$, $n_{\text{x}}(t)$ increases rapidly, destabilizing the phonon occupation. (c) When $\omega_0/J = 3.0$, the driving frequency lies sufficiently far above the two-triplon band that NESS exist even when $\gamma_{\text{s}}/J = 0$. (d) When $\omega_0/J = 0.75$, the driving frequency lies well below the two-triplon band but the second harmonic, $2\omega_0$, lies within it. In this case, when $\gamma_{\text{s}}/J = 0$ the lattice approximates a NESS, but with this near-constant driving of the spin system a NESS cannot be formed. 56

4.3 (a) Response of the spin system, measured by $n_{\text{x}}(t)$, to the driving phonon frequencies $\omega_0/J = 0.5, 1.0, 1.5, 2.0, 2.5$, and 3.0 at fixed $a/\gamma_{\text{ph}} = 0.2$, $g/J = 0.1$, and $\gamma_{\text{s}}/J = 0.01$. $n_{\text{x}}(t)$ in the spin NESS is shown at (b) $\omega_0/J = 0.5$, (c) $\omega_0/J = 1.5$, and (d) $\omega_0/J = 2.5$, where we compare results in the time window $1160 \leq t \leq 1200$ with those at $9960 \leq t \leq 10000$. All blue long-time traces are shifted by a phase $0 \leq \phi < 2\pi$ to see whether the red and blue states can be mapped to each other – as a characterization for the true NESS. 57

4.4 Creation of the NESS established with $a/\gamma_{\text{ph}} = 0.2$ and $g/J = 0.1$ for the driving frequency $\omega_0/J = 1.5$ and spin damping $\gamma_{\text{s}}/J = 0.01$; these are also the parameters of the green line in Fig. 4.3(a). (a) $n_{\text{ph}}(t)$, (b) $n_{\text{x}}(t)$, (c) $u_{k=0}$, and (d) $u_{k=\pi}$. Also shown is the relaxation of each variable when the driving is removed after 3000 time steps. 58

4.5 The same as Fig. 4.4, but for $u_{k_{\text{res}}}(t)$ 59

4.6 Average value of the driven phonon occupation number, $\bar{n}_{\text{ph}0}$, in a NESS, displayed as a function of $(a/\gamma_{\text{ph}})^2$ for various driving frequencies at fixed $\gamma_{\text{ph}} = 0.02\omega_0$ and $\gamma_{\text{s}}/J = 0.01$. (a) In the decoupled case, $g = 0$, and (b) in the presence of a given SPC, $g/J = 0.1$ 60

4.7 (a) Dependence of the average triplon occupation, $\bar{n}_{\text{x}0}$, in the NESS on the fluence, shown as $(a/\gamma_{\text{ph}})^2$, at driving phonon frequencies $\omega_0/J = 0.5, 1.0, 1.5, 2.0, 2.5$, and 3.0 . The fixed system parameters are $g/J = 0.1$, $\gamma_{\text{ph}} = 0.02\omega_0$, and $\gamma_{\text{s}}/J = 0.01$. Only the $\omega_0/J = 0.5$ and 1.5 phonons at very high fluences show deviations from a linear form. (b) Dependence of $\bar{n}_{\text{x}0}$ on the SPC constant, g , for driving phonons of the same six frequencies at fixed $a/\gamma_{\text{ph}} = 0.2$. A well-defined g^2 dependence at all small couplings gives way to a suppression of $\bar{n}_{\text{x}0}$ at larger g values whose onset depends on ω_0 61

4.8 Dependence of $\tilde{\Gamma}_{\text{max}}$ on the phonon frequency ω_0/J for four values of the driving strength, $D = ga/J\gamma_{\text{ph}}$ on the weak-coupling regime. 64

- 4.9 Average k -component of triplon occupation, \bar{u}_{k0} , in the NESS at fixed parameters $\gamma_{\text{ph}} = 0.02\omega_0$, $a/\gamma_{\text{ph}} = 0.2$, $g/J = 0.05$, and $\gamma_s/J = 0.01$ shown as a function of the driving frequency, ω_0 , for $k = 0, \pi/4, \pi/2 + \epsilon, 3\pi/4$, and π ; $\epsilon = \pi/N$ is an offset from the band center, where $u_{k=\pi/2} = 0$. Black squares show the maxima, u_{k0}^{max} , of the \bar{u}_{k0} functions referring to different wave vectors k_{res} across the Brillouin zone. At all frequencies below the two-triplon band, $\omega_0 < 2\omega_{\text{min}}$, the strongest peak is found in $u_{k=0}$ and at $\omega_0 > 2\omega_{\text{max}}$ in $u_{k=\pi}$. The analytical results provided in Eqs. (4.6) and (4.10) are shown with dotted red lines in the band. The discrepancy observed at the band edges between the analytic and numeric results originates from detuning effects. 65
- 4.10 Threshold value, $(a/\gamma_{\text{ph}})_t$, of the normalized laser electric field strength required to achieve the maximum steady-state triplon occupation of $n_x = 0.2$, shown as a function of γ_s/J and ω_0/J for fixed $g/J = 0.05$ and $\gamma_{\text{ph}} = 0.02\omega_0$. We draw attention to the three regimes of behavior below, in, and above the two-triplon bands, $\omega'_1 = 2\omega_{\text{min}}$ and $\omega_1 = 2\omega_{\text{max}}$. Also one-triplon band is shown by the frequencies $\omega'_2 = \omega_{\text{min}}$ and $\omega_2 = \omega_{\text{max}}$, where unlike Fig. 4.9 no additional structure is visible in $(a/\gamma_{\text{ph}})_t$ 66
- 4.11 The temporal behavior of quantities (a) $n_{\text{ph}}(t)$, (c) $n_x(t)$, (e) $V(t)$, (g) $u_{k=0}(t)$, and (i) $u_{k=\pi}(t)$ in the NESS at fixed $a/\gamma_{\text{ph}} = 0.2$, $g/J = 0.05$, $\gamma_s/J = 0.01$, and $\omega_0/J = 1.5$. Juxtaposed in the right panels (b), (d), (f), (h), and (j) show the corresponding Fourier decompositions. 67
- 4.12 Coefficients of the Fourier transforms of (a) $n_x(t)$ and (b) $V(t)$ in the NESS at fixed $\gamma_{\text{ph}} = 0.02\omega_0$, $a/\gamma_{\text{ph}} = 0.2$, $g/J = 0.05$, and $\gamma_s/J = 0.01$ shown as a function of the driving phonon frequency, $\omega = \omega_0$ 68
- 4.13 (a) Average triplon occupation, \bar{n}_{x0} , in the NESS at fixed $\gamma_{\text{ph}} = 0.02\omega_0$, $a/\gamma_{\text{ph}} = 0.2$, and $g/J = 0.05$ as a function of ω_0 for different values of γ_s . The band-edge features become increasingly prominent as γ_s decreases, as does the peak at $\omega_0 = \omega_{\text{min}}$, but for most other phonon frequencies far from the band edges and ω_{min} , \bar{n}_{x0} is insensitive to the spin damping. (b) Corresponding off-diagonal response, shown by the dominant component $|V_1|$ 69
- 4.14 A schematic representation of energy flows in the driven spin-lattice system coupled to the phononic bath. All the energies are defined to be positive in the direction of the arrows. 70
- 4.15 Average energy flows through the driven spin-lattice system coupled to the phononic bath, depicted in Figs. 3.2 and 4.14, as a function of $\omega = \omega_0$ at fixed $\gamma_{\text{ph}} = 0.02\omega_0$, $a/\gamma_{\text{ph}} = 0.2$, $g/J = 0.05$, and $\gamma_s/J = 0.01$. (a) Power absorbed by the driving phonon from the laser field ($\bar{P}_0^{\text{L,P}}$), power dissipated directly to the bath from this driven phonon ($\bar{P}_0^{\text{P,B}}$) and the power transferred towards the SPC part from this phonon ($\bar{P}_0^{\text{P,SP}}$). For clarity the powers are normalized to ω_0^2 and the solid (dotted) line in $\bar{P}_0^{\text{P,SP}}$ stands for for a positive (negative) power. (b) Once more power transferred towards the SPC part ($\bar{P}_0^{\text{P,SP}}$), power delivered to the spin system from SPC part ($\bar{P}_0^{\text{SP,S}}$), power entered the bath by the SPC part ($\bar{P}_0^{\text{SP,B}}$), and power dissipated by the effect of the bath on the spin system ($\bar{P}_0^{\text{S,B}}$). . . . 72

4.16	(a) The first sum rule, $\overline{P}_0^{L,P} = \overline{P}_0^{P,B} + \overline{P}_0^{P,SP}$, and (b) the second sum rule, $\overline{P}_0^{P,SP} = \overline{P}_0^{SP,S} + \overline{P}_0^{SP,B}$, as a function of $\omega = \omega_0$ at fixed $\gamma_{ph} = 0.02\omega_0$, $a/\gamma_{ph} = 0.2$, $g/J = 0.05$, and $\gamma_s/J = 0.01$	73
4.17	$P_0^{L,P}$ shown as a function of ω for $\gamma_{ph} = 0.02\omega_0$, $a/\gamma_{ph} = 0.2$, $g/J = 0.1$, and $\gamma_s/J = 0.01$, for systems with one phonon at a frequency (a) $\omega_0/J = 0.5$, (b) $\omega_0/J = 2.0$, and (c) $\omega_0/J = 3.0$	74
4.18	Proposition of a simple experimental setup for the effect of a high-quality Al heat sink at temperature T_f with a sample (CuGeO_3) thickness and area, respectively, 20 nm and 1 mm ²	76
5.1	Time evolution of the (a) phonon occupation $n_{ph}(t)$ and (b) triplon occupation $n_x(t)$ with the driving turning on at time $t = 0$ and turning off at $t/J^{-1} = 1500$. The set of parameters: $N = 2000$, $\gamma_{ph} = 0.02\omega_0$, $a/\gamma_{ph} = 0.2$, $\gamma_s/J = 0.01$, and $\omega_0 = \omega_{min}$. The same for $\omega_0 = 2\omega_{min}$ in panels (c) and (d).	81
5.2	Long-time behavior of the (a) phonon occupation $n_{ph}(t)$ and (b) triplon occupation $n_x(t)$ deduced respectively by their average \overline{n}_{ph0} and \overline{n}_{x0} in the NESS at $N = 2000$, $\gamma_{ph} = 0.02\omega_0$, $a/\gamma_{ph} = 0.2$, $\gamma_s/J = 0.01$, and $\omega_0 = \omega_{min}$. The same for $\omega_0 = 2\omega_{min}$ in panels (c) and (d).	83
5.3	Averaged phonon occupation in the NESS signal, \overline{n}_{ph0} , for five Δt_i with $i \in \{1, 2, 3, 4, 5\}$, corresponding respectively to the time intervals [900, 1000], [4900, 5000], [11900, 12000], [24900, 25000], and [49900, 50000] at $N = 2000$, $a/\gamma_{ph} = 0.2$, $\gamma_s/J = 0.01$, $g/J = 0.3$, $\gamma_{ph} = 0.02\omega_0$ and different driving frequencies ω_0/J	84
5.4	(a) Phonon and (b) triplon occupation response at fixed $N = 2000$, $\gamma_{ph} = 0.02\omega_0$, $a/\gamma_{ph} = 0.2$, and $\gamma_s/J = 0.01$ as a function of g/J for various frequencies ω_0/J	84
5.5	Average $k = 0, \pi$ and k_{res} -component of the dressed triplon occupation, \overline{n}_{x0} response at fixed $a/\gamma_{ph} = 0.2$, $\gamma_s/J = 0.01$, $N = 2000$, and $\gamma_{ph} = 0.02\omega_0$ as a function of g/J at $\omega_0/J = 1.7$	85
5.6	Average phonon occupation response to the resonant driving frequency $\omega = \omega_0$ for different SPCs at fixed $N = 2000$, $\gamma_{ph} = 0.02\omega_0$, $a/\gamma_{ph} = 0.2$, and $\gamma_s/J = 0.01$	86
5.7	(a) Average triplon occupation response to the resonant driving frequency $\omega = \omega_0$ for different SPCs at fixed $N = 2000$, $\gamma_{ph} = 0.02\omega_0$, $a/\gamma_{ph} = 0.2$, and $\gamma_s/J = 0.01$. The normalized \overline{n}_{x0} to \overline{n}_{ph0} is presented in (b).	87
5.8	Average (a) $k = 0$, (b) $\pi/4$, (c) $3\pi/4$ and (d) π -component of the triplon occupation at fixed $a/\gamma_{ph} = 0.2$, $\gamma_s/J = 0.01$, $N = 2000$, and $\gamma_{ph} = 0.02\omega_0$ as a function of driving frequency ω_0/J for different SPCs.	88
5.9	Average triplon occupation, \overline{n}_{x0} , response at fixed $a/\gamma_{ph} = 0.2$, $\omega_0 = 2\omega_{max}$, $N = 2000$, and $\gamma_{ph} = 0.02\omega_0$ as a function of spin damping γ_s/J for different SPCs.	89

- 5.10 (a) and (b) Average energy flows through the driven spin-lattice system coupled to the phononic bath as a function of $\omega = \omega_0$ at fixed $\gamma_{\text{ph}} = 0.02\omega_0$, $a/\gamma_{\text{ph}} = 0.2$, a large SPC $g/J = 0.3$, and $\gamma_{\text{s}}/J = 0.01$. For clarity the powers are normalized to ω_0^2 and the solid (dashed) line in $\overline{P}_0^{\text{P,SP}}$ and $\overline{P}_0^{\text{SP,B}}$ stands for for a positive (negative) power. 90
- 5.11 Phonon occupation response at fixed $N = 2000$, $\gamma_{\text{ph}} = 0.02\omega_0$, $a/\gamma_{\text{ph}} = 0.2$, $\gamma_{\text{s}}/J = 0.01$, and $g/J = 0.3$ to the driving frequency ω/J in off-resonance with the phonon frequency for three different $\omega_0/J = 1, 2$ and 3 respectively below, in, and above the two-triplon band. 92
- 5.12 Average phonon occupation response in the NESS to the driving frequency ω/J in off-resonance with the phonon frequency at fixed $N = 2000$, $\gamma_{\text{ph}} = 0.02\omega_0$, $a/\gamma_{\text{ph}} = 0.2$, and $\gamma_{\text{s}}/J = 0.01$ for (a) $\omega_0/J = 1.35$, (b) $\omega_0/J = 1.45$, (c) $\omega_0/J = 2.40$, and (d) $\omega_0/J = 2.50$. Corresponding normalized average phonon occupations in off-resonance $\omega \neq \omega_0$ to the average phonon occupation in resonance $\omega = \omega_0$ in the NESS as a function of the driving frequency ω/J are shown in (e)-(h). 93
- 5.13 The same as Fig. 5.12, but for the average triplon occupation. 94
- 5.14 Average occupations in off-resonance $\omega \neq \omega_0$ in the NESS as a function of the driving frequency ω/J at fixed $N = 2000$, $\gamma_{\text{ph}} = 0.02\omega_0$, $a/\gamma_{\text{ph}} = 0.2$, and $\gamma_{\text{s}}/J = 0.01$ for (a) phonon occupation (dotted lines) and triplon occupation (solid lines) for various SPCs and (b) k -components of the spin response at $\omega_0/J = 0.6$ and $g/J = 0.5$ far from the two-triplon band edges. The same for $\omega_0/J = 3$ in panels (c) and (d). 95
- 5.15 The characteristic frequencies of phonon and spin occupations are taken from Figs. 5.12 and 5.13 for phonon frequencies around the (a) lower and (b) upper band edge. For the symbols, see the text. 96
- 5.16 The response of the average k -component of the triplon occupation in the NESS to the triplon mode k at $\omega = \omega_0$ for (a) $\omega_0/J = 1.45$, (b) $\omega_0/J = 1.75$, (c) $\omega_0/J = 2.20$ and (d) $\omega_0/J = 2.40$ at various SPCs at fixed $N = 3000$, $\gamma_{\text{ph}} = 0.02\omega_0$, $a/\gamma_{\text{ph}} = 0.2$, and $\gamma_{\text{s}}/J = 0.01$ 97
- 5.17 Comparison between the coefficients of the Fourier transforms of $n_{\text{x}}(t)$ at fixed $N = 2000$, $\gamma_{\text{ph}} = 0.02\omega_0$, $a/\gamma_{\text{ph}} = 0.2$, $\gamma_{\text{s}}/J = 0.01$, and $g/J = 0.3$ for below, in, and above the band regime, and $\gamma_{\text{ph}} = 0.02\omega_0$ 98
- 5.18 Average input energy response in the NESS to the driving frequency ω/J in off-resonance with the phonon frequency at fixed $N = 2000$, $\gamma_{\text{ph}} = 0.02\omega_0$, $a/\gamma_{\text{ph}} = 0.2$, and $\gamma_{\text{s}}/J = 0.01$ for (a) $\omega_0/J = 1.35$, (b) $\omega_0/J = 1.45$, (c) $\omega_0/J = 2.40$ and (d) $\omega_0/J = 2.50$. Normalized average triplon occupations in off-resonance $\omega \neq \omega_0$ to the average phonon occupation in resonance $\omega = \omega_0$ in the NESS as a function of the driving frequency ω/J are represented in (e)-(h), respectively. 100

6.1	Schematic of a driven-dissipative quantum magnet based on the J' -model under study consisting of the spin system, driven Einstein phonon, laser field, and the bath. The spin-spin coupling, interdimer coupling, the SPC, phonon damping, and spin damping are described respectively by $J = 10$ meV, $J'/J = 1/2$, g' , γ_{ph} , and γ_{s} . The laser continuously pumps energy into the system and then drives it out of equilibrium. Blue ellipses display dimer singlets, while the red one shows a triplon excitation, which is the excitation considered in the present thesis.	105
6.2	A comparison between the J and J' models through temporal behaviors of (a) phonon occupation, (b) triplon occupation, (c) $k = 0$ component, and (d) $k = \pi$ component of the triplon occupation at fixed $N = 2000$, $\omega_0/J = 1.7$, $\gamma_{\text{ph}} = 0.02\omega_0$, $a/\gamma_{\text{ph}} = 0.2$, and $\gamma_{\text{s}}/J = 0.01$. In the case of J -model, we fix $g/J = 0.5$, while $g'/J = 0.25$ is fixed for the J' -model. The driving field is turned off at $t/J^{-1} = 3000$ to approach the NESS to its equilibrium state.	107
6.3	A comparison between the J and J' models through time-average behaviors of (a) phonon occupation and (b) triplon occupation at fixed $N = 2000$, $\omega_0/J = 1.7$, $\gamma_{\text{ph}} = 0.02\omega_0$, $a/\gamma_{\text{ph}} = 0.2$, and $\gamma_{\text{s}}/J = 0.01$. In the case of SPC, we again fix $g/J = 0.5$ and $g'/J = 0.25$ for the J and J' models, respectively.	108
6.4	A comparison between the J and J' models through the time-average behaviors of (a) phonon occupation and (b) triplon occupation at fixed $N = 2000$, $\omega_0/J = 1.7$, $\gamma_{\text{ph}} = 0.02\omega_0$, $a/\gamma_{\text{ph}} = 0.2$, and $\gamma_{\text{s}}/J = 0.01$. The relation $y'_k < y_k$ and the difference factor J/J' in the SPCs in the models makes the observed discrepancies and one expects the same trends shown at $g'J/J' = g$	109
6.5	A comparison between the J and J' models through time-average behaviors of (a) phonon occupation and (b) triplon occupation as a function of driving phonon frequency at fixed $N = 2000$, $\gamma_{\text{ph}} = 0.02\omega_0$, $a/\gamma_{\text{ph}} = 0.2$, and $\gamma_{\text{s}}/J = 0.01$. In the case of J (J') model, we have fixed $g/J = 0.5$ ($g'/J = 0.25$).	110
6.6	Illustration of the comparison between the J and J' models over a wide range of phonon frequencies at fixed $N = 2000$, $\gamma_{\text{ph}} = 0.02\omega_0$, $a/\gamma_{\text{ph}} = 0.2$, and $\gamma_{\text{s}}/J = 0.01$	111
6.7	A comparison between (left y -axis, dotted lines) phonon and (right y -axis, solid lines) triplon occupation of the J and J' models as a function of driving laser frequency in off-resonant condition $\omega \neq \omega_0$ at fixed $\gamma_{\text{ph}} = 0.02\omega_0$, $a/\gamma_{\text{ph}} = 0.2$, $g/J = 0.5$ (J -model), $g'/J = 0.25$ (J' -model) for (a) $\omega_0/J = 0.6$, (b) 1.35, (c) 1.45, (d) 2.40, (e) 2.50, and (f) 3.0.	112
6.8	A comparison between the J and J' models through time-average behaviors of k -components of the spin system at (a) $\omega = \omega_0 = 1.8$ and (b) $\omega = \omega_0 = 2.20$ at fixed $N = 3000$, $\gamma_{\text{ph}} = 0.02\omega_0$, $a/\gamma_{\text{ph}} = 0.2$, and $\gamma_{\text{s}}/J = 0.01$. In the case of J (J') model, we fix $g/J = 0.5$ ($g'/J = 0.25$).	113
7.1	(a) Average phonon displacement \bar{q}_0 in the NESS for various SPCs at fixed $N = 2000$, $\gamma_{\text{ph}} = 0.02\omega_0$, $a/\gamma_{\text{ph}} = 0.2$, and $\gamma_{\text{s}}/J = 0.01$. The \bar{q}_0 normalized to $\bar{n}_{\text{ph}0}$, Fig. 5.6, is shown in (b).	116

7.2	(a) SPC-induced spin-band frequency shift, Eq. (7.2), for various SPCs at $\omega = \omega_0 = 2.2J$ at fixed $N = 2000$, $\gamma_{\text{ph}} = 0.02\omega_0$, $a/\gamma_{\text{ph}} = 0.2$, and $\gamma_{\text{s}}/J = 0.01$. Panel (b) shows the change of modulated leading magnetic interaction $\tilde{J} = J + g\bar{q}_0$ with g for two arbitrary frequencies $\omega_0/J = 1.8$ and 2.2 around the band center.	117
7.3	(a) A comparison between two models through time-average behaviors of phonon displacement at fixed $N = 2000$, $\gamma_{\text{ph}} = 0.02\omega_0$, $a/\gamma_{\text{ph}} = 0.2$, and $\gamma_{\text{s}}/J = 0.01$. In the case of J (J') model, we have fixed $g/J = 0.5$ ($g'/J = 0.25$). (b) A comparison between J and J' models to indicate the change of modulated leading magnetic interaction $\tilde{J} = J + g\bar{q}_0$ with g as well as modulated next-nearest magnetic interaction $\tilde{J}' = J' + g'\bar{q}_0^{J'}$ with g' for phonon frequency $\omega_0/J = 2.2$.	120
7.4	A new picture of (a) J -model and (b) J' -model with the probe driving field $E_1(t)$. The probe beam is addressed with the frequency Ω .	121
7.5	Average value of (a) $k = 0$ and (b) $k = \pi$ component of the spin response in the J -model, deducted by their resonant values for a better resolution of peaks, as a function of the probe frequency, Ω/J , at $N = 2000$, $\gamma_{\text{ph}} = 0.02\omega_0$, $a/\gamma_{\text{ph}} = 0.2$, $\gamma_{\text{s}}/J = 0.01$, and $a_{\text{pr}}/a = 0.2$ for various SPCs and driving frequency $\omega = \omega_0 = 2.2J$ far from the band edges. The dotted vertical lines show the driving-renormalized two-triplon bands at strong SPCs. Panels (c) and (d) investigate the same treatments (without any deduction this time) at another driving frequency $\omega = \omega_0 = 1.45J$ close to the lower band edge.	122
7.6	As Fig. 7.5 but in the J' -model.	123
7.7	Three first coefficients of the Fourier transform of phonon displacement in the (a) J -model with $g/J = 0.5$ and (b) J' -model with $g'/J = 0.25$ at fixed $N = 2000$, $\omega = \omega_0 = 2.2J$, $\gamma_{\text{ph}} = 0.02\omega_0$, $a/\gamma_{\text{ph}} = 0.2$, and $\gamma_{\text{s}}/J = 0.01$. The inset panels indicate the late-time evolution of the phonon displacements.	125
7.8	Pump driving effect on the phonon displacement in the (a) J -model and (b) J' -model at fixed $N = 2000$, $\gamma_{\text{ph}} = 0.02\omega_0$, $g/J = 0.5$, $g'/J = 0.25$, and $\gamma_{\text{s}}/J = 0.01$.	127
7.9	Pump driving effect on the dynamic spin-band renormalization in the {(a),(b)} J -model and {(c),(d)} J' -model at fixed $N = 2000$, $\omega = \omega_0 = 2.2J$, $\gamma_{\text{ph}} = 0.02\omega_0$, $g/J = 0.5$, $g'/J = 0.25$, and $\gamma_{\text{s}}/J = 0.01$.	128
7.10	Probe driving effect on the dynamic spin-band renormalization in the {(a),(b)} J -model and {(c),(d)} J' -model at fixed $N = 2000$, $\omega = \omega_0 = 2.2J$, $\gamma_{\text{ph}} = 0.02\omega_0$, $g/J = 0.5$, $g'/J = 0.25$, and $\gamma_{\text{s}}/J = 0.01$. In panels (b) and (d) the pump driving field is turned on, $a/\gamma_{\text{ph}} = 0.2$. In the panels $\delta\omega_{\text{hyb}}$ refers to the energy difference between the peak positions and the bare band edges induced by the probe driving field and/or self-hybrid effect.	129
7.11	Probe driving effect on the phonon spectrum around the (a) lower and (b) upper band edge in the J -model at fixed $N = 2000$, $\omega = \omega_0 = 2.2J$, $\gamma_{\text{ph}} = 0.02\omega_0$, $g/J = 0.5$, $g'/J = 0.5$, and $\gamma_{\text{s}}/J = 0.01$.	130

Bibliography

Articles

- ³J. Eisert, M. Friesdorf, and C. Gogolin, “Quantum many-body systems out of equilibrium”, *Nature Physics* **11**, 124–130 (2015) (cited on page 13).
- ⁴C. Gross and I. Bloch, “Quantum simulations with ultracold atoms in optical lattices”, *Science* **357**, 995–1001 (2017) (cited on page 13).
- ⁵V. I. Yudin, A. V. Taichenachev, and M. Y. Basalaev, “Dynamic steady state of periodically driven quantum systems”, *Phys. Rev. A* **93**, 013820 (2016) (cited on pages 13, 15).
- ⁸P. Zoller, T. Beth, D. Binosi, R. Blatt, H. Briegel, D. Bruss, T. Calarco, J. I. Cirac, D. Deutsch, J. Eisert, A. Ekert, C. Fabre, N. Gisin, P. Grangiere, M. Grassl, S. Haroche, A. Imamoglu, A. Karlson, J. Kempe, L. Kouwenhoven, S. Kröll, G. Leuchs, M. Lewenstein, D. Loss, N. Lütkenhaus, S. Massar, J. E. Mooij, M. B. Plenio, E. Polzik, S. Popescu, G. Rempe, A. Sergienko, D. Suter, J. Twamley, G. Wendin, R. Werner, A. Winter, J. Wrachtrup, and A. Zeilinger, “Quantum information processing and communication”, *The European Physical Journal D - Atomic, Molecular, Optical and Plasma Physics* **36**, 203–228 (2005) (cited on page 13).
- ⁹A. Polkovnikov, K. Sengupta, A. Silva, and M. Vengalattore, “Colloquium: Nonequilibrium dynamics of closed interacting quantum systems”, *Rev. Mod. Phys.* **83**, 863–883 (2011) (cited on page 13).
- ¹⁰A. Eckardt, “Colloquium: Atomic quantum gases in periodically driven optical lattices”, *Rev. Mod. Phys.* **89**, 011004 (2017) (cited on page 13).

- ¹¹C. Giannetti, M. Capone, D. Fausti, M. Fabrizio, F. Parmigiani, and D. Mihailovic, “Ultrafast optical spectroscopy of strongly correlated materials and high-temperature superconductors: A non-equilibrium approach”, *Advances in Physics* **65**, 58–238 (2016) (cited on page 13).
- ¹²M. Gandolfi, G. L. Celardo, F. Borgonovi, G. Ferrini, A. Avella, F. Banfi, and C. Giannetti, “Emergent ultrafast phenomena in correlated oxides and heterostructures”, *Physica Scripta* **92**, 034004 (2017) (cited on page 13).
- ¹³I. Bloch, J. Dalibard, and W. Zwerger, “Many-body physics with ultracold gases”, *Rev. Mod. Phys.* **80**, 885–964 (2008) (cited on page 13).
- ¹⁴J. Dalibard, F. Gerbier, G. Juzeliūnas, and P. Öhberg, “Colloquium: Artificial gauge potentials for neutral atoms”, *Rev. Mod. Phys.* **83**, 1523–1543 (2011) (cited on page 13).
- ¹⁵D. N. Basov, R. D. Averitt, and D. Hsieh, “Towards properties on demand in quantum materials”, *Nature Materials* **16**, 1077–1088 (2017) (cited on page 13).
- ¹⁶J. Zhang and R. Averitt, “Dynamics and control in complex transition metal oxides”, *Annual Review of Materials Research* **44**, 19–43 (2014) (cited on page 13).
- ¹⁷J. H. Mentink and M. Eckstein, “Ultrafast quenching of the exchange interaction in a Mott insulator”, *Phys. Rev. Lett.* **113**, 057201 (2014) (cited on page 13).
- ¹⁸J. H. Mentink, K. Balzer, and M. Eckstein, “Ultrafast and reversible control of the exchange interaction in Mott insulators”, *Nature Communications* **6**, 6708 (2015) (cited on page 13).
- ¹⁹L. Stojchevska, I. Vaskivskyi, T. Mertelj, P. Kusar, D. Svetin, S. Brazovskii, and D. Mihailovic, “Ultrafast switching to a stable hidden quantum state in an electronic crystal”, *Science* **344**, 177–180 (2014) (cited on page 13).
- ²⁰J. Zhang, P. W. Hess, A. Kyprianidis, P. Becker, A. Lee, J. Smith, G. Pagano, I.-D. Potirniche, A. C. Potter, A. Vishwanath, N. Y. Yao, and C. Monroe, “Observation of a discrete time crystal”, *Nature* **543**, 217–220 (2017) (cited on page 13).
- ²¹S. Choi, J. Choi, R. Landig, G. Kucsko, H. Zhou, J. Isoya, F. Jelezko, S. Onoda, H. Sumiya, V. Khemani, C. von Keyserlingk, N. Y. Yao, E. Demler, and M. D. Lukin, “Observation of discrete time-crystalline order in a disordered dipolar many-body system”, *Nature* **543**, 221–225 (2017) (cited on page 13).
- ²²Y. A. Gerasimenko, P. Karpov, I. Vaskivskyi, S. Brazovskii, and D. Mihailovic, “Intertwined chiral charge orders and topological stabilization of the light-induced state of a prototypical transition metal dichalcogenide”, *npj Quantum Materials* **4**, 32 (2019) (cited on page 13).

- ²³D. Fausti, R. I. Tobey, N. Dean, S. Kaiser, A. Dienst, M. C. Hoffmann, S. Pyon, T. Takayama, H. Takagi, and A. Cavalleri, “Light-induced superconductivity in a stripe-ordered cuprate”, *Science* **331**, 189–191 (2011) (cited on page 13).
- ²⁴A. Cavalleri, “Photo-induced superconductivity”, *Contemporary Physics* **59**, 31–46 (2018) (cited on page 13).
- ²⁵A. C. Potter, T. Morimoto, and A. Vishwanath, “Classification of interacting topological Floquet phases in one dimension”, *Phys. Rev. X* **6**, 041001 (2016) (cited on page 13).
- ²⁶V. Khemani, A. Lazarides, R. Moessner, and S. L. Sondhi, “Phase structure of driven quantum systems”, *Phys. Rev. Lett.* **116**, 250401 (2016) (cited on page 13).
- ³⁰R. J. Schoelkopf and S. M. Girvin, “Wiring up quantum systems”, *Nature* **451**, 664–669 (2008) (cited on page 13).
- ³¹J. G. Bohnet, B. C. Sawyer, J. W. Britton, M. L. Wall, A. M. Rey, M. Foss-Feig, and J. J. Bollinger, “Quantum spin dynamics and entanglement generation with hundreds of trapped ions”, *Science* **352**, 1297–1301 (2016) (cited on page 13).
- ³²L. E. Bruhat, J. J. Viennot, M. C. Dartiailh, M. M. Desjardins, T. Kontos, and A. Cottet, “Cavity photons as a probe for charge relaxation resistance and photon emission in a quantum dot coupled to normal and superconducting continua”, *Phys. Rev. X* **6**, 021014 (2016) (cited on page 13).
- ³³O. Parlavecchio, C. Altimiras, J.-R. Souquet, P. Simon, I. Safi, P. Joyez, D. Vion, P. Roche, D. Esteve, and F. Portier, “Fluctuation-dissipation relations of a tunnel junction driven by a quantum circuit”, *Phys. Rev. Lett.* **114**, 126801 (2015) (cited on page 13).
- ³⁴S. Diehl, A. Tomadin, A. Micheli, R. Fazio, and P. Zoller, “Dynamical phase transitions and instabilities in open atomic many-body systems”, *Phys. Rev. Lett.* **105**, 015702 (2010) (cited on page 13).
- ³⁵J. Keeling, M. J. Bhaseen, and B. D. Simons, “Collective dynamics of Bose-Einstein condensates in optical cavities”, *Phys. Rev. Lett.* **105**, 043001 (2010) (cited on page 13).
- ³⁶A. A. Houck, H. E. Türeci, and J. Koch, “On-chip quantum simulation with superconducting circuits”, *Nature Physics* **8**, 292–299 (2012) (cited on page 13).
- ³⁷C. Grezes, B. Julsgaard, Y. Kubo, M. Stern, T. Umeda, J. Isoya, H. Sumiya, H. Abe, S. Onoda, T. Ohshima, V. Jacques, J. Esteve, D. Vion, D. Esteve, K. Mølmer, and P. Bertet, “Multimode storage and retrieval of microwave fields in a spin ensemble”, *Phys. Rev. X* **4**, 021049 (2014) (cited on page 13).
- ³⁸J. M. Fink, A. Dombi, A. Vukics, A. Wallraff, and P. Domokos, “Observation of the photon-blockade breakdown phase transition”, *Phys. Rev. X* **7**, 011012 (2017) (cited on page 13).

- ³⁹M. Kulkarni, B. Öztop, and H. E. Türeci, “Cavity-mediated near-critical dissipative dynamics of a driven condensate”, *Phys. Rev. Lett.* **111**, 220408 (2013) (cited on page 13).
- ⁴⁰M. Fitzpatrick, N. M. Sundaresan, A. C. Y. Li, J. Koch, and A. A. Houck, “Observation of a dissipative phase transition in a one-dimensional circuit QED lattice”, *Phys. Rev. X* **7**, 011016 (2017) (cited on page 13).
- ⁴¹O. Scarlatella, R. Fazio, and M. Schiró, “Emergent finite frequency criticality of driven-dissipative correlated lattice bosons”, *Phys. Rev. B* **99**, 064511 (2019) (cited on page 13).
- ⁴²R. Ma, B. Saxberg, C. Owens, N. Leung, Y. Lu, J. Simon, and D. I. Schuster, “A dissipatively stabilized Mott insulator of photons”, *Nature* **566**, 51–57 (2019) (cited on page 13).
- ⁴³I. Carusotto and C. Ciuti, “Quantum fluids of light”, *Rev. Mod. Phys.* **85**, 299–366 (2013) (cited on page 13).
- ⁴⁴Z. Zhiqiang, C. H. Lee, R. Kumar, K. J. Arnold, S. J. Masson, A. S. Parkins, and M. D. Barrett, “Nonequilibrium phase transition in a spin-1 Dicke model”, *Optica* **4**, 424–429 (2017) (cited on page 13).
- ⁴⁵A. Morales, D. Dreon, X. Li, A. Baumgärtner, P. Zupancic, T. Donner, and T. Esslinger, “Two-mode Dicke model from nondegenerate polarization modes”, *Phys. Rev. A* **100**, 013816 (2019) (cited on page 13).
- ⁴⁶E. I. R. Chiacchio and A. Nunnenkamp, “Emergence of continuous rotational symmetries in ultracold atoms coupled to optical cavities”, *Phys. Rev. A* **98**, 023617 (2018) (cited on page 13).
- ⁴⁷N. Lambert, S. Ahmed, M. Cirio, and F. Nori, “Modelling the ultra-strongly coupled spin-boson model with unphysical modes”, *Nature Communications* **10**, 3721 (2019) (cited on page 13).
- ⁴⁸N. BOGOLUBOV, “On the theory of superfluidity”, *J. Phys.* **XI**, 23–32 (1947) (cited on page 13).
- ⁴⁹J. G. Valatin, “Comments on the theory of superconductivity”, *Il Nuovo Cimento (1955-1965)* **7**, 843–857 (1958) (cited on page 13).
- ⁵⁰M. Bukov, L. D’Alessio, and A. Polkovnikov, “Universal high-frequency behavior of periodically driven systems: From dynamical stabilization to Floquet engineering”, *Advances in Physics* **64**, 139–226 (2015) (cited on page 13).
- ⁵¹J. H. Shirley, “Solution of the Schrödinger equation with a Hamiltonian periodic in time”, *Phys. Rev.* **138**, B979–B987 (1965) (cited on page 13).
- ⁵²G. Jotzu, M. Messer, R. Desbuquois, M. Lebrat, T. Uehlinger, D. Greif, and T. Esslinger, “Experimental realization of the topological Haldane model with ultracold fermions”, *Nature* **515**, 237–240 (2014) (cited on page 13).

- ⁵³G. Jotzu, M. Messer, F. Görg, D. Greif, R. Desbuquois, and T. Esslinger, “Creating state-dependent lattices for ultracold fermions by magnetic gradient modulation”, *Phys. Rev. Lett.* **115**, 073002 (2015) (cited on page 13).
- ⁵⁴J. Struck, C. Ölschläger, R. Le Targat, P. Soltan-Panahi, A. Eckardt, M. Lewenstein, P. Windpassinger, and K. Sengstock, “Quantum simulation of frustrated classical magnetism in triangular optical lattices”, *Science* **333**, 996–999 (2011) (cited on page 13).
- ⁵⁵N. Fläschner, B. S. Rem, M. Tarnowski, D. Vogel, D.-S. Lühmann, K. Sengstock, and C. Weitenberg, “Experimental reconstruction of the Berry curvature in a Floquet Bloch band”, *Science* **352**, 1091–1094 (2016) (cited on page 13).
- ⁵⁶M. Aidelsburger, M. Atala, M. Lohse, J. T. Barreiro, B. Paredes, and I. Bloch, “Realization of the Hofstadter Hamiltonian with ultracold atoms in optical lattices”, *Phys. Rev. Lett.* **111**, 185301 (2013) (cited on page 13).
- ⁵⁷H. Miyake, G. A. Siviloglou, C. J. Kennedy, W. C. Burton, and W. Ketterle, “Realizing the Harper Hamiltonian with laser-assisted tunneling in optical lattices”, *Phys. Rev. Lett.* **111**, 185302 (2013) (cited on page 13).
- ⁵⁸R. Singla, G. Cotugno, S. Kaiser, M. Först, M. Mitrano, H. Y. Liu, A. Cartella, C. Manzoni, H. Okamoto, T. Hasegawa, S. R. Clark, D. Jaksch, and A. Cavalleri, “THz-frequency modulation of the Hubbard U in an organic Mott insulator”, *Phys. Rev. Lett.* **115**, 187401 (2015) (cited on page 13).
- ⁵⁹M. Knap, M. Babadi, G. Refael, I. Martin, and E. Demler, “Dynamical cooper pairing in nonequilibrium electron-phonon systems”, *Phys. Rev. B* **94**, 214504 (2016) (cited on page 13).
- ⁶⁰D. A. Abanin, W. De Roeck, W. W. Ho, and F. Huveneers, “Effective Hamiltonians, prethermalization, and slow energy absorption in periodically driven many-body systems”, *Phys. Rev. B* **95**, 014112 (2017) (cited on page 13).
- ⁶¹M. A. Sentef, “Light-enhanced electron-phonon coupling from nonlinear electron-phonon coupling”, *Phys. Rev. B* **95**, 205111 (2017) (cited on page 13).
- ⁶²Y. Murakami, N. Tsuji, M. Eckstein, and P. Werner, “Nonequilibrium steady states and transient dynamics of conventional superconductors under phonon driving”, *Phys. Rev. B* **96**, 045125 (2017) (cited on page 13).
- ⁶³J. R. Coulthard, S. R. Clark, S. Al-Assam, A. Cavalleri, and D. Jaksch, “Enhancement of superexchange pairing in the periodically driven Hubbard model”, *Phys. Rev. B* **96**, 085104 (2017) (cited on page 13).
- ⁶⁴S. Kitamura, T. Oka, and H. Aoki, “Probing and controlling spin chirality in Mott insulators by circularly polarized laser”, *Phys. Rev. B* **96**, 014406 (2017) (cited on page 13).

- ⁶⁵D. M. Kennes, A. de la Torre, A. Ron, D. Hsieh, and A. J. Millis, “Floquet engineering in quantum chains”, *Phys. Rev. Lett.* **120**, 127601 (2018) (cited on page 13).
- ⁶⁶N. Tancogne-Dejean, M. A. Sentef, and A. Rubio, “Ultrafast modification of Hubbard U in a strongly correlated material: *Ab initio* high-harmonic generation in NiO”, *Phys. Rev. Lett.* **121**, 097402 (2018) (cited on page 13).
- ⁶⁷H. P. O. Collado, J. Lorenzana, G. Usaj, and C. A. Balseiro, “Population inversion and dynamical phase transitions in a driven superconductor”, *Phys. Rev. B* **98**, 214519 (2018) (cited on page 13).
- ⁶⁸A. Subedi, A. Cavalleri, and A. Georges, “Theory of nonlinear phononics for coherent light control of solids”, *Phys. Rev. B* **89**, 220301 (2014) (cited on page 13).
- ⁶⁹A. von Hoegen, R. Mankowsky, M. Fechner, M. Först, and A. Cavalleri, “Probing the interatomic potential of solids with strong-field nonlinear phononics”, *Nature* **555**, 79–82 (2018) (cited on page 13).
- ⁷⁰M. Först, C. Manzoni, S. Kaiser, Y. Tomioka, Y. Tokura, R. Merlin, and A. Cavalleri, “Nonlinear phononics as an ultrafast route to lattice control”, *Nature Physics* **7**, 854–856 (2011) (cited on page 13).
- ⁷⁴S. Gasparinetti, K. L. Viisanen, O.-P. Saira, T. Faivre, M. Arzeo, M. Meschke, and J. P. Pekola, “Fast electron thermometry for ultrasensitive calorimetric detection”, *Phys. Rev. Applied* **3**, 014007 (2015) (cited on page 14).
- ⁷⁵K. L. Viisanen, S. Suomela, S. Gasparinetti, O.-P. Saira, J. Ankerhold, and J. P. Pekola, “Incomplete measurement of work in a dissipative two level system”, *New Journal of Physics* **17**, 055014 (2015) (cited on page 14).
- ⁷⁶R. Schmidt, M. F. Carusela, J. P. Pekola, S. Suomela, and J. Ankerhold, “Work and heat for two-level systems in dissipative environments: Strong driving and non-Markovian dynamics”, *Phys. Rev. B* **91**, 224303 (2015) (cited on page 14).
- ⁷⁷F. W. J. Hekking and J. P. Pekola, “Quantum jump approach for work and dissipation in a two-level system”, *Phys. Rev. Lett.* **111**, 093602 (2013) (cited on page 14).
- ⁷⁸S. Suomela, P. Solinas, J. P. Pekola, J. Ankerhold, and T. Ala-Nissila, “Moments of work in the two-point measurement protocol for a driven open quantum system”, *Phys. Rev. B* **90**, 094304 (2014) (cited on page 14).
- ⁷⁹J. Ankerhold and J. P. Pekola, “Heat due to system-reservoir correlations in thermal equilibrium”, *Phys. Rev. B* **90**, 075421 (2014) (cited on page 14).
- ⁸⁰H. D. Zeh, “On the interpretation of measurement in quantum theory”, *Foundations of Physics* **1**, 69–76 (1970) (cited on page 14).

- ⁸³S. A. Wolf, D. D. Awschalom, R. A. Buhrman, J. M. Daughton, S. von Molnár, M. L. Roukes, A. Y. Chtchelkanova, and D. M. Treger, “Spintronics: A spin-based electronics vision for the future”, *Science* **294**, 1488–1495 (2001) (cited on pages 14, 37).
- ⁸⁴E. Beaurepaire, J.-C. Merle, A. Daunois, and J.-Y. Bigot, “Ultrafast spin dynamics in ferromagnetic nickel”, *Phys. Rev. Lett.* **76**, 4250–4253 (1996) (cited on pages 14, 37).
- ⁸⁵T. Kampfrath, A. Sell, G. Klatt, A. Pashkin, S. Mährlein, T. Dekorsy, M. Wolf, M. Fiebig, A. Leitenstorfer, and R. Huber, “Coherent terahertz control of antiferromagnetic spin waves”, *Nature Photonics* **5**, 31–34 (2011) (cited on pages 14, 37).
- ⁸⁶C. D. Stanciu, F. Hansteen, A. V. Kimel, A. Kirilyuk, A. Tsukamoto, A. Itoh, and T. Rasing, “All-optical magnetic recording with circularly polarized light”, *Phys. Rev. Lett.* **99**, 047601 (2007) (cited on pages 14, 37).
- ⁸⁷I. Radu, K. Vahaplar, C. Stamm, T. Kachel, N. Pontius, H. A. Dürr, T. A. Ostler, J. Barker, R. F. L. Evans, R. W. Chantrell, A. Tsukamoto, A. Itoh, A. Kirilyuk, T. Rasing, and A. V. Kimel, “Transient ferromagnetic-like state mediating ultrafast reversal of antiferromagnetically coupled spins”, *Nature* **472**, 205–208 (2011) (cited on pages 14, 15, 37).
- ⁸⁸A. Stupakiewicz, K. Szerenos, D. Afanasiev, A. Kirilyuk, and A. V. Kimel, “Ultrafast nonthermal photo-magnetic recording in a transparent medium”, *Nature* **542**, 71–74 (2017) (cited on pages 14, 37).
- ⁸⁹G. Ju, J. Hohlfeld, B. Bergman, R. J. M. van de Veerdonk, O. N. Mryasov, J.-Y. Kim, X. Wu, D. Weller, and B. Koopmans, “Ultrafast generation of ferromagnetic order via a laser-induced phase transformation in ferri thin films”, *Phys. Rev. Lett.* **93**, 197403 (2004) (cited on pages 14, 37).
- ⁹⁰T. ž. Prosen and I. Pi žorn, “Quantum phase transition in a far-from-equilibrium steady state of an XY spin chain”, *Phys. Rev. Lett.* **101**, 105701 (2008) (cited on page 14).
- ⁹¹D. Karevski and T. Platini, “Quantum nonequilibrium steady states induced by repeated interactions”, *Phys. Rev. Lett.* **102**, 207207 (2009) (cited on page 14).
- ⁹²T. ž. Prosen, “Open XXZ spin chain: Nonequilibrium steady state and a strict bound on ballistic transport”, *Phys. Rev. Lett.* **106**, 217206 (2011) (cited on page 14).
- ⁹³T. ž. Prosen, “Exact nonequilibrium steady state of a strongly driven open XXZ chain”, *Phys. Rev. Lett.* **107**, 137201 (2011) (cited on page 14).
- ⁹⁴T. ž. Prosen and E. Ilievski, “Nonequilibrium phase transition in a periodically driven XY spin chain”, *Phys. Rev. Lett.* **107**, 060403 (2011) (cited on page 14).

- ⁹⁵M. Vogl, G. Schaller, and T. Brandes, “Criticality in transport through the quantum Ising chain”, *Phys. Rev. Lett.* **109**, 240402 (2012) (cited on page 14).
- ⁹⁶M. Foss-Feig, J. T. Young, V. V. Albert, A. V. Gorshkov, and M. F. Maghrebi, “Solvable family of driven-dissipative many-body systems”, *Phys. Rev. Lett.* **119**, 190402 (2017) (cited on page 14).
- ⁹⁷V. Popkov, T. ž. Prosen, and L. Zadnik, “Exact nonequilibrium steady state of open XXZ/XYZ spin-1/2 chain with dirichlet boundary conditions”, *Phys. Rev. Lett.* **124**, 160403 (2020) (cited on pages 14, 15).
- ⁹⁸I. S. Jacobs, J. W. Bray, H. R. Hart, L. V. Interrante, J. S. Kasper, G. D. Watkins, D. E. Prober, and J. C. Bonner, “Spin-Peierls transitions in magnetic donor-acceptor compounds of tetrathiafulvalene (TTF) with bisdithiolene metal complexes”, *Phys. Rev. B* **14**, 3036–3051 (1976) (cited on pages 14, 37, 39).
- ⁹⁹F. D. M. Haldane, “Nonlinear field theory of large-spin heisenberg antiferromagnets: semiclassically quantized solitons of the one-dimensional easy-axis néel state”, *Phys. Rev. Lett.* **50**, 1153–1156 (1983) (cited on pages 14, 16, 37).
- ¹⁰⁰J. P. Renard, M. Verdaguer, L. P. Regnault, W. A. C. Erkelens, J. Rossat-Mignod, and W. G. Stirling, “Presumption for a quantum energy gap in the quasi-one-dimensional $S = 1$ Heisenberg antiferromagnet $\text{Ni}(\text{C}_2\text{H}_8\text{N}_2)_2\text{NO}_2(\text{ClO}_4)$ ”, *Europhysics Letters (EPL)* **3**, 945–952 (1987) (cited on pages 14, 37).
- ¹⁰¹K. Katsumata, H. Hori, T. Takeuchi, M. Date, A. Yamagishi, and J. P. Renard, “Magnetization process of an $S = 1$ linear-chain Heisenberg antiferromagnet”, *Phys. Rev. Lett.* **63**, 86–88 (1989) (cited on pages 14, 37).
- ¹⁰²Y. Ajiro, T. Goto, H. Kikuchi, T. Sakakibara, and T. Inami, “High-field magnetization of a quasi-one-dimensional $S = 1$ antiferromagnet $\text{Ni}(\text{C}_2\text{H}_8\text{N}_2)_2\text{NO}_2(\text{ClO}_4)$: Observation of the Haldane gap”, *Phys. Rev. Lett.* **63**, 1424–1427 (1989) (cited on pages 14, 37).
- ¹⁰⁴S.-W. Cheong, J. Thompson, and Z. Fisk, “Properties of La_2CuO_4 and related compounds”, *Physica C: Superconductivity* **158**, 109–126 (1989) (cited on pages 14, 37).
- ¹⁰⁵A. V. Sologubenko, K. Giannó, H. R. Ott, U. Ammerahl, and A. Revcolevschi, “Thermal conductivity of the hole-doped spin ladder system $\text{Sr}_{14-x}\text{Ca}_x\text{Cu}_{24}\text{O}_{41}$ ”, *Phys. Rev. Lett.* **84**, 2714–2717 (2000) (cited on page 14).
- ¹⁰⁶C. Hess, C. Baumann, U. Ammerahl, B. Büchner, F. Heidrich-Meisner, W. Brenig, and A. Revcolevschi, “Magnon heat transport in $(\text{Sr}, \text{Ca}, \text{La})_{14}\text{Cu}_{24}\text{O}_{41}$ ”, *Phys. Rev. B* **64**, 184305 (2001) (cited on page 14).
- ¹⁰⁷N. Hlubek, P. Ribeiro, R. Saint-Martin, A. Revcolevschi, G. Roth, G. Behr, B. Büchner, and C. Hess, “Ballistic heat transport of quantum spin excitations as seen in SrCuO_2 ”, *Phys. Rev. B* **81**, 020405 (2010) (cited on pages 14, 77).

- ¹⁰⁸H. Kühne, H.-H. Klauss, S. Grossjohann, W. Brenig, F. J. Litterst, A. P. Reyes, P. L. Kuhns, M. M. Turnbull, and C. P. Landee, “Quantum critical dynamics of an $S = \frac{1}{2}$ antiferromagnetic Heisenberg chain studied by ^{13}C NMR spectroscopy”, *Phys. Rev. B* **80**, 045110 (2009) (cited on page 14).
- ¹⁰⁹L. S. Wu, W. J. Gannon, I. A. Zaliznyak, A. M. Tsvelik, M. Brockmann, J.-S. Caux, M. S. Kim, Y. Qiu, J. R. D. Copley, G. Ehlers, A. Podlesnyak, and M. C. Aronson, “Orbital-exchange and fractional quantum number excitations in an f-electron metal, $\text{Yb}_2\text{Pt}_2\text{Pb}$ ”, *Science* **352**, 1206–1210 (2016) (cited on page 15).
- ¹¹⁰M. Mourigal, M. Enderle, A. Klöpperpieper, J.-S. Caux, A. Stunault, and H. M. Rønnow, “Fractional spinon excitations in the quantum Heisenberg antiferromagnetic chain”, *Nature Physics* **9**, 435–441 (2013) (cited on page 15).
- ¹¹¹B. Lake, D. A. Tennant, J.-S. Caux, T. Barthel, U. Schollwöck, S. E. Nagler, and C. D. Frost, “Multispinon continua at zero and finite temperature in a near-ideal Heisenberg chain”, *Phys. Rev. Lett.* **111**, 137205 (2013) (cited on page 15).
- ¹¹²T. Fukuhara, A. Kantian, M. Endres, M. Cheneau, P. Schauß, S. Hild, D. Bellem, U. Schollwöck, T. Giamarchi, C. Gross, I. Bloch, and S. Kuhr, “Quantum dynamics of a mobile spin impurity”, *Nature Physics* **9**, 235–241 (2013) (cited on page 15).
- ¹¹³J. P. Ronzheimer, M. Schreiber, S. Braun, S. S. Hodgman, S. Langer, I. P. McCulloch, F. Heidrich-Meisner, I. Bloch, and U. Schneider, “Expansion dynamics of interacting bosons in homogeneous lattices in one and two dimensions”, *Phys. Rev. Lett.* **110**, 205301 (2013) (cited on page 15).
- ¹¹⁴F. Meinert, M. J. Mark, E. Kirilov, K. Lauber, P. Weinmann, A. J. Daley, and H.-C. Nägerl, “Quantum quench in an atomic one-dimensional Ising chain”, *Phys. Rev. Lett.* **111**, 053003 (2013) (cited on page 15).
- ¹¹⁵M. Fagotti, M. Collura, F. H. L. Essler, and P. Calabrese, “Relaxation after quantum quenches in the spin- $\frac{1}{2}$ Heisenberg XXZ chain”, *Phys. Rev. B* **89**, 125101 (2014) (cited on page 15).
- ¹¹⁶L. Piroli, E. Vernier, P. Calabrese, and M. Rigol, “Correlations and diagonal entropy after quantum quenches in XXZ chains”, *Phys. Rev. B* **95**, 054308 (2017) (cited on page 15).
- ¹¹⁷A. V. Kimel, A. Kirilyuk, P. A. Usachev, R. V. Pisarev, A. M. Balbashov, and T. Rasing, “Ultrafast non-thermal control of magnetization by instantaneous photomagnetic pulses”, *Nature* **435**, 655–657 (2005) (cited on page 15).
- ¹¹⁸T. Satoh, S.-J. Cho, R. Iida, T. Shimura, K. Kuroda, H. Ueda, Y. Ueda, B. A. Ivanov, F. Nori, and M. Fiebig, “Spin oscillations in antiferromagnetic NiO triggered by circularly polarized light”, *Phys. Rev. Lett.* **105**, 077402 (2010) (cited on page 15).

- ¹¹⁹D. Bossini, A. M. Kalashnikova, R. V. Pisarev, T. Rasing, and A. V. Kimel, “Controlling coherent and incoherent spin dynamics by steering the photoinduced energy flow”, *Phys. Rev. B* **89**, 060405 (2014) (cited on page 15).
- ¹²⁰A. M. Kalashnikova, A. V. Kimel, R. V. Pisarev, V. N. Gridnev, P. A. Usachev, A. Kirilyuk, and T. Rasing, “Impulsive excitation of coherent magnons and phonons by subpicosecond laser pulses in the weak ferromagnet FeBO₃”, *Phys. Rev. B* **78**, 104301 (2008) (cited on page 15).
- ¹²¹A. M. Kalashnikova, A. V. Kimel, R. V. Pisarev, V. N. Gridnev, A. Kirilyuk, and T. Rasing, “Impulsive generation of coherent magnons by linearly polarized light in the easy-plane antiferromagnet FeBO₃”, *Phys. Rev. Lett.* **99**, 167205 (2007) (cited on page 15).
- ¹²²T. Li, A. Patz, L. Mouchliadis, J. Yan, T. A. Lograsso, I. E. Perakis, and J. Wang, “Femtosecond switching of magnetism via strongly correlated spin–charge quantum excitations”, *Nature* **496**, 69–73 (2013) (cited on page 15).
- ¹²³A. Kirilyuk, A. V. Kimel, and T. Rasing, “Ultrafast optical manipulation of magnetic order”, *Rev. Mod. Phys.* **82**, 2731–2784 (2010) (cited on page 15).
- ¹²⁴T. Kubacka, J. A. Johnson, M. C. Hoffmann, C. Vicario, S. de Jong, P. Beaud, S. Grübel, S.-W. Huang, L. Huber, L. Patthey, Y.-D. Chuang, J. J. Turner, G. L. Dakovski, W.-S. Lee, M. P. Minitti, W. Schlotter, R. G. Moore, C. P. Hauri, S. M. Koohpayeh, V. Scagnoli, G. Ingold, S. L. Johnson, and U. Staub, “Large-amplitude spin dynamics driven by a THz pulse in resonance with an electromagnon”, *Science* **343**, 1333–1336 (2014) (cited on page 15).
- ¹²⁵S. Bonetti, M. C. Hoffmann, M.-J. Sher, Z. Chen, S.-H. Yang, M. G. Samant, S. S. P. Parkin, and H. A. Dürr, “THz-driven ultrafast spin-lattice scattering in amorphous metallic ferromagnets”, *Phys. Rev. Lett.* **117**, 087205 (2016) (cited on page 15).
- ¹²⁶A. V. Kimel, R. V. Pisarev, J. Hohlfeld, and T. Rasing, “Ultrafast quenching of the antiferromagnetic order in FeBO₃: Direct optical probing of the phonon-magnon coupling”, *Phys. Rev. Lett.* **89**, 287401 (2002) (cited on page 15).
- ¹²⁷K. Uchida, S. Takahashi, K. Harii, J. Ieda, W. Koshibae, K. Ando, S. Maekawa, and E. Saitoh, “Observation of the spin seebeck effect”, *Nature* **455**, 778–781 (2008) (cited on page 15).
- ¹²⁸K. Uchida, J. Xiao, H. Adachi, J. Ohe, S. Takahashi, J. Ieda, T. Ota, Y. Kajiwara, H. Umezawa, H. Kawai, G. E. W. Bauer, S. Maekawa, and E. Saitoh, “Spin seebeck insulator”, *Nature Materials* **9**, 894–897 (2010) (cited on page 15).
- ¹²⁹P.-H. Shih, C.-L. Cheng, and S. Y. Wu, “Short-range spin-phonon coupling in in-plane CuO nanowires: A low-temperature raman investigation”, *Nanoscale Research Letters* **8**, 398 (2013) (cited on page 15).

- ¹³⁰J.-W. Kim, M. Vomir, and J.-Y. Bigot, “Ultrafast magnetoacoustics in nickel films”, *Phys. Rev. Lett.* **109**, 166601 (2012) (cited on page 15).
- ¹³¹T. F. Nova, A. Cartella, A. Cantaluppi, M. Först, D. Bossini, R. V. Mikhaylov, A. V. Kimel, R. Merlin, and A. Cavalleri, “An effective magnetic field from optically driven phonons”, *Nature Physics* **13**, 132–136 (2017) (cited on page 15).
- ¹³²A. V. Scherbakov, A. S. Salasyuk, A. V. Akimov, X. Liu, M. Bombeck, C. Brüggemann, D. R. Yakovlev, V. F. Sapega, J. K. Furdyna, and M. Bayer, “Coherent magnetization precession in ferromagnetic (Ge,Mn)As induced by picosecond acoustic pulses”, *Phys. Rev. Lett.* **105**, 117204 (2010) (cited on page 15).
- ¹³³M. Fechner, A. Sukhov, L. Chotorlishvili, C. Kenel, J. Berakdar, and N. A. Spaldin, “Magnetophononics: Ultrafast spin control through the lattice”, *Phys. Rev. Materials* **2**, 064401 (2018) (cited on pages 15, 45).
- ¹³⁴F. Giorgianni, B. Wehinger, S. Allenspach, N. Colonna, C. Vicario, P. Puphal, E. Pomjakushina, B. Normand, and C. Rüegg, “Nonlinear quantum magnetophononics in $\text{SrCu}_2(\text{BO}_3)_2$ ”, (2021) (cited on pages 15, 50, 80).
- ¹³⁵G. Lindblad, “On the generators of quantum dynamical semigroups”, *Comm. Math. Phys.* **48**, 119–130 (1976) (cited on pages 15, 31, 40, 53).
- ¹³⁶C.-K. Chan, T. E. Lee, and S. Gopalakrishnan, “Limit-cycle phase in driven-dissipative spin systems”, *Phys. Rev. A* **91**, 051601 (2015) (cited on page 15).
- ¹³⁷R. M. Wilson, K. W. Mahmud, A. Hu, A. V. Gorshkov, M. Hafezi, and M. Foss-Feig, “Collective phases of strongly interacting cavity photons”, *Phys. Rev. A* **94**, 033801 (2016) (cited on page 15).
- ¹³⁸M. Schiró, C. Joshi, M. Bordyuh, R. Fazio, J. Keeling, and H. E. Türeci, “Exotic attractors of the nonequilibrium Rabi-Hubbard model”, *Phys. Rev. Lett.* **116**, 143603 (2016) (cited on page 15).
- ¹³⁹J. Jin, D. Rossini, R. Fazio, M. Leib, and M. J. Hartmann, “Photon solid phases in driven arrays of nonlinearly coupled cavities”, *Phys. Rev. Lett.* **110**, 163605 (2013) (cited on page 15).
- ¹⁴⁰J. Jin, D. Rossini, M. Leib, M. J. Hartmann, and R. Fazio, “Steady-state phase diagram of a driven QED-cavity array with cross-Kerr nonlinearities”, *Phys. Rev. A* **90**, 023827 (2014) (cited on page 15).
- ¹⁴¹T. E. Lee, H. Häffner, and M. C. Cross, “Antiferromagnetic phase transition in a nonequilibrium lattice of c atoms”, *Phys. Rev. A* **84**, 031402 (2011) (cited on page 15).
- ¹⁴²M. Marcuzzi, E. Levi, S. Diehl, J. P. Garrahan, and I. Lesanovsky, “Universal nonequilibrium properties of dissipative Rydberg gases”, *Phys. Rev. Lett.* **113**, 210401 (2014) (cited on page 15).

- ¹⁴³F. Letscher, O. Thomas, T. Niederprüm, M. Fleischhauer, and H. Ott, “Bistability versus metastability in driven dissipative Rydberg gases”, *Phys. Rev. X* **7**, 021020 (2017) (cited on page 15).
- ¹⁴⁴C. D. Parmee and N. R. Cooper, “Phases of driven two-level systems with nonlocal dissipation”, *Phys. Rev. A* **97**, 053616 (2018) (cited on page 15).
- ¹⁴⁵M. Foss-Feig, P. Niroula, J. T. Young, M. Hafezi, A. V. Gorshkov, R. M. Wilson, and M. F. Maghrebi, “Emergent equilibrium in many-body optical bistability”, *Phys. Rev. A* **95**, 043826 (2017) (cited on page 15).
- ¹⁴⁶M. Biondi, G. Blatter, H. E. Türeci, and S. Schmidt, “Nonequilibrium gas-liquid transition in the driven-dissipative photonic lattice”, *Phys. Rev. A* **96**, 043809 (2017) (cited on page 15).
- ¹⁴⁷N. Tsuji, T. Oka, and H. Aoki, “Nonequilibrium steady state of photoexcited correlated electrons in the presence of dissipation”, *Phys. Rev. Lett.* **103**, 047403 (2009) (cited on page 15).
- ¹⁴⁸D. Vorberg, W. Wustmann, R. Ketzmerick, and A. Eckardt, “Generalized Bose-Einstein condensation into multiple states in driven-dissipative systems”, *Phys. Rev. Lett.* **111**, 240405 (2013) (cited on page 15).
- ¹⁴⁹K. I. Seetharam, C.-E. Bardyn, N. H. Lindner, M. S. Rudner, and G. Refael, “Controlled population of Floquet-Bloch states via coupling to Bose and Fermi baths”, *Phys. Rev. X* **5**, 041050 (2015) (cited on page 15).
- ¹⁵⁰A. Tomadin, S. Diehl, and P. Zoller, “Nonequilibrium phase diagram of a driven and dissipative many-body system”, *Phys. Rev. A* **83**, 013611 (2011) (cited on page 15).
- ¹⁵¹T. Qin and W. Hofstetter, “Nonequilibrium steady states and resonant tunneling in time-periodically driven systems with interactions”, *Phys. Rev. B* **97**, 125115 (2018) (cited on page 15).
- ¹⁵²A. Panda and S. Banerjee, “Entanglement in nonequilibrium steady states and many-body localization breakdown in a current-driven system”, *Phys. Rev. B* **101**, 184201 (2020) (cited on page 15).
- ¹⁵³M. Carrega, P. Solinas, M. Sassetti, and U. Weiss, “Energy exchange in driven open quantum systems at strong coupling”, *Phys. Rev. Lett.* **116**, 240403 (2016) (cited on page 15).
- ¹⁵⁴H. Landa, M. Schiró, and G. Misguich, “Multistability of driven-dissipative quantum spins”, *Phys. Rev. Lett.* **124**, 043601 (2020) (cited on page 15).
- ¹⁵⁵H. Landa, M. Schiró, and G. Misguich, “Correlation-induced steady states and limit cycles in driven dissipative quantum systems”, *Phys. Rev. B* **102**, 064301 (2020) (cited on page 15).

- ¹⁵⁶S. Yamamoto, “Critical exponent η in $S = 1$ antiferromagnetic heisenberg chains with alternating interaction”, *Phys. Rev. B* **52**, 10170–10176 (1995) (cited on page 16).
- ¹⁵⁷M. Hase, I. Terasaki, and K. Uchinokura, “Observation of the spin-Peierls transition in linear Cu^{2+} (spin-1/2) chains in an inorganic compound CuGeO_3 ”, *Phys. Rev. Lett.* **70**, 3651–3654 (1993) (cited on pages 16, 38, 80).
- ¹⁵⁸M. Azuma, T. Saito, Y. Fujishiro, Z. Hiroi, M. Takano, F. Izumi, T. Kamiyama, T. Ikeda, Y. Narumi, and K. Kindo, “High-pressure form of $(\text{VO})_2\text{P}_2\text{O}_7$: a spin- $\frac{1}{2}$ antiferromagnetic alternating-chain compound with one kind of chain and a single spin gap”, *Phys. Rev. B* **60**, 10145–10149 (1999) (cited on page 16).
- ¹⁵⁹G. S. Uhrig, “Symmetry and dimension of the magnon dispersion of inorganic spin-Peierls systems”, *Phys. Rev. Lett.* **79**, 163–166 (1997) (cited on pages 16, 38, 74, 80).
- ¹⁶⁰I. Loa, S. Gronemeyer, C. Thomsen, and R. Kremer, “Spin gap and spin-phonon interaction in CuGeO_3 ”, *Solid State Communications* **99**, 231–235 (1996) (cited on pages 16, 39, 80).
- ¹⁶¹R. Werner, C. Gros, and M. Braden, “Microscopic spin-phonon coupling constants in CuGeO_3 ”, *Phys. Rev. B* **59**, 14356–14366 (1999) (cited on pages 16, 39, 41, 80).
- ¹⁶²D. C. Johnston, J. W. Johnson, D. P. Goshorn, and A. J. Jacobson, “Magnetic susceptibility of $(\text{VO})_2\text{P}_2\text{O}_7$: A one-dimensional spin-1/2 Heisenberg antiferromagnet with a ladder spin configuration and a singlet ground state”, *Phys. Rev. B* **35**, 219–222 (1987) (cited on pages 16, 39, 80).
- ¹⁶³T. Barnes and J. Riera, “Susceptibility and excitation spectrum of $(\text{VO})_2\text{P}_2\text{O}_7$ in ladder and dimer-chain models”, *Phys. Rev. B* **50**, 6817–6822 (1994) (cited on pages 16, 39, 80).
- ¹⁶⁴G. S. Uhrig and B. Normand, “Magnetic properties of $(\text{VO})_2\text{P}_2\text{O}_7$ from frustrated interchain coupling”, *Phys. Rev. B* **58**, R14705–R14708 (1998) (cited on pages 16, 39, 80).
- ¹⁶⁵G. S. Uhrig and B. Normand, “Magnetic properties of $(\text{VO})_2\text{P}_2\text{O}_7$: two-plane structure and spin-phonon interactions”, *Phys. Rev. B* **63**, 134418 (2001) (cited on pages 16, 39, 80).
- ¹⁶⁶D. A. Tennant, B. Lake, A. J. A. James, F. H. L. Essler, S. Notbohm, H.-J. Mikeska, J. Fielden, P. Kögerler, P. C. Canfield, and M. T. F. Telling, “Anomalous dynamical line shapes in a quantum magnet at finite temperature”, *Phys. Rev. B* **85**, 014402 (2012) (cited on pages 16, 39, 76).

- ¹⁶⁷U. Arjun, K. M. Ranjith, B. Koo, J. Sichelschmidt, Y. Skourski, M. Baenitz, A. A. Tsirlin, and R. Nath, “Singlet ground state in the alternating spin- $\frac{1}{2}$ chain compound NaVOAsO₄”, *Phys. Rev. B* **99**, 014421 (2019) (cited on pages 17, 39).
- ¹⁶⁸N. Ahmed, P. Khuntia, K. M. Ranjith, H. Rosner, M. Baenitz, A. A. Tsirlin, and R. Nath, “Alternating spin chain compound AgVOAsO₄ probed by ⁷⁵As NMR”, *Phys. Rev. B* **96**, 224423 (2017) (cited on pages 17, 39).
- ¹⁶⁹M. Yarmohammadi, C. Meyer, B. Fauseweh, B. Normand, and G. S. Uhrig, “Dynamical properties of a driven dissipative dimerized $S = 1/2$ chain”, *Phys. Rev. B* **103**, 045132 (2021) (cited on pages 17, 53, 71, 80, 82, 99).
- ¹⁷⁰M. Yarmohammadi, M. Krebs, G. S. Uhrig, and B. Normand, “Giant resonant self-blocking in magnetophononically driven quantum magnets”, (2021) (cited on pages 17, 80, 103, 116).
- ¹⁷¹S. Sachdev and R. N. Bhatt, “Bond-operator representation of quantum spins: Mean-field theory of frustrated quantum Heisenberg antiferromagnets”, *Phys. Rev. B* **41**, 9323–9329 (1990) (cited on pages 21, 22, 42).
- ¹⁷²K. P. Schmidt, C. Knetter, and G. S. Uhrig, “Spectral properties of the dimerized and frustrated $S = 1/2$ chain”, *Phys. Rev. B* **69**, 104417 (2004) (cited on page 21).
- ¹⁷³B. Normand and C. Rüegg, “Complete bond-operator theory of the two-chain spin ladder”, *Phys. Rev. B* **83**, 054415 (2011) (cited on pages 21, 43, 44).
- ¹⁷⁴C. Knetter and G. S. Uhrig, “Perturbation theory by flow equations: Dimerized and frustrated $S = 1/2$ chain”, *The European Physical Journal B - Condensed Matter and Complex Systems* **13**, 209–225 (2000) (cited on pages 21, 43, 110).
- ¹⁷⁵S. Gopalan, T. M. Rice, and M. Sigrist, “Spin ladders with spin gaps: A description of a class of cuprates”, *Phys. Rev. B* **49**, 8901–8910 (1994) (cited on pages 21, 42).
- ¹⁷⁶B. Kumar, “Bond operators and triplon analysis for spin- S dimer antiferromagnets”, *Phys. Rev. B* **82**, 054404 (2010) (cited on page 21).
- ¹⁷⁷W. Magnus, “On the exponential solution of differential equations for a linear operator”, *Communications on Pure and Applied Mathematics* **7**, 649–673 (1954) (cited on page 24).
- ¹⁷⁸D. N. Basov, R. D. Averitt, D. van der Marel, M. Dressel, and K. Haule, “Electrodynamics of correlated electron materials”, *Rev. Mod. Phys.* **83**, 471–541 (2011) (cited on page 26).
- ¹⁸²P. Pearle, “Simple derivation of the Lindblad equation”, *European Journal of Physics* **33**, 805–822 (2012) (cited on page 31).
- ¹⁸⁵F. A. Lindemann, “The calculation of molecular vibration frequencies”, *Phys. Z.* **11**, 609–612 (1910) (cited on pages 33, 80).

- ¹⁸⁶D. A. Kofke and P. G. Bolhuis, “Freezing of polydisperse hard spheres”, *Phys. Rev. E* **59**, 618–622 (1999) (cited on page 33).
- ¹⁸⁷P. G. Bolhuis and D. A. Kofke, “Monte Carlo study of freezing of polydisperse hard spheres”, *Phys. Rev. E* **54**, 634–643 (1996) (cited on page 33).
- ¹⁸⁸F. H. Stillinger and T. A. Weber, “Lindemann melting criterion and the Gaussian core model”, *Phys. Rev. B* **22**, 3790–3794 (1980) (cited on page 33).
- ¹⁸⁹J. E. Lorenzo, K. Hirota, G. Shirane, J. M. Tranquada, M. Hase, K. Uchinokura, H. Kojima, I. Tanaka, and Y. Shibuya, “Soft longitudinal modes in spin-singlet CuGeO_3 ”, *Phys. Rev. B* **50**, 1278–1281 (1994) (cited on page 38).
- ¹⁹⁰M. Nishi, O. Fujita, and J. Akimitsu, “Neutron-scattering study on the spin-Peierls transition in a quasi-one-dimensional magnet CuGeO_3 ”, *Phys. Rev. B* **50**, 6508–6510 (1994) (cited on page 38).
- ¹⁹¹J. Riera and A. Dobry, “Magnetic susceptibility in the spin-Peierls system CuGeO_3 ”, *Phys. Rev. B* **51**, 16098–16102 (1995) (cited on page 38).
- ¹⁹²K. Fabricius, A. Klümper, U. Löw, B. Büchner, T. Lorenz, G. Dhalenne, and A. Revcolevschi, “Reexamination of the microscopic couplings of the quasi-one-dimensional antiferromagnet CuGeO_3 ”, *Phys. Rev. B* **57**, 1102–1107 (1998) (cited on page 38).
- ¹⁹³M. Arai, M. Fujita, M. Motokawa, J. Akimitsu, and S. M. Bennington, “Quantum spin excitations in the spin-Peierls system CuGeO_3 ”, *Phys. Rev. Lett.* **77**, 3649–3652 (1996) (cited on page 38).
- ¹⁹⁴J. P. Schoeffel, J. P. Pouget, G. Dhalenne, and A. Revcolevschi, “Spin-Peierls lattice fluctuations of pure and si- and zn-substituted CuGeO_3 ”, *Phys. Rev. B* **53**, 14971–14979 (1996) (cited on page 38).
- ¹⁹⁵P. H. M. van Loosdrecht, J. P. Boucher, G. Martinez, G. Dhalenne, and A. Revcolevschi, “Inelastic light scattering from magnetic fluctuations in CuGeO_3 ”, *Phys. Rev. Lett.* **76**, 311–314 (1996) (cited on page 38).
- ¹⁹⁶G. Els, P. H. M. van Loosdrecht, P. Lemmens, H. Vonberg, G. Güntherodt, G. S. Uhrig, O. Fujita, J. Akimitsu, G. Dhalenne, and A. Revcolevschi, “Observation of three-magnon light scattering in CuGeO_3 ”, *Phys. Rev. Lett.* **79**, 5138–5141 (1997) (cited on page 38).
- ¹⁹⁷G. Castilla, S. Chakravarty, and V. J. Emery, “Quantum magnetism of CuGeO_3 ”, *Phys. Rev. Lett.* **75**, 1823–1826 (1995) (cited on page 38).
- ¹⁹⁸R. Chitra, S. Pati, H. R. Krishnamurthy, D. Sen, and S. Ramasesha, “Density-matrix renormalization-group studies of the spin-1/2 Heisenberg system with dimerization and frustration”, *Phys. Rev. B* **52**, 6581–6587 (1995) (cited on page 38).

- ¹⁹⁹G. S. Uhrig and H. J. Schulz, “Magnetic excitation spectrum of dimerized antiferromagnetic chains”, *Phys. Rev. B* **54**, R9624–R9627 (1996) (cited on page 38).
- ²⁰⁰W. Brenig, “Magnetic excitations in quasi-two-dimensional spin-Peierls systems”, *Phys. Rev. B* **56**, 14441–14448 (1997) (cited on page 38).
- ²⁰¹G. Bouzerar, A. P. Kampf, and G. I. Japaridze, “Elementary excitations in dimerized and frustrated Heisenberg chains”, *Phys. Rev. B* **58**, 3117–3123 (1998) (cited on page 38).
- ²⁰²M. Braden, G. Wilkendorf, J. Lorenzana, M. Am, G. J. McIntyre, M. Behruzi, G. Heger, G. Dhalenne, and A. Revcolevschi, “Structural analysis of CuGeO_3 : Relation between nuclear structure and magnetic interaction”, *Phys. Rev. B* **54**, 1105–1116 (1996) (cited on page 38).
- ²⁰⁴G. Khaliullin and V. Oudovenko, “Spin and orbital excitation spectrum in the kugel-khomskii model”, *Phys. Rev. B* **56**, R14243–R14246 (1997) (cited on page 39).
- ²⁰⁵K. I. Kugel’ and D. I. Khomskii, “The jahn-teller effect and magnetism: transition metal compounds”, *Soviet Physics Uspekhi* **25**, 231–256 (1982) (cited on page 39).
- ²⁰⁶M. C. Cross and D. S. Fisher, “A new theory of the spin-Peierls transition with special relevance to the experiments on TTFCuBDT ”, *Phys. Rev. B* **19**, 402–419 (1979) (cited on page 39).
- ²⁰⁷S. Huizinga, J. Kommandeur, G. A. Sawatzky, B. T. Thole, K. Kopinga, W. J. M. de Jonge, and J. Roos, “Spin-Peierls transition in n-methyl-n-ethyl-morpholinium-ditetra-cyanoquinodimethanide $[\text{MEM}-(\text{TCNQ})_2]$ ”, *Phys. Rev. B* **19**, 4723–4732 (1979) (cited on page 39).
- ²⁰⁸Y. Miura, R. Hirai, Y. Kobayashi, and M. Sato, “Spin-gap behavior of $\text{Na}_3\text{CuSbO}_6$ with distorted honeycomb structure”, *Journal of the Physical Society of Japan* **75**, 084707 (2006) (cited on page 39).
- ²⁰⁹M. B. Stone, W. Tian, M. D. Lumsden, G. E. Granroth, D. Mandrus, J.-H. Chung, N. Harrison, and S. E. Nagler, “Quantum spin correlations in an organometallic alternating-sign chain”, *Phys. Rev. Lett.* **99**, 087204 (2007) (cited on page 39).
- ²¹⁰G. S. Uhrig, “Nonadiabatic approach to spin-Peierls transitions via flow equations”, *Phys. Rev. B* **57**, R14004–R14007 (1998) (cited on page 40).
- ²¹¹A. Weiße, G. Wellein, and H. Fehske, “Quantum lattice fluctuations in a frustrated Heisenberg spin-Peierls chain”, *Phys. Rev. B* **60**, 6566–6573 (1999) (cited on page 40).

- ²¹²R. J. Bursill, R. H. McKenzie, and C. J. Hamer, “Phase diagram of a Heisenberg spin-Peierls model with quantum phonons”, *Phys. Rev. Lett.* **83**, 408–411 (1999) (cited on page 40).
- ²¹³A. W. Sandvik and D. K. Campbell, “Spin-Peierls transition in the Heisenberg chain with finite-frequency phonons”, *Phys. Rev. Lett.* **83**, 195–198 (1999) (cited on page 40).
- ²¹⁵S. Bräuninger, U. Schwarz, M. Hanfland, T. Zhou, R. K. Kremer, and K. Syassen, “Crystal structure of CuGeO_3 under pressure”, *Phys. Rev. B* **56**, R11357–R11360 (1997) (cited on page 41).
- ²¹⁶S. Streib and P. Kopietz, “Hard-core boson approach to the spin $-\frac{1}{2}$ triangular-lattice antiferromagnet Cs_2CuCl_4 at finite temperatures in magnetic fields higher than the saturation field”, *Phys. Rev. B* **92**, 094442 (2015) (cited on page 42).
- ²¹⁷C. Knetter, K. P. Schmidt, and G. S. Uhrig, “The structure of operators in effective particle-conserving models”, *Journal of Physics A: Mathematical and General* **36**, 7889–7907 (2003) (cited on page 43).
- ²¹⁸H. Krull, N. A. Drescher, and G. S. Uhrig, “Enhanced perturbative continuous unitary transformations”, *Phys. Rev. B* **86**, 125113 (2012) (cited on page 43).
- ²²³T. Lorenz, H. Kierspel, S. Kleefisch, B. Büchner, E. Gamper, A. Revcolevschi, and G. Dhalenne, “Specific heat, thermal expansion, and pressure dependencies of the transition temperatures of doped CuGeO_3 ”, *Phys. Rev. B* **56**, R501–R504 (1997) (cited on page 75).
- ²²⁴C. Ecolivet, M. Saint-Paul, G. Dhalenne, and A. Revcolevschi, “Brillouin scattering and ultrasonic measurements of the elastic constants of CuGeO_3 ”, *Journal of Physics: Condensed Matter* **11**, 4157–4162 (1999) (cited on page 75).
- ²²⁵M. Hofmann, T. Lorenz, A. Freimuth, G. Uhrig, H. Kageyama, Y. Ueda, G. Dhalenne, and A. Revcolevschi, “Heat transport in $\text{SrCu}_2(\text{BO}_3)_2$ and CuGeO_3 ”, *Physica B: Condensed Matter* **312-313**, The International Conference on Strongly Correlated Electron Systems, 597–599 (2002) (cited on page 75).
- ²²⁶P. Duthil, “Material properties at low temperature”, CERN Yellow Report CERN **5**, 77–95 (2014) (cited on page 76).
- ²²⁷N. Hlubek, P. Ribeiro, R. Saint-Martin, S. Nishimoto, A. Revcolevschi, S.-L. Drechsler, G. Behr, J. Trinckauf, J. E. Hamann-Borrero, J. Geck, B. Büchner, and C. Hess, “Bond disorder and breakdown of ballistic heat transport in the spin- $\frac{1}{2}$ antiferromagnetic Heisenberg chain as seen in Ca-doped SrCuO_2 ”, *Phys. Rev. B* **84**, 214419 (2011) (cited on page 77).

- ²²⁸A. Mohan, N. S. Beesetty, N. Hlubek, R. Saint-Martin, A. Revcolevschi, B. Büchner, and C. Hess, “Bond disorder and spinon heat transport in the $S = \frac{1}{2}$ Heisenberg spin chain compound Sr_2CuO_3 : From clean to dirty limits”, *Phys. Rev. B* **89**, 104302 (2014) (cited on page 77).
- ²²⁹A. L. Chernyshev and A. V. Rozhkov, “Heat transport in spin chains with weak spin-phonon coupling”, *Phys. Rev. Lett.* **116**, 017204 (2016) (cited on page 77).
- ²³⁰X. Chen, J. Carrete, S. Sullivan, A. van Roekeghem, Z. Li, X. Li, J. Zhou, N. Mingo, and L. Shi, “Coupling of spinons with defects and phonons in the spin chain compound Ca_2CuO_3 ”, *Phys. Rev. Lett.* **122**, 185901 (2019) (cited on page 77).

Books and Dissertations

- ¹J. Sakurai and J. Napolitano, *Modern quantum mechanics* (Addison-Wesley, 2011) (cited on pages 12, 23).
- ²D. Griffiths, *Introduction to quantum mechanics* (Cambridge University Press, 2017) (cited on page 12).
- ⁶M. Nielsen and I. Chuang, *Quantum computation and quantum information: 10th anniversary edition* (Cambridge University Press, 2010) (cited on page 13).
- ⁷S. Stenholm and K. Suominen, *Quantum approach to informatics* (Wiley, 2005) (cited on page 13).
- ²⁷H. Breuer and F. Petruccione, *The theory of open quantum systems* (OUP Oxford, 2007) (cited on pages 13, 15, 40, 53).
- ²⁸S. Haroche, J. Raimond, and O. U. Press, *Exploring the quantum: Atoms, cavities, and photons*, Oxford Graduate Texts (OUP Oxford, 2006) (cited on page 13).
- ²⁹Y. Yamamoto, F. Tassone, and H. Cao, *Semiconductor cavity quantum electrodynamics*, Springer Tracts in Modern Physics (Springer Berlin Heidelberg, 2000) (cited on page 13).
- ⁷¹W. Demtröder, *Laser spectroscopy*, Topics in Current Chemistry (Springer Berlin Heidelberg, 1971) (cited on page 14).
- ⁷²V. Letokhov and V. Chebotayev, *Nonlinear laser spectroscopy*, Springer Optical Sciences Ser, Vol. 4 (Springer-Verlag, 1977) (cited on page 14).
- ⁷³C. Gardiner, P. Zoller, and P. Zoller, *Quantum noise: A handbook of Markovian and non-Markovian quantum stochastic methods with applications to quantum optics*, Springer Series in Synergetics (Springer, 2004) (cited on page 14).
- ⁸¹W. T. Strunz, *Decoherence in quantum physics*, edited by A. Buchleitner and K. Hornberger (Springer Berlin Heidelberg, Berlin, Heidelberg, 2002), pages 199–233 (cited on page 14).

- ⁸²G.-L. Ingold, *Path integrals and their application to dissipative quantum systems*, edited by A. Buchleitner and K. Hornberger (Springer Berlin Heidelberg, Berlin, Heidelberg, 2002), pages 1–53 (cited on page 14).
- ¹⁰³D. M. Ginsberg, *Physical properties of high temperature superconductors iii* (WORLD SCIENTIFIC, 1992) (cited on pages 14, 37).
- ¹⁷⁹R. Prasankumar and A. Taylor, *Optical techniques for solid-state materials characterization* (CRC Press, 2016) (cited on page 26).
- ¹⁸⁰J. Cheng and X. Xie, *Coherent raman scattering microscopy*, Series in Cellular and Clinical Imaging (Taylor & Francis, 2012) (cited on page 26).
- ¹⁸¹H. Breuer, P. Breuer, F. Petruccione, and S. Petruccione, *The theory of open quantum systems* (Oxford University Press, 2002) (cited on page 31).
- ¹⁸³B.-G. Englert and G. Morigi, *Five lectures on dissipative master equations*, edited by A. Buchleitner and K. Hornberger (Springer Berlin Heidelberg, Berlin, Heidelberg, 2002), pages 55–106 (cited on page 32).
- ¹⁸⁴C. Gardiner, C. Gardiner, and P. Zoller, *Quantum noise: A handbook of Markovian and non-Markovian quantum stochastic methods with applications to quantum optics*, Springer series in synergetics (Springer, 2000) (cited on page 32).
- ²⁰³R. Werner, *The spin-Peierls transition in CuGeO_3* (Technische Universität Dortmund, 1999) (cited on page 38).
- ²¹⁴J. Miller, *Extended linear chain compounds*, Extended Linear Chain Compounds v. 3 (Plenum Press, 1982) (cited on page 41).
- ²¹⁹M. Galassi and *et al.*, *Gnu scientific library reference manual (3rd ed.)* Network Theory Ltd. (2009) (cited on page 50).
- ²²⁰C. Meyer, *Dynamics of a dimerized $S = 1/2$ chain continuously driven via a coupled phonon* (2018) (cited on page 50).
- ²²¹MATLAB, *9.7.0.1190202 (r2019b)* (The MathWorks Inc., Natick, Massachusetts, 2018) (cited on page 50).
- ²²²W. Nolting, *Grundkurs theoretische physik 1: Klassische mechanik*, Springer-Lehrbuch (Springer Berlin Heidelberg, 2010) (cited on page 55).